

ASSESSMENT OF TUNNEL INDUCED DEFORMATION FIELD  
THROUGH 3-DIMENSIONAL NUMERICAL MODELS  
(NECATIBEY SUBWAY STATION, ANKARA, TURKEY)

A THESIS SUBMITTED TO  
THE GRADUATE SCHOOL OF NATURAL AND APPLIED SCIENCES  
OF  
MIDDLE EAST TECHNICAL UNIVERSITY

BY

ÖZGÜR AKTÜRK

IN PARTIAL FULFILMENT OF THE REQUIREMENTS  
FOR  
THE DEGREE OF DOCTOR OF PHILOSOPHY  
IN  
GEOLOGICAL ENGINEERING

SEPTEMBER 2010

Approval of the thesis:

**ASSESSMENT OF TUNNEL INDUCED DEFORMATION FIELD  
THROUGH 3-DIMENSIONAL NUMERICAL MODELS  
(NECATIBEY SUBWAY STATION, ANKARA, TURKEY)**

submitted by **ÖZGÜR AKTÜRK** in partial fulfillment of the requirements for the degree of **Doctor of Philosophy in Geological Engineering Department, Middle East Technical University** by,

Prof. Dr. Canan Özgen  
Dean, Graduate School of Natural and Applied Sciences

\_\_\_\_\_

Prof. Dr. M. Zeki Çamur  
Head of Department, **Geological Engineering**

\_\_\_\_\_

Prof. Dr. Vedat Doyuran  
Supervisor, **Geological Engineering Dept., METU**

\_\_\_\_\_

**Examining Committee Members:**

Prof. Dr. Nurkan Karahanoğlu  
Geological Engineering Dept., METU

\_\_\_\_\_

Prof. Dr. Vedat Doyuran  
Geological Engineering Dept., METU

\_\_\_\_\_

Prof. Dr. Reşat Ulusay  
Geological Engineering Dept., Hacettepe University

\_\_\_\_\_

Prof. Dr. Kemal Önder Çetin  
Civil Engineering Dept., METU

\_\_\_\_\_

Assist. Prof. Dr. Nihat Sinan Işık  
Construction Dept., Faculty of Technical Education, Gazi University

\_\_\_\_\_

**Date:** September 17, 2010

**I hereby declare that all information in this document has been obtained and presented in accordance with academic rules and ethical conduct. I also declare that, as required by these rules and conduct, I have fully cited and referenced all material and results that are not original to this work.**

Name, Last name: Özgür Aktürk

Signature :

## **ABSTRACT**

### **ASSESSMENT OF TUNNEL INDUCED DEFORMATION FIELD THROUGH 3-DIMENSIONAL NUMERICAL MODELS (NECATIBEY SUBWAY STATION, ANKARA, TURKEY)**

Aktürk, Özgür

Ph.D., Department of Geological Engineering

Supervisor: Prof. Dr. Vedat Doyuran

September 2010, 262 pages

In heavily settled areas, deformations induced by the tunnel excavation may cause serious damage to nearby structures. In this study it is aimed to model ground deformations induced by main tunnels and connection tunnels excavations as well as groundwater drainage. Therefore, it is necessary to study effective means of controlling tunnel induced deformations. The main parameters affecting the failure and deformation state of the soil around a circular underground opening are the physical characteristics of the soil, the diameter of the opening, and the support pressure. During the construction stage of Necatibey Station of Kızılay-Çayyolu metro line (Ankara, Turkey), challenging ground conditions involving highly heterogeneous and locally water saturated foundation soils have been encountered. Possibility of damage at the surface and/or on the underground structures can be estimated using finite difference method (FDM) of analysis.

In this study, two geophysical methods namely Electrical Resistivity Imaging (ERI) and Ground Penetrating Radar (GPR) were utilized to distinguish soil types at the study area. By correlating these geophysical survey results with the boring



logs, 3-Dimensional soil profile was revealed at the study area to build up a basis for numerical models.

3-Dimensional (3D) FDM analyses were conducted to assess tunneling induced deformations, along with movements around shallow soft ground main tunnels and connection tunnels. During sequential excavations, temporary and permanent shotcrete lining was also simulated. The soil behavior is assumed to be governed by an elastic-perfectly plastic constitutive relation based on the Mohr–Coulomb criterion. The computed deformations around these openings have been compared with the in-situ measurements. The results of the study revealed that the 3-D elasto-plastic analyses yield comparably good correlation with the in-situ measurements. Also, in this study, the effects of main tunnels excavations on each other and the effects of connection tunnels excavations on main tunnels were identified in terms of ground deformations. In order to simulate induced surface settlement due to groundwater withdrawal at the site 3-D fully coupled (fluid-mechanical) numerical models were run using different time durations. The model studies revealed that deformations monitored at the ground surface are directly related with the tunnel construction practice. Pumping groundwater has very little or no effect on the measured deformations.

**Key words:** Kızılay-Çayyolu metro line, Necatibey Station, circular opening, ERI, GPR, 3-D numerical modeling, finite difference method, elastic-perfectly plastic constitutive relation.

## ÖZ

### **TÜNEL ÇEVRESİNDEKİ DEFORMASYON ALANININ 3-BOYUTLU SAYISAL MODELLER İLE DEĞERLENDİRİLMESİ (NECATİBEY METRO İSTASYONU, ANKARA, TÜRKİYE)**

Aktürk, Özgür

Doktora, Jeoloji Mühendisliği Bölümü

Tez Yöneticisi: Prof. Dr. Vedat Doyuran

Eylül 2010, 262 sayfa

Yoğun yerleşim alanlarında tünel inşaatından kaynaklanan deformasyonlar çevredeki yapılarda hasarlara yol açabilir. Bu çalışmanın amacı, peron tünelleri ve bağlantı tünelleri kazıları ile yeraltısu drenajından kaynaklanan deformasyonları modellemektir. Bu nedenle, tünel inşasından kaynaklanacak deformasyonların boyutunun belirlenmesi gerekmektedir. Dairesel bir açıklığın çevresindeki zeminde yenilme ve deformasyon durumunu etkileyen ana parametreler; zeminin fiziksel özellikleri, açıklığın çapı ve destek basıncıdır. Kızılay-Çayyolu metro hattı, Necatibey İstasyonu (Ankara, Türkiye) kazıları sırasında heterojen ve suya doygun zemin koşullarınının yol açtığı önemli sorunlarla karşılaşmıştır. Bu çalışmada yüzey ve yeraltı yapılarında beklenen olası hasarlar için sonlu farklar yöntemi (FDM) kullanılmıştır.

Çalışma alanındaki zemin türlerini ayırt etmek için Elektrik Rezistivite Görüntülemesi (ERI) ve Yer Radarı (GPR) olmak üzere iki ayrı jeofizik yöntem kullanılmıştır. Bu yöntemlerden elde edilen sonuçların sondaj logları ile

karşılaştırmalı yorumlanmasıyla, sayısal modellere başlangıç oluşturması amacıyla inceleme alanının 3-boyutlu zemin profili oluşturulmuştur.

Tünel inşasından kaynaklanan ve peron ve bağlantı tünelleri boyunca oluşan deformasyonları değerlendirmek amacıyla üç boyutlu (3D) sonlu farklar yöntemine dayalı analizler yapılmıştır. Birbirini izleyen kazı aşamaları sırasında kullanılan geçici ve kalıcı püskürtme beton kaplama da ayrıca modellenmiştir. Zemin davranışının Mohr-Coulomb yenilme ölçütünü temel alan elastik-mükemmel plastik koşullara uyduğu kabul edilmiştir. Tüneller etrafındaki hesaplanan deformasyonlar yerinde ölçümlerle karşılaştırılmıştır. 3-boyutlu elasto-plastik analiz sonuçlarının yerinde ölçümlerle uyumlu olduğu görülmüştür. Bu çalışmada ayrıca, peron tünelleri kazılarının birbirlerine ve bağlantı tünelleri kazılarının da peron tünelleri üzerindeki etkileri deformasyonlar açısından belirlenmiştir. Çalışma alanındaki yeraltısu drenajından kaynaklanan deformasyonları simule etmek için değişik zaman aralıkları kullanılarak 3-boyutlu bağlaşıklık (coupled) analizler yapılmıştır. Model çalışmaları; yüzeyde ölçülen yerdeğiştirmelerin doğrudan tünel kazıları ile ilişkili ve su atım uygulamalarının etkisinin ise çok az ya da ihmal edilebilir düzeyde olduğunu göstermiştir.

**Anahtar kelimeler:** Kızılay-Çayyolu Metro hattı, Necatibey İstasyonu, dairesel açıklık, ERI, GPR, 3-D sayısal model, sonlu farklar yöntemi, elastik-mükemmel plastik koşul.

*To My Father, who offered me unconditional love and support throughout my life.*

## ACKNOWLEDGEMENTS

Prof. Dr. Vedat Doyuran... What this name means to me is more than I can possibly express. Prof. Doyuran was of great help and support for me throughout my studies. I had really hard times working on my thesis. Without Prof. Doyuran's expertise, supervision and great experience on the subject, it would have been impossible for me to complete my work. It was his invaluable guidance, endless patience and never ending encouragement that helped me find my path through the difficulties I had to encounter during this long and tiring and yet satisfying period. I feel lucky to have had the opportunity to work with such a person whose brilliance cannot be appreciated by some people. I should also state that I am happy to be his last student or else I would be jealous of the next ones. Lastly, I would like to extend my gratefulness to his wife for her encouragement as well.

Thanks are also due to the members of my dissertation committee: Prof. Dr. Nurkan Karahanoğlu and Assist. Prof. Dr. Nihat Sinan Işık, for their constructive suggestions and subjective comments throughout this research period.

I owe further thanks to Prof. Dr. Kemal Önder Çetin for his positive approach during my graduate studies and supplying data for this thesis.

I would like to thank to Prof. Dr. Reşat Ulusay for his valuable contributions through the manuscript.

I would also like to thank to Prof. Dr. Eric C. Drumm for his positive approach, motivation and considerable support during my studies in the Department of Civil and Environmental Engineering at the University of Tennessee as a research scholar.

I am very grateful to my beloved friend, Öykü Aslan, for standing beside me. Her great help and caring motivation made it a lot easier to complete this challenging work.

I am also grateful to my friend, Lale Tüzün and her daughter Oya Burçin Demirtaş, for all the fun and continuous support during this long time period.

Funding for these studies was provided by Scientific Research Development Program, and this support is gratefully acknowledged.

There is no doubt that there are many other people who helped me during this period, whose names have not been mentioned above. I am grateful to all of them.

Last, but not least, I would like to acknowledge the immeasurable support and love from my family who never left me alone. They deserve many thanks for always being with me and for their endless encouragement, assistance and patience for not only during this limited time but also throughout my entire life.

## TABLE OF CONTENTS

ABSTRACT .....	iv
ÖZ.....	vi
ACKNOWLEDGEMENTS .....	ix
TABLE OF CONTENTS .....	xi
LIST OF TABLES .....	xv
LIST OF FIGURES .....	xvii
CHAPTERS	
1. INTRODUCTION.....	1
1.1. Research statement .....	1
1.2. Location of the study area .....	2
1.3. Boring logs .....	7
1.4. Method of the study.....	11
1.5. Structure of the thesis .....	12
2. PREVIOUS RESEARCHES .....	14
2.1. Introduction .....	14
2.2. Causes of ground movements around tunnels in soft ground .....	14
2.2.1. Characterization of soft ground.....	14
2.2.2 Ground movements and volume loss due to an advancing tunnel heading .....	15
2.2.3. Short, medium and long term ground movements .....	16
2.3. The prediction of ground movements due to tunneling .....	17
2.3.1. Empirical ‘greenfield’ settlement troughs.....	17
2.3.2 Mechanisms of short-term settlement response .....	20
2.3.3. Laboratory and centrifuge testing.....	23
2.3.4. Numerical modeling of the short-term settlement trough .....	23

2.3.5. Constitutive models for short term tunneling settlements.....	25
2.4. Summary .....	27
3. GEOPHYSICAL INVESTIGATIONS .....	29
3.1. Introduction .....	29
3.2. Electrical Resistivity Imaging (ERI) studies .....	30
3.2.1. Data acquisition and processing .....	35
3.2.2. Considerations and limitations .....	40
3.2.3. Field application: Data acquisition, processing, interpretation .....	40
3.3. Ground Penetrating Radar (GPR) studies .....	60
3.3.1. Physical properties and parameters .....	60
3.3.2. Data acquisition and processing .....	64
3.3.3. Considerations and limitations .....	71
3.3.4. Field application: Data acquisition, processing, interpretation .....	72
4. 3-DIMENSIONAL NUMERICAL SIMULATION OF GROUND DEFORMATIONS INDUCED BY MECHANICAL EXCAVATION AT NECATIBEY STATION .....	94
4.1. Introduction .....	94
4.2. Introducing <i>FLAC 3D</i> code .....	95
4.2.1. General concept of the code .....	95
4.2.2. General features of the code .....	97
4.2.3. Mechanics of using <i>FLAC 3D</i> .....	98
4.3. Steps towards numerical models .....	100
4.3.1. Grid generation.....	100
4.3.2. Constitutive behavior .....	103
4.3.3. Material properties .....	103
4.3.3.1. Mass density .....	104
4.3.3.2. Deformability properties .....	104
4.3.3.3. Strength properties.....	105
4.3.4. Boundary and initial conditions .....	106
4.4. Assumptions .....	108
4.5. Construction stages.....	109



4.6. Deformation measurements.....	129
4.7. Results .....	132
5. EFFECTS OF CONNECTION TUNNEL EXCAVATIONS ON GROUND DEFORMATIONS.....	147
5.1. Introduction .....	147
5.2. Steps towards numerical models .....	148
5.3. Construction stages.....	148
5.4. Results .....	165
6. EFFECTS OF GROUNDWATER DRAINAGE ON GROUND DEFORMATIONS.....	182
6.1. Introduction .....	182
6.2. Fluid-mechanical coupling.....	183
6.2.1. Properties and units for fluid flow analysis.....	183
6.2.1.1. Permeability coefficient .....	183
6.2.1.2. Mass density .....	184
6.2.1.3. Fluid bulk modulus.....	184
6.2.1.4. Porosity.....	185
6.2.1.5. Saturation.....	185
6.2.1.6. Fluid tension limit .....	185
6.2.2. Fluid-flow boundary conditions .....	186
6.2.3. Coupled fluid-mechanical calculations .....	187
6.3. Steps towards numerical models .....	187
6.3.1. Grid generation.....	188
6.3.2. Boundary and initial conditions .....	190
6.4. Assumptions .....	191
6.5. Deformation measurements.....	192
6.6. Results .....	193
7. DISCUSSIONS .....	210
7.1. Geophysical studies.....	210
7.2. Numerical modeling studies.....	211

8. CONCLUSIONS AND RECOMMENDATIONS.....	214
REFERENCES.....	219

APPENDICES

A. MEASURED RESISTIVITY DATA.....	230
B. RECORDED DEFORMATION MEASUREMENTS.....	252
CURRICULUM VITAE .....	259

## LIST OF TABLES

### TABLES

<b>Table 3.1.</b> Typical values of relative permittivity (real component) and static conductivity for common subsurface materials at an antenna frequency of 100 MHz (Jol, 2009). .....	63
<b>Table 3.2.</b> Length of each profiles. ....	75
<b>Table 4.1.</b> Selected elastic constants for soils (Das, 1994).....	105
<b>Table 4.2.</b> Selected strength properties for soils (Ortiz et al., 1986). ....	106
<b>Table 4.3.</b> Excavation stages for main tunnels. ....	110
<b>Table 4.4.</b> Maximum recorded settlement values above the Line 2 tunnel axis. ....	131
<b>Table 4.5.</b> Calibrated soil properties used to obtain curve 8. ....	134
<b>Table 4.6.</b> Maximum z-displacement values along with distance in y-direction to form curve 8. ....	134
<b>Table 5.1.</b> Excavation stages for connection tunnels.....	149
<b>Table 5.2.</b> Line 1 tunnel axis deformations. ....	172
<b>Table 5.3.</b> Line 2 tunnel axis deformations. ....	173
<b>Table 5.4.</b> Connection 1 tunnel axis deformations. ....	174
<b>Table 5.5.</b> Connection 2 tunnel axis deformations. ....	175
<b>Table 6.1.</b> Properties of fluid-flow analysis and physical soil parameters. ....	186
<b>Table 6.2.</b> Maximum z-displacement and maximum pore pressure values with varying time.....	195
<b>Table A.1.</b> Measured resistivity data of Schlumberger N6 Dipole Dipole N4 electrode configuration for profile 1. ....	230

<b>Table A.2.</b> Measured resistivity data of Dipole Dipole N6 S1 electrode configuration for profile 1. ....	232
<b>Table A.3.</b> Measured resistivity data of Schlumberger N6 electrode configuration for profile 1. ....	235
<b>Table A.4.</b> Measured resistivity data of Wenner Alpha electrode configuration for profile 1. ....	237
<b>Table A.5.</b> Measured resistivity data of Schlumberger N6 Dipole Dipole N4 electrode configuration for profile 2. ....	238
<b>Table A.6.</b> Measured resistivity data of Dipole Dipole N6 S1 electrode configuration for profile 2. ....	240
<b>Table A.7.</b> Measured resistivity data of Schlumberger N6 electrode configuration for profile 2. ....	242
<b>Table A.8.</b> Measured resistivity data of Wenner Alpha electrode configuration for profile 2. ....	244
<b>Table A.9.</b> Measured resistivity data of Schlumberger N6 Dipole Dipole N4 electrode configuration for profile 3. ....	245
<b>Table A.10.</b> Measured resistivity data of Dipole Dipole N6 S1 electrode configuration for profile 3. ....	247
<b>Table A.11.</b> Measured resistivity data of Schlumberger N6 electrode configuration for profile 3. ....	249
<b>Table A.12.</b> Measured resistivity data of Wenner Alpha electrode configuration for profile 3. ....	251

## LIST OF FIGURES

### FIGURES

<b>Figure 1.1.</b> Location of the study area (GoogleEarth, 2007).....	3
<b>Figure 1.2.</b> Plan view of Necatibey station and boring locations (not to scale). ....	4
<b>Figure 1.3.</b> Dikmen Creek catchment area (scale: 1/50000). ....	6
<b>Figure 1.4.</b> Line 1 boring logs. ....	7
<b>Figure 1.5.</b> Boring logs between Line1 and Line 2. ....	8
<b>Figure 1.6.</b> Line 2 boring logs. ....	8
<b>Figure 1.7.</b> Line 2 boring logs (cont'd). ....	9
<b>Figure 1.8.</b> Line 2 boring logs (cont'd). ....	10
<b>Figure 2.1.</b> The Gaussian model of transverse tunneling induced settlements (Peck, 1969).....	18
<b>Figure 2.2.</b> Empirical longitudinal settlement trough based on Gaussian model (Attewell and Woodman, 1982). ....	20
<b>Figure 2.3.</b> Geometric parameters of a tunnel heading for calculation of stability number at collapse (Chow, 1994).....	21
<b>Figure 2.4.</b> Translation of nested yield surfaces in kinematic hardening model under action of stress path from origin to A and back (Houlsby, 1999). ....	26
<b>Figure 3.1.</b> The resistivity instrument used in this study; a) ARES Automatic Resistivity System, b) intelligent cable. ....	32
<b>Figure 3.2.</b> Common arrays used in resistivity surveys and their geometric factors (Loke, 2004). ....	33
<b>Figure 3.3.</b> The resistivity values of rocks, soils and minerals.....	34
<b>Figure 3.4.</b> The arrangement of electrodes for a 2-D electrical survey and the sequence of measurements used to build up a pseudosection (Loke, 2004). ....	36

<b>Figure 3.5.</b> A comparison of the (i) electrode configuration and (ii) pseudosection data pattern for Electric Profiling (Wenner array) and Vertical Electric Sounding (Schlumberger array) (Loke, 2004).....	39
<b>Figure 3.6.</b> The use of the roll-along method to extend the area covered by a 2-D survey (Loke, 2001). .....	39
<b>Figure 3.7.</b> Study area and resistivity profile locations (Google Earth, 2007).....	41
<b>Figure 3.8.</b> Arrangement of the blocks used in a model together with the data points in the pseudosection (RES2DINV, 2004).....	42
<b>Figure 3.9.a.</b> Interpretation of Schlumberger N6 Dipole Dipole N4 electrode configuration for profile 1. ....	44
<b>Figure 3.9.b.</b> Interpretation of Dipole Dipole N4 S1 electrode configuration for profile 1. ....	45
<b>Figure 3.9.c.</b> Interpretation of Schlumberger N6 electrode configuration for profile 1. ....	46
<b>Figure 3.9.d.</b> Interpretation of Wenner Alpha electrode configuration for profile 1. ....	47
<b>Figure 3.10.a.</b> Interpretation of Schlumberger N6 Dipole Dipole N4 electrode configuration for profile 2. ....	48
<b>Figure 3.10.b.</b> Interpretation of Dipole Dipole N4 S1 electrode configuration for profile 2. ....	49
<b>Figure 3.10.c.</b> Interpretation of Schlumberger N6 electrode configuration for profile 2. ....	50
<b>Figure 3.10.d.</b> Interpretation of Wenner Alpha electrode configuration for profile 2. ....	51
<b>Figure 3.11.a.</b> Interpretation of Schlumberger N6 Dipole Dipole N4 electrode configuration for profile 3. ....	52
<b>Figure 3.11.b.</b> Interpretation of Dipole Dipole N4 S1 electrode configuration for profile 3. ....	53
<b>Figure 3.11.c.</b> Interpretation of Schlumberger N6 electrode configuration for profile 3. ....	54
<b>Figure 3.11.d.</b> Interpretation of Wenner Alpha electrode configuration for profile 3. ....	55

<b>Figure 3.12.</b> Regional 3D subsurface panel diagram created by interpreting 2D electrical resistivity images and borehole logs together (South to North). .....	58
<b>Figure 3.13.</b> Regional 3D subsurface panel diagram created by interpreting 2D electrical resistivity images and borehole logs together (North to South). .....	59
<b>Figure 3.14.</b> Ground penetrating radar (GPR) uses radio waves to probe the subsurface of lossy dielectric materials. Two modes of measurement are common. In the first, reflected or scattered energy is detected. In the second, effects on energy transmitted through the material are observed (Jol, 2009). .....	60
<b>Figure 3.15.</b> Ground penetrating radar (GPR) cross section obtained with a 50-MHz system traversing over two road tunnels. Ground penetrating radar signal amplitude is displayed as a function of position (horizontal axis) and travel time (vertical axis) (Jol, 2009). .....	61
<b>Figure 3.16.</b> A sketch illustrating GPR data acquisition mode using a monostatic GPR unit (Alshuhail, 2006). .....	65
<b>Figure 3.17.</b> An illustration of the GPR data acquisition mode using bistatic GPR system (Alshuhail, 2006). .....	65
<b>Figure 3.18.</b> Cobra Locator GPR System produced by Radarteam Sweden AB.	73
<b>Figure 3.19.</b> Region A, Line 1, Line 2, Line 3 and Line 4 profiles (profile number 1, 2, 3, 4, 5, 6, 7, 8, 9, 10, 11, 12). .....	74
<b>Figure 3.20.</b> Region B, Line 1 and Line 2 profiles (profile number 13, 14). .....	74
<b>Figure 3.21.</b> Region C, Line 1 profile (profile number 15). .....	75
<b>Figure 3.22.</b> Region A, Line 1, Profile 1. .....	77
<b>Figure 3.23.</b> Region A, Line 1, Profile 2. .....	78
<b>Figure 3.24.</b> Region A, Line 1, Profile 3. .....	79
<b>Figure 3.25.</b> Region A, Line 1, Profile 4. .....	80
<b>Figure 3.26.</b> Region A, Line 2, Profile 5. .....	81
<b>Figure 3.27.</b> Region A, Line 2, Profile 6. .....	82
<b>Figure 3.28.</b> Region A, Line 2, Profile 7. .....	83
<b>Figure 3.29.</b> Region A, Line 2, Profile 8. .....	84
<b>Figure 3.30.</b> Region A, Line 2, Profile 9. .....	85
<b>Figure 3.31.</b> Region A, Line 2, Profile 10. .....	86
<b>Figure 3.32.</b> Region A, Line 3, Profile 11. .....	87
<b>Figure 3.33.</b> Region A, Line 4, Profile 12. .....	88

<b>Figure 3.34.</b> Region B, Line 1, Profile 13. ....	89
<b>Figure 3.35.</b> Region B, Line 2, Profile 14. ....	90
<b>Figure 3.36.</b> Region C, Line 1, Profile 15. ....	91
<b>Figure 3.37.</b> 3 Dimensional view of GPR results at Region A.....	93
<b>Figure 4.1.</b> General solution procedure in <i>FLAC 3D</i> ( <i>FLAC 3D User’s Manuel</i> , 2005).....	99
<b>Figure 4.2.</b> <i>FLAC 3D</i> grid showing the geometry of the problem. ....	101
<b>Figure 4.3.</b> <i>FLAC 3D</i> grid showing the analyzed geometry of the problem. ....	102
<b>Figure 4.4.</b> Sketch illustration of main tunnels and connection tunnels.....	102
<b>Figure 4.5.</b> Boundary conditions for this study. ....	107
<b>Figure 4.6.</b> Step 1; a) excavation of segment 1, b) installation of temporary lining to segment 1.....	112
<b>Figure 4.7.</b> Step 2; a) removal of temporary lining at segment 1, b) excavation of segment 2, c) installation of permanent lining at segment 1, d) installation of temporary lining at segment 2. ....	113
<b>Figure 4.8.</b> Step 3; a) excavation of segment 3, b) removal of permanent and temporary linings, c) installation of permanent linings at segment 1 and 2, d) installation of temporary lining at segment 3.....	115
<b>Figure 4.9.</b> Step 4; a) excavation of segment 4, b) removal of temporary lining at segment 3, c) removal of permanent lining at segment 2, d) installation of permanent lining at segment 3, e) installation of permanent lining at segment 2, f) installation of temporary lining at segment 4.....	117
<b>Figure 4.10.</b> Step 1; a) excavation of segment 1, b) installation of temporary lining to segment 1. ....	121
<b>Figure 4.11.</b> Step 2; a) removal of temporary lining at segment 1, b) excavation of segment 2, c) installation of permanent lining at segment 1, d) installation of temporary lining at segment 2. ....	122
<b>Figure 4.12.</b> Step 3; a) excavation of segment 3, b) removal of permanent and temporary linings, c) installation of permanent linings at segment 1 and 2, d) installation of temporary lining at segment 3.....	124
<b>Figure 4.13.</b> Step 4; a) excavation of segment 4, b) removal of temporary lining at segment 3, c) removal of permanent lining at segment 2, d) installation of	



permanent lining at segment 3, e) installation of permanent lining at segment 2, f) installation of temporary lining at segment 4.....	126
<b>Figure 4.14.</b> Location of the surface deformation measurements points (red region includes surface deformation points 8, 9, 10, 11, 12, 13, 14, 15, 16, 17, 18, 19, 20 for line 2 tunnel).....	130
<b>Figure 4.15.</b> Maximum recorded settlements above the tunnel axis at surface points 8, 9, 10, 11, 12, 13, 14, 15, 16, 17, 18, 19, 20 for line 2 tunnel.....	131
<b>Figure 4.16.</b> Different settlement curves obtained during calibration phase for Line 2 deformation values.....	132
<b>Figure 4.17.</b> Correlation of recorded deformations and numerical analyses results for Line 2 tunnel.....	133
<b>Figure 4.18.</b> 15 m excavation and support of Line 2 tunnel.....	136
<b>Figure 4.19.</b> 15 m excavation and support of Line 2 tunnel, 5 m excavation and support of Line 1 tunnel.....	136
<b>Figure 4.20.</b> 20 m excavation and support of Line 2 tunnel, 5 m excavation and support of Line 1 tunnel.....	137
<b>Figure 4.21.</b> 20 m excavation and support of Line 2 tunnel, 10 m excavation and support of Line 1 tunnel.....	137
<b>Figure 4.22.</b> 25 m excavation and support of Line 2 tunnel, 10 m excavation and support of Line 1 tunnel.....	138
<b>Figure 4.23.</b> 25 m excavation and support of Line 2 tunnel, 15 m excavation and support of Line 1 tunnel.....	138
<b>Figure 4.24.</b> 30 m excavation and support of Line 2 tunnel, 15 m excavation and support of Line 1 tunnel.....	139
<b>Figure 4.25.</b> 30 m excavation and support of Line 2 tunnel, 20 m excavation and support of Line 1 tunnel.....	139
<b>Figure 4.26.</b> 35 m excavation and support of Line 2 tunnel, 20 m excavation and support of Line 1 tunnel.....	140
<b>Figure 4.27.</b> 35 m excavation and support of Line 2 tunnel, 25 m excavation and support of Line 1 tunnel.....	140
<b>Figure 4.28.</b> 40 m excavation and support of Line 2 tunnel, 25 m excavation and support of Line 1 tunnel.....	141

<b>Figure 4.29.</b> 40 m excavation and support of Line 2 tunnel, 30 m excavation and support of Line 1 tunnel. ....	141
<b>Figure 4.30.</b> 45 m excavation and support of Line 2 tunnel, 30 m excavation and support of Line 1 tunnel. ....	142
<b>Figure 4.31.</b> 45 m excavation and support of Line 2 tunnel, 35 m excavation and support of Line 1 tunnel. ....	142
<b>Figure 4.32.</b> 50 m excavation and support of Line 2 tunnel, 35 m excavation and support of Line 1 tunnel. ....	143
<b>Figure 4.33.</b> 50 m excavation and support of Line 2 tunnel, 40 m excavation and support of Line 1 tunnel. ....	143
<b>Figure 4.34.</b> 55 m excavation and support of Line 2 tunnel, 40 m excavation and support of Line 1 tunnel. ....	144
<b>Figure 4.35.</b> 55 m excavation and support of Line 2 tunnel, 45 m excavation and support of Line 1 tunnel. ....	144
<b>Figure 4.36.</b> 60 m excavation and support of Line 2 tunnel, 45 m excavation and support of Line 1 tunnel. ....	145
<b>Figure 4.37.</b> 60 m excavation and support of Line 2 tunnel, 50 m excavation and support of Line 1 tunnel. ....	145
<b>Figure 4.38.</b> 60 m excavation and support of Line 2 tunnel, 55 m excavation and support of Line 1 tunnel. ....	146
<b>Figure 4.39.</b> 60 m excavation and support of Line 2 tunnel, 60 m excavation and support of Line 1 tunnel. ....	146
<b>Figure 5.1.</b> Step 1; a) excavation of upper inner part, b) installation of temporary lining to upper inner part. ....	150
<b>Figure 5.2.</b> Stage 2; a) excavation of upper outer part, b) removal of temporary lining from upper inner part, c) installation of permanent lining to upper inner part, d) installation of temporary lining to upper outer part. ....	151
<b>Figure 5.3.</b> Stage 3; a) excavation of lower half part, b) removal of all linings, c) installation of permanent linings to upper inner and upper outer parts, d) installation of temporary lining to lower half part. ....	153

<b>Figure 5.4.</b> Stage 4; a) removal of all linings, b) excavation of second upper inner part, . c) insatallatin of permanent linings to upper inner, upper outer and lower half parts, d) installation of temporary lining to second upper inner part. ....	155
<b>Figure 5.5.</b> Step 1; a) excavation of upper inner part, b) installation of temporary lining to upper inner part. ....	158
<b>Figure 5.6.</b> Stage 2; a) excavation of upper outer part, b) removal of temporary lining from upper inner part, c) installation of permanent lining to upper inner part, d) installation of temporary lining to upper outer part. ....	159
<b>Figure 5.7.</b> Stage 3; a) excavation of lower half part, b) removal of all linings, c) installation of permanent linings to upper inner and upper outer parts, d) installation of temporary lining to lower half part. ....	161
<b>Figure 5.8.</b> Stage 4; a) removal of all linings, b) excavation of second upper inner part, c) insatallatin of permanent linings to upper inner, upper outer and lower half parts, d) installation of temporary lining to second upper inner part. ....	163
<b>Figure 5.9.</b> Connection 1 tunnel axis deformations after connection 1 tunnel excavation.....	167
<b>Figure 5.10.</b> Line 1 tunnel axis deformations after connection 1 tunnel excavation.....	167
<b>Figure 5.11.</b> Line 2 tunnel axis deformations after connection tunnel 1 excavation.....	168
<b>Figure 5.12.</b> Connection 2 tunnel axis deformations after connection 2 tunnel excavation.....	168
<b>Figure 5.13.</b> Correlation of connection 1 tunnel axis deformations and connection 2 tunnel axis deformations after their excavations.....	169
<b>Figure 5.14.</b> Correlation of connection 1 tunnel axis deformations after connection 1 and 2 tunnel excavations.....	169
<b>Figure 5.15.</b> Correlation of Line 1 tunnel axis deformations after connection 1 and 2 tunnel excavations. ....	170
<b>Figure 5.16.</b> Correlation of Line 2 tunnel axis deformations after connection 1 and 2 tunnel excavations. ....	170
<b>Figure 5.17.</b> 7 m excavation and support of connection 1 tunnel.....	176
<b>Figure 5.18.</b> 11 m excavation and support of connection 1 tunnel.....	177
<b>Figure 5.19.</b> 15 m excavation and support of connection 1 tunnel.....	177

<b>Figure 5.20.</b> 19 m excavation and support of connection 1 tunnel.....	178
<b>Figure 5.21.</b> 23.5 m excavation and support of connection 1 tunnel.....	178
<b>Figure 5.22.</b> 7 m excavation and support of connection 2 tunnel.....	179
<b>Figure 5.23.</b> 11 m excavation and support of connection 2 tunnel.....	179
<b>Figure 5.24.</b> 15 m excavation and support of connection 2 tunnel.....	180
<b>Figure 5.25.</b> 19 m excavation and support of connection 2 tunnel.....	180
<b>Figure 5.26.</b> 23.5 m excavation and support of connection 2 tunnel.....	181
<b>Figure 6.1.</b> <i>FLAC 3D</i> grid showing the geometry of fluid-flow analysis.....	188
<b>Figure 6.2.</b> <i>FLAC 3D</i> grid showing the analyzed geometry of the problem. ....	189
<b>Figure 6.3.</b> Boundary conditions for fluid-flow analysis. ....	190
<b>Figure 6.4.</b> Maximum recorded deformations at the end of three months period for Line 2 surface points 8, 9, 10, 11, 12, 13, 14, 15, 16, 17, 18, 19, 20.....	192
<b>Figure 6.5.</b> Maximum numerical deformations at the end of three months period for Line 2 surface points 8, 9, 10, 11, 12, 13, 14, 15, 16, 17, 18, 19, 20.....	193
<b>Figure 6.6.</b> Contour plot of a) z-displacement, b) pore pressure for 1 day. ....	196
<b>Figure 6.7.</b> Contour plot of a) z-displacement, b) pore pressure for 2 days.....	197
<b>Figure 6.8.</b> Contour plot of a) z-displacement, b) pore pressure for 3 days.....	198
<b>Figure 6.9.</b> Contour plot of a) z-displacement, b) pore pressure for 4 days.....	199
<b>Figure 6.10.</b> Contour plot of a) z-displacement, b) pore pressure for 5 days. ....	200
<b>Figure 6.11.</b> Contour plot of a) z-displacement, b) pore pressure for 6 days. ....	201
<b>Figure 6.12.</b> Contour plot of a) z-displacement, b) pore pressure for 7 days. ....	202
<b>Figure 6.13.</b> Contour plot of a) z-displacement, b) pore pressure for 14 days...	203
<b>Figure 6.14.</b> Contour plot of a) z-displacement, b) pore pressure for 28 days...	204
<b>Figure 6.15.</b> Contour plot of a) z-displacement, b) pore pressure for 60 days...	205
<b>Figure 6.16.</b> Contour plot of a) z-displacement, b) pore pressure for 90 days...	206
<b>Figure 6.17.</b> Contour plot of a) z-displacement, b) pore pressure for 120 days.	207
<b>Figure 6.18.</b> Contour plot of a) z-displacement, b) pore pressure for 150 days.	208
<b>Figure 6.19.</b> Contour plot of a) z-displacement, b) pore pressure for 180 days.	209
<b>Figure 7.1.</b> Correlation of linear trends of measured and computed data. ....	213
<b>Figure B.1.</b> Recorded deformation measurements at point 8. ....	252

<b>Figure B.2.</b> Recorded deformation measurements at point 9. ....	253
<b>Figure B.3.</b> Recorded deformation measurements at point 10. ....	253
<b>Figure B.4.</b> Recorded deformation measurements at point 11. ....	254
<b>Figure B.5.</b> Recorded deformation measurements at point 12. ....	254
<b>Figure B.6.</b> Recorded deformation measurements at point 13. ....	255
<b>Figure B.7.</b> Recorded deformation measurements at point 14. ....	255
<b>Figure B.8.</b> Recorded deformation measurements at point 15. ....	256
<b>Figure B.9.</b> Recorded deformation measurements at point 16. ....	256
<b>Figure B.10.</b> Recorded deformation measurements at point 17. ....	257
<b>Figure B.11.</b> Recorded deformation measurements at point 18. ....	257
<b>Figure B.12.</b> Recorded deformation measurements at point 19. ....	258
<b>Figure B.13.</b> Recorded deformation measurements at point 20. ....	258

# CHAPTER 1

## INTRODUCTION

### 1.1. Research statement

The high cost of urban space has significantly increased the demand for tunnels in big urban centers. In such areas, deformations induced by the tunnel excavation and groundwater drainage may cause serious damage to nearby structures. Therefore, it is necessary to presuppose and to investigate effective means of controlling tunnel induced deformations.

The focus of this study is to estimate the ground deformations taking place at the Ankara Subway System Necatibey Station and its close vicinity due to the tunnel excavations and groundwater drainage. This study mainly aims to investigate the efficiency of numerical models for calculating settlements caused by main tunnel excavations, connection tunnel excavations and groundwater drainage. With this scope 3-Dimensional (3D) numerical analyses were performed to investigate mechanical effects of main and connection tunnel excavations on the amount of deformations firstly. Then 3-D coupled analyses were generated to simulate removal of groundwater. The results were then verified by recorded deformation measurements at the site.

It is recognized that there are other approaches distinct from numerical modeling that could be taken to explore this area, for example gathering case history data for an empirical study, small-scale laboratory testing or centrifuge modeling. However, the aim of this dissertation is to exploit specific advantages of three-dimensional non-linear numerical analyses for this purpose. These are the ability to model any geometry without having to simplify to two dimensions,

representation of the advance of a tunnel heading, and the ability to vary the parameters of the constitutive models of soil.

It is common for major cities (e.g., the city of Ankara) to be founded on alluvial deposits of clays, silts and sands, usually classified as soft ground. Ground movements in response to the groundwater drainage and excavation of the tunnel will be transmitted to the surface. In order to estimate those movements (deformations) numerically, one has to construct soil profile precisely. Identifying critical soil profile at the working area is the basis of any numerical modeling. In this study, two geophysical methods namely Electrical Resistivity Imaging (ERI) and Ground Penetrating Radar (GPR) were utilized to distinguish soil types at the study area. By correlating these geophysical test results with the boring logs, 3-dimensional soil profile was revealed at the study area to build up a basis for numerical models.

Although tunneling projects may cause many short- and long-term disturbances, this study specifically emphasizes the settlements due to the tunnel excavations and the drawdown of groundwater table. The settlement calculation process is the usual work to be done in every subway tunneling project and it is done in an intensive manner for the sake of the project. Every factor is carefully taken into account in detail within the project works to ensure an engineering accomplishment that will be satisfactory for its lifetime. Meanwhile the outcome of this study will represent an alternative point of view regarding the calculation methods and will be crucially important depending on the density of the population and constructions at the project area.

## **1.2. Location of the study area**

The study area is the Ankara Subway System Kızılay-Çayyolu Line Necatibey Station located among the buildings of Turkish General Staff, Turkish Air Force and General Directorate of Highways (Figure 1.1).

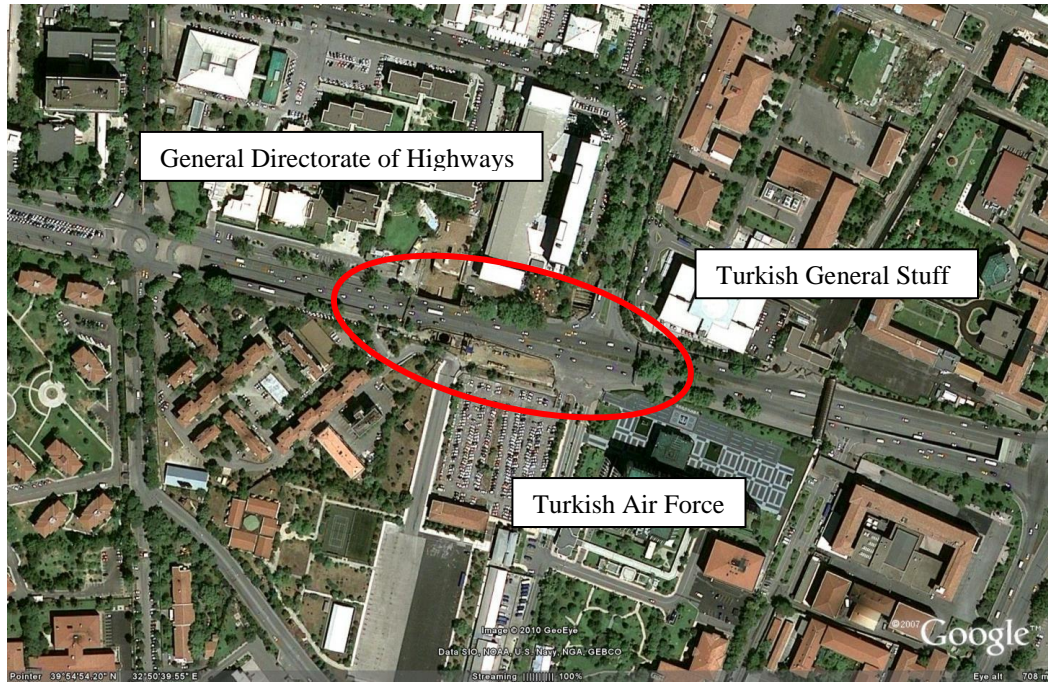


**Figure 1. 1.** Location of the study area (GoogleEarth, 2007).

Necatibey Station is about 140 m long (Figure 1.2). It has two horse-shoe shape main tunnels each 9 meters high and 11 meters wide. There are also four connection tunnels between them (Figure 1.2). Above the tunnel floor there will be a pedestrian floor and a shopping center. Three escalators were also planned for the pedestrians.

Since the project is located among residential, governmental and military buildings, the construction stage is undergoing major challenges. The project works have to be performed under extreme care in order not to damage any of the surrounding structures above ground or service infrastructure founded below the ground as well as not to interfere with daily lives of the population within the vicinity of the neighborhood. Passing by many important residential and governmental areas the project would have a major effect on the city of Ankara. Although the project is designed to make this a positive one, a minor mistake in the engineering applications can cause a mess in this critical area.



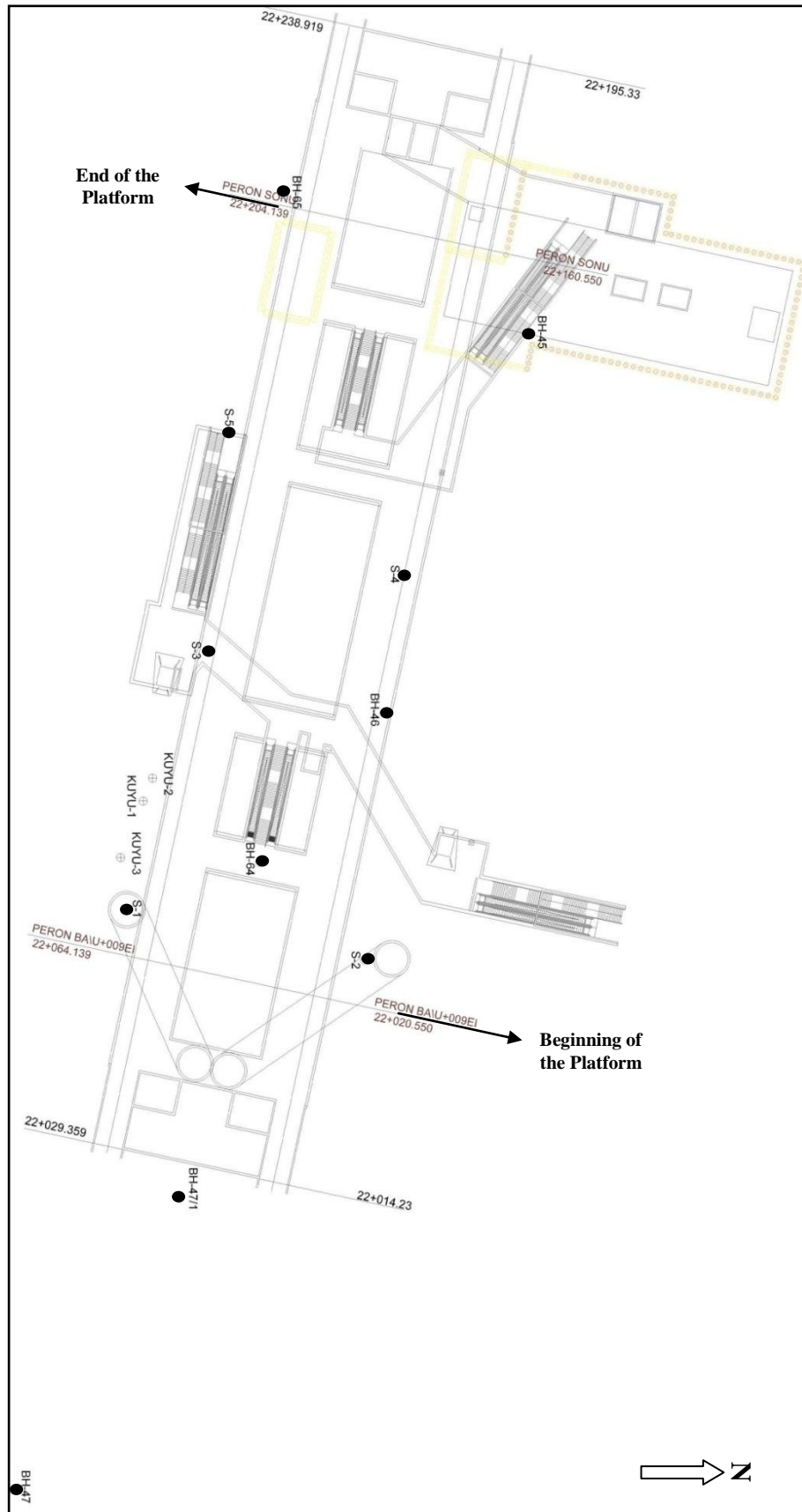
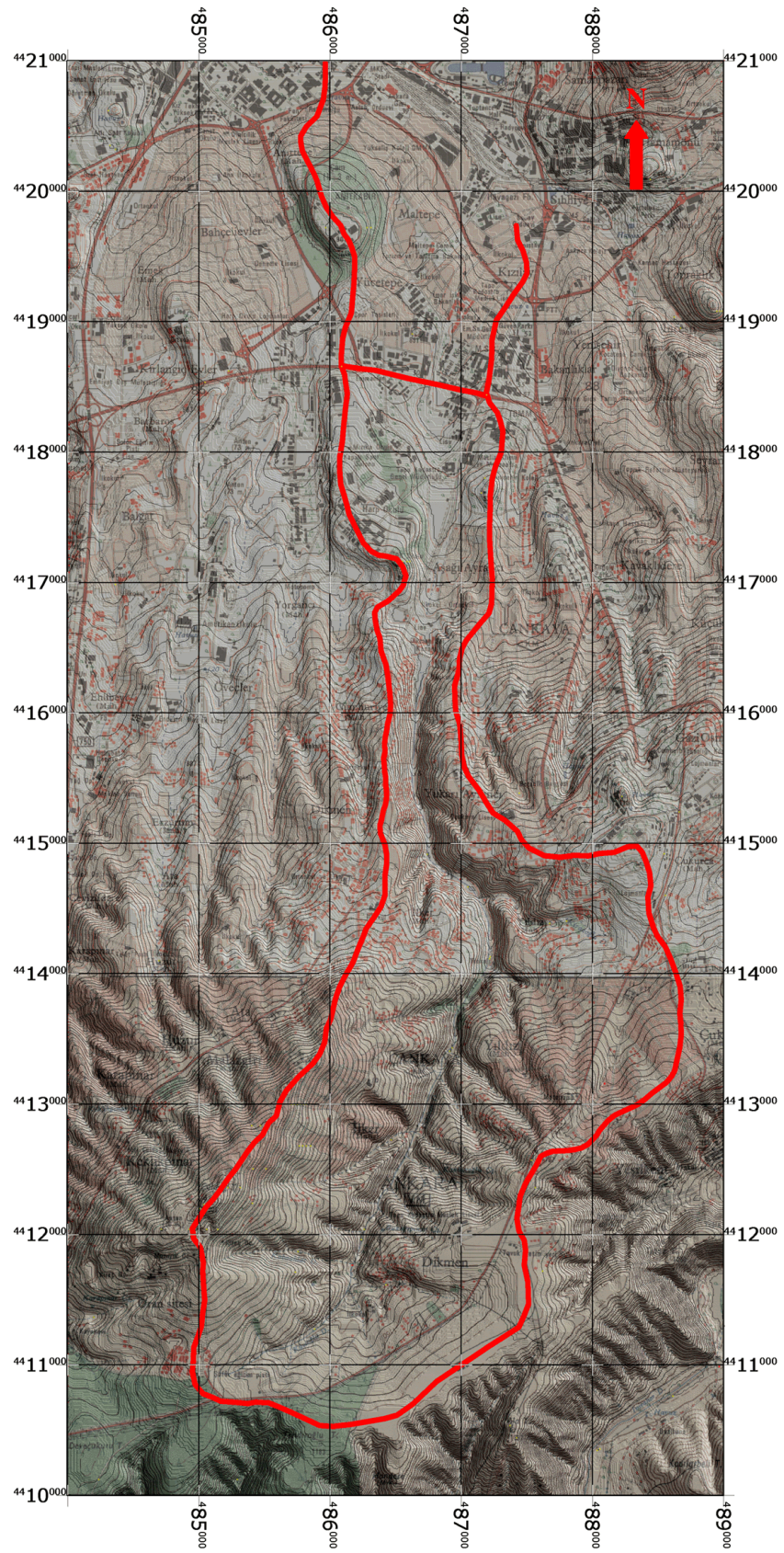


Figure 1.2. Plan view of Necatibey station and boring locations (not to scale).

The reason which makes this project special and construction works difficult is that the extension of the Necatibey Station passes through the alluvium of the Dikmen Creek almost perpendicular. Dikmen Creek watershed starts from the south ridge of Dikmen and extends towards Sıhhiye (Figure 1.3). Its catchment area is about 13.5 km<sup>2</sup>. Çaldağ Hill at the North of Oran Site is the highest peak in the catchment area and the elevation around the Eskişehir road is about 890 meters. Average slope of the valley is about 8 degrees. The intersection area of Eskişehir road and Dikmen Valley is just west of the Turkish Air Force and between Turkish General Staff and Necatibey Street. Since the topography is getting flat in this part Dikmen Valley spreads out laterally and continues towards Sıhhiye roughly.



**Figure 1.3.** Dikmen Creek catchment area (scale: 1/50000).

### 1.3. Boring logs

In order to reveal the geology along the Necatibey Station a number of boreholes were planned. A total of 11 boreholes were drilled by TOKER Drilling and Construction Co. (TOKER, 2003) to figure out the type, thickness, contact relationships, geological and geotechnical properties of lithological units present along the Necatibey Station. Details regarding these boreholes are given.

By considering soil groups (according to Unified Soil Classification System), color index and SPT values the units belonging to alluvium and Ankara clay (Gölbaşı formation) were separated. Boring logs, whose locations are indicated in Figure 1.2, were reinterpreted and illustrated in Figure 1.4 through Figure 1.8 by considering their level and coordinates and by constituting cross-sections.

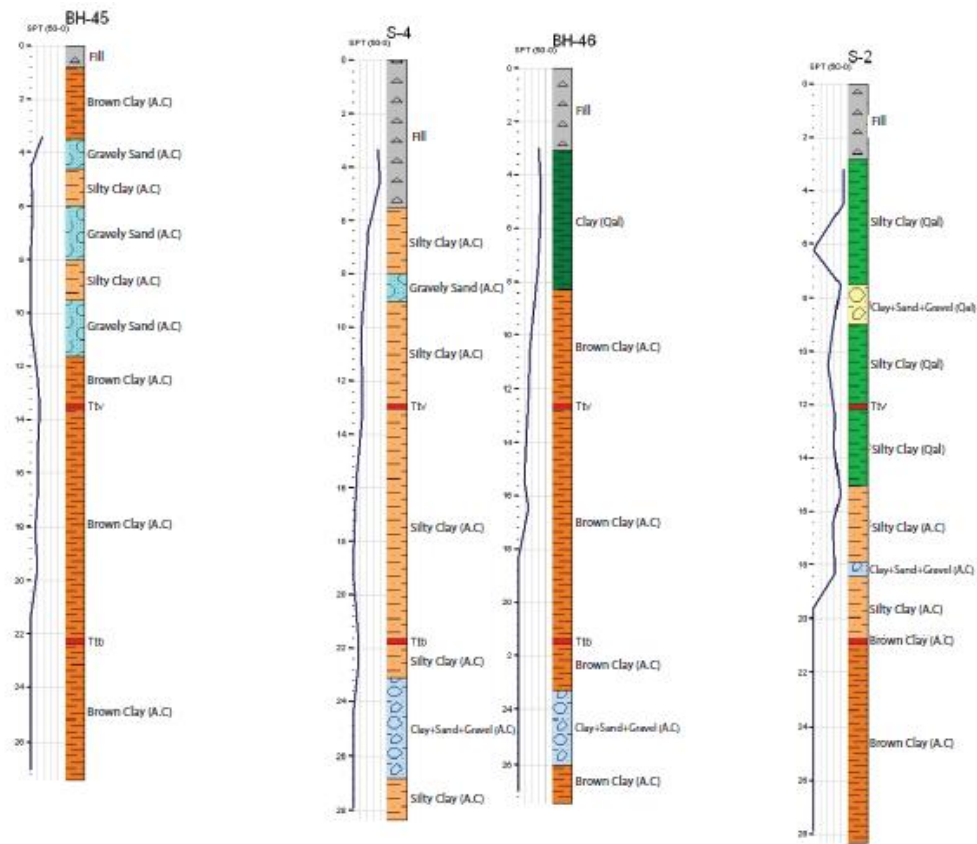


Figure 1.4. Line 1 boring logs.



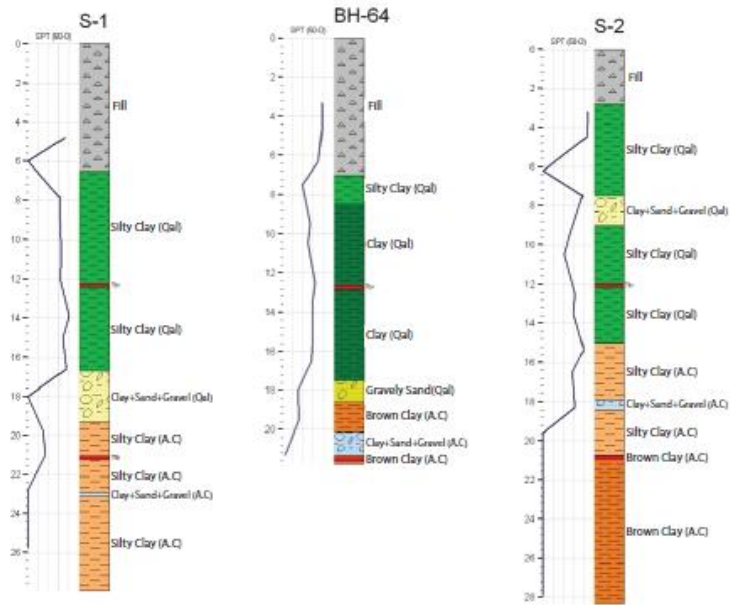


Figure 1.5. Boring logs between Line1 and Line 2.

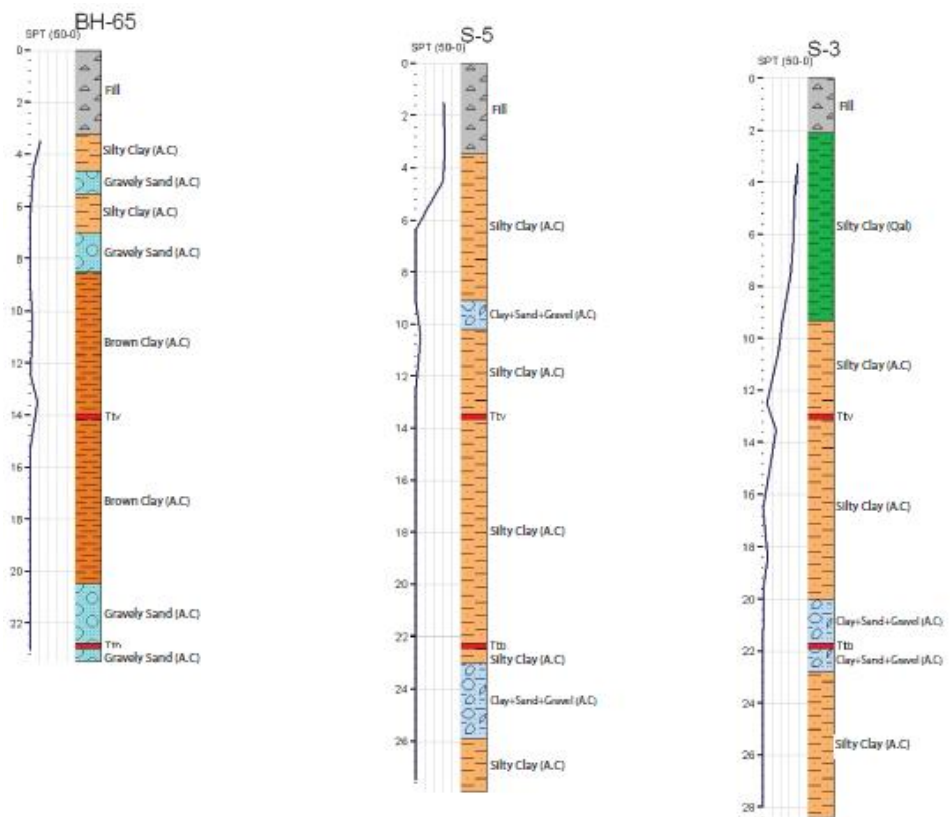


Figure 1.6. Line 2 boring logs.

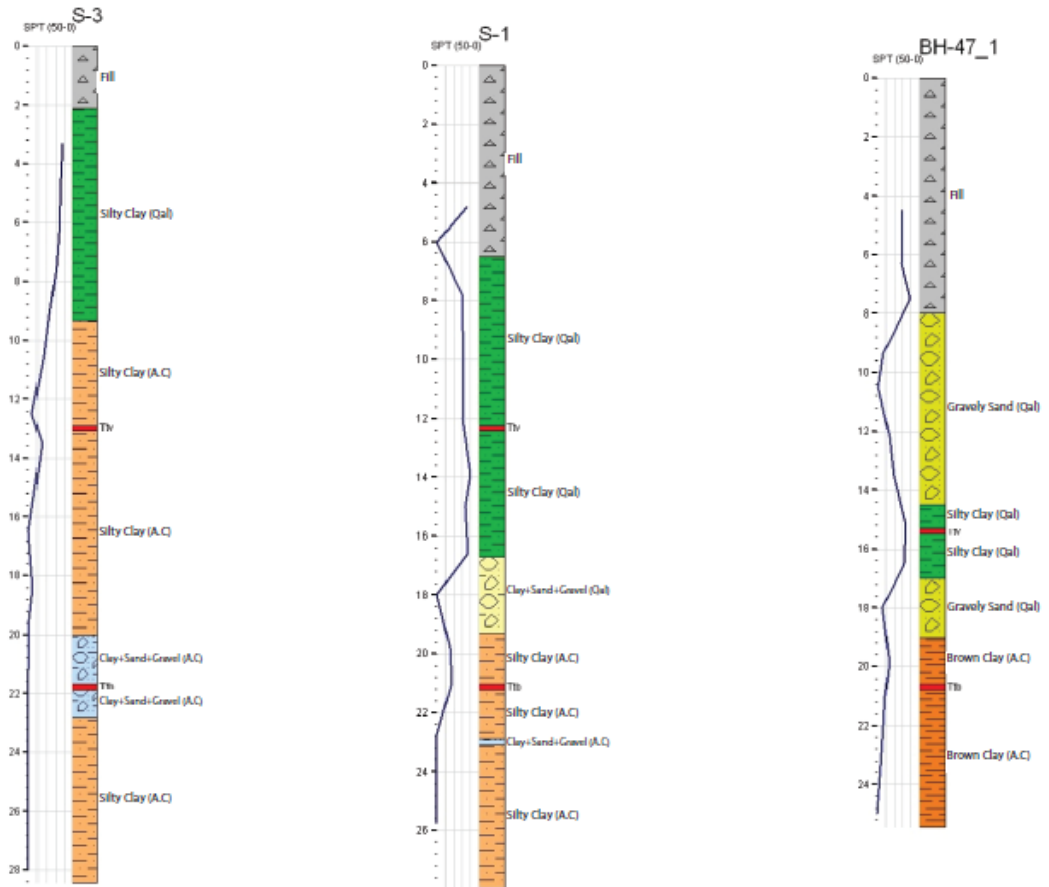
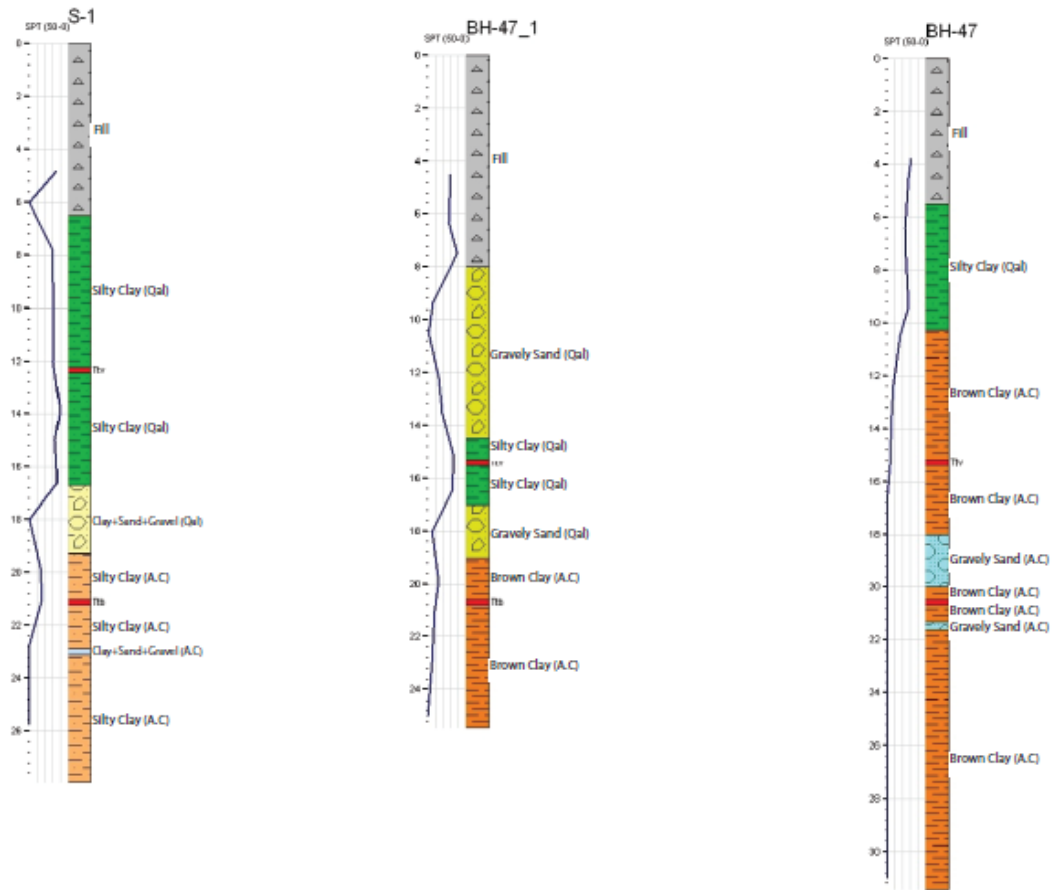


Figure 1.7. Line 2 boring logs (cont'd).



**Figure 1.8.** Line 2 boring logs (cont'd).

Boring logs indicate that clayey, silty and sandy gravelly levels belong to Dikmen Creek alluvium and are observed at BH-46, BH-64, S-1, S-2, S-3, BH-47-1 and BH-47. Boring logs BH-46, BH-47 and S-3 penetrate thru clay and silty clay levels of the Dikmen Creek alluvium. Sandy gravelly levels are encountered within boring S-1 (16.70-19.30 m), S-2 (above tunnel roof, 7.50-9.00 m), BH-64 (17.50-18.60 m), BH-47-1 (8.00-14.50 m and 17.00-19.00 m). The thickest channel fill (gravelly sand, 6.50 m) of the Dikmen Valley is observed in BH-47-1. At 2.50 m. below this channel fill there is another gravelly sand unit (2.00 meters thick) representing probably an old river bed.

The alluvium of the Dikmen Valley cuts Necatibey Station almost perpendicularly and it is composed of clay, silty clay and gravelly sand units. Aforementioned

alluvium aquifer is the only reason for high rate (8 l/sec) and continuous groundwater flow during construction of main tunnels (Doyuran, 2006).

The Ankara clay is dominantly composed of silty and/or sandy clays with occasional sand and gravel lenses. Even though fine-grained deposits are dominant, the sand and gravel lenses are also encountered. The Ankara clay is of Pliocene age (TOKER, 2003). It is basically silty clay and gravelly, sandy clay that is red, brown and beige, fissured, contains carbonate concretions, partly has layers of sand and gravel, either low or high in plasticity, very stiff and over-consolidated.

#### **1.4. Method of the study**

This study aims to estimate the ground deformations taking place at the Ankara Subway System Necatibey Station and its close vicinity due to tunnel excavations (main tunnels and connection tunnels) and groundwater drainage.

In order to do this, firstly, borehole data were gathered and reinterpreted. Since any numerical investigation requires well defined soil geometry, geophysical investigations were also planned to support boring log data. Electrical Resistivity Imaging and Ground Penetrating Radar investigations were applied at the study area to understand the soil profile and to fill the gaps between the boreholes. By considering boring log data and geophysical investigation results together 3-dimensional soil profile at the site were established.

Secondly, by examining the established 3-dimensional soil profiles a critical soil profile was chosen to set off a basis for numerical models. At this point, the primary aim of numerical models was to calibrate soil properties (e.g., bulk modulus, shear modulus, cohesion, etc.) by modeling mechanical excavation of main tunnels at the site. To do this a considerable amount of 3-dimensional numerical models were run and results were continuously correlated with the recorded deformation measurements taken from the site. Trials were continued until numerical results matched with the recorded measurements. Soil properties



at the instant of matching were accepted as correct ones and used throughout the model study.

Third step was to maintain 3-Dimensional numerical models to simulate mechanical excavation of connection tunnels. Soil properties obtained from previous step were used at this step. As mentioned before, there were main tunnels and connection tunnels between them at the site. Sequential excavations of each tunnel and the effects of excavation process of one tunnel to another were investigated. The results were presented in terms of deformations caused by excavation process at the study area.

Finally, effects of groundwater drainage were investigated at the site. 3-dimensional fully coupled (fluid-mechanical) numerical models were created to estimate the consolidation settlements taking place at the Ankara Subway System Necatibey Station and its close vicinity due to the groundwater drainage using different time durations.

### **1.5. Structure of the thesis**

Following this introduction, in Chapter 2, an overview of existing studies focusing on theoretical background of settlement phenomena, numerical investigations of tunnel construction and constitutive models for short term tunneling settlements were presented.

In Chapter 3, geophysical investigations were discussed. Theory, application and field studies about Electrical Resistivity Imaging and Ground Penetrating Radar studies were presented. 3-Dimensional soil profiles obtained from these studies were also given.

Chapter 4 supplied information about *FLAC 3D* code firstly. And then, step by step procedure was mentioned about numerical modeling concept. Information about assumptions made to improve numerical models quality was followed by construction stages part and recorded deformation measurements part. Finally,

numerical model results and correlation with recorded deformation measurements were included in results part.

In Chapter 5, firstly, very short information about step by step procedure was mentioned about numerical modeling concept. And then, construction stages were illustrated using screen captures from the *FLAC 3D* code. Finally, results part was included numerical model results and graphs of correlation between deformations occurred on different tunnel axes due to the connection tunnel excavations.

Information about *FLAC 3D* code's fluid-mechanical coupling option and step by step procedure about numerical modeling concept were mentioned at the same time in Chapter 6. Itemized assumptions made to improve numerical models quality and results part illustrating graphical plots and numerical model outputs were also represented.

Finally, Chapter 7 and Chapter 8 represent discussions and major conclusions of the thesis respectively.

## **CHAPTER 2**

### **PREVIOUS RESEARCHES**

#### **2.1. Introduction**

Subway systems are being seen as an environmentally preferable means of providing infrastructure such as transportation and utilities to densely populated urban areas. It is often cost-effective as an alternative to over-ground solutions, when the risk and cost of disruption during construction is taken into account.

It is common for major cities (e.g., the city of Ankara) to be founded on alluvial deposits of clays, silts and sands, usually classified as soft ground. Ground deformations resulting from the excavation of the tunnel will be transmitted to the ground surface. If there are surface structures, these may be affected.

Previous studies have explored how ground movements close to the tunnel are translated into a distribution of settlements on the ground surface. The initial studies were confined to field observations; later work has applied analytical solutions, laboratory and centrifuge modeling and numerical modeling techniques. These are described in this thesis, after a description of the fundamental reasons why movements occur around tunnels in soft ground.

#### **2.2. Causes of ground movements around tunnels in soft ground**

##### **2.2.1. Characterization of soft ground**

Soft ground may consist of cohesive or cohesionless material. Sites used as case histories are frequently classified as one of these two types, although in reality no

site ever fits either definition exactly. Previous researchers have recognized a difference in ground movements due to tunneling in the two types of material. Movements in cohesionless ground appear to be restricted to a narrower region above the tunnel than in cohesive soils (Mair, 1979; Potts, 1976).

This study will be limited to the numerical modeling of stiff over consolidated clays, common in parts of the city of Ankara (e.g., Ankara clay) that were overlain by Alluvium. However, there is no reason why the modeling procedures may not be applied to softer clays and cohesionless materials, subject to the verification of suitable constitutive models.

### **2.2.2 Ground movements and volume loss due to an advancing tunnel heading**

Ground movements are an inevitable consequence of constructing a tunnel in soft ground. It is not possible to create a void instantaneously and provide an infinitely stiff lining to fill it exactly. In the time taken to excavate, the ground around the tunnel is able to displace inwards since stress relief is taking place. Therefore it will always be necessary to remove a larger volume of ground than the volume of the final void. This extra volume excavated is termed as the ‘volume loss’.

The net volume of the surface settlement trough will be approximately equal to the volume loss at the tunnel in most ground conditions. If the ground response is at constant volume (i.e. undrained), the relationship will be exact. This assumption, usually made for stiff clays, enables a measure of the volume loss to be made, which would otherwise be difficult to obtain directly at the tunnel.

Prediction of the total amount of volume loss would be useful for tunnel designers, but is difficult because volume loss apparently depends on a number of factors that are not known at the design stage. These include the tunneling machine type, the construction sequence and the effectiveness of the grouting behind the lining, the latter being a ‘workmanship’ factor. The designer ideally knows the soil properties and in situ stress state. It is also known from observation

(McCaul et al., 1986) that volume loss does not necessarily increase with stress (or depth). Macklin and Field (1999) after earlier work by Mair et al. (1981) and O'Reilly (1988) combined case history and centrifuge modeling results to propose a prediction method for volume loss in overconsolidated clays. His method used the concept of stability number, explained later.

### **2.2.3. Short, medium and long term ground movements**

Time dependency in the mechanical behavior of soil influences ground movements resulting from tunneling, leading to the classification of short, medium and long-term movements. Each of these regimes of behavior is itself a steady-state response of the ground to changes in internal or external conditions.

Short-term ground movements are identified to occur during at most the first four days after excavation. This is a timescale that is shorter than, or comparable with, the time taken by the advance of the tunnel heading that is the cause of ground movements. Macklin and Field (1999) reported short-term settlements taking place at a section over a period of 24 hours before and after the passage of the shield. There is evidence that the movements start and stop almost instantaneously with advance of the tunnel heading. The response of the ground is at constant volume to the suddenly imposed new stress regime, which is essentially one of unloading at the tunnel boundary. Rowe and Lee (1989) proposed that it was the extension modulus in clays that was particularly relevant to tunneling problems. The response may be entirely elastic or include irrecoverable strains. Apart from very locally to the tunnel, strains are small (say less than 0.1%) and not enough to cause failure or alter the structure of the soil significantly. Thus the constitutive model for the soil can be assumed unchanged during this phase.

Medium and long-term settlements are thought to be the result of creep, ageing and consolidation (Mitchell et al., 1997), i.e. alterations in the properties of the soil at constant load. The timescale over which they occur depends on the ground conditions, ranging from weeks or months for sands and soft clays to years for stiff clays.

The relative magnitude of short and long-term movements depends on many factors and it is hard to generalize. Case histories suggest that for a typical site on stiff clay, around 60% of the total settlement occurs in the short term (Simons and Som, 1970; Morton and Au, 1975). Attewell and Selby (1989) observed long-term settlements up to 2.5 times the short term, but also that the long-term trough widths tended to be wider. This meant that the curvature of the trough, the factor most likely to cause damage to structures, was similar to that in the short term. In addition, surface structures are more able to accommodate long-term settlements by creep and stress redistribution. Thus it is the short-term movements that remain the chief issue of concern for engineers, and are the subject of this study.

### **2.3. The prediction of ground movements due to tunneling**

Detailed understanding of the mechanisms by which ground deformations occur at tunnel excavations could be useful in predicting the volume loss and designing countermeasures against settlement. Empirical methods based on case history data, analytical methods (upper and lower bound and closed-form), laboratory 1g model testing, centrifuge modeling and numerical analysis have all been employed. For the potential value of numerical analysis to be realized, a sufficiently accurate constitutive model for the soil in the appropriate stress/strain range is required. Any modeling technique, either laboratory or numerical, must represent the tunneling process to an acceptable degree of accuracy.

#### **2.3.1. Empirical ‘greenfield’ settlement troughs**

Peck (1969) described settlement data from over twenty case histories available at that time, and was able to infer that the short-term transverse settlement trough in the ‘greenfield’ could be approximated by a normal distribution or Gaussian curve (Peck, 1969; Schmidt, 1969). The equation for the assumed trough shape is thus:

$$S = S_{\max} \exp(-y/2i^2) \quad (2.1)$$

where  $S$ : surface settlement

$S_{\max}$ : maximum surface settlement (over tunnel axis)

$y$ : transverse distance from tunnel centerline

$i$ : trough width parameter, analogous to the standard deviation of the normal distribution

The important features of the trough shape are shown in Figure 2.1. The value of the trough width parameter  $i$ , the distance from the axis to the point of inflexion of the trough (assumed symmetric) determines the maximum settlement for a given volume loss.

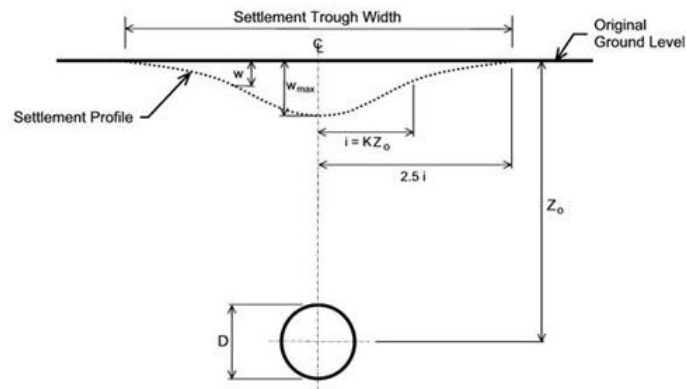


**Figure 2.1.** The Gaussian model of transverse tunneling induced settlements (Peck, 1969).

Peck noticed that soils of different classes, for example cohesionless or cohesive, gave distinct ratios of trough width parameter to tunnel depth. Following from this, O'Reilly and New (1982) expressed the trough width parameter in the form:

$$i = Kz_0 \quad (2.2)$$

where  $K$  is a dimensionless constant, depending on soil type and  $z_0$  is the depth of the tunnel axis below ground level.

Based on data from 19 locations at 11 sites on cohesive ground and 16 locations at 5 sites on cohesionless soils, all in the United Kingdom, O'Reilly and New (1982) proposed the empirical relationships:

$$i = 0.43z_0 + 1.1 \text{ for cohesive soil} \quad (2.3)$$

$$i = 0.28z_0 - 0.1 \text{ for non-cohesive soil} \quad (2.4)$$

The fit to the available data was found to be better for cohesive soils. The data used covered a wide range of tunnel axis depths, from 3.4 m to over 34 m. It thus appeared justified to take  $K$  as a constant value, independent of both tunnel depth and diameter.

The volume of the trough at the surface, commonly equated to the volume loss at the tunnel is evaluated as the integral of the Gaussian distribution curve:

$$\begin{aligned} V_s &= S_{max} \int \exp(-y^2/2i^2) dy \\ &= (2\pi)^{1/2} i S_{max} = V_L \end{aligned} \quad (2.5)$$

The expression for  $S$  may be rewritten, substituting for  $S_{max}$ , as:

$$S = V_L / (2\pi)^{1/2} \cdot i \exp(-y^2/2i^2) \quad (2.6)$$

Attewell and Woodman (1982) extended this model to derive a settlement trough in the longitudinal direction (Fig. 2.2.), using a cumulative Gaussian distribution. It is assumed that exactly half the total settlement has occurred at the position of the heading and that the longitudinal trough parameter is equal to the trough width parameter. The latter assumption is somewhat conservative, as observed longitudinal troughs show a flatter distribution.

Mair et al. (1993) extended the tools available to the engineer for empirical assessment based on the Gaussian model by using case history data to derive formulae for subsurface settlements due to tunneling in clays.



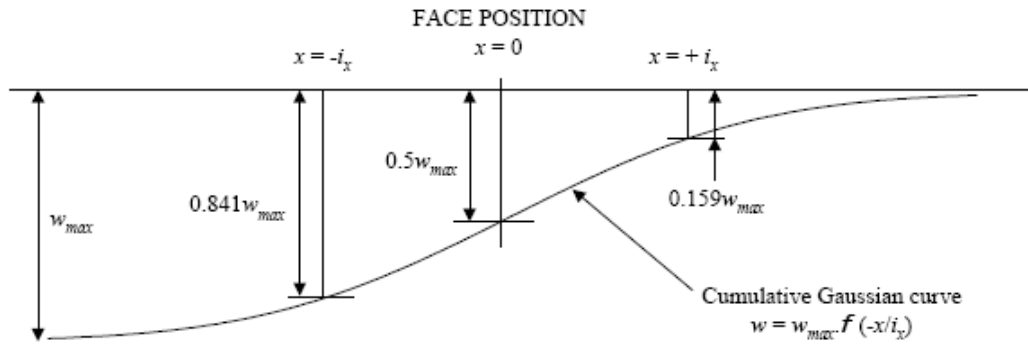


**Figure 2.2.** Empirical longitudinal settlement trough based on Gaussian model (Attewell and Woodman, 1982).

A method for prediction of horizontal ground surface movements was proposed by O'Reilly and New (1982). There was acknowledged to be relatively little field data for corroboration, but centrifuge testing (e.g. Mair, 1979) suggested that the vectors of ground movements above a tunnel in stiff clay generally converged on a point somewhere between the tunnel axis and the tunnel invert. O'Reilly and New approximated the 'sink' thus formed to be at the tunnel axis. Thus:

$$S_H/S = y/z_0 \quad (2.7)$$

$$\text{Hence } S_H = S \cdot y/z_0 \quad (2.8)$$

where  $S_H$  is the horizontal ground movement, and the other terms are as defined previously.

### 2.3.2 Mechanisms of short-term settlement response

Analytical approaches often require the identification of non-dimensional groups of the important parameters influencing a problem. One such group is the stability number (or overload factor)  $N$  defined by Broms and Bennermark (1967) as:

$$N = \frac{\sigma_z - \sigma_T}{\gamma S_U} \quad (2.9)$$

where  $\sigma_z$ : overburden pressure at tunnel axis

$\sigma_T$ : tunnel support pressure (if any)

$S_U$ : undrained shear strength of clay

Centrifuge model tests (Mair, 1979; Kimura and Mair, 1981) on tunnel headings in kaolin clay showed how the stability number at collapse ( $N_{TC}$ ) could be correlated with parameters describing the tunnel heading geometry (Fig. 2.3). Mair et al. (1981) defined the ‘load factor’ (LF) as the ratio  $N/N_{TC}$ . They correlated the volume loss obtained in centrifuge experiments and in 2-D finite element analysis of unlined tunnels with LF, and showed how the LF concept could be used to compare results from geometrically different tunnels.

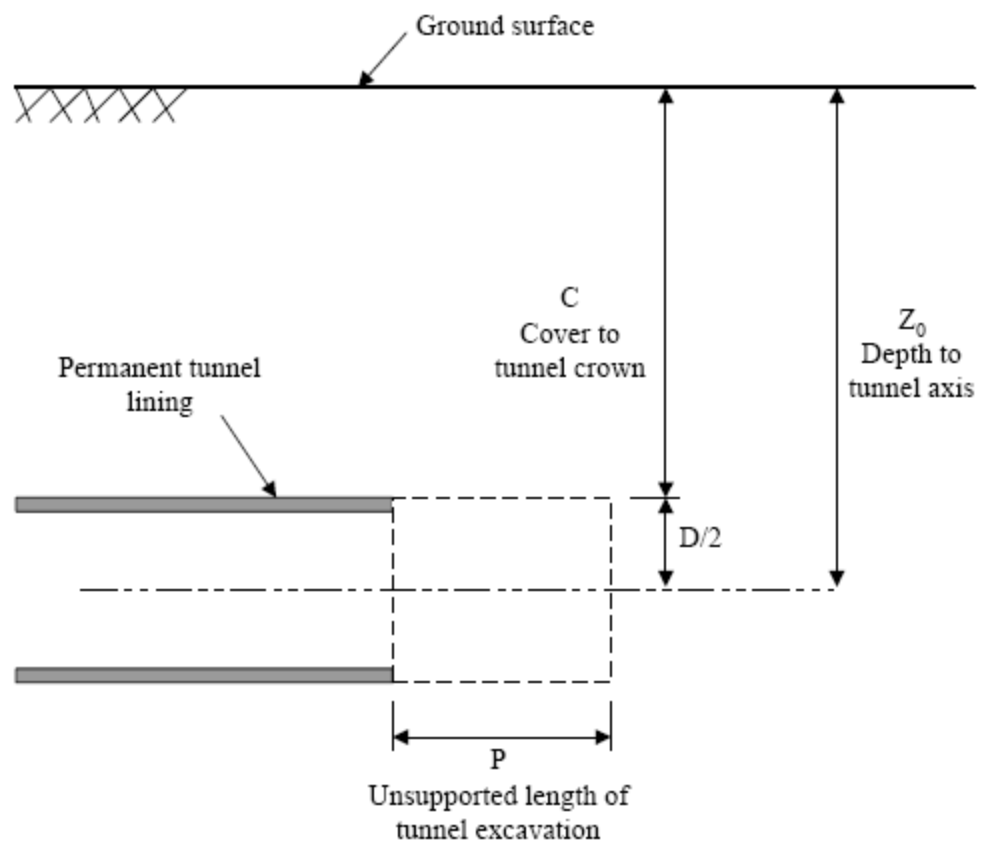


**Figure 2.3.** Geometric parameters of a tunnel heading for calculation of stability number at collapse (Chow, 1994).

Davis et al. (1980) presented lower and upper bound analytical solutions for the collapse load of a shallow tunnel with support pressure in a cohesive soil. They considered the cases of a plane strain unlined circular tunnel (radial ground movements), a plane strain heading (face movements) and a circular tunnel heading (the full three-dimensional case). The difference between the lower and upper bound collapse loads was greatest (with almost a factor of two between them) for the three-dimensional case, indicating the difficulty in applying analytical solutions in three dimensions. They plotted their analytical solutions in terms of  $N_{TC}$  against the cover to diameter ratio ( $C/D$ ). Data from centrifuge modeling (Mair, 1979) confirmed the solutions for a plane strain unlined circular heading, with best agreement for  $C/D$  less than 3.

Observations from centrifuge tests have been used directly to give more information on the soil behavior above tunnels (Mair, 1979; Potts, 1976). Macklin and Field (1999) compared vectors of subsurface movement above tunnels with such data.

Verruijt and Booker (1996) presented approximate analytical solutions for the surface settlements resulting from uniform shrinkage and from ovalisation of a tunnel in elastic half-space. Uniform shrinkage gave a wider settlement trough than observed in practice, but the ovalisation gave a much narrower trough with some heave either side of the tunnel. It thus appeared that practical trough shapes could be explained in terms of a combination of radial shrinkage (representing ground loss due to over-excavation) and ovalisation of the tunnel lining. It was also appreciated that the material model used was linear elastic and that the small strain soil stiffness was not modeled.

Mair and Taylor (1993) developed solutions for the growth of plasticity and excess pore pressure around deep tunnel openings.

### **2.3.3. Laboratory and centrifuge testing**

Laboratory 1g testing can perform a useful role to identify the main influences in a problem such as tunneling. Kim et al. (1996) report tests on the interaction between closely spaced tunnels, finding that significant bending moments could be induced in a tunnel lining due to excavation of another tunnel within two diameters. De Moor and Taylor (1989) carried out model tests using a 250 mm diameter triaxial test apparatus with the tunnel represented as a hollow open-ended brass cylinder aligned in the axial direction. Nakai et al. (2000) report tests on tunneling in sand, where the finished tunnel is modeled by a solid cylinder and the volume loss due to the advance of the tunnel by removal of 4mm thick rods arranged around the annulus of the cylinder.

Centrifuge modeling is used to reproduce the in situ stress state, and hence soil properties, more accurately. Mair (1979) used the centrifuge to model the collapse of a shallow unlined tunnel in clay. Grant and Taylor (2000) used centrifuge modeling in an attempt to verify the analytical solutions of Mair and Taylor (1993) with reasonable agreement. Areas of disagreement were related to the finite depth of the tunnel in the centrifuge, compared to the assumption of an axisymmetric stress state in the analysis.

### **2.3.4. Numerical modeling of the short-term settlement trough**

Previous researchers have attempted to reproduce in numerical modeling the main characteristics of the transverse trough shape.

Rowe et al. (1983) modeled a two-dimensional plane strain heading using an elastic, perfectly plastic soil model. The desired volume loss was modeled by starting the analysis with a ‘gap’ between the outside of the rigid lining and the excavated surface of the soil. This gap was intended to model not only the physical annulus between lining and soil in the optimum case, but also an allowance for workmanship factors such as the advancing shield wandering off its theoretical line. They noted that heave of the invert of the tunnel in the model due

to the stress relief by the excavation had a dramatic effect in reducing the resulting surface settlements. This, however, was not usually observed in the field. By increasing the stiffness of the soil beneath the tunnel, the heave was greatly reduced. They concluded that in this case it was the extension modulus of the soil in the invert that was important, rather than the compression modulus.

El Nahhas et al. (1992) were interested in the response of the lining, and modeled it in two dimensions by excavating soil elements in the tunnel and allowing the soil to deform, switching on a rigid lining when the appropriate volume loss was reached.

Finno and Clough (1985) conducted 2-D analyses in plane strain in the transverse and longitudinal directions, and compared the results with site data in soft clay. A modified Cam-clay soil model was used. Pore pressure changes were limited to a region within two diameters of the tunnel face. The model predicted the heave occurring ahead of the face with an earth pressure balance machine.

Subsidence due to large amounts of fluid withdrawal is explained by the consolidation of sedimentary deposits as the result of increasing effective stress (Bell et al., 1986). Pratt and Johnson (1926) demonstrated that land subsidence resulted directly from lowering of the piezometric surface due to fluid extraction. Poland and Davis (1969) showed that the centers of subsidence in the Santa Clara valley, California, coincided with the centers of major pumping and development of subsidence increasingly occurred with the continuing groundwater utilization. In addition, Abidin et al. (2001) have proven that excessive groundwater extraction in Jakarta caused a serious land subsidence incident. Karlsrud (2001) included a valuable study to the literature by emphasizing that the water leakage that takes place during tunneling under urban areas of the Oslo region possessed a great subsidence threat. Furthermore, Chen et al. (2003) have shown that land subsidence in Suzhou City was directly related with groundwater exploitation through a complex aquifer system.

### **2.3.5. Constitutive models for short term tunneling settlements**

Some researchers (e.g., Chow, 1994; Jardine et al., 1986) have shown that the choice of constitutive model for the soil is very important to the calculated response of the ground, especially the ground deformations. The trough shape at the surface is a result of soil response at small strains, less than 0.1%, over a wide area above the tunnel. Although anisotropy and horizontal stress ratio may have some influence, the most important issue is the relatively high initial stiffness of the soil at very small strains. Numerical models with linear elastic soil properties give significantly wider settlement troughs than observed in the field.

Jardine et al. (1986) presented a non-linear elastic constitutive model for low plasticity (over-consolidated) clays. This model allowed for a high initial stiffness, gradually reducing with strain. This was shown to give rise to an apparent increase of stiffness with depth, which is often observed in the field and sometimes applied to linear elastic models. The model was not demonstrated for a tunneling problem, which has the particular feature that the ground is undergoing unloading.

An alternative family of constitutive models has been developed, based on an assumption of work-hardening plasticity. These are capable of capturing the effects of stress history on soil behavior, and can therefore in theory model unloading and cyclic loading. Stallebrass and Taylor (1997) demonstrated a model with three nested yield surfaces – an initial yield surface, history surface and critical state failure surface. They applied this model to the case of a 2-D plane strain foundation, showing how the displacements close to the footing, and the redistribution of stress beneath the footing, compared favorably to centrifuge modeling data.

Houlsby (1999) has also developed a kinematic hardening model, from plasticity theory based upon fundamental thermodynamics (Collins and Houlsby, 1997). Nested yield surfaces are surrounded by an outer failure envelope. Figure 2.4 shows the response of the yield surfaces on translation in stress space from the

origin 'O' to 'A' and back to 'O'. The model is not complicated to apply, requiring only a set of non-dimensional hardening and shear strength parameters that describe the reduction in shear stiffness as each yield surface is reached.

In the current implementation of the kinematic hardening model, the outer surface is a perfectly plastic von Mises surface. Once this surface is reached, the material loses all stiffness and load is shed elsewhere, meaning that consolidation and contractile yielding, as encountered in critical state models, cannot be reproduced. An enhancement to cater for this is under development. In the meantime, the model is still suitable for representing general small strain (pre-failure) deformation of stiff clays.

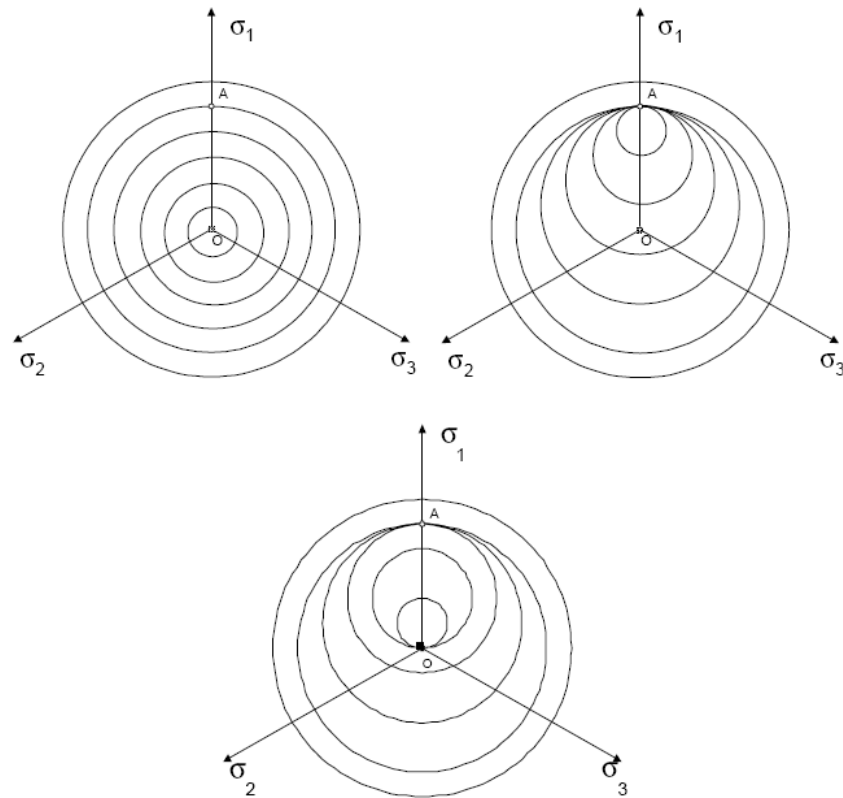


**Figure 2.4.** Translation of nested yield surfaces in kinematic hardening model under action of stress path from origin to A and back (Houlsby, 1999).

## 2.4. Summary

It is well known that ground movements and settlements occur when tunnels are excavated in soft ground. The fundamental cause of most of the movement is ‘volume loss’, which takes place as the soil moves into the advancing face and radially onto the lining as the tunnel advances. The mechanism of volume loss is inherently linked to the type of tunneling process taking place.

Often the volume loss can be predicted based on experience of previous sites in similar ground conditions with similar tunneling processes. Researchers have also demonstrated more rational techniques for prediction, based on a correlation of volume loss with load factor (a measure of the factor of safety of the tunnel heading against collapse) together with an allowance for workmanship effects.

The short-term settlement response of the ground is regarded as the most important for its effects on surface structures. During this phase, the soil properties may be assumed unchanged and it responds with small strain behavior. Medium and long-term settlements due to consolidation and other effects tend to be more widely distributed, and many structures can accommodate them by creep.

A prediction technique for short term ‘greenfield’ settlements that is universally applied in practice is based on a survey of case history information, in which it was found that the transverse surface settlement trough due to tunneling typically followed a Gaussian or normal distribution profile. Researchers have found that the ratio between a measure of the trough width and the tunnel depth depended chiefly on the soil type, and much effort has been expended in assessing this parameter  $K$ . The techniques have also been extended longitudinal, horizontal and subsurface ground movements, all based on the original Gaussian model. These techniques are very convenient to use for estimating ‘greenfield’ surface settlements but it is hard to see how the philosophy of carrying out a survey of case history information and proposing a design curve could be extended to cases including surface structures, as the number of possible configurations and structural forms is vast, and case history data is very limited.



Closed form solutions, laboratory 1g and centrifuge testing have also all played an important part in gaining an understanding of the ‘greenfield’ response of the ground. However, these techniques are also difficult to extend to include buildings. Therefore, researchers recently have been focusing more on the use of numerical analysis, and this is also the direction taken by this thesis.

Any numerical analysis technique must include a credible representation of the tunneling process, in particular the volume loss occurring. It must also use an appropriate constitutive model for the soil. It is recognized that linear elastic soil models give trough widths that are too wide, and that it is necessary to model the small strain behavior of the soil. Models based on work hardening plasticity involving kinematic hardening have been found to be appropriate, as they can model small strain behavior, the effect of stress history and cyclic loading.

## CHAPTER 3

### GEOPHYSICAL INVESTIGATIONS

#### 3.1. Introduction

The Necatibey Metro Station is located within the alluvial deposits of Dikmen stream and the so-called Ankara clay. At the metro station a number of boreholes were drilled. However, due to the spacing of the boreholes the boundary between alluvium and Ankara clay deposits could not be separated precisely. Thus, geophysical studies have been planned for the delineation of the boundaries of the two deposits.

Two geophysical methods are used in this thesis, namely Electrical Resistivity Imaging (ERI) and Ground Penetrating Radar (GPR). These two methods are among the most popular near-surface geophysical methods, especially with the advancement in equipment and computing technology. Generally they are time- and cost- effective and relatively easy to execute. They share a significant physical parameter namely electrical conductivity. This physical parameter provides the means with which the methods are to be integrated as it is the main parameter that governs the ERI technique and it highly affects the propagation of the GPR signals.

ERI measurements are usually made by passing an electrical current into the ground using a pair of (current) electrodes and measuring the resulting potential gradient within the subsurface with a second (potential) electrode pair. The resistance data collected in this way is then converted to apparent resistivity readings by applying a geometric factor based on the type of electrode configuration being used (Sheriff, 1999; Reynolds, 2000).

In applied geophysics the true subsurface electrical resistivity is mostly interested in and in order to recover the true resistivity, the apparent resistivity measurements have to undergo a process called inversion, which estimates the true resistivity by determining the best least squares fit to the measured apparent resistivity (Loke and Barker, 1995).

In GPR, a transmitting antenna radiates an electromagnetic pulse into the ground that behaves kinematically similar to an acoustic wave. The pulse is transmitted, reflected, and diffracted by features that correspond to changes in the electrical properties of the earth. The waves that are reflected and diffracted back toward the earth's surface may be detected by a receiving antenna, amplified, digitized, displayed, and stored for further analysis. The time it takes for the wave to return can be calculated and then equated to the distance the target is from the transmitter / receiver (Daniels et al., 1988; Davis and Annan, 1989).

GPR has the highest resolution of any geophysical method for imaging the subsurface, with centimeter scale resolution sometimes possible. By analyzing some of characteristics properties of the returned pulse, small details and significant information about the target and ultimately the subsurface can be obtained (Daniels et al., 1988; Davis and Annan, 1989).

### **3.2. Electrical Resistivity Imaging (ERI) studies**

Electrical Resistivity (ER), also called DC Resistivity, is one of the oldest and most popular geophysical techniques in the field of near surface geophysics. During the last two decades the technique has been revolutionized in terms of data acquisition systems, i.e. the development of multi-electrode and capacitively-coupled resistivity systems and processing software. After these developments, the method has been more frequently referred to as Electrical Resistivity Imaging (ERI) or Electrical Resistivity Tomography (ERT).

Electrical Resistivity Imaging (ERI) is based on injecting electrical current into the subsurface using a pair of electrode (current electrodes) and measuring the potential gradient between another pair of electrode (potential electrodes). The

measured resistance is then converted into apparent resistivity by multiplying the resistance by an appropriate geometric factor, which depends on the type of acquisition array being used. The apparent resistivity is then inverted in order to come up with the true subsurface resistivity and to reveal the thickness and depth of individual resistivity layers within the subsurface. Inversion is a fundamental step in all modern resistivity imaging surveys. It is, basically, a mathematical procedure by which the subsurface physical parameter distribution is estimated based on a set of field measurements (Telford et al., 1990; Reynolds, 2000).

Typical resistivity instruments mainly consists of three major components namely a source (current electrodes), a receiver (potential electrodes) and a control unit that makes the measurements and controls the acquisition sequence. Figure 3.1 illustrates the resistivity instrument used in this study.

Two different types of acquisition modes are commonly employed in resistivity surveys: resistivity sounding or resistivity profiling. The former is based on increasing the electrode separation around a central position in order to increase the depth of imaging while the latter is based on moving the electrodes layout along the horizontal axis in order to map lateral variations in the subsurface resistivity (Telford et al., 1990).

There are three different means by which electric current flows in the subsurface namely electronic, electrolytic, and dielectric conduction (which also dominates in GPR). Since most of the mineral grains encountered in geophysical surveying are insulators, and since electrical resistivity operates at low frequency, it is the second type of conduction that we observe, i.e., current flow by ions such as in water and clay (Telford et al., 1990).



(a)



(b)

**Figure 3.1.** The resistivity instrument used in this study; a) ARES Automatic Resistivity System, b) intelligent cable.

Common arrays used in electrical resistivity surveys and geometric factors ( $k$ ) based on the electrode configuration are given in Figure 3.2. Note that the dipole-dipole, pole-dipole and Wenner-Schlumberger arrays have two parameters, “ $a$ ” and “ $n$ ”;  $a$  is the unit electrode spacing in meter and  $n$  is the separation factor.  $C_1$ ,  $C_2$ ,  $P_1$  and  $P_2$  refer to the locations of the positive and negative current and potential electrodes  $+I$ ,  $-I$ ,  $+V$  and  $-V$  respectively (Loke, 2004).

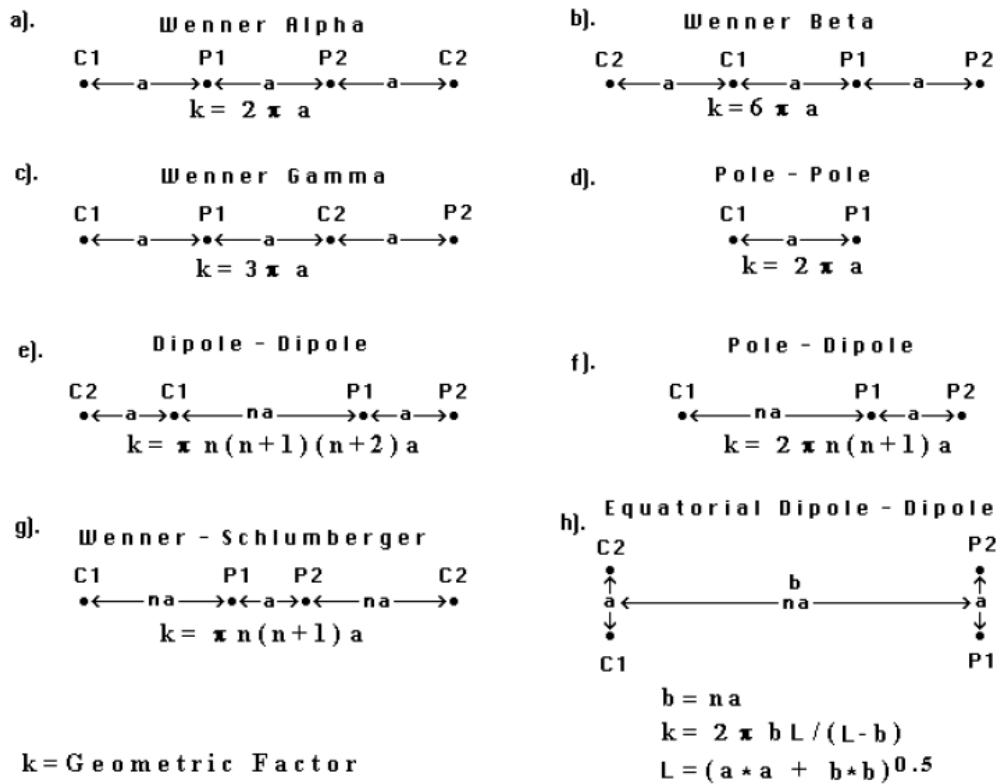


**Figure 3.2.** Common arrays used in resistivity surveys and their geometric factors (Loke, 2004).

The resistivity of common rocks, soil materials and chemicals (Keller and Frischknecht, 1966; Daniels and Alberty, 1966; Telford et al., 1990) is shown in Figure 3.3. Igneous and metamorphic rocks typically have high resistivity values. The resistivity of these rocks is greatly dependent on the degree of fracturing, and the percentage of the fractures filled with groundwater. Thus a given rock type can have a large range of resistivity, from about 1000 to 10 million  $\Omega\text{m}$ , depending on whether it is wet or dry. This characteristic is useful in the detection of fracture zones and other weathering features, such as in engineering and groundwater surveys.

Sedimentary rocks, which are usually more porous and have higher water content, normally have lower resistivity values. The resistivity values are largely dependent on the porosity of the rocks, and the salinity of the contained water.

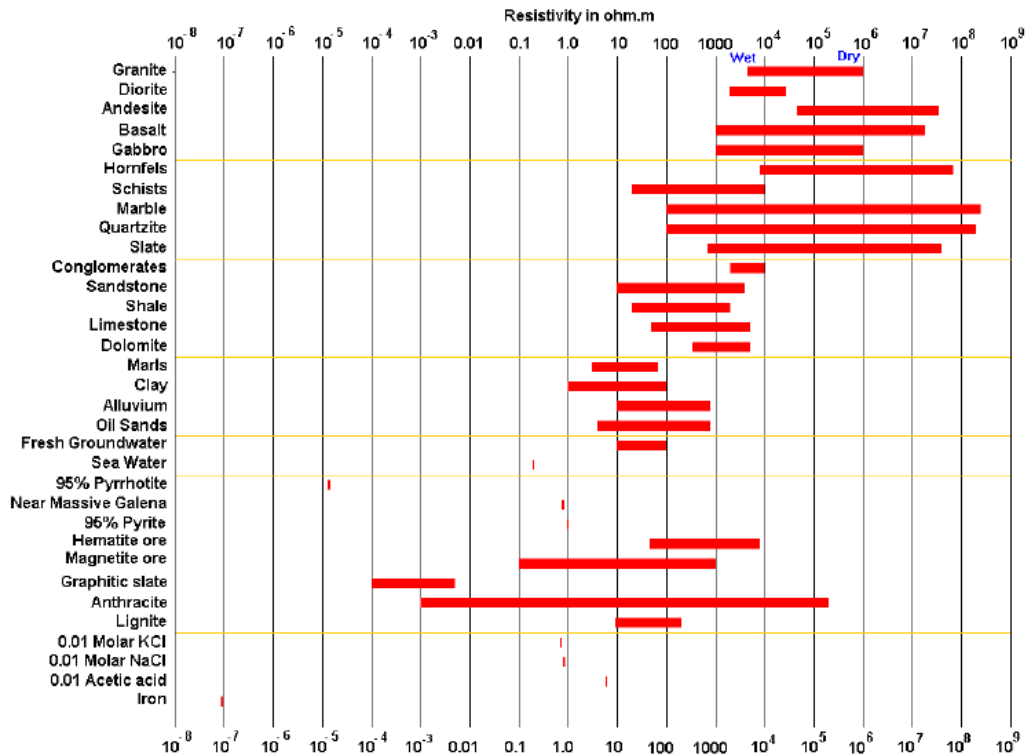


**Figure 3.3.** The resistivity values of rocks, soils and minerals (Keller and Frischknecht, 1966; Daniels and Alberty, 1966; Telford et al., 1990).

Unconsolidated sediments generally have even lower resistivity values than sedimentary rocks, with values ranging from about 10 to less than 1000  $\Omega$ m. The resistivity value is dependent on the porosity (assuming all the pores are saturated) as well as the clay content. Clayey soil normally has a lower resistivity value than sandy soil. However, note the overlap in the resistivity values of the different classes of rocks and soils. This is because the resistivity of a particular rock or soil sample depends on a number of factors such as the porosity, the degree of water saturation and the concentration of dissolved salts.

Apparent resistivity ( $\rho_a$ ) is defined as the resistivity of an equivalent homogeneous ground that will give the same resistance value for the same electrode configuration. In order to recover the true resistivity, the apparent resistivity measurements have to be inverted.

In geophysical inversion, we seek to find a model that gives a response that is similar to the actual measured values. The model is an idealized mathematical representation of a section of the earth. The model has a set of model parameters that are the physical quantities we want to estimate from the observed data. The model response is the synthetic data that can be calculated from the mathematical relationships defining the model for a given set of model parameters. All inversion methods essentially try to determine a model for the subsurface whose response agrees with the measured data subject to certain restrictions (Loke, 2004). In the cell-based method used by the RES2DINV and RES3DINV programs, the model parameters are the resistivity values of the model cells, while the data is the measured apparent resistivity values. The mathematical link between the model parameters and the model response for the 2-D and 3-D resistivity models is provided by the finite-difference (Dey and Morrison, 1979a, 1979b) or finite-element methods (Silvester and Ferrari, 1990).

### **3.2.1. Data acquisition and processing**

Electrical resistivity field data are collected using a resistivity instrument, electrodes (sensors), an electrical source (transmitter), and some sort of cable or wire interconnection between them.

There are various electrode configurations which can be used in resistivity surveying (Figure 3.2). A typical survey consists of some variation of a four electrode array with two electrodes forming a transmitting pair whereby electrical current is injected into the earth and two electrodes forming a receiver pair that measures the voltage difference due to the impressed current. The standard separation distance between the electrodes is called the unit electrode spacing or simply electrode spacing ( $a$ ). The separation factor ( $n$ ) is a multiplication, for most arrays an integer between 1 and 6, of the unit electrode spacing. The apparent resistivity measured by an array depends on the geometry of the electrodes and the section generated by plotting these apparent resistivity measurements is called a pseudosection (Figure 3.4).



In a typical survey, most of the fieldwork is in laying out the cable and electrodes. After that, the measurements are taken automatically and stored in the computer. Most of the survey time is spent waiting for the resistivity meter to complete the set of measurements. To obtain a good 2-D picture of the subsurface, the coverage of the measurements must be 2-D as well. As an example, Figure 3.4 shows a possible sequence of measurements for the Wenner electrode array for a system with 20 electrodes. In this example, the spacing between adjacent electrodes is “a”. The first step is to make all the possible measurements with the Wenner array with electrode spacing of “1a”. For the first measurement, electrodes number 1, 2, 3 and 4 are used. Notice that electrode 1 is used as the first current electrode C1, electrode 2 as the first potential electrode P1, electrode 3 as the second potential electrode P2 and electrode 4 as the second current electrode C2. For the second measurement, electrodes number 2, 3, 4 and 5 are used for C1, P1, P2 and C2 respectively. This is repeated down the line of electrodes until electrodes 17, 18, 19 and 20 are used for the last measurement with “1a” spacing. For a system with 20 electrodes, note that there are 17 (20 - 3) possible measurements with “1a” spacing for the Wenner array.

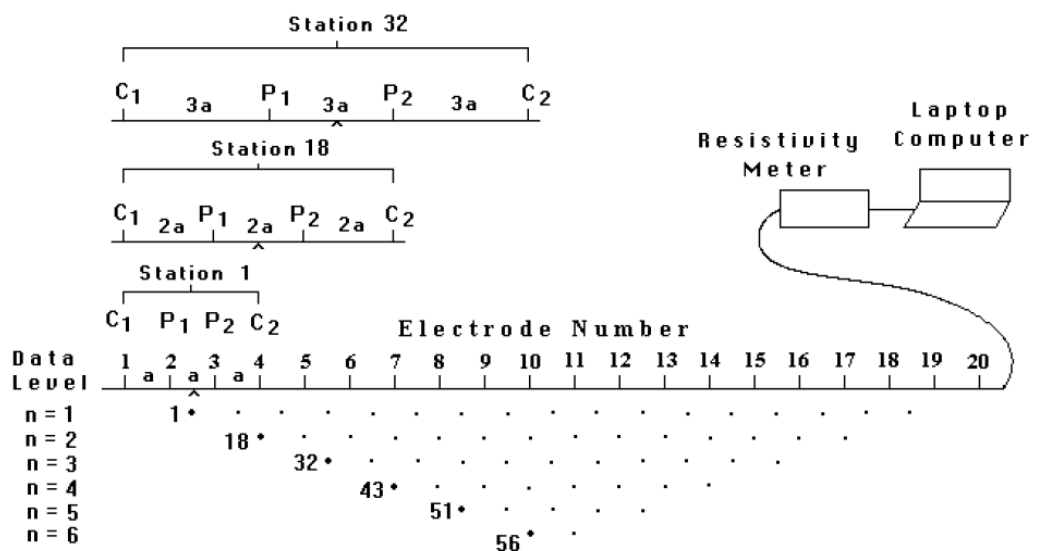


**Figure 3.4.** The arrangement of electrodes for a 2-D electrical survey and the sequence of measurements used to build up a pseudosection (Loke, 2004).

After completing the sequence of measurements with “1a” spacing, the next sequence of measurements with “2a” electrode spacing is made. First electrodes 1, 3, 5 and 7 are used for the first measurement. The electrodes are chosen so that the spacing between adjacent electrodes is “2a”. For the second measurement, electrodes 2, 4, 6 and 8 are used. This process is repeated down the line until electrodes 14, 16, 18 and 20 are used for the last measurement with spacing “2a”. For a system with 20 electrodes, note that there are 14 ( $20 - 2 \times 3$ ) possible measurements with “2a” spacing.

The same process is repeated for measurements with “3a”, “4a”, “5a” and “6a” spacing. To get the best results, the measurements in a field survey should be carried out in a systematic manner so that, as far as possible, all the possible measurements are made. This will affect the quality of the interpretation model obtained from the inversion of the apparent resistivity measurements (Dahlin and Loke, 1998).

It should be noted that as the electrode spacing increases, the number of measurements decreases. The number of measurements that can be obtained for each electrode spacing for a given number of electrodes along the survey line depends on the type of array used. The Wenner array gives the smallest number of possible measurements compared to the other common arrays that are used in 2-D surveys.

The survey procedure with the pole-pole array is similar to that used for the Wenner array. For a system with 20 electrodes, firstly 19 of measurements with a spacing of “1a” are made, followed by 18 measurements with “2a” spacing, followed by 17 measurements with “3a” spacing, and so on. For the dipole-dipole, Wenner-Schlumberger and pole-dipole arrays (Figure 3.2), the survey procedure is slightly different. As an example, for the dipole-dipole array, the measurement usually starts with a spacing of “1a” between the C1-C2 (and also the P1-P2) electrodes. The first sequence of measurements is made with a value of 1 for the “n” factor (which is the ratio of the distance between the C1-P1 electrodes to the C1-C2 dipole length), followed by “n” equals to 2 while keeping the C1-C2 dipole pair spacing fixed at “1a”. When “n” is equals to 2, the distance of the C1

electrode from the P1 electrode is twice the C1-C2 dipole length. For subsequent measurements, the “ $n$ ” spacing factor is usually increased to a maximum value of about 6, after which accurate measurements of the potential are difficult due to very low potential values. To increase the depth of investigation, the spacing between the C1-C2 dipole pair is increased to “ $2a$ ”, and another series of measurements with different values of “ $n$ ” is made. If necessary, this can be repeated with larger values of the spacing of the C1-C2 (and P1-P2) dipole pairs. A similar survey technique can be used for the Wenner-Schlumberger and pole-dipole arrays where different combinations of the “ $a$ ” spacing and “ $n$ ” factor can be used (Loke, 2004).

In resistivity surveys, there are two main modes of deployment: vertical electric sounding (VES) and electric profiling (EP) (Figure 3.5). In the vertical sounding mode the center point of the array is kept constant while the electrode spacing is varied for each measurement in order to determine changes in resistivity with depth. In the electric profiling mode the electrode spacing is fixed while the center of the array is varied in order to detect lateral variations in resistivity. In addition to VES and EP, roll-along is a technique that is frequently used in resistivity surveys (Figure 3.6). It is based on increasing the number of data points in each  $n$  level by taking overlapping measurements (with different combinations of “ $a$ ” and “ $n$ ”) while extending the horizontal coverage. Therefore the technique does not only help in accommodating vertical and horizontal variations but also in improving the quality of the data and the efficiency of the survey (Alshuhail, 2006).

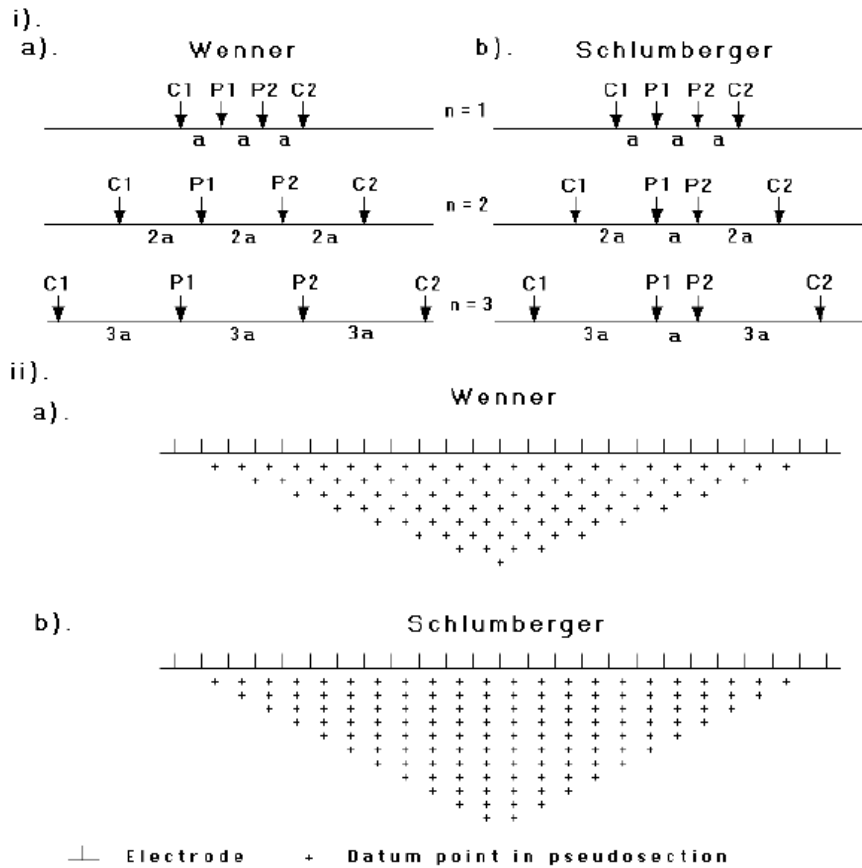


**Figure 3.5.** A comparison of the (i) electrode configuration and (ii) pseudosection data pattern for Electric Profiling (Wenner array) and Vertical Electric Sounding (Schlumberger array) (Loke, 2004).

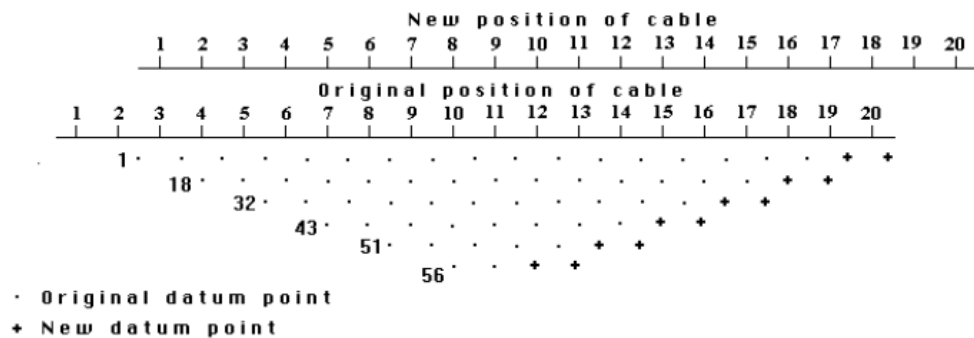


**Figure 3.6.** The use of the roll-along method to extend the area covered by a 2-D survey (Loke, 2001).

### **3.2.2. Considerations and limitations**

There are different factors that affect the movement of current in the subsurface and therefore the performance of the ERI: water content, temperature, ions (their concentration and mobility), metal content, porosity, permeability, clay content and skin depth. Like any other geophysical method, there must be a sufficient contrast in the subsurface physical properties (resistivity) in order for the method to be successful in imaging the subsurface and detecting the target. Furthermore a given material can have a large range of resistivity and therefore overlapping values could pose a problem when interpreting the resistivity data.

One of the difficulties associated with ERI is finding sufficient accessible space, especially with the pole-pole and pole-dipole arrays. Another challenge is that highly conductive surface materials will confine the current flow in the top layer and therefore limit the amount of information coming from deeper layers. The method is also susceptible to interference from nearby grounded metal fences, buried pipes, cables, etc.

It is always important to keep in mind the resolution capability of the technique and the used acquisition parameters when inverting the resistivity measurements. The resistivity phenomenon is based on the diffusion equations, so its resolution is inherently poorer than the seismic or GPR methods at depths greater than one wavelength (Sheriff, 1999).

### **3.2.3. Field application: Data acquisition, processing, interpretation**

The exact locations of resistivity profiles were superimposed on Figure 1.1 using red lines and illustrated again as Figure 3.7. As it can be seen from the Figure 3.7, the study area is located among the buildings of Turkish General Staff, Turkish Air Force and General Directorate of Highways. Due to the highly settled area there was a lack of place for intelligent cables to extend. The profile lengths were 30 m with 2 m electrode spacing for profile 1, 52.5 m with 3.5 m electrode spacing for profile 2 and 75 m with 5 m electrode spacing for profile 3.

For every profile four different electrode arrays were utilized. These were namely a) Schlumberger N6 Dipole Dipole N4, b) Dipole Dipole N6 S1, c) Schlumberger N6, and d) Wenner Alpha. The measured resistivity data (Appendix A) were then need to be inverted to get true resistivity values of the subsurface. In order to invert measured resistivity values RES2DINV inversion software was used. RES2DINV is a computer program that will automatically determine a two-dimensional (2D) resistivity model for the subsurface for the data obtained from electrical imaging surveys (Griffiths and Barker, 1993). Since it is Windows based software, all Windows compatible graphic cards and printers are automatically supported. Figure 3.4 shows an example of the electrodes arrangement and measurement sequence that can be used for a 2D electrical imaging survey. This software is designed to invert large data sets (with about 200 to 21000 data points) collected with a system with a large number of electrodes.

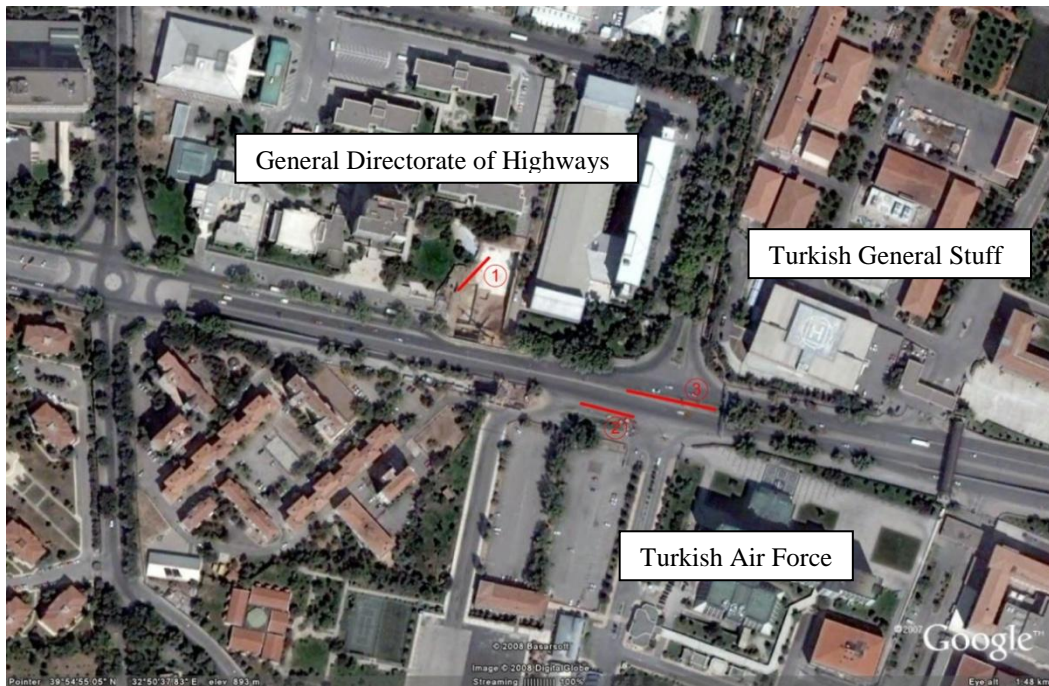


**Figure 3.7.** Study area and resistivity profile locations shown by red lines (Google Earth, 2007).

The 2D model used by the inversion software which consists of a number of rectangular blocks is shown in Figure 3.8. The arrangement of the blocks is loosely tied to the distribution of the data points in the pseudosection. The distribution and size of the blocks is automatically generated by the software using the distribution of the data points as a rough guide. The depth of the bottom row of the blocks is set to be approximately equal to the equivalent depth of investigation of the data points with the largest electrode spacing (Edwards, 1977). The survey is usually carried out with a system where the electrodes are arranged along a line with a constant spacing between adjacent electrodes.

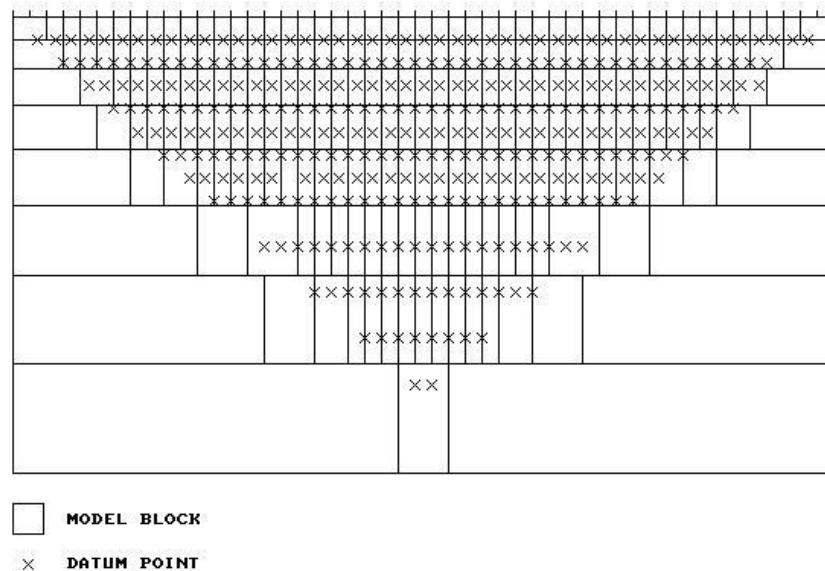


**Figure 3.8.** Arrangement of the blocks used in a model together with the data points in the pseudosection (RES2DINV, 2004).

A forward modeling subroutine is used to calculate the apparent resistivity values, and a non-linear least-square optimization technique is used for the inversion routine (deGroot-Hedlin and Constable, 1990; Loke and Barker, 1996). The software supports both the finite difference and finite element forward modeling techniques. This software can be used for surveys using the Wenner, pole pole,

dipole dipole, pole dipole, Wenner Schlumberger and equatorial dipole dipole arrays. In addition to these common arrays, the program even supports non-conventional arrays with an almost unlimited number of possible electrode configurations.

After inversion process, resultant 2D resistivity images were illustrated in Figure 3.9 through Figure 3.11 to interpret subsurface profile and results were correlated with boring logs. As mentioned before, four different array configuration were used for every profile and the letters a, b, c and d indicate these different electrode configurations. For example, Figure 3.9.a means resistivity profile 1 with Schlumberger N6 Dipole Dipole N4 array configuration.



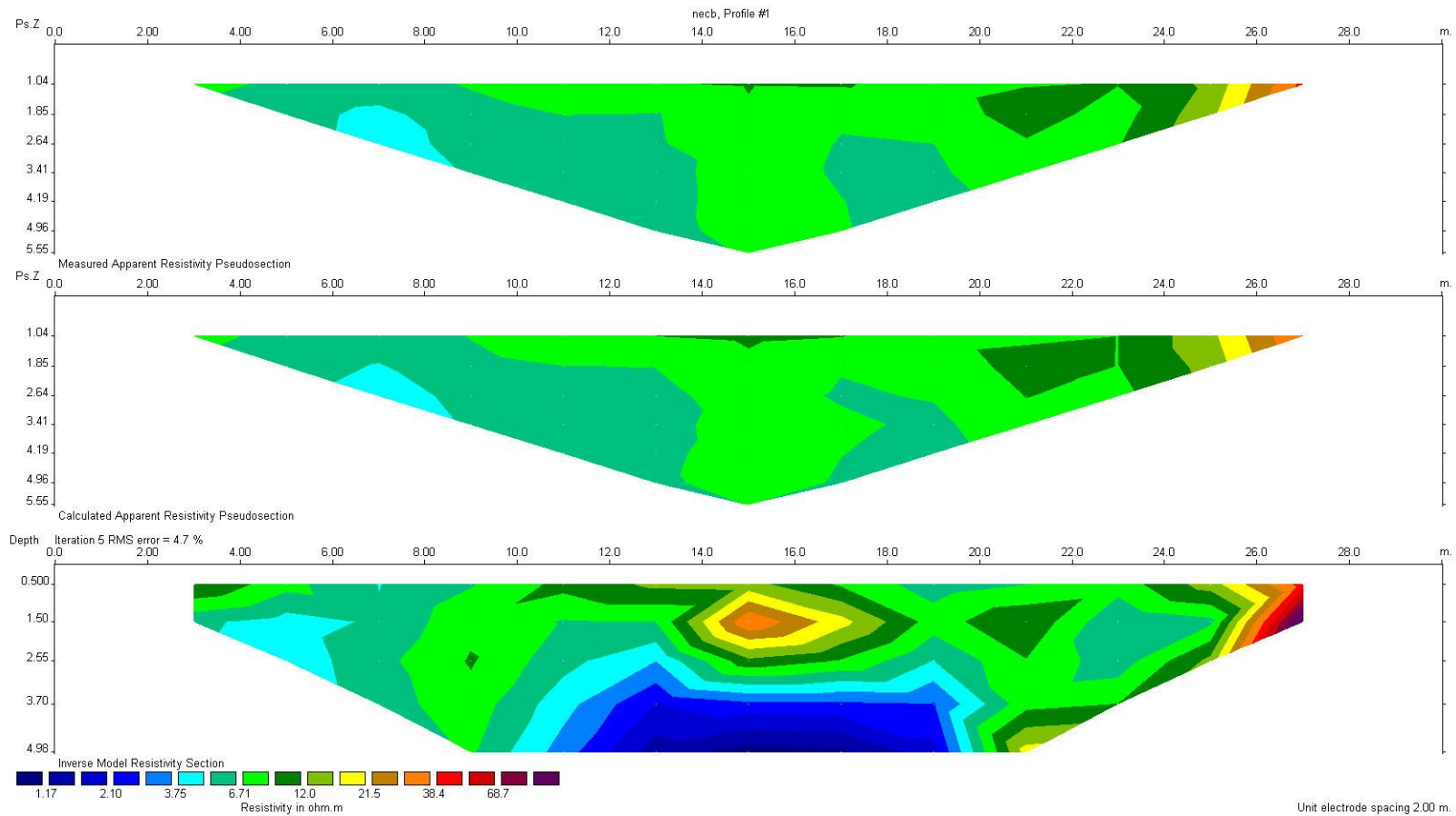


**Figure 3.9.a.** Interpretation of Schlumberger N6 Dipole Dipole N4 electrode configuration for profile 1.

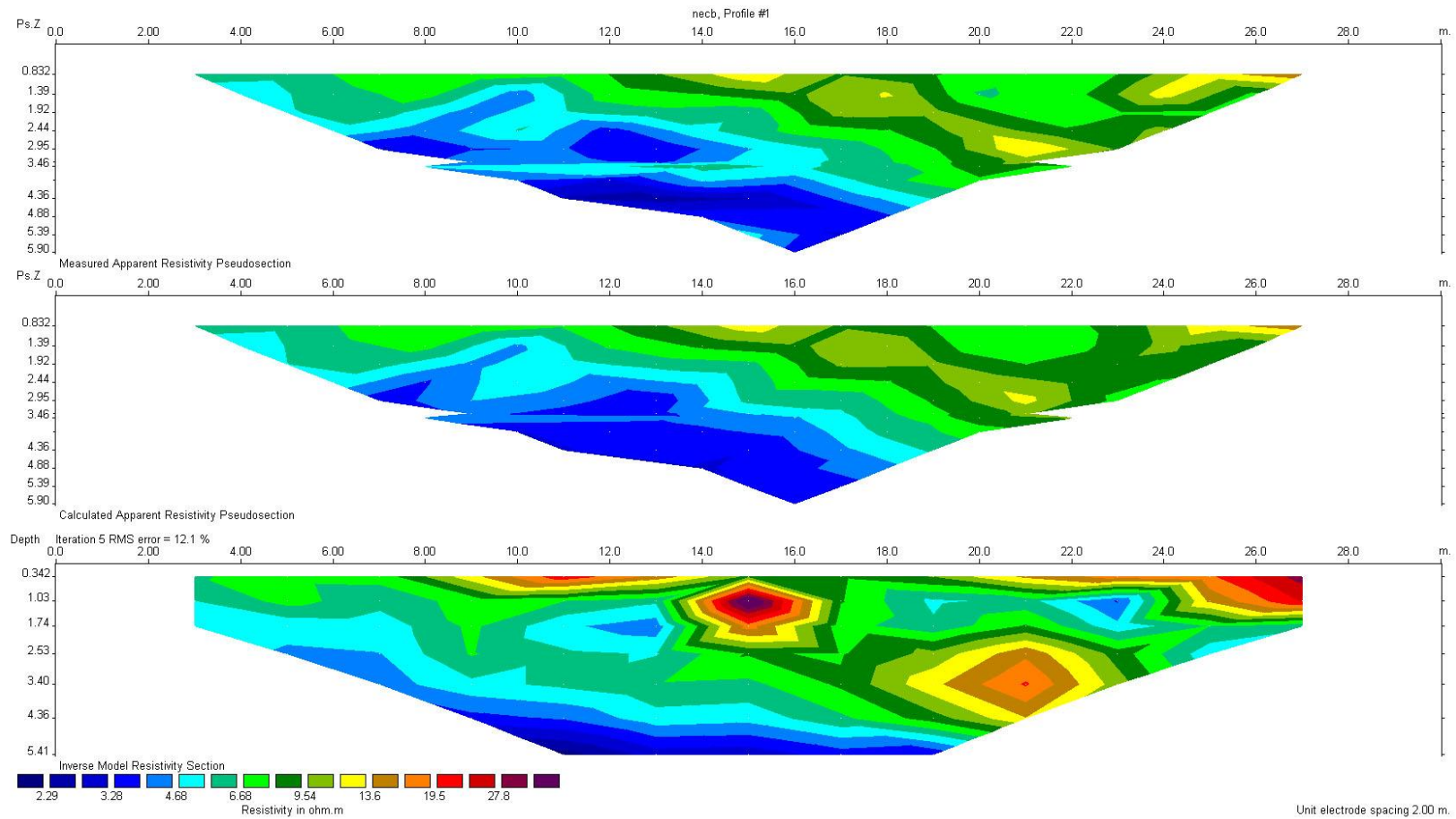


**Figure 3.9.b.** Interpretation of Dipole Dipole N6 S1 electrode configuration for profile 1.

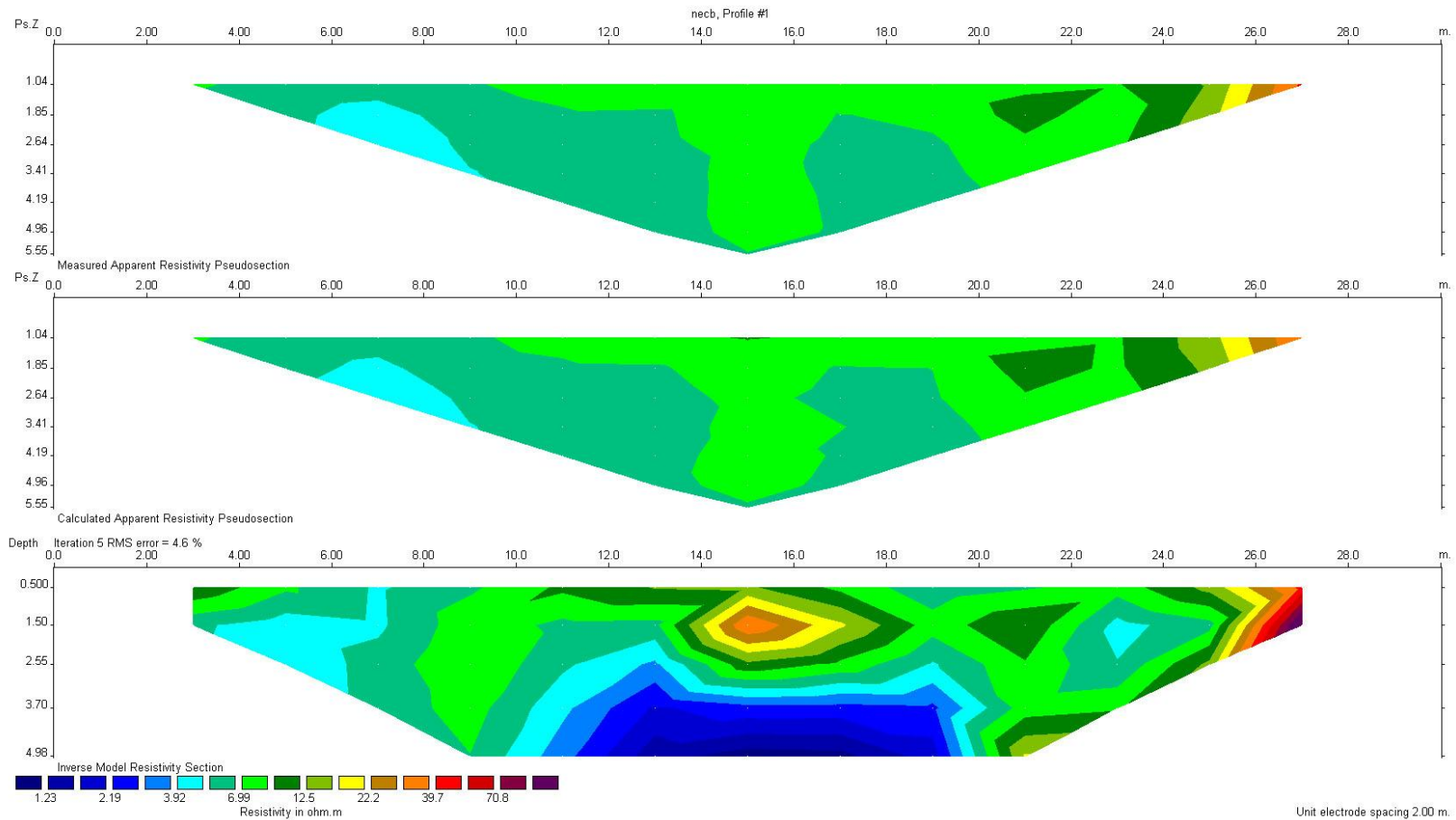


**Figure 3.9.c.** Interpretation of Schlumberger N6 electrode configuration for profile 1.

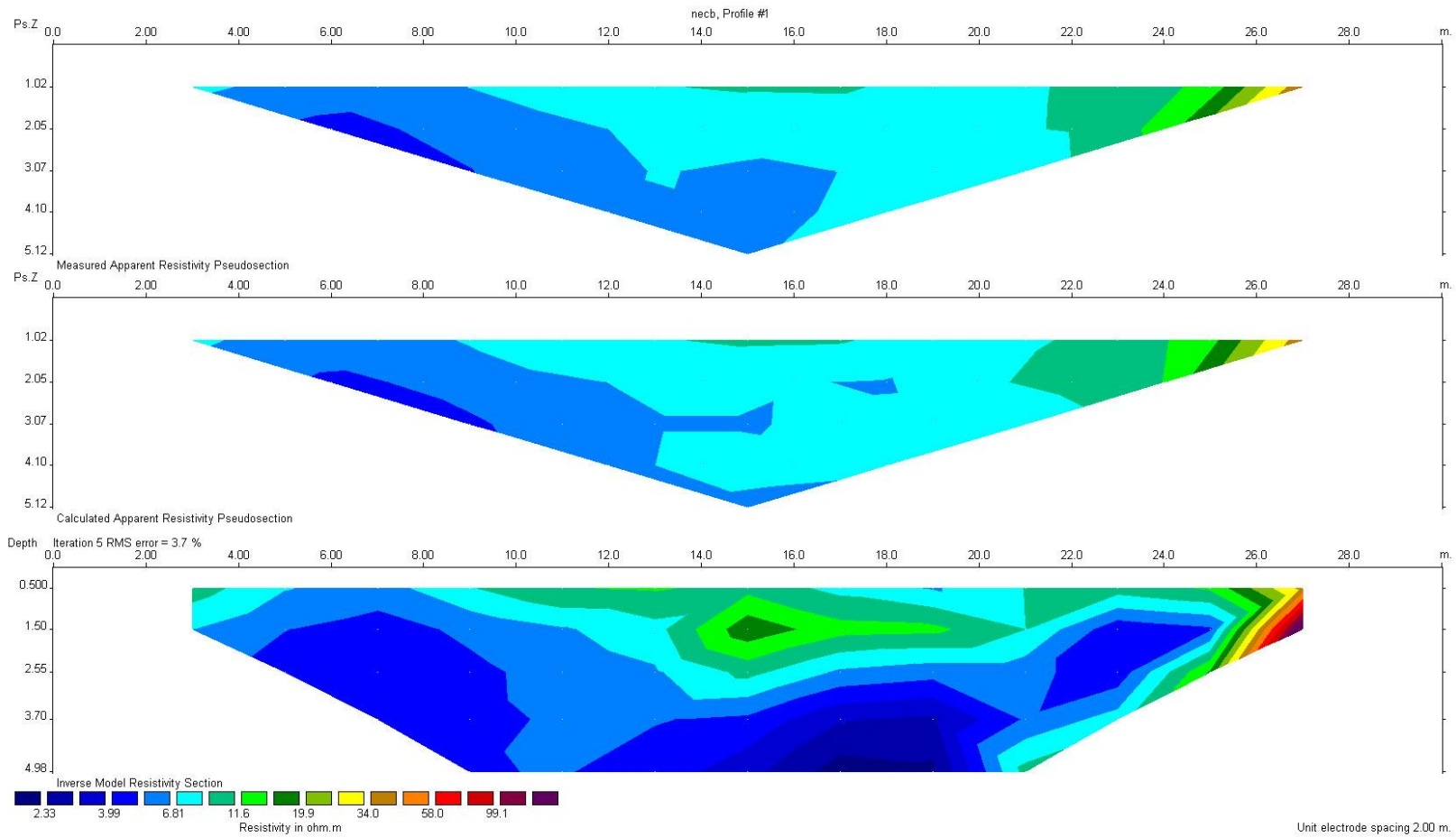


**Figure 3.9.d.** Interpretation of Wenner Alpha electrode configuration for profile 1.

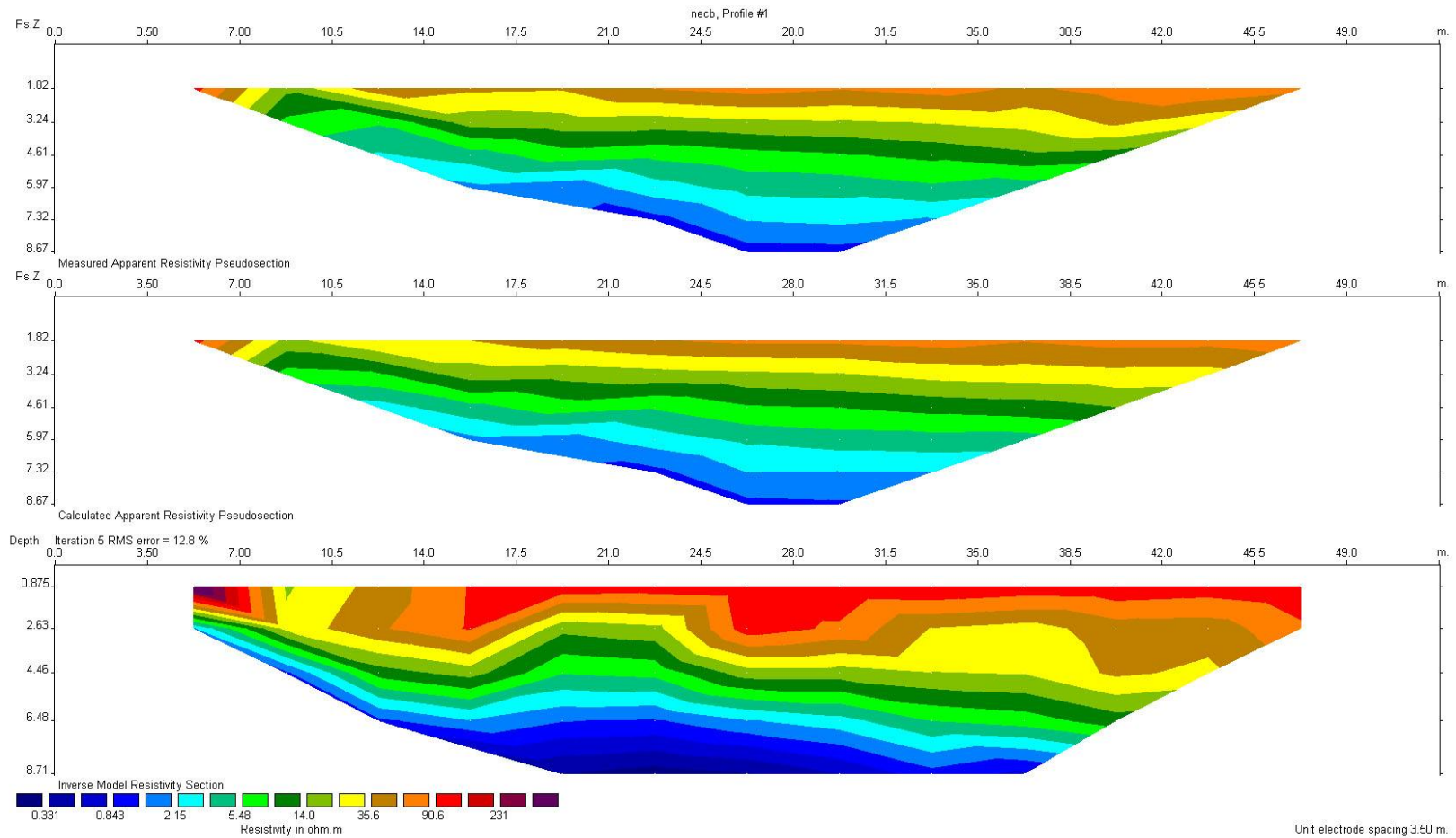


**Figure 3.10.a.** Interpretation of Schlumberger N6 Dipole Dipole N4 electrode configuration for profile 2.

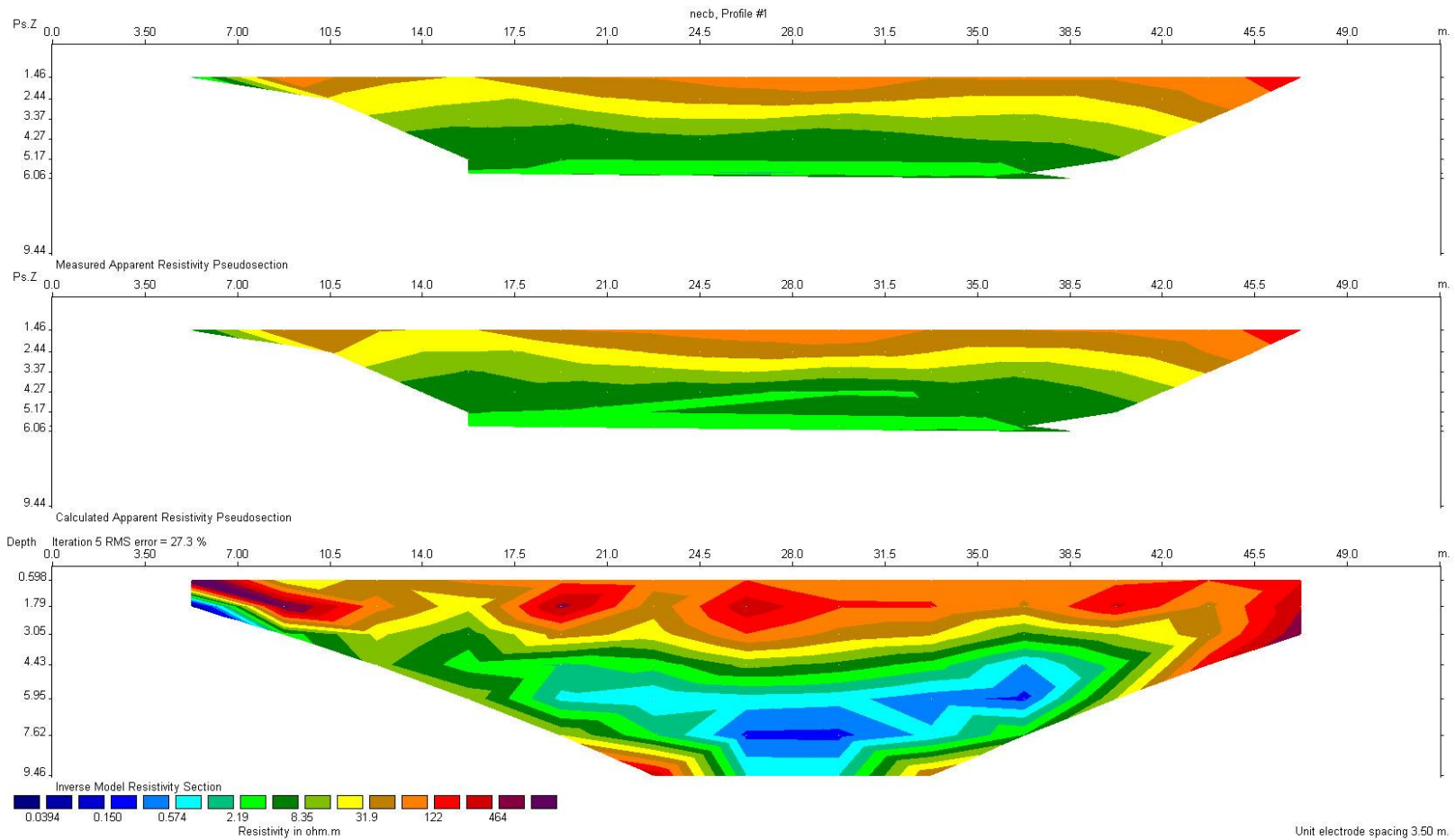


**Figure 3.10.b.** Interpretation of Dipole Dipole N6 S1 electrode configuration for profile 2.



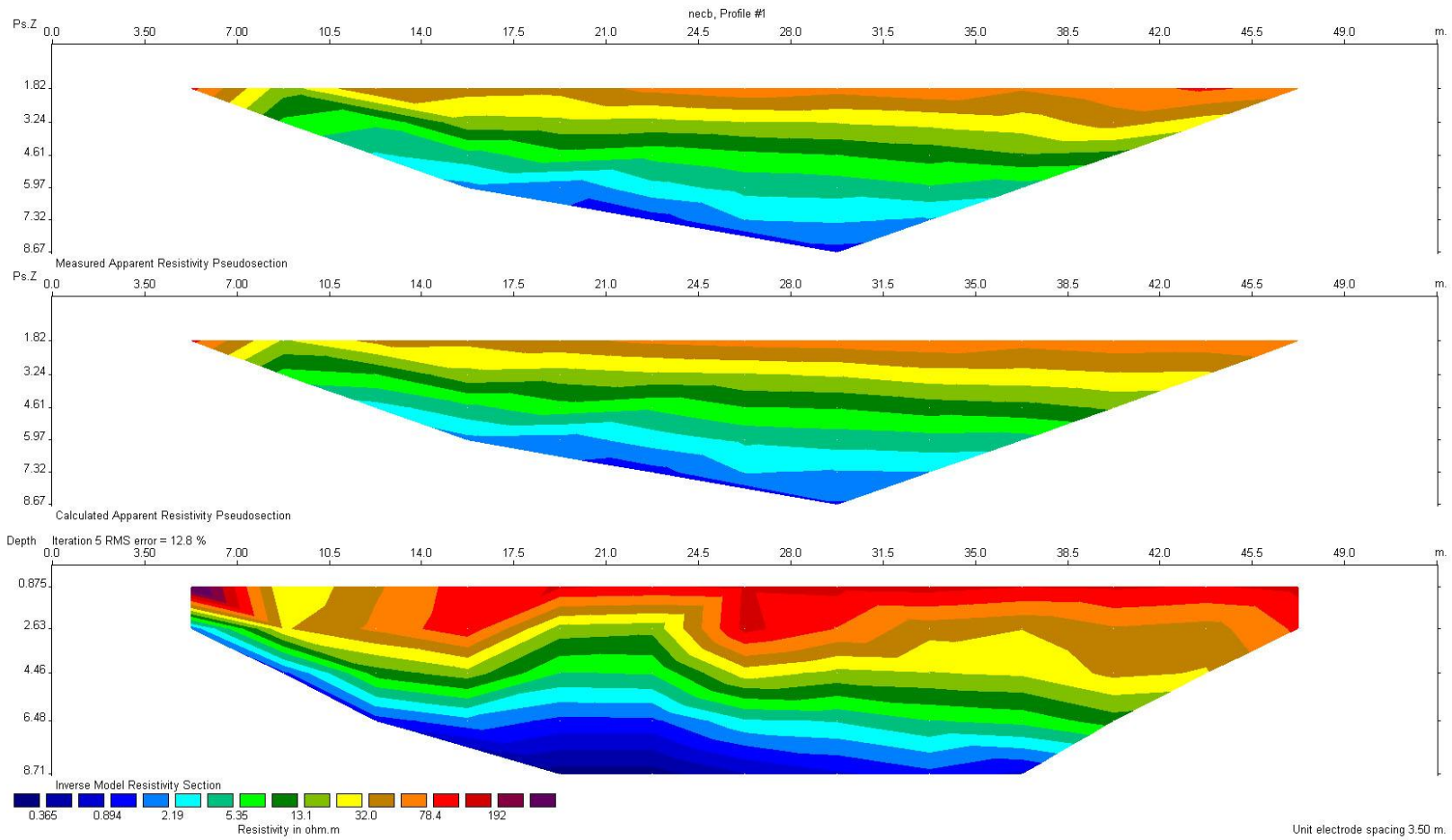
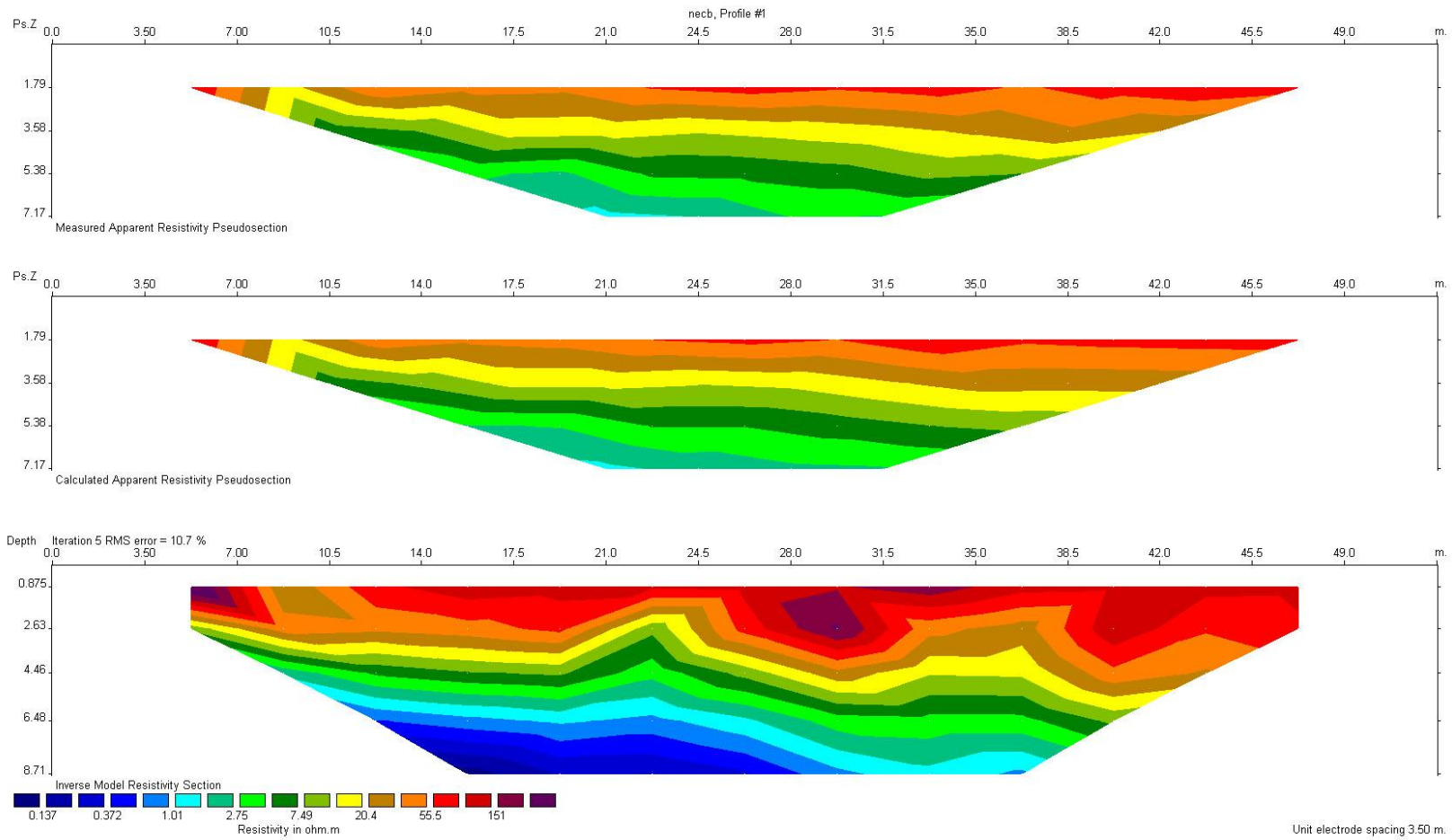
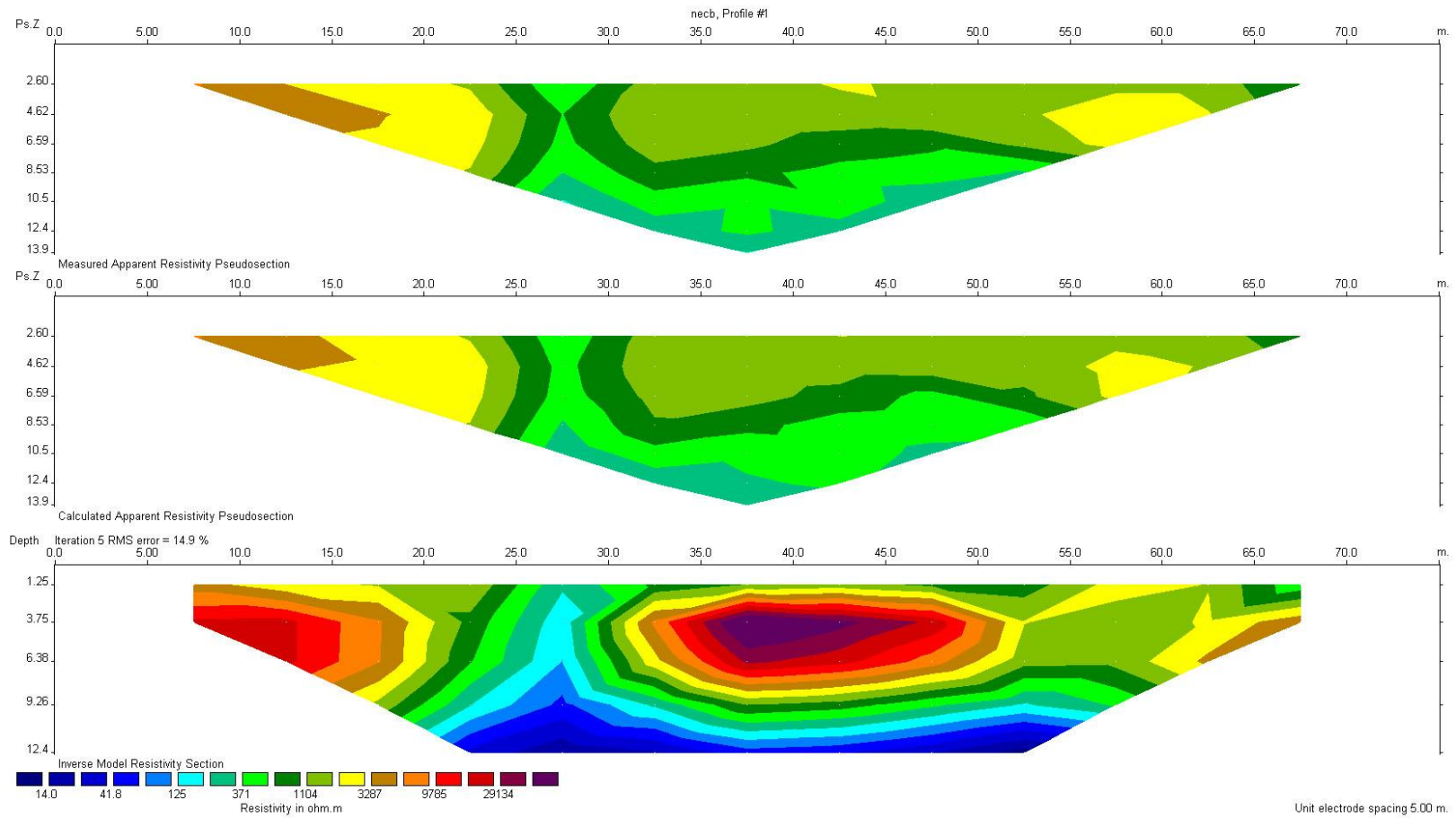


Figure 3.10.c. Interpretation of Schlumberger N6 electrode configuration for profile 2.



**Figure 3.10.d.** Interpretation of Wenner Alpha electrode configuration for profile 2.





**Figure 3.11.a.** Interpretation of Schlumberger N6 Dipole Dipole N4 electrode configuration for profile 3.

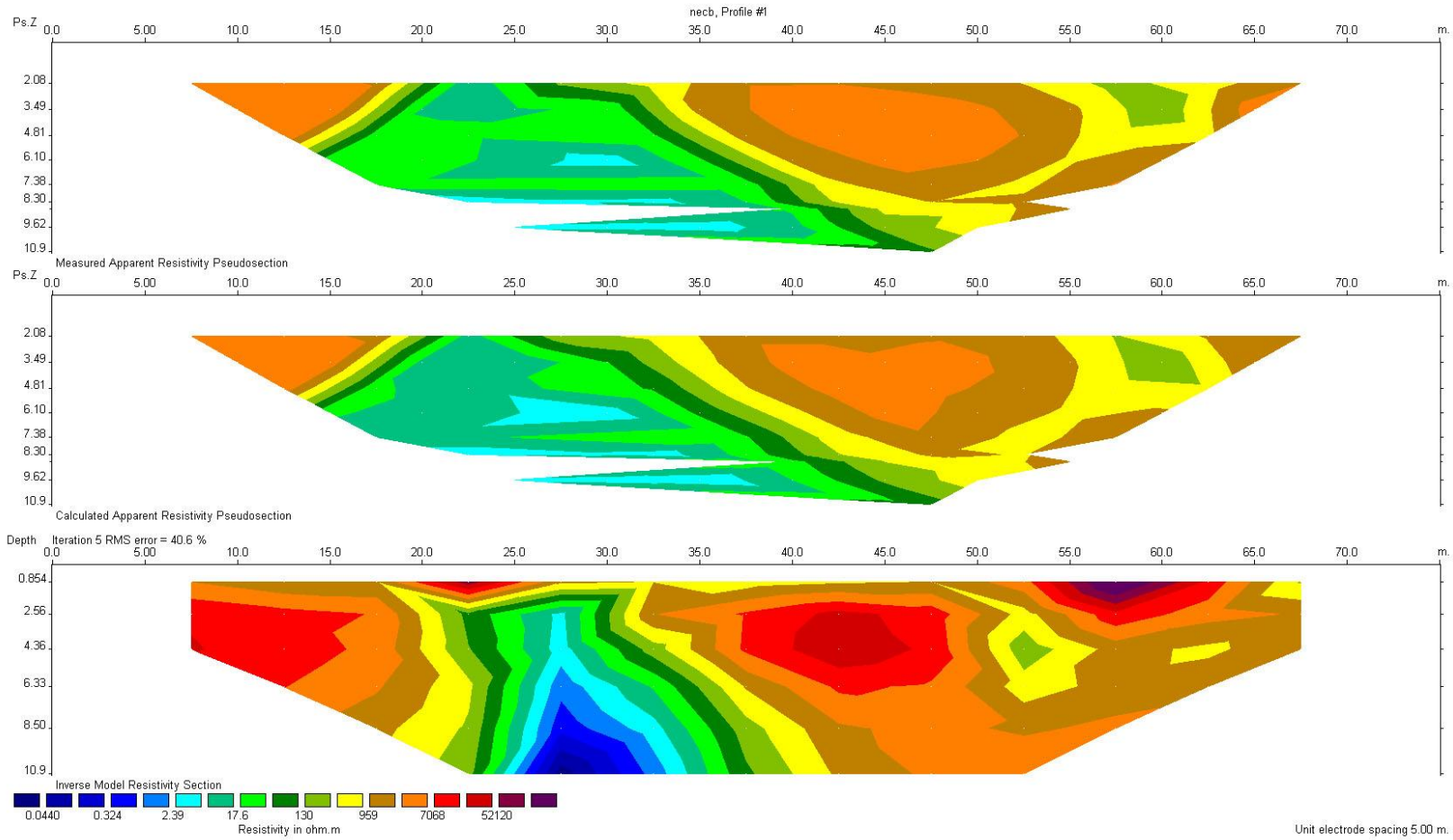
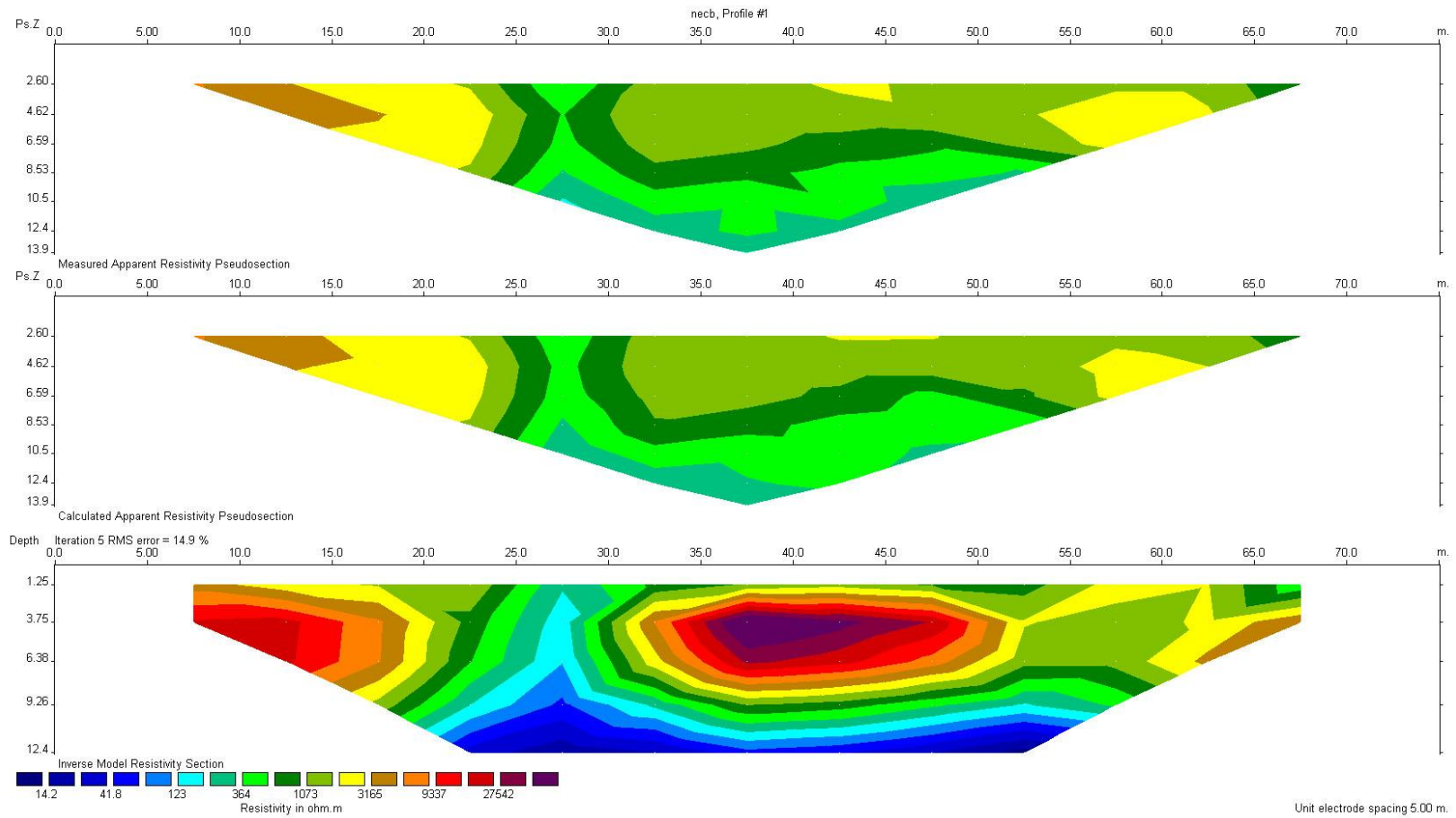


Figure 3.11.b. Interpretation of Dipole Dipole N6 S1 electrode configuration for profile 3.



**Figure 3.11.c.** Interpretation of Schlumberger N6 electrode configuration for profile 3.

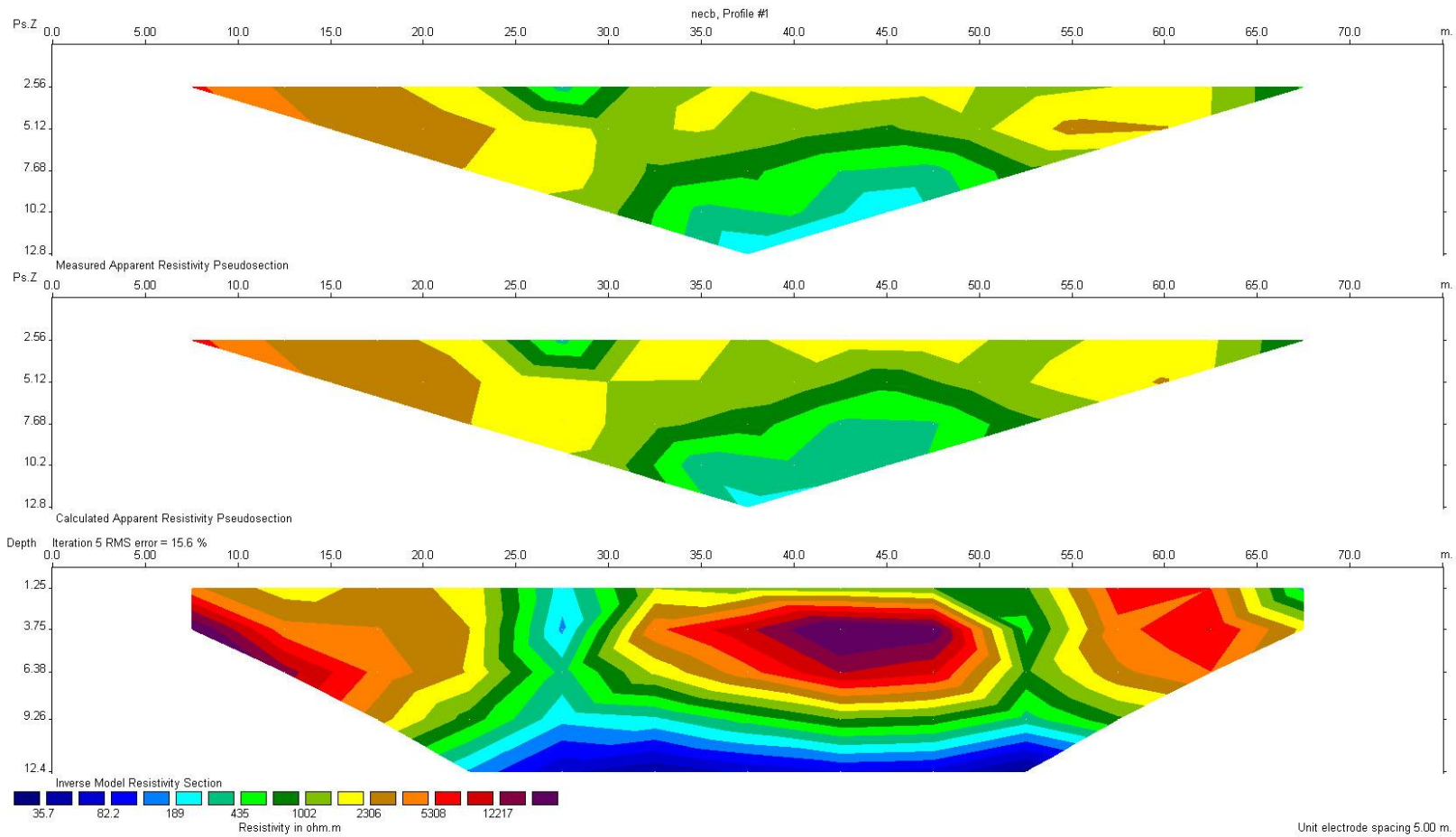


Figure 3.11.d. Interpretation of Wenner Alpha electrode configuration for profile 3.

The shape of the contours in the pseudosection produced by the different arrays over the same structure can be very different. The arrays most commonly used for resistivity surveys were shown in Figure 3.2. The choice of the “best” array for a field survey depends on the type of structure to be mapped, the sensitivity of the resistivity meter and the background noise level. In practice, the arrays that are most commonly used for 2-D imaging surveys are the (a) Wenner, (b) dipole-dipole (c) Wenner-Schlumberger (d) pole-pole and (d) pole-dipole. Among the characteristics of an array that should be considered are (i) the depth of investigation, (ii) the sensitivity of the array to vertical and horizontal changes in the subsurface resistivity, (iii) the horizontal data coverage and (iv) the signal strength (Loke, 2004).

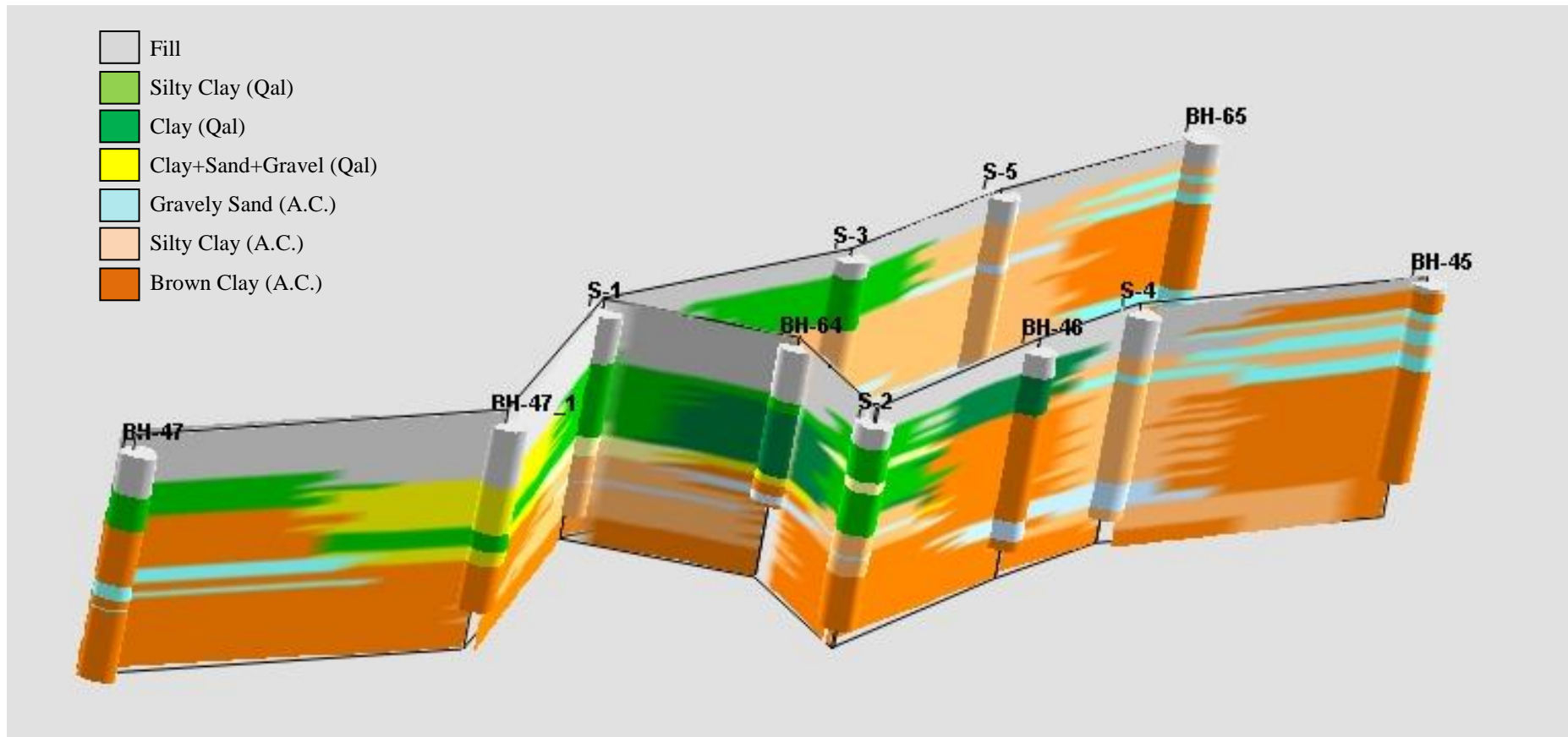
The length of profile 1 was 30 m with 2 m electrode spacing as illustrated in Figure 3.9.a, b, c and d. Since penetration depth is directly proportional to profile length and electrode spacing, the penetration depth for profile 1 was limited and it was about 5 m. First 1 to 1.5 m was interpreted as “fill” due to the resistivity values between 9 to 15  $\Omega\text{m}$ . After 1.5 m depth, “clayey soil” took place up to deepest point of the section (5 m) with 2-3  $\Omega\text{m}$  resistivity values. The closest boring log to the profile 1 is BH 45 (Figure 1.4) and the lithology constructed by interpreting profile 1 resistivity values is reasonably in agreement with the BH 45 log for the uppermost 5 m.

Figure 3.10.a, b, c and d illustrate 2D resistivity image for profile 2. As seen, profile length was 52.5 m and reachable depth was about 9 m. First 3-4 m depth was occupied by “fill material” with 5-13  $\Omega\text{m}$  resistivity values. This part (3-4 m) was underlain by “wet clayey soil” with low resistivity values. The closest borehole logs (S3 and S5 logs (Figure 1.6) are in a good agreement with interpretation of profile 2 resistivity values.

Profile 3 was the longest section and its 2D images were illustrated in Figure 3.11.a, b, c and d. The length of the profile is 75 m and 12.5 m depth was displayed. It was thought that first 7-8 m occupied by “fill material” and after that depth “silty clayey alluvium” took place. The abrupt increase in resistivity values

at 4-5 m depth may indicate a concrete structure. BH 64 (Figure 1.5) log that is the closest borehole to the profile is in accordance with the interpretations.

With the interpretation of 2D electrical resistivity images and borehole logs together, the regional 3D subsurface panel diagrams were constructed and presented in Figure 3.12 (looking South to North) and Figure 3.13 (looking North to South). The colors used in 3D panel diagrams are compatible with borehole logs.



**Figure 3.12.** Regional 3D subsurface panel diagram created by interpreting 2D electrical resistivity images and borehole logs together (North to South).



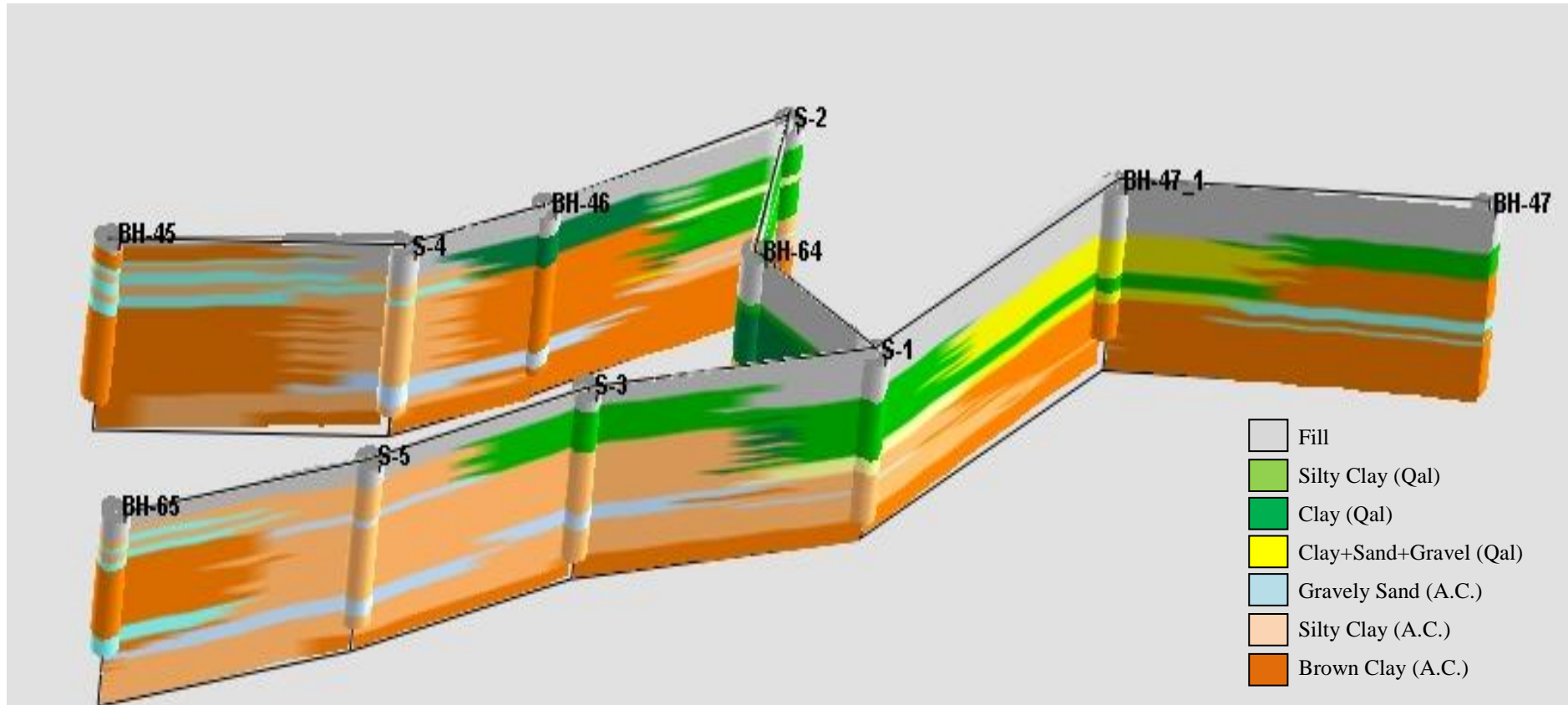


**Figure 3.13.** Regional 3D subsurface panel diagram created by interpreting 2D electrical resistivity images and borehole logs together (South to North).



### 3.3. Ground Penetrating Radar (GPR) studies

Ground penetrating radar (GPR) is well-accepted geophysical technique. The method uses radio waves to probe “the ground” which means any low loss dielectric material.

The most common form of GPR measurements deploys a transmitter and a receiver in a fixed geometry, which are moved over the surface to detect reflections from subsurface features. In some applications, transillumination of the volume under investigation is more useful. Both concepts are depicted in Figure 3.14. An example of GPR response is shown in Figure 3.15.

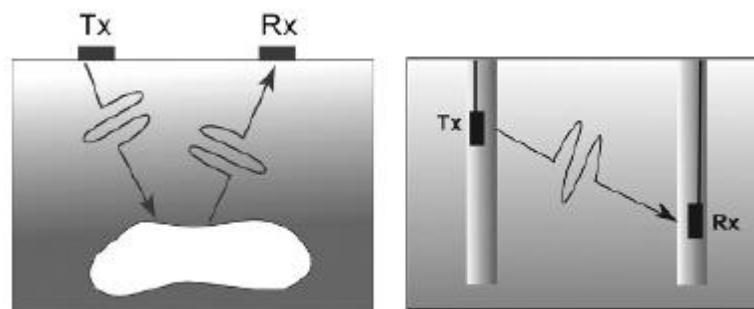


**Figure 3.14.** Ground penetrating radar (GPR) uses radio waves to probe the subsurface of lossy dielectric materials. Two modes of measurement are common. In the first, reflected or scattered energy is detected. In the second, effects on energy transmitted through the material are observed (Jol, 2009).

#### 3.3.1. Physical properties and parameters

GPR signals is a form of electromagnetic waves, which are energy waves produced by the oscillation or acceleration of an electron and propagate, at high frequency, typically between 10 and 1000 MHz, as a periodic disturbance.

Electromagnetic waves have both electric and magnetic components, which are perpendicular to each other and propagation of the EM waves is perpendicular to both, associated with the field resulted from the motion of electric charge.

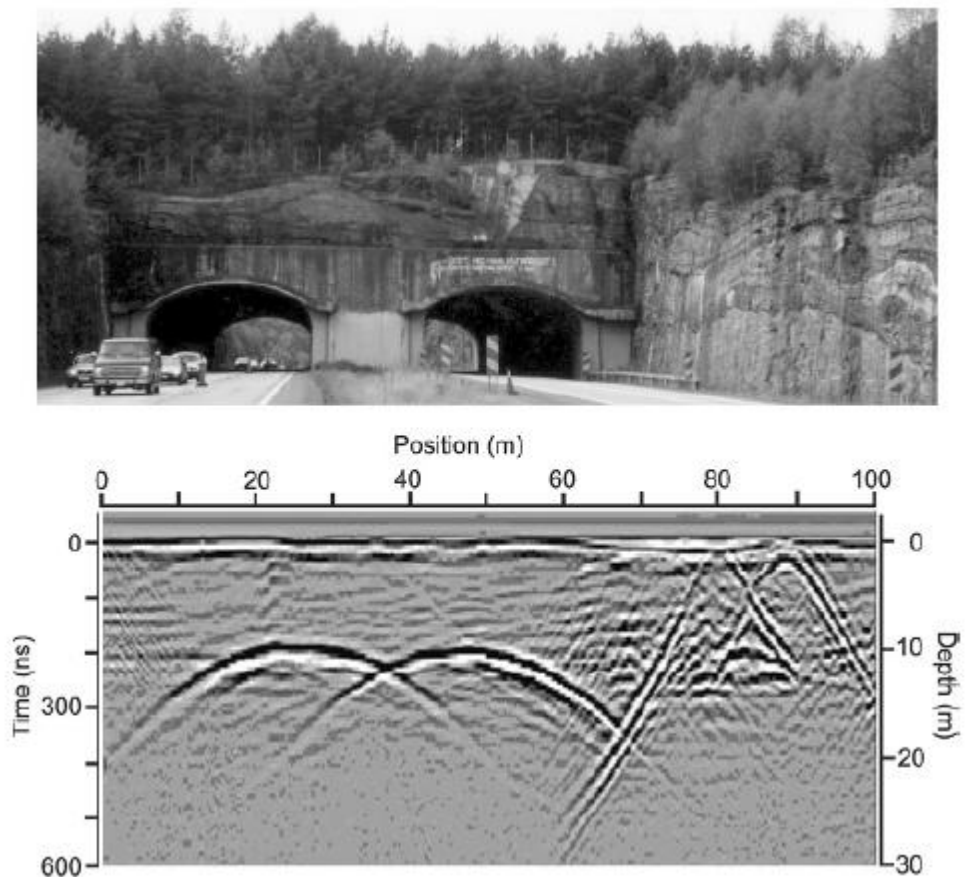


**Figure 3.15.** Ground penetrating radar (GPR) cross section obtained with a 50-MHz system traversing over two road tunnels. Ground penetrating radar signal amplitude is displayed as a function of position (horizontal axis) and travel time (vertical axis) (Jol, 2009).

Unlike seismic waves, EM waves are described by their electric and magnetic fields components through Maxwell's equations. Since subsurface geological materials have different physical and chemical properties it is possible to exploit

GPR to map the variations in some of these properties, namely electrical and magnetic properties, and therefore characterize the subsurface geology. The main properties and parameters affecting the propagation of the GPR signal are conductivity ( $\sigma$ , the ability of a material to conduct electrical current); relative dielectric permittivity ( $\epsilon_r$ , the capacity of material to store charge when an electric field is applied); relative magnetic permeability ( $\mu_r$ , the degree of magnetization of a material that responds linearly to an applied magnetic field); loss factor ( $P$ ); velocity ( $v$ , speed with which the radiowaves propagate in low loss materials over the range of GPR frequency); attenuation (reduction in amplitude or energy caused by physical characteristics of the transmitting media or system); quality factor ( $Q$ , measure of the GPR system performance); depth of penetration (the depth below the surface to which GPR system can effectively explore); and reflection coefficient ( $R$ , the ratio of the amplitude of the displacement of a reflected wave to that of the incident wave).

In simple uniform materials, conductivity is usually the dominant factor and it affects both the Electrical Resistivity Imaging (ERI) and Ground Penetrating Radar (GPR) techniques.

The permittivity of subsurface materials can vary dramatically, especially in the presence of free and bound water, and is usually a complex, frequency-dependent quantity with real (storage) and imaginary (loss) components. Table 3.1 lists the relative permittivity and conductivity of some common subsurface materials at 100 MHz and their typical range under natural conditions. They are ‘typical’ values derived from experiment and illustrate the influence of free and bound water, i.e., wetter higher, drier lower (Table adapted from Conyers and Goodman, 1997; Reynolds, 1997; Daniels, 2004 by Jol, 2009).

The complex magnetic permeability of magnetically lossy materials varies significantly with percentage composition, grain size, mineral type and, of course, porosity.

**Table 3.1.** Typical values of relative permittivity (real component) and static conductivity for common subsurface materials at an antenna frequency of 100 MHz (Jol, 2009).

Material	Static conductivity, $\sigma_s$ (mS/m)	Relative permittivity, $\epsilon_{ave}$
Air	0	1
Clay – dry	1–100	2–20
Clay – wet	100–1000	15–40
Concrete – dry	1–10	4–10
Concrete – wet	10–100	10–20
Freshwater	0.1–10	78 (25 °C)–88
Freshwater ice	1–0.000001	3
Seawater	4000	81–88
Seawater ice	10–100	4–8
Permafrost	0.1–10	2–8
Granite – dry	0.001–0.00001	5–8
Granite – fractured and wet	1–10	5–15
Limestone – dry	0.001–0.0000001	4–8
Limestone – wet	10–100	6–15
Sandstone – dry	0.001–0.0000001	4–7
Sandstone – wet	0.01–0.001	5–15
Shale – saturated	10–100	6–9
Sand – dry	0.0001–1	3–6
Sand – wet	0.1–10	10–30
Sand – coastal, dry	0.01–1	5–10
Soil – sandy, dry	0.1–100	4–6
Soil – sandy, wet	10–100	15–30
Soil – loamy, dry	0.1–1	4–6
Soil – loamy, wet	10–100	10–20
Soil – clayey, dry	0.1–100	4–6
Soil – clayey, wet	100–1000	10–15
Soil – average	5	16

In low loss materials, the loss factor ( $P$ ) < 1 while in high loss materials the loss factor ( $P$ ) > 1. The loss factor = 1 when both conduction and displacement currents are of equal importance (Sharma, 1997; Reynolds, 2000). For GPR to serve as an effective tool for high-resolution subsurface imaging, the loss factor must be less than 1. This corresponds to the case where energy storage mechanisms (i.e., polarization) dominate over energy loss mechanism (i.e., conduction) (Irving and Knight, 2003).

Radiowaves decrease exponentially and soon becomes undetectable in energy absorbing materials. The attenuation coefficient,  $\alpha$ , is primarily determined by the

ability of the material to conduct electrical currents. In simple uniform materials, conductivity ( $\sigma$ ) is usually the dominant factor; thus a measurement of electrical conductivity (or resistivity) determines attenuation (Davis and Annan, 1989).

Depth of penetration depends on the antenna frequency, spacing, property contrast, body geometry, and signal to noise ratio.

### **3.3.2. Data acquisition and processing**

GPR data can be acquired in monostatic or bistatic mode (Figure 3.16, Figure 3.17). In monostatic mode adopted in this study one antenna device is used as both transmitter and receiver while in bistatic mode two separate antennas are used with one serving as a transmitter and the other as a receiver (Davis and Annan, 1989).

A contrast in dielectric properties across an interface causes reflection of part of a radar pulse according to the reflection coefficient ( $R$ ). In low loss medium, radiowaves velocities are controlled by the dielectric constant ( $\epsilon_r$ ) and the relative magnetic permeability ( $\mu_r$ ) which is close to unity for nonmagnetic rocks. Radiowaves travel at high speed in subsurface (between 0.05 to 0.15 m/ns).

GPR data can be collected using different acquisition mode: Zero-Offset (ZOS), Constant-Offset (COS), Common-Shot Gather (CSG), Common-Midpoint (CMP), and borehole surveys. In the ZOS acquisition mode, the transmitter and the receiver are located within the same unit and data is collected in continuous mode along survey profiles. When data is collected continuously the horizontal scale on each GPR record is determined by the antenna speed or by an attached survey wheel, which collects data at a specific increment rather than actual continuous mode. Survey stations can be manually recorded on GPR records by pressing a marker button as the antenna's centerline passes each grid node. It is a common practice in GPR applications to acquire 3D data by combining parallel or orthogonal profiles (McMechan et al., 1997; Jol and Kaminsky, 2000; Cristallini and Almendinger, 2001).

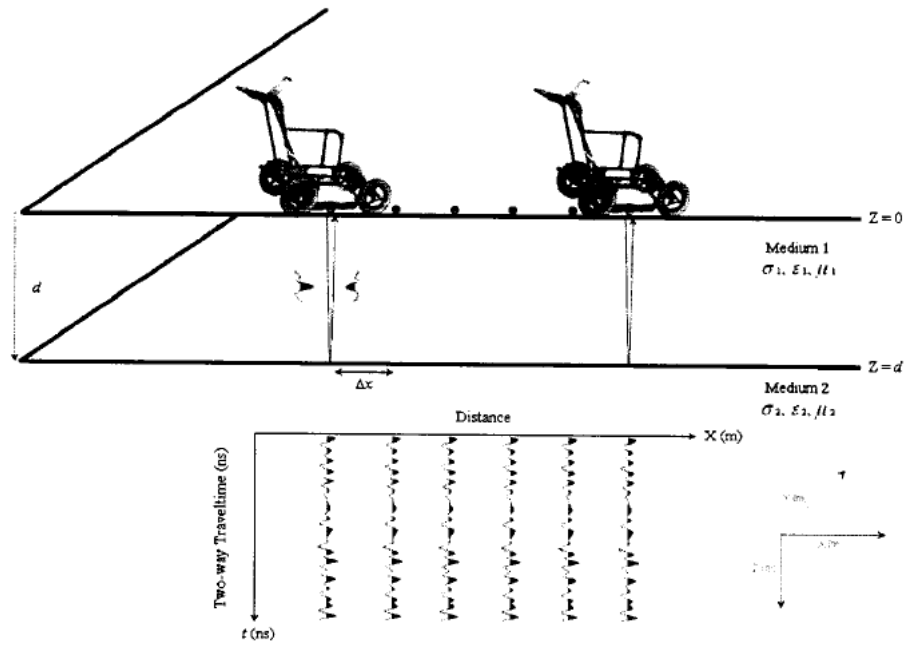


**Figure 3.16.** A sketch illustrating GPR data acquisition mode using a monostatic GPR unit (Alshuhail, 2006).

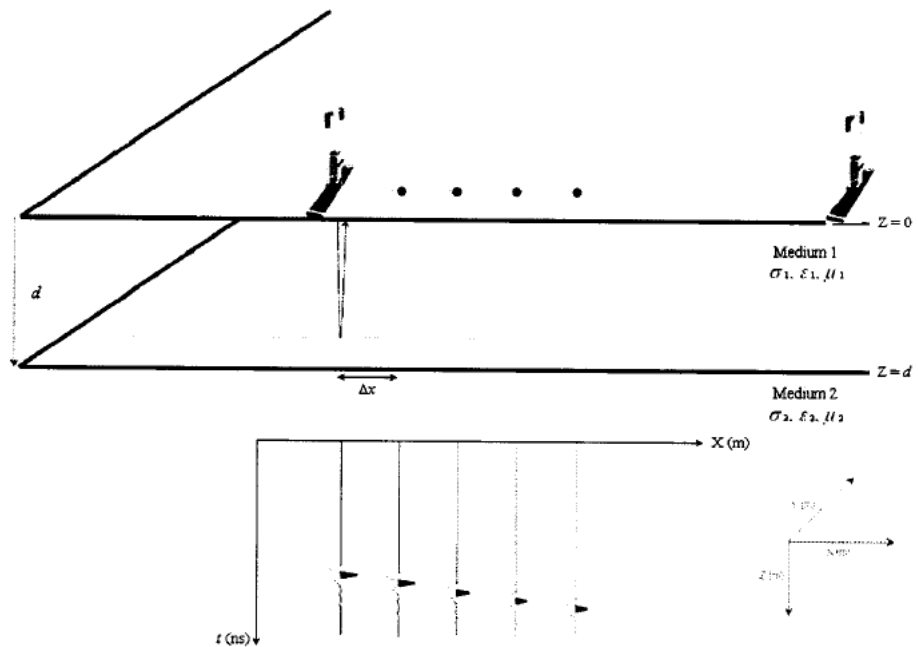


**Figure 3.17.** An illustration of the GPR data acquisition mode using bistatic GPR system (Alshuhail, 2006).

In reflection surveying, which is the most common way to acquire GPR data, the GPR instrument records the time it takes the signal to travel from the transmitter to the target, or an interface that separates two layers with different dielectric properties, and back to the receiver. The two-way traveltime ( $t$  in nanoseconds) recorded this way is given by:

$$t^2 = \frac{x^2}{v^2} + t_0^2 = \frac{x^2}{v^2} + \frac{4d^2}{v^2} \quad (3.1)$$

where  $x$  is the offset (the distance between the transmitter and the receiver) in m,  $v$  is GPR signal velocity in m/ns,  $t_0$  is vertical incidence traveltime in ns,  $d$  is the depth to the interface, or target, in m.

In a monostatic acquisition mode the GPR section approximates a Zero-Offset Section (ZOS), i.e., the separation between the source and the receiver is very small ( $x \approx 0$ ). Therefore Equation 3.1 simplifies into:

$$t^2 = \frac{4d^2}{v^2} \quad (3.2)$$

Thus the depth to the reflector (target) can be calculated from the two-way travel time ( $t$ ) of the reflected signal:

$$d = \frac{tv}{2} \quad (3.3)$$

where  $t$  is the two-way traveltime measured by the GPR instrument in ns, and  $v$  is GPR signal velocity in m/ns. The division by 2 is because the GPR instrument records the two-way traveltime.

The most important parameter in any GPR data acquisition design is the antenna frequency. Annan (2003) suggests that the following constraint on the central (antenna) frequency  $f$  could be used when designing a GPR survey:

$$f = 1200 \frac{\sqrt{\varepsilon_r - 1}}{D} \quad (3.4)$$

where  $D$  is target depth in m, and  $\varepsilon_r$  is the dielectric constant. The above relation assumes a beam footprint to target depth ratio of 4. GPR signals returning from small subsurface heterogeneity, such as fine scale bedding or pebbles, is known as cluttering. At high frequency cluttering may dominate the radargram to a degree in which one cannot distinguish between different events or see into the desired depth. In order to overcome this problem, the signal wavelength has to be much longer than the clutter dimension:

$$f = \frac{30}{\Delta L \sqrt{\varepsilon_r}} \quad (3.5)$$

where  $f$  is the central frequency in MHz,  $\Delta L$  is spatial separation to be resolved in m, and  $\varepsilon_r$  is the dielectric constant (Annan, 2003).

The depth of penetration of GPR signal depends upon its frequency and the electrical conductivity of the medium. Annan (2003) suggests if one knows or has a good estimate of the conductivity, velocity and/or the attenuation, the following approximation can be used to estimate the depth of investigation of GPR:

$$D \leq \frac{30}{\alpha} \quad (3.6)$$

$$D \leq \frac{35}{\sigma} \quad (3.7)$$

where  $\sigma$  is the conductivity in milli-siemens/m,  $\alpha$  is the attenuation in dB/m, and  $D$  is the maximum depth of investigation in m (Reynolds, 2000; Annan, 2003). Smith and Jol (1995) provide a good discussion on the probable optimum choice for the antenna frequency and antenna separation as well as the probable maximum depth of penetration in Quaternary sediments.



The time window ( $t$ ) for recording the GPR data at each increment is given by:

$$t = 1.3 \frac{2 \times D}{v} \quad (3.8)$$

where  $D$  is the maximum depth in m and  $v$  is the minimum velocity expected in the survey area in m/ns. Note that the above relation allows for 30% increase in the estimated time due to uncertainty in depth and velocity (Annan, 2003).

The choice of the temporal and spatial sampling intervals is defined by the sampling theorem and given by:

$$f_N = \frac{1}{2\Delta t} \quad (3.9)$$

where  $f_N$  is the Nyquist temporal frequency in MHz, which is the maximum frequency that can be observed once a continuous signal is sampled, and  $\Delta t$  is the temporal sampling interval in ns. It is always recommended to take the frequency bandwidth, and therefore the maximum frequency of the GPR system, into account as well as a safety factor of two in selecting the temporal sampling interval. Thus Equation 3.9 becomes:

$$\Delta t = \frac{1}{2 \times 2 \times 1.5f} = \frac{1}{6f} \quad (3.10)$$

where  $f$  is the central frequency of the antenna in MHz, and  $\Delta t$  is the temporal sampling interval in ns. The above relation assumes a frequency bandwidth of 1.5 the central frequency which is the of most radar system (Milsom, 2000). The condition for choosing the spatial sampling interval is given by:

$$k_N = \frac{1}{2\Delta x} \quad (3.11)$$

where  $k_N$  in m is the Nyquist spatial frequency, and  $\Delta x$  is the spatial sampling interval in m (Yilmaz, 2001). When acquiring data in continuous mode, the spatial sampling inline, i.e., along the 2D profiles is usually sufficient so that no aliasing will occur. However the choice of spatial sampling interval is less obvious when moving crossline (i.e., acquiring 3D data), especially in areas with lots of diffractions. Still it is possible to calculate a proper spatial sampling interval by using the following relation:

$$\Delta x = \frac{c}{4f\sqrt{\varepsilon_r}} = \frac{\lambda}{4} \quad (3.12)$$

where  $c = 3.0 \times 10^8$  is the speed of EM waves in air in m/s,  $f$  is the antenna frequency in MHz,  $\varepsilon_r$  is the dielectric constant, and  $\lambda$  is the wavelength of the GPR signal in m ( $\lambda = 2\pi/k$ ) (Annan, 2003). Aliasing is one of the most important issues associated with data acquisition and is defined as frequency ambiguity resulting from the sampling process. In other words, frequency aliasing is a phenomenon caused by under-sampling. To avoid aliasing in time, anti-aliasing filters are applied to the data before digitization (Yilmaz, 2001). However when acquiring orthogonal profiles, spatial sampling is discrete in nature. Yilmaz (2001) suggest that the best way to avoid spatial aliasing is to apply a spatial anti-aliasing filter. Grasmueck and Weger (2003) and Grasmueck et al. (2005) present a good discussion of spatial sampling and resolution of GPR data.

It is always desirable to estimate the resolution capability associated with the selected acquisition parameters. The vertical spatial resolution can be estimated by using following equation:

$$\Delta z = \frac{150}{f\sqrt{\varepsilon_r}} \quad (3.13)$$

where  $f$  is the central frequency in MHz,  $\Delta z$  is spatial separation to be resolved in m, and  $\varepsilon_r$  is the dielectric constant (Milsom, 2000). Lateral spatial resolution is defined by Fresnel zone, in which the target has to be as close as possible to A:

$$A = \frac{\lambda}{4} + \frac{D}{\sqrt{\varepsilon_r + 1}} \quad (3.14)$$

where  $A$  is the long axis radius of the GPR footprint at depth  $D$  in m,  $\lambda$  is the wavelength in m, and  $\varepsilon_r$  is the dielectric constant (Conyers and Goodman, 1997). In general antennas are oriented perpendicularly to the profile direction in order to optimize the GPR footprint. More discussion on the GPR data acquisition can be found in Conyers and Goodman (1997), Sharma (1997), Reynolds (2000), and Annan (2003).

Typical post-survey data processing includes editing, filtering, gain analysis, spherical divergence correction, velocity analysis, Normal Moveout (NMO) correction for multi-offset data, static correction, and migration. The time to depth conversion can be accomplished by on site calibration of the radar antenna over an object of known depth which can also help in optimizing data acquisition parameters. When direct measurements are not practical, GPR velocities estimation, and the time to depth conversion, can be carried out using information from Common Shot Gather (CSG), Common Midpoint (CMP) analysis, diffraction analysis, or velocity approximated using typical soil dielectric values and propagation velocities from tables or similar sites (Young et al., 1995; Annan, 2003).

In similar manner to 3D seismic reflection surveys, 3D GPR data is acquired by combining parallel or orthogonal 2D profiles rather than acquiring a true 3D dataset. The interpretable pseudo 3D volume is constructed by combining the individually processed 2D profiles (McMechan et al., 1997; Jol and Kaminsky, 2000; Cristallini, 2001). More about the processing of the GPR data can be found in Daniels et al. (1988), Young et al. (1995), Conyers and Goodman (1997), Annan (1999, 2002 and 2003), Jol and Kaminsky (2000), Alshuhail (2006) and Reynolds (2000).

### **3.3.3. Considerations and limitations**

GPR penetration and resolution depend on the objective of the survey and the system performance. There are many factors that affect the GPR signal propagation: attenuation, transmission, scattering, layer thickness, roughness of the interface, water content, temperature etc.

GPR results are very site-specific because of the limited depth of penetration of radar in conductive environments, such as in clay and water bearing sediments. The amplitude of EM fields decreases exponentially with depth. In most materials energy is lost to scattering from material variability. The signal propagates well in sand and gravel while conductive soils such as clay, or fill saturated with conductive groundwater cause GPR signal attenuation and loss of target resolution, i.e., limited detection of small objects (Reynolds, 2000; Annan, 2003; Olhoeft et al., 1994).

GPR signal penetration is determined by the dielectric properties of the soil or man-made materials, the conductivity and the moisture content of the soil and fills materials. In most cases such as when working in consolidated and unconsolidated sediments environments, the electrical properties are much more important and dominant than the magnetic properties. However the magnetic properties have to be taken into consideration when working in areas with significant variations in the magnetic susceptibility, e.g., areas with significant volcanic materials or with metallic objects (Reynolds, 2000).

Water has two effects; first, water contains ions which contribute to bulk conductivity. Second, the water molecule absorbs electromagnetic energy at high frequencies. In addition to water, there are some other properties that affect the propagation of the EM waves, e.g., temperature, electrochemical reactions and polarization. An increase in temperature increases the mobility of ions present in water, which adds to the conductivity (Sharma, 1997).

One critical factor that controls the GPR signal and which we have control over is the antenna frequency. The higher the frequency, the higher the resolution and the lower the penetration depth and system performance and vice versa. This is due to the inherent properties of the earth that typically allow lower-frequency waves to travel further within the subsurface (Reynolds, 2000). Annan (2003) presents different criteria, based on desired resolution and penetration depth, which can be used to estimate the antenna frequency to be used in a GPR survey. Nonetheless, care should be taken when designing a survey, especially if one has no prior information about specific target.

Finally, as with other geophysical techniques, GPR is an interpretive method, based on the subjective identification of reflectors or targets, and may not uniquely identify an object. Furthermore, the effects of several factors, such as the antenna polarization (Guy et al., 1999; Tsoflias et al., 2004), scattering-cluttering (Young et al., 1995), and facies in unconsolidated sediments (Van Overmeeren, 1998) on the GPR response may need to be examined more closely. For example, Grasmueck and Weger, (2003) report that for geologic application of GPR on natural surfaces, with soil, vegetation, and elevation changes, the survey wheel approach is not precise enough.

#### **3.3.4. Field application: Data acquisition, processing, interpretation**

In the context of geophysical explorations, GPR surveys were also planned at almost the same locations (Figure 3.7) where Electrical Resistivity measurements taken for the purpose of correlation. During fieldwork Cobra Locator GPR System (Figure 3.18) produced by Radarteam Sweden AB was used with the contribution of GPRscan Engineering Foreign Trade.

According to primary assessments it was decided to use 64 ns and 128 ns temporal sampling interval. Data gathered by using GAS data capture software.

After that, study locations were entitled as A, B, and C regions and data gathered in different directions within every region. While planning profile directions it was attentive to take measurements from parallel and perpendicular profiles in order to construct 3-Dimensional soil profile of the study area. Figure 3.19 and Figure 3.20 show survey profile numbers at region A and B, respectively.



**Figure 3.18.** Cobra Locator GPR System produced by Radarteam Sweden AB.

The distances between parallel profiles at Region A Line 1 are 1.5 m between profile 1 and 2; 2 m between profile 2 and 3; 1.5 m between profile 3 and 4. At Line 2 distance between parallel profiles is about 10 m.



**Figure 3.19.** Region A, Line 1, Line 2, Line 3 and Line 4 profiles (profile number 1, 2, 3, 4, 5, 6, 7, 8, 9, 10, 11, 12).



**Figure 3.20.** Region B, Line 1 and Line 2 profiles (profile number 13, 14).

Region C, as shown in Figure 3.21, is a side of the road and consists of only one long profile namely profile 15.





**Figure 3.21.** Region C, Line 1 profile (profile number 15).

As seen from above figures, GPR measurements were taken from a total of fifteen profiles and total length of the profiles was about 460 m. Table 3.2 indicates length of each profile.

**Table 3.2.** Length of each profiles.

Region	A												B	C	
Profile	1	2	3	4	5	6	7	8	9	10	11	12	13	14	15
Length (m)	50	54.2	50	53.2	9.5	10	8.2	5.5	9.5	10	10	11	28.8	12	138

During GPR measurements on aforementioned profiles at different regions some data gathering specifications were as follows.

- Scanning type: 64 ns and 128 ns
- Data gain: 5 dB (start), 15 dB (end)
- Filter: HP 130 MHz, LP 700 MHz (HP: High Pass, LP: Low Pass)



- Trace frequency: 25 trace/sec.
- Offset: 18 ns
- Data output: 16 bit
- Data format: \*.gsf (geoscanners format)

In order to process raw data, GPRsoft PRO data process software was utilized. The steps followed during data process studies were itemized below in an order:

- Static correction: 1 ns
- DC shift (1B filter)
- Dewow (1B filter)
- Gain control: logarithmic start 5dB, end 10dB
- Opaueness scanning
- Suitable amplitude scale scanning

As a result of the data process studies, resultant radagrams were illustrated in Figure 3.22 through Figure 3.36 to interpret subsurface profile at the location of study.

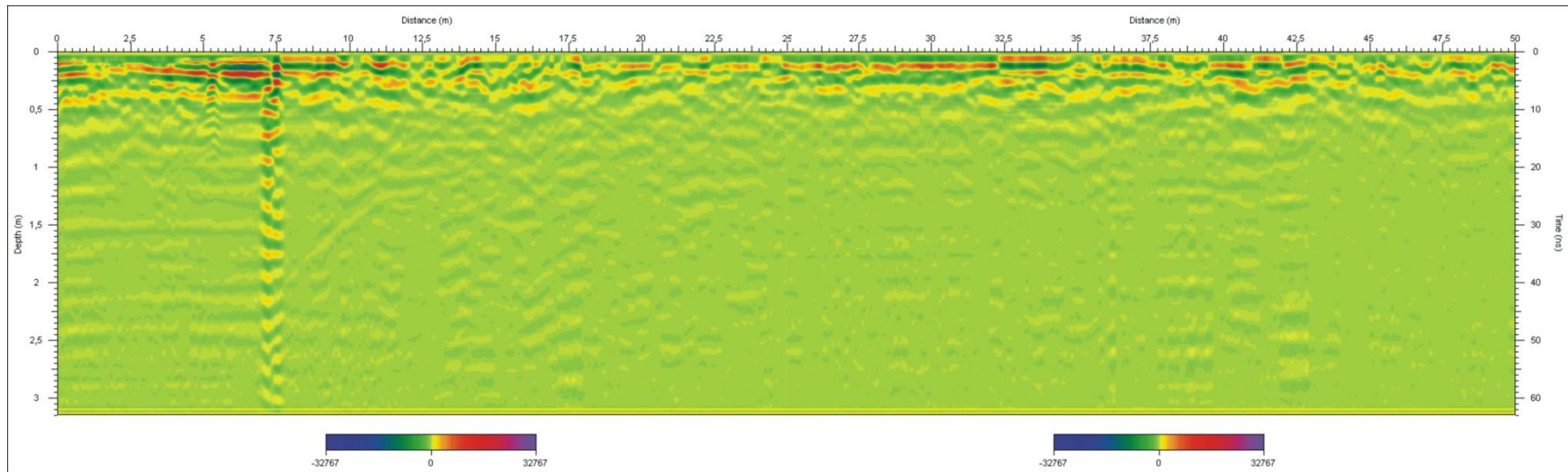


**Figure 3.22.** Region A, Line 1, Profile 1.

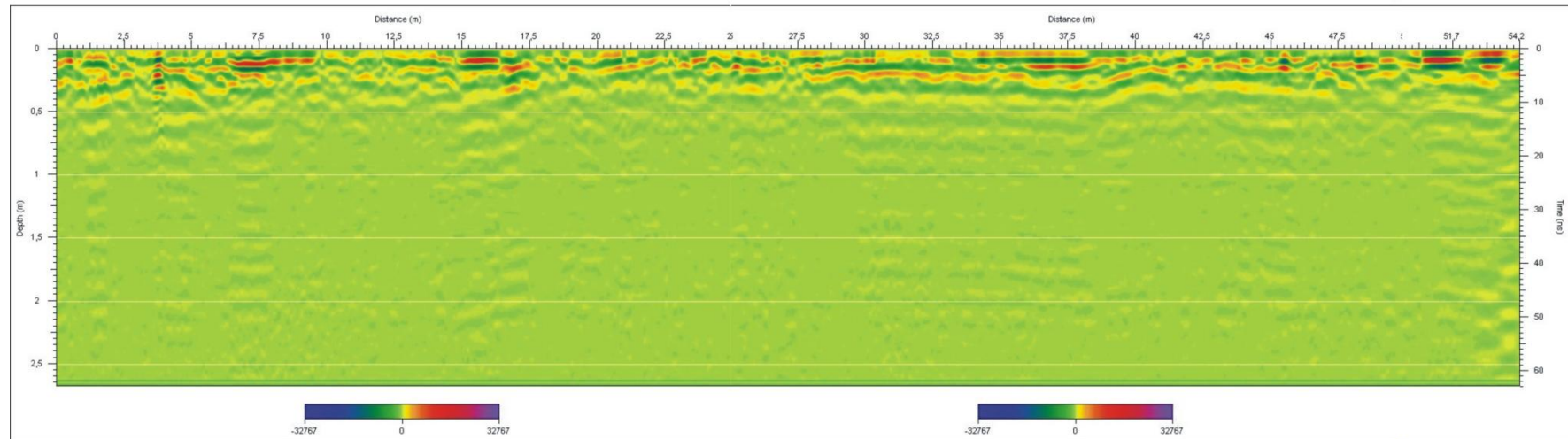


**Figure 3.23.** Region A, Line 1, Profile 2.

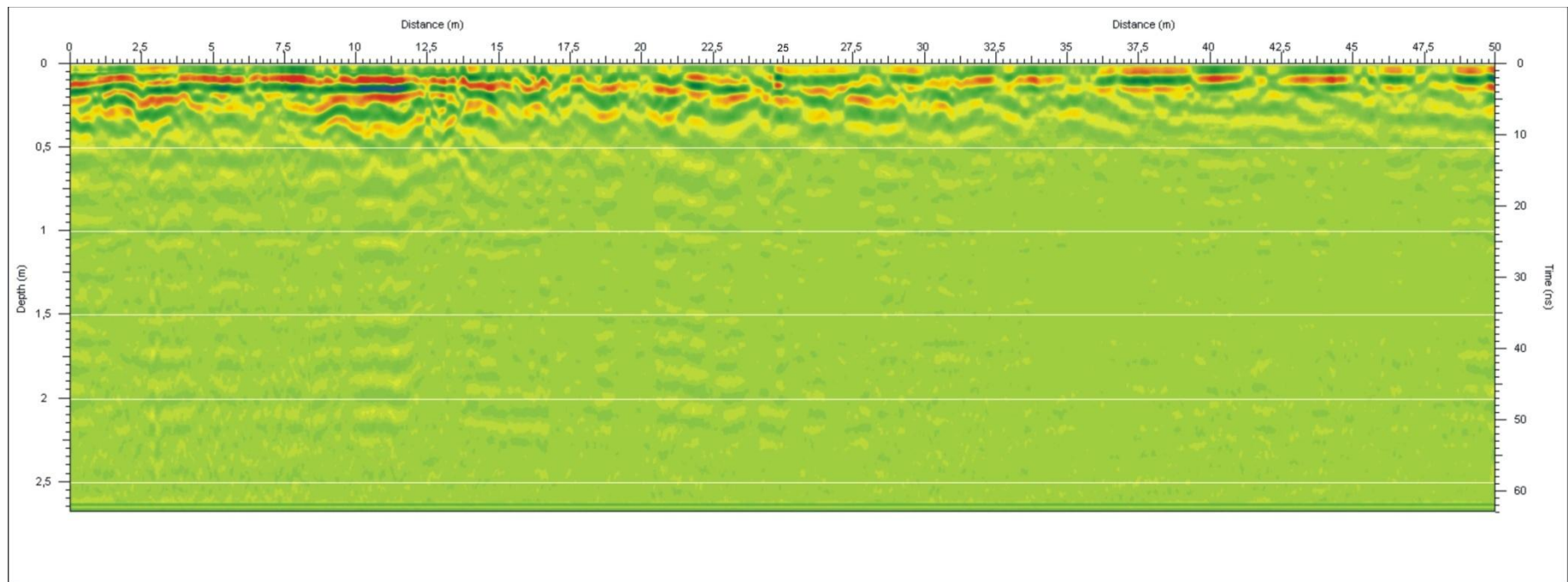


**Figure 3.24.** Region A, Line 1, Profile 3.

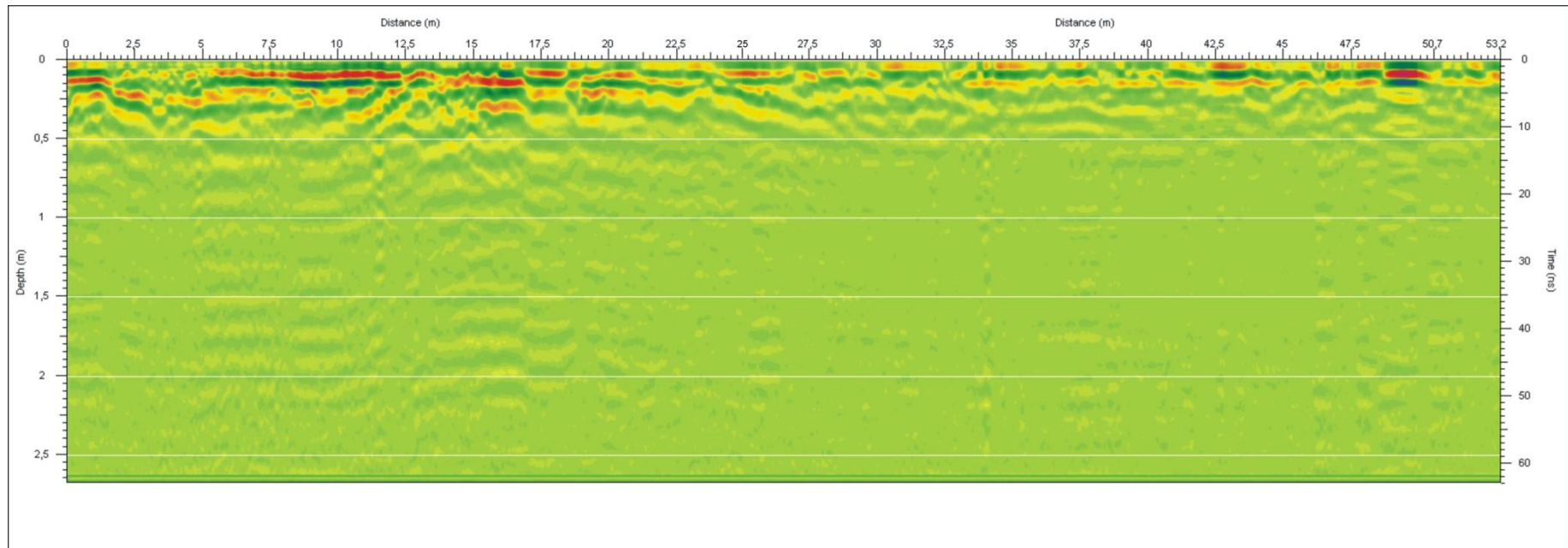


**Figure 3.25.** Region A, Line 1, Profile 4.



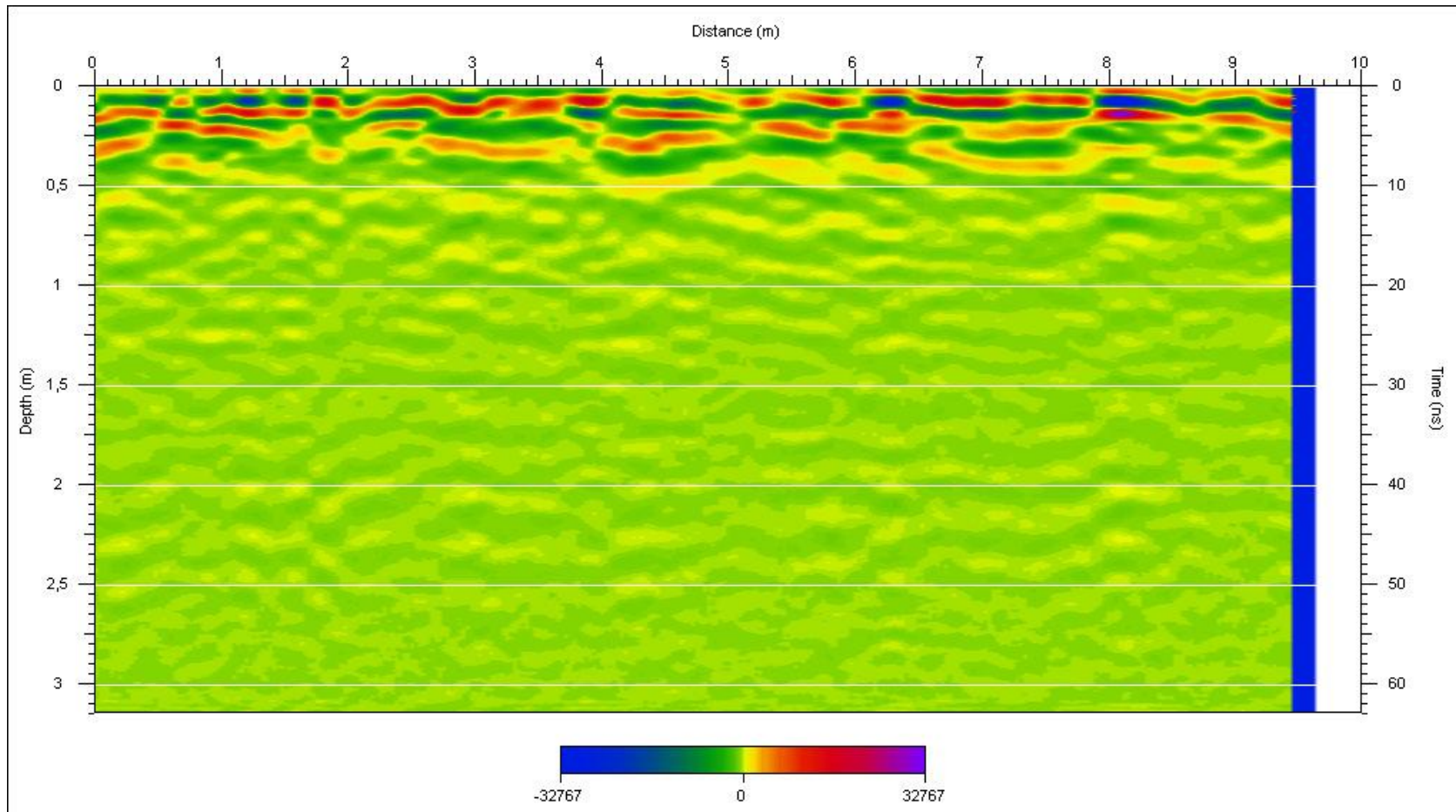


**Figure 3.26.** Region A, Line 2, Profile 5.

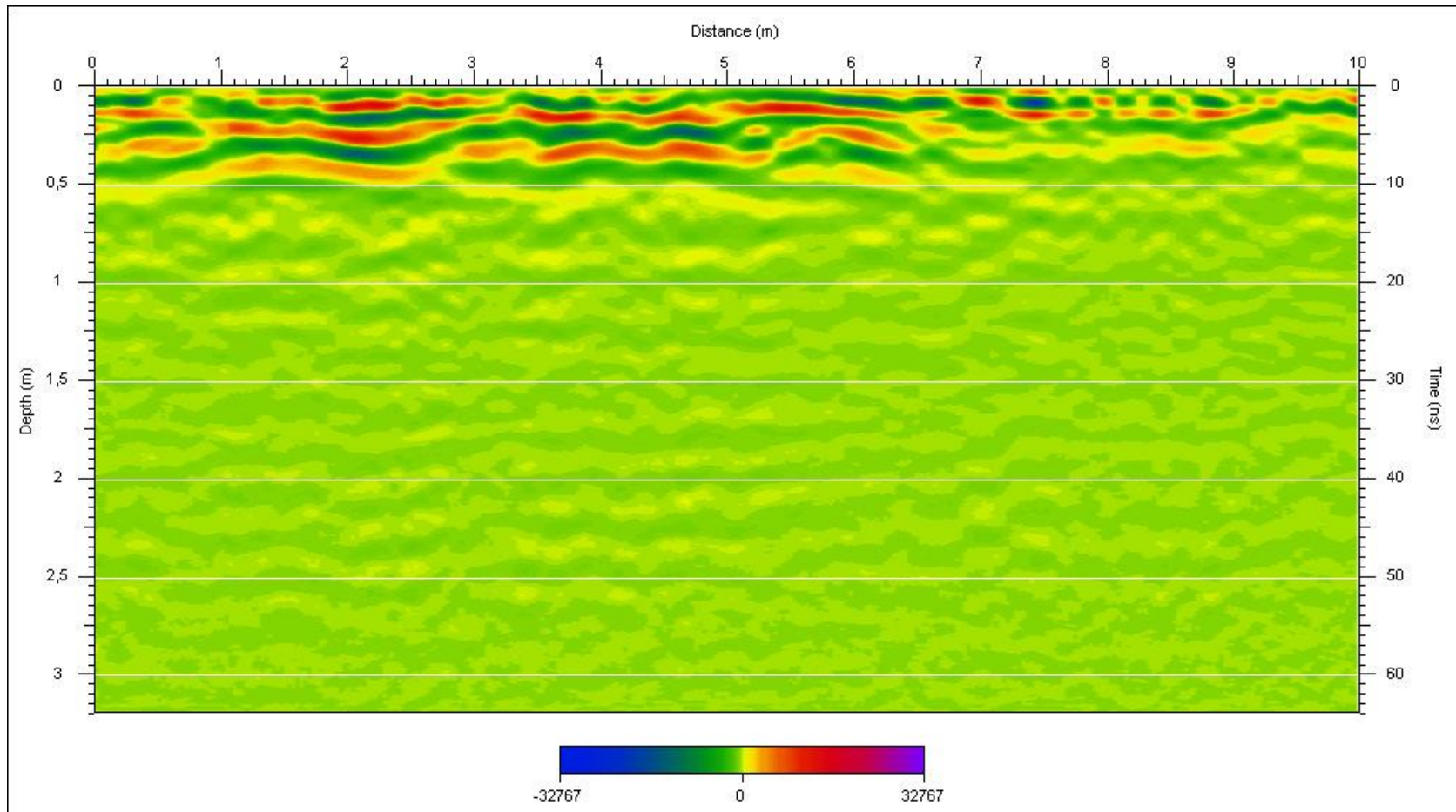


**Figure 3.27.** Region A, Line 2, Profile 6.

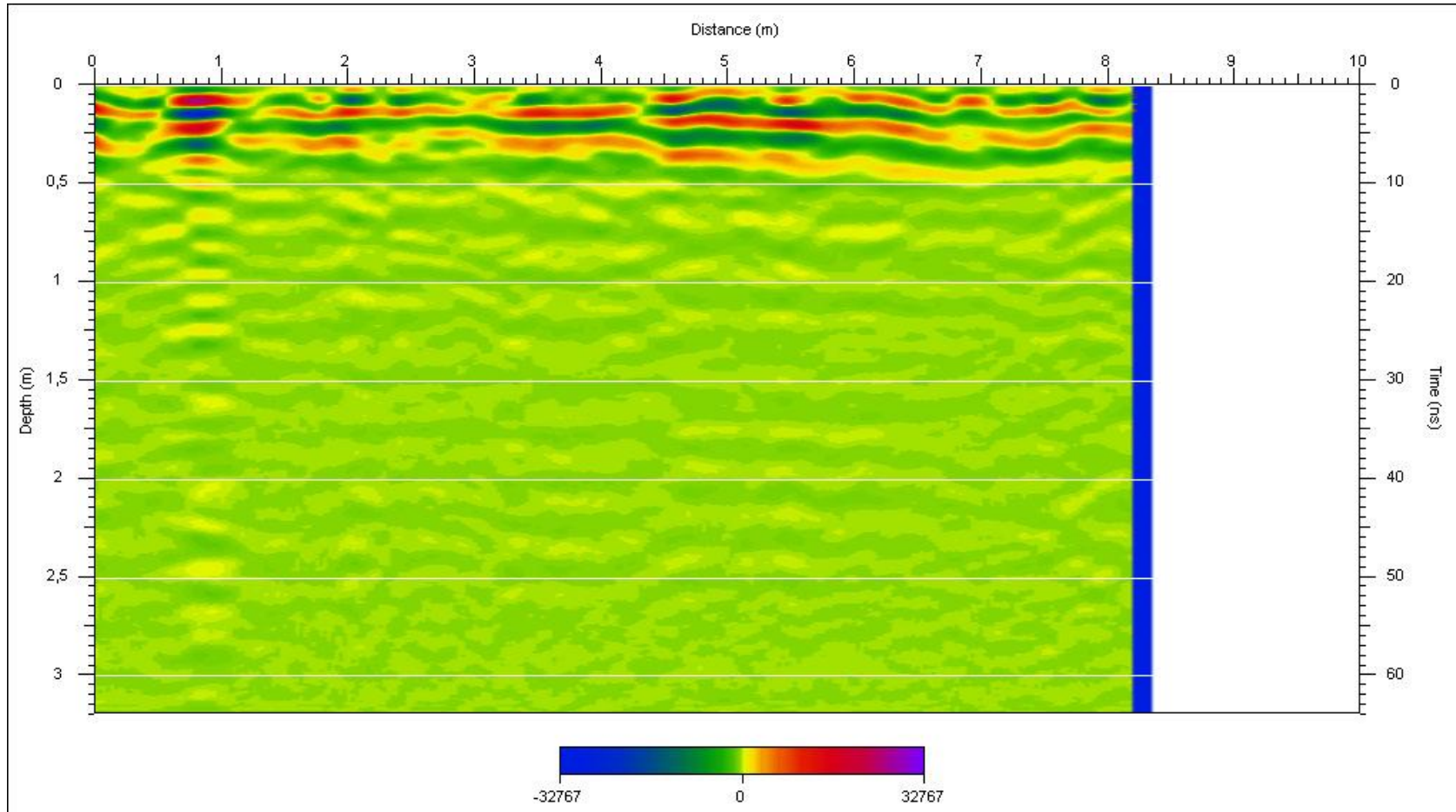


**Figure 3.28.** Region A, Line 2, Profile 7.



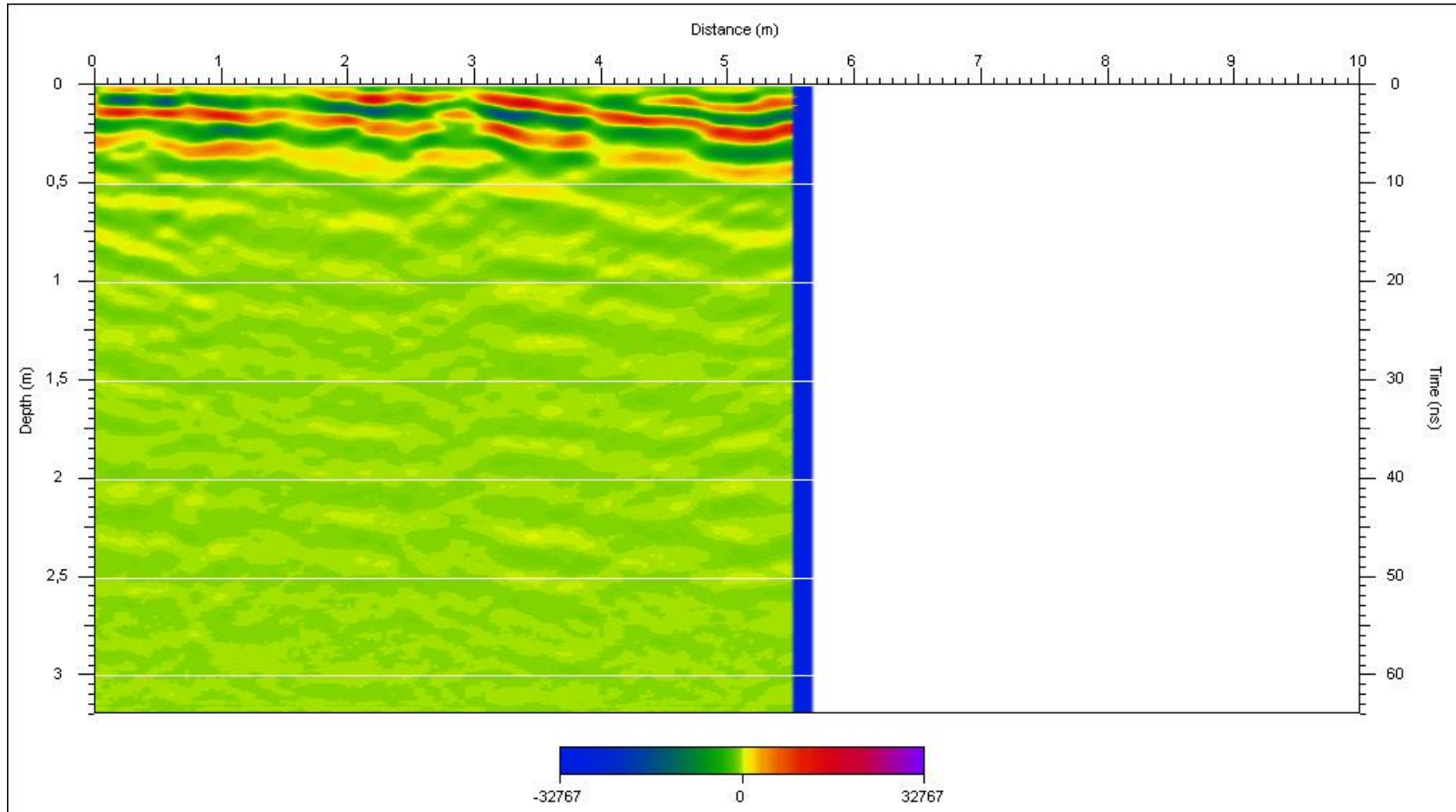


**Figure 3.29.** Region A, Line 2, Profile 8.

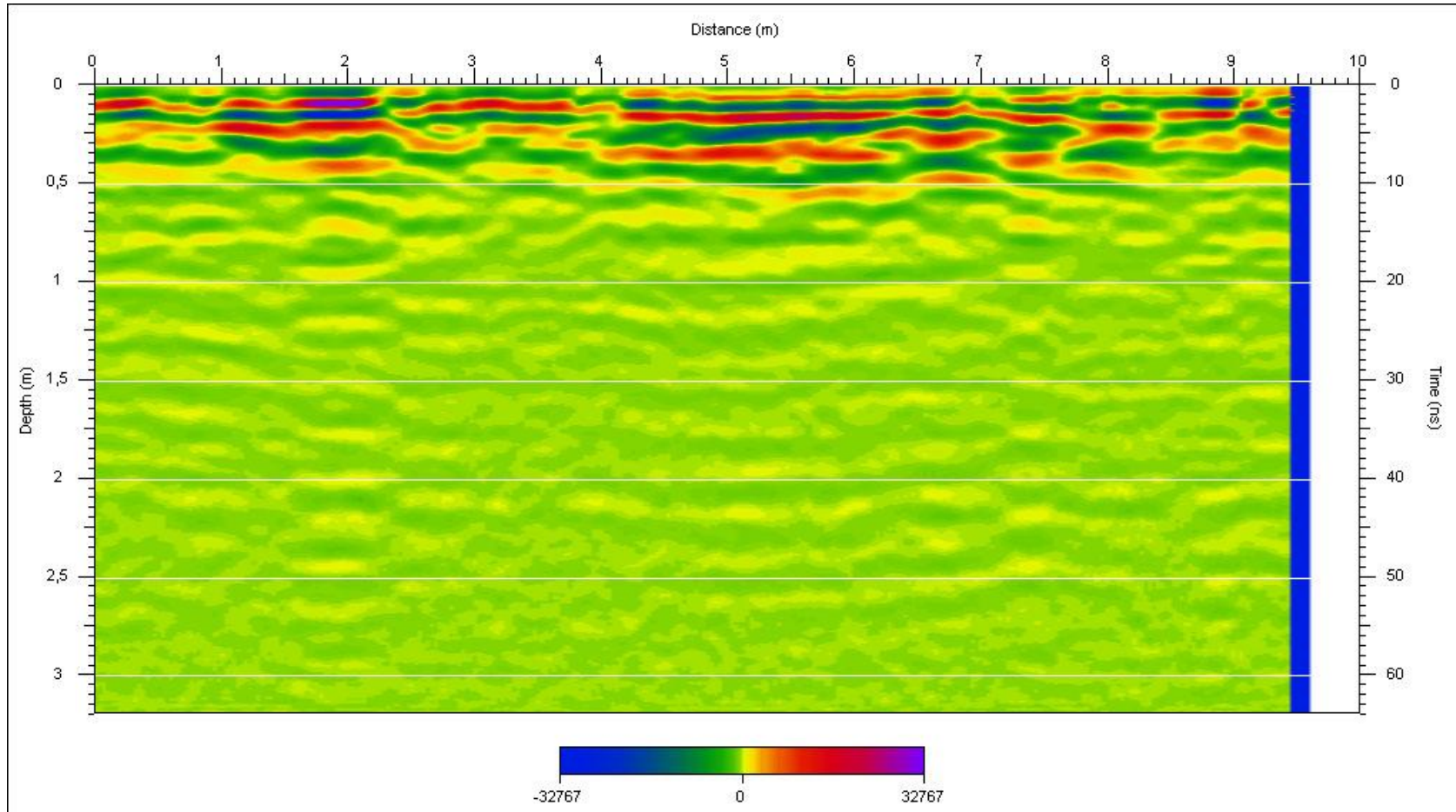


**Figure 3.30.** Region A, Line 2, Profile 9.

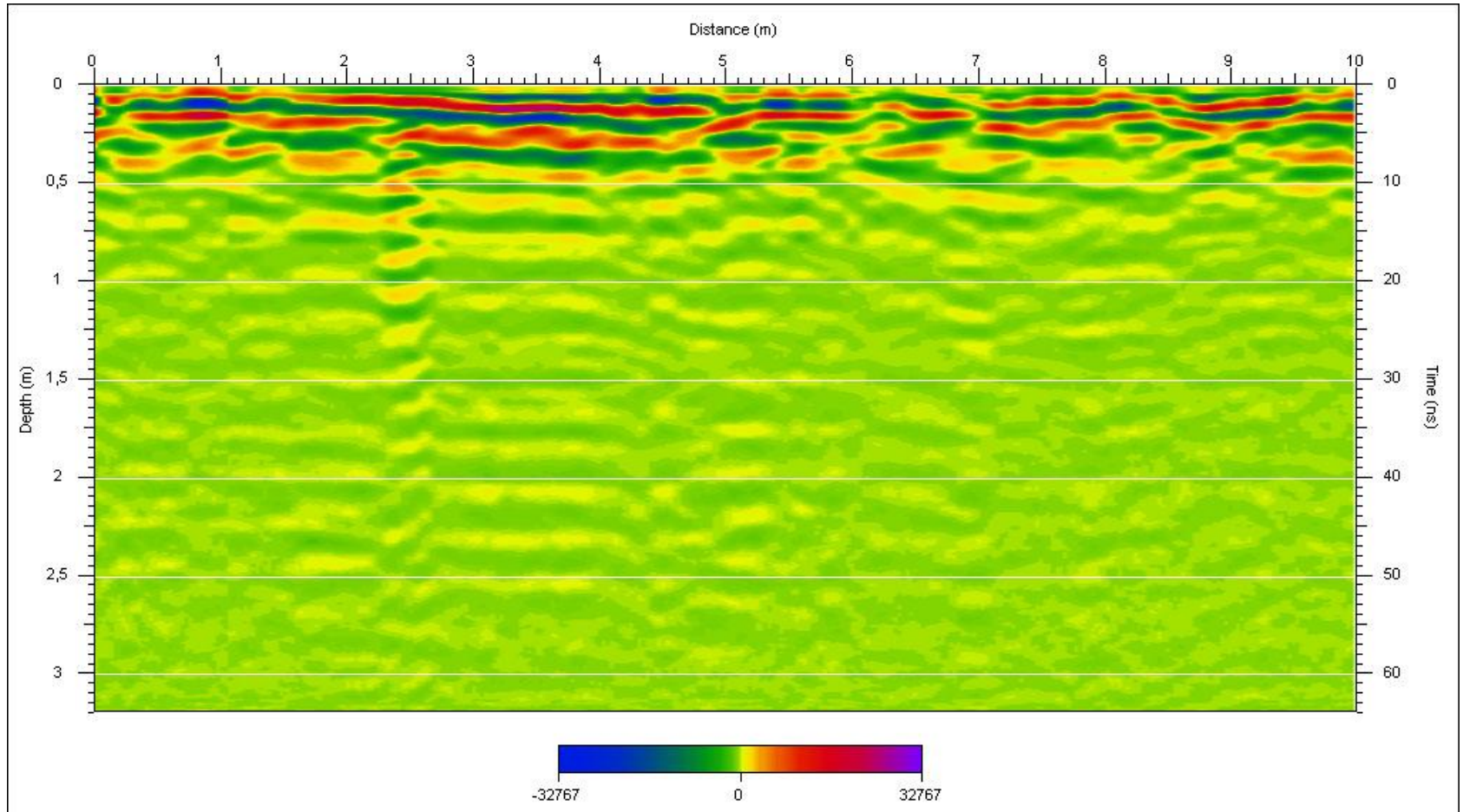
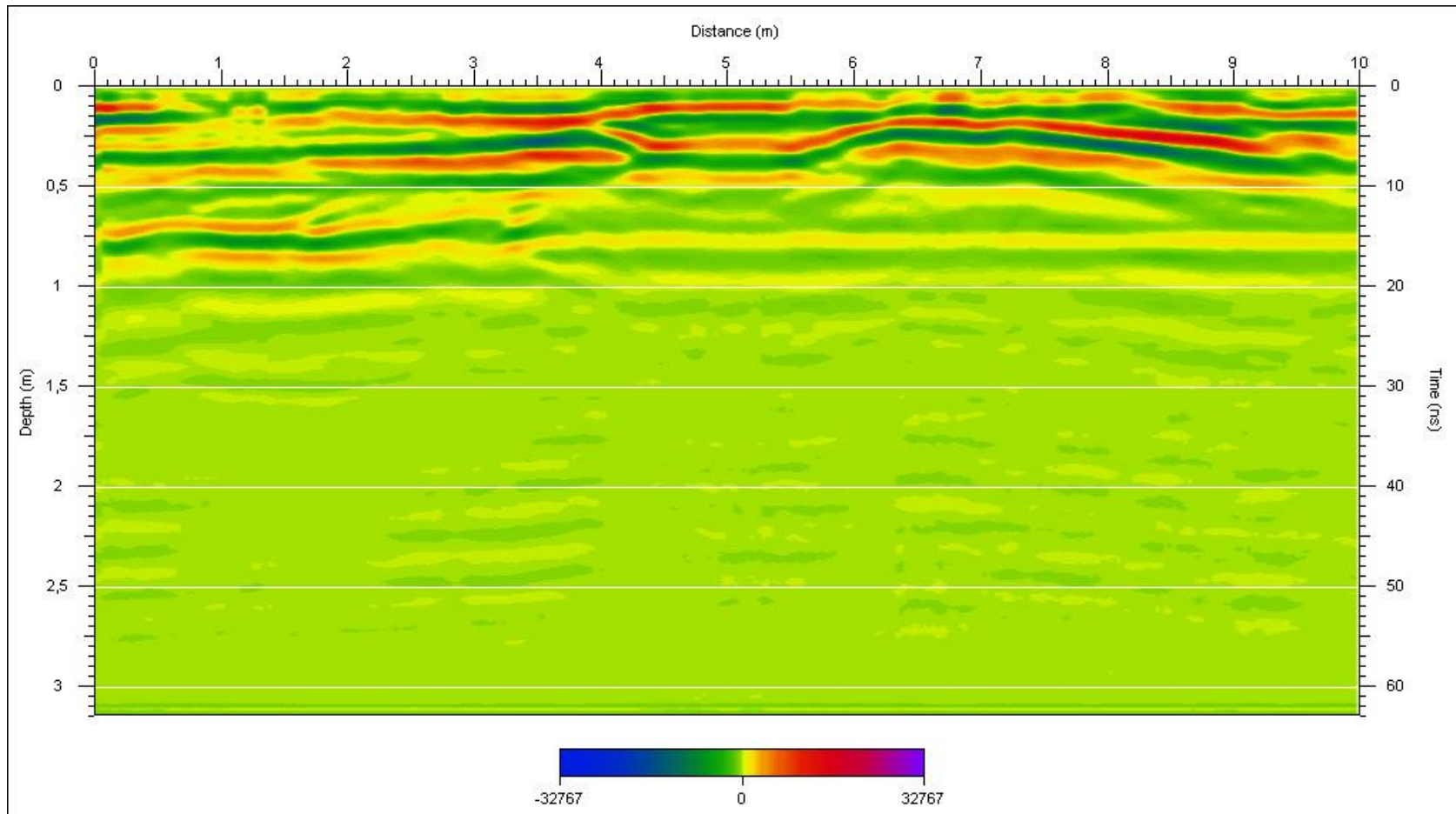
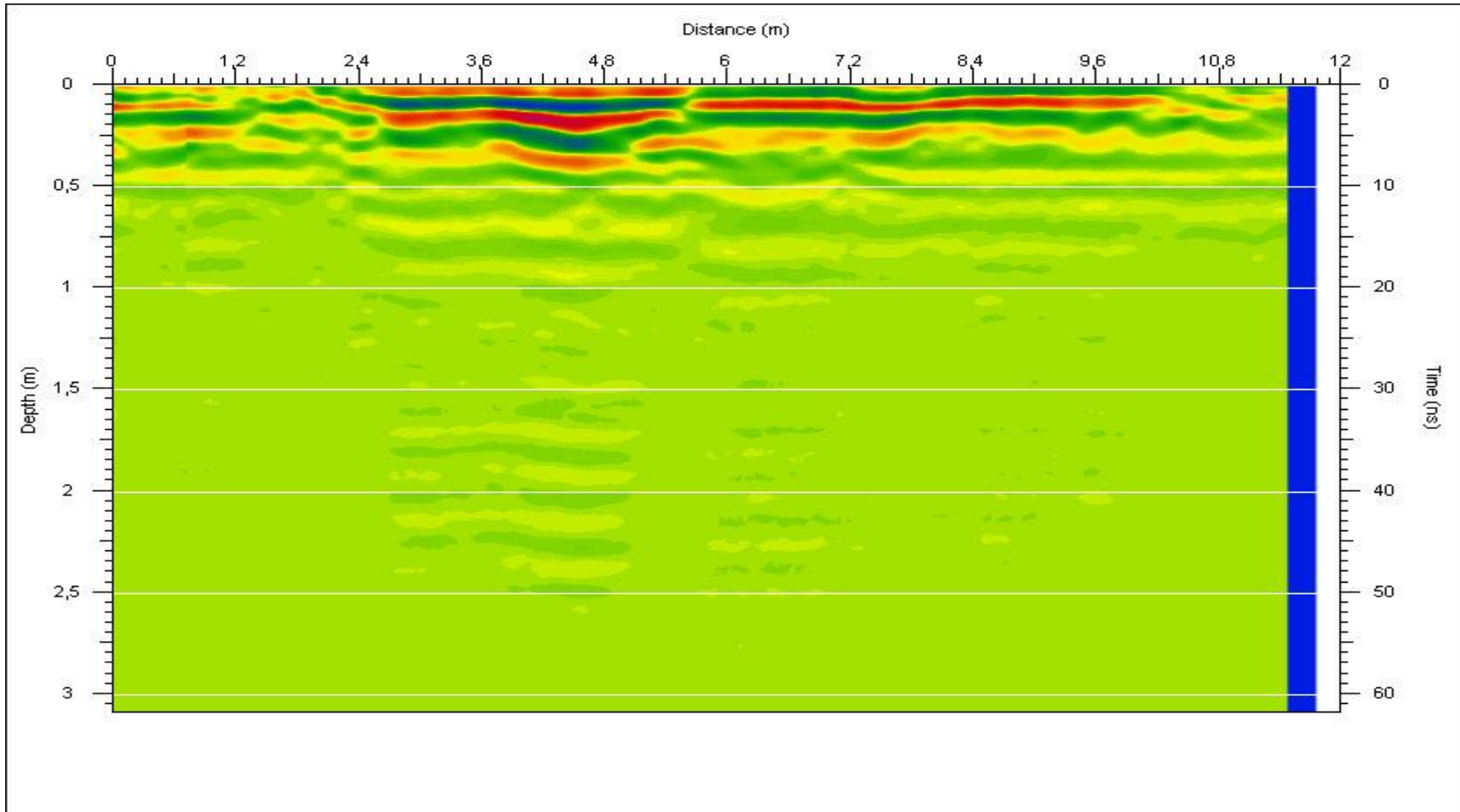


Figure 3.31. Region A, Line 2, Profile 10.



**Figure 3.32.** Region A, Line 3, Profile 11.





**Figure 3.33.** Region A, Line 4, Profile 12.

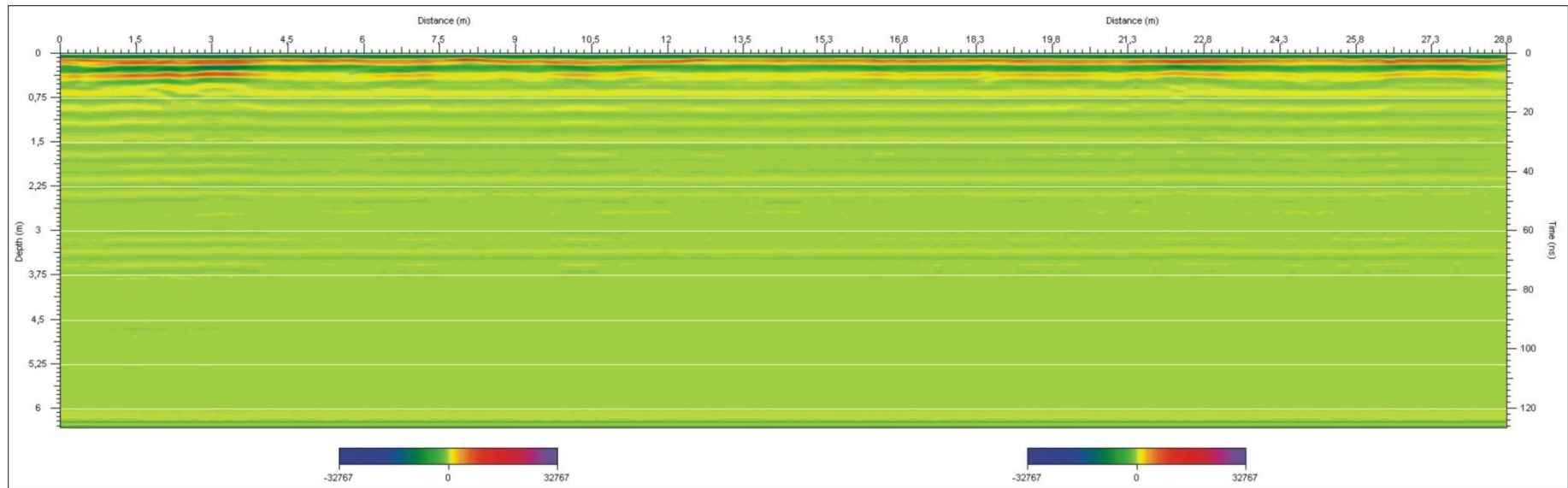


**Figure 3.34.** Region B, Line 1, Profile 13.

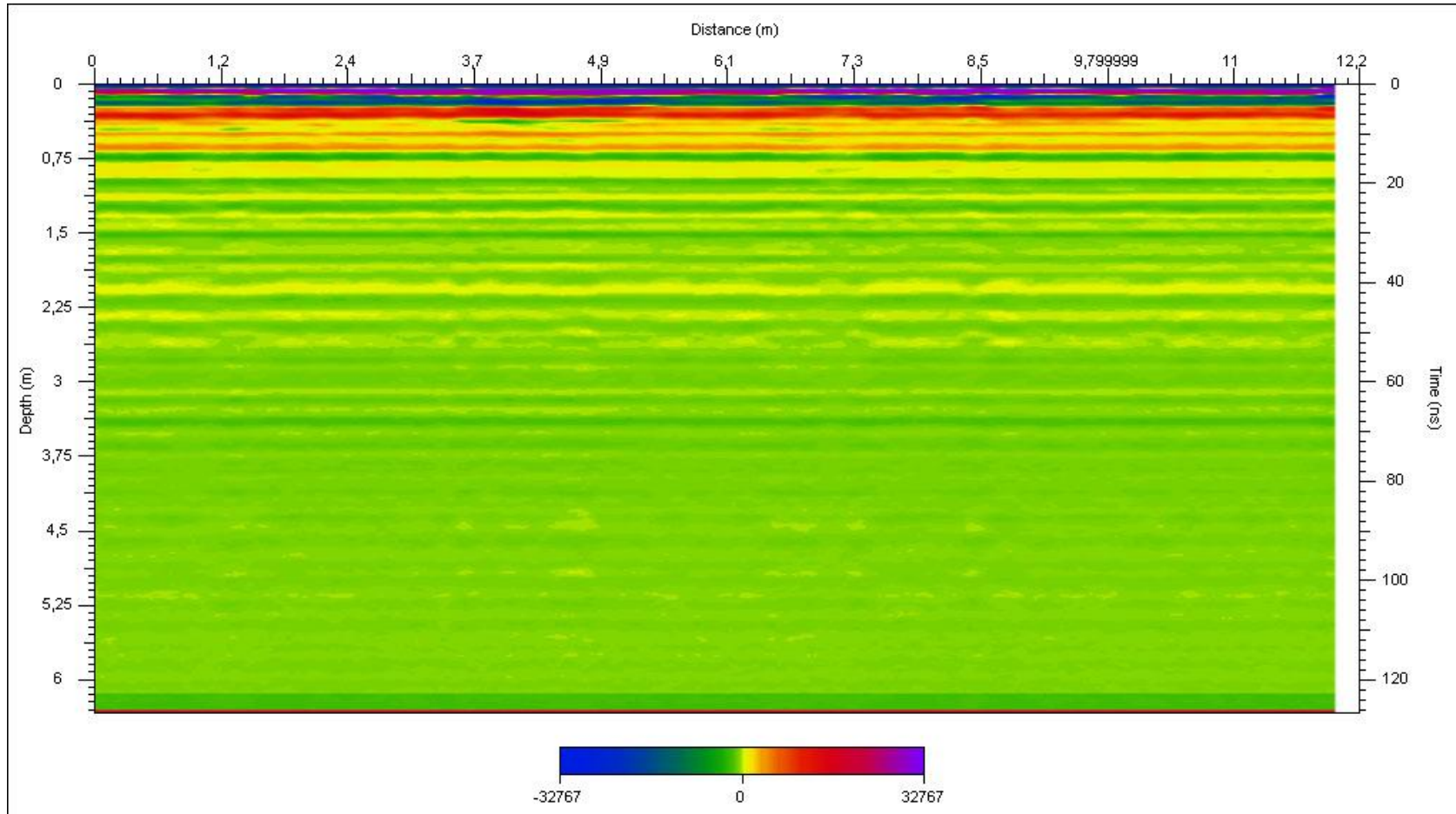
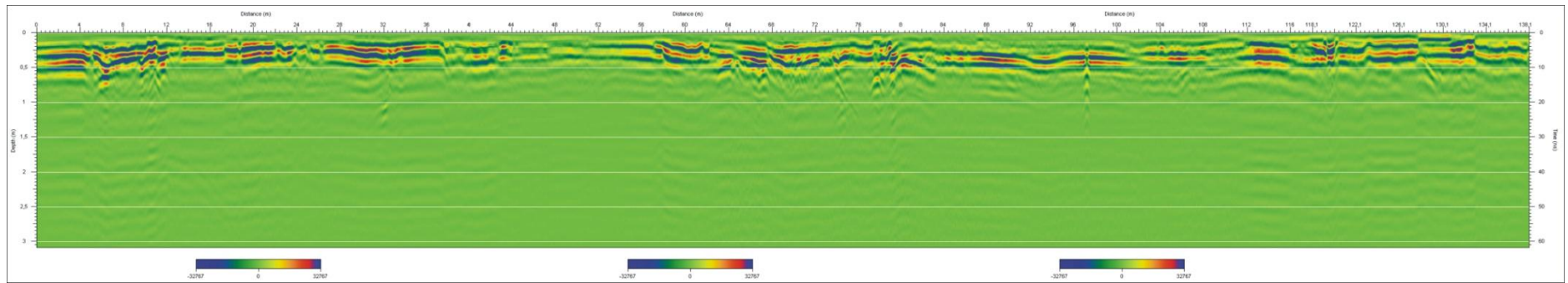


Figure 3.35. Region B, Line 2, Profile 14.



**Figure 3.36.** Region C, Line 1, Profile 15.



As it has been mentioned before, GPR results are very site-specific because of the limited depth of penetration of radar in conductive environments, such as in clay and water bearing sediments as it was in the study area. The amplitude of EM fields decreases exponentially with depth. In most materials, energy is lost to scattering from material variability. The signal propagates well in sand and gravel while conductive soils such as clay, or fill saturated with conductive groundwater cause GPR signal attenuation and loss of target resolution, i.e., limited detection of small objects (Reynolds, 2000; Annan, 2003; Olhoeft et al., 1994).

In a general sense, at three region identified in the study area, clayey and alluvium units were observed after 1-1.5 m depth. These units can be seen especially at Region A, Line 3, 4 and at Region B, Line 1, 2 (Figures 3.32 through 3.35). Other bands observed in the radagrams can be interpreted as sandy units.

At Region A, there exists compressed sandy fill up to 1 m in both line profiles. After 1 m, Line 1 profiles consist of clayey and alluvium units while Line 2 profiles showing scattered signals in the radagrams. That proves alluvium accumulation at the site occurred in the same direction with Line 2 profiles.

In the direction from profile 1 to profile 4 at Region A, the thickness of the clayey and alluvium units tends to increase. In the same direction, at Region B and Region C, clayey and alluvium units can be seen densely especially after 1-1.5 m depth. By considering the depth and thickness of the units we can come up with the conclusion that the clayey and alluvium units are getting thicker from North to South at the study area.

Using perpendicular profiles at Region A, an attempt was made to construct a 3 Dimensional subsurface profile at the region. Resultant image was illustrated in Figure 3.37.

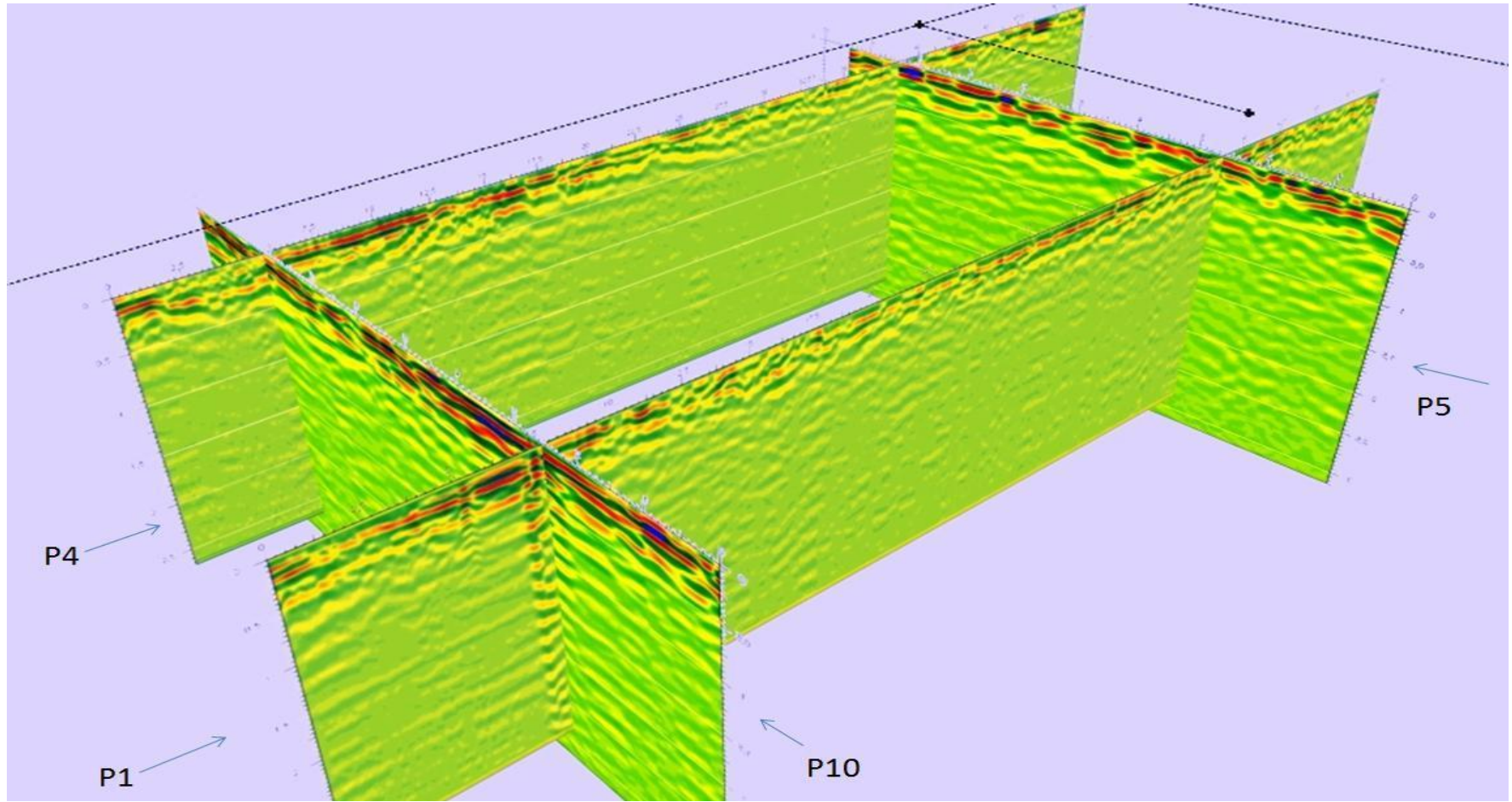


**Figure 3.37.** 3 Dimensional view of GPR results at Region A.

## CHAPTER 4

### 3-DIMENSIONAL NUMERICAL SIMULATION OF GROUND DEFORMATIONS INDUCED BY MECHANICAL EXCAVATION AT NECATIBEY STATION

#### 4.1. Introduction

This chapter summarizes the concept of 3-dimensional numerical models (mechanical) created to estimate the ground deformations taking place at the Ankara Subway System Necatibey Station and its close vicinity due to the mechanical excavation.

In order to simulate mechanical excavation of tunnels a critical soil profile was chosen to set off a basis for numerical models by examining just established 3-dimensional soil profiles in Chapter 3. In fact, the soil profile used for the numerical models consists of three layers namely fill (dm), alluvium (qa) and Ankara clay (Tg) from top to bottom. Although soil properties for fill and Ankara clay layers are reported in (Erol and Çetin, 2006 in Erol, 2006), it is very well known the fact that alluvium unit of Dikmen Valley changes its characteristics very often in horizontal direction at the site. Therefore, the primary aim of numerical models was to calibrate soil properties (e.g., bulk modulus, shear modulus, cohesion, etc.) for alluvium layer by modeling excavation steps at the site.

To do this a considerable amount of 3-dimensional numerical models were run and results were continuously correlated with the recorded deformation measurements taken from the site. Trials were continued until numerical results

matched fairly well with the recorded measurements. Soil properties at the instant of matching were accepted as real ones and used at the rest of this study.

This chapter supplies information about *FLAC 3D* code firstly. And then, step by step procedure will be mentioned about numerical modeling concept. Information about assumptions made to improve numerical models quality will be followed by construction stages part and recorded deformation measurements part. Finally, results part includes numerical model results and correlation with recorded deformation measurements.

## **4.2. Introducing *FLAC 3D* code**

### **4.2.1. General concept of the code**

*FLAC3D* is a 3-dimensional explicit finite-difference program for engineering mechanics computation. *FLAC3D* has the analysis capability of three dimensions, simulating the behavior of 3D structures built of soil, rock or other materials that undergo plastic flow when their yield limits are reached. Materials are represented by polyhedral elements within a three-dimensional grid that is adjusted by the user to fit the shape of the object to be modeled. Each element behaves according to a prescribed linear or nonlinear stress/strain law in response to applied forces or boundary restraints. The material can yield and flow and the grid can deform (in large-strain mode) and move with the material that is represented. The explicit, Lagrangian, calculation scheme and the mixed-discretization zoning technique used in *FLAC3D* ensure that plastic collapse and flow are modeled very accurately. *FLAC3D* offers an ideal analysis tool for solution of three-dimensional problems in geotechnical engineering (FLAC 3D User's Manuel, 2005).

Both finite element and finite difference methods translate a set of differential equations into matrix equations for each element, relating forces at nodes to displacements at nodes. Although *FLAC3D*'s equations are derived by the finite difference method, the resulting element matrices, for an elastic material, are

identical to those of the finite element method (for constant-strain tetrahedra). However, *FLAC3D* differs in the following respects.

(a) The “mixed discretization” scheme (Marti and Cundall, 1982) is used for accurate modeling of plastic collapse loads and plastic flow. This scheme is believed to be physically more justifiable than the “reduced integration” scheme commonly used with finite elements.

(b) The full dynamic equations of motion are used, even when modeling systems are essentially static. This enables *FLAC3D* to follow physically unstable processes without numerical distress.

(c) An “explicit” solution scheme is used (in contrast to the more usual implicit methods). Explicit schemes can follow arbitrary nonlinearity in stress/strain laws in almost the same computer time as linear laws, whereas implicit solutions can take significantly longer to solve nonlinear problems. Furthermore, it is not necessary to store any matrices, which means: (a) a large number of elements may be modeled with a modest memory requirement; and (b) a large-strain simulation is hardly more time-consuming than a small-strain run, because there is no stiffness matrix to be updated.

(d) *FLAC3D* is robust in the sense that it can handle any constitutive model with no adjustment to the solution algorithm; many finite element codes need different solution techniques for different constitutive models.

These differences are mainly in *FLAC3D*’s favor, but there are two disadvantages.

(a) Linear simulations run slower with *FLAC3D* than with equivalent finite element programs. *FLAC3D* is most effective when applied to nonlinear or large-strain problems, or to situations in which physical instability may occur.

(b) The solution time with *FLAC3D* is determined by the ratio of the longest natural period to the shortest natural period in the system being modeled. Thus

certain problems are very inefficient to model (e.g., beams, represented by solid elements rather than structural elements, or problems that contain large disparities in elastic moduli or element sizes) (FLAC 3D User's Manuel, 2005).

#### **4.2.2. General features of the code**

As defined User's Manuel (2005) *FLAC3D* offers a wide range of capabilities to solve complex problems in mechanics, and especially in geomechanics. *FLAC3D* embodies special numerical representations for the mechanical response of geologic materials. The program has eleven basic built-in material models: the "null" model; three elasticity models (isotropic, transversely isotropic and orthotropic elasticity); and seven plasticity models (Drucker-Prager, Mohr-Coulomb, strain-hardening/softening, ubiquitous-joint, bilinear strain-hardening/softening ubiquitous-joint, double-yield and modified Cam-clay). Additionally, an interface, or slip-plane, model is available to represent distinct interfaces between two or more portions of the grid. The interfaces are planes upon which slip and/or separation are allowed, thereby simulating the presence of faults, joints or frictional boundaries.

*FLAC3D* contains an automatic 3D grid generator in which grids are created by manipulating and connecting pre-defined shapes. The generator permits the creation of intersecting internal regions (e.g., intersecting tunnels).

Boundary conditions and initial conditions can be specified either velocity (and displacement) boundary conditions, or stress (and force) boundary conditions. Initial stress conditions, including gravitational loading, may also be given, and a water table may be defined for effective stress calculations.

*FLAC3D* incorporates the facility to model groundwater flow and pore-pressure dissipation, and the full coupling between a deformable porous solid and a viscous fluid flowing within the pore space. Fixed pore pressure and constant-flow boundary conditions may be used, and sources and sinks (wells) may be modeled.

Structures, such as tunnel liners, piles, sheet piles, cables, rock bolts or geotextiles that interact with the surrounding rock or soil may be modeled with the structural element logic in *FLAC3D*.

A factor of safety can be calculated automatically for any *FLAC3D* model composed of Mohr-Coulomb material. The calculation is based on a “strength reduction technique” that performs a series of simulations while changing the strength properties to determine the condition at which an unstable state exists.

*FLAC3D* also contains a powerful built-in programming language, *FISH*, which enables the user to define new variables and functions.

Also, four optional features (for dynamic analysis, thermal analysis, modeling creep-material behavior, and writing user-defined constitutive models) are available as separate modules.

#### **4.2.3. Mechanics of using *FLAC 3D***

In order to set up a model to run a simulation with *FLAC3D*, three fundamental components of a problem must be specified:

- (i) a finite difference grid;
- (ii) constitutive behavior and material properties; and
- (iii) boundary and initial conditions.

The grid defines the geometry of the problem. The constitutive behavior and associated material properties dictate the type of response the model will display upon disturbance (e.g., deformational response due to excavation). Boundary and initial conditions define the in-situ state (i.e., the condition before a change or disturbance in the problem state is introduced).

The general solution procedure, illustrated in Figure 4.1, is convenient because it represents the sequence of processes that occurs in the physical environment.

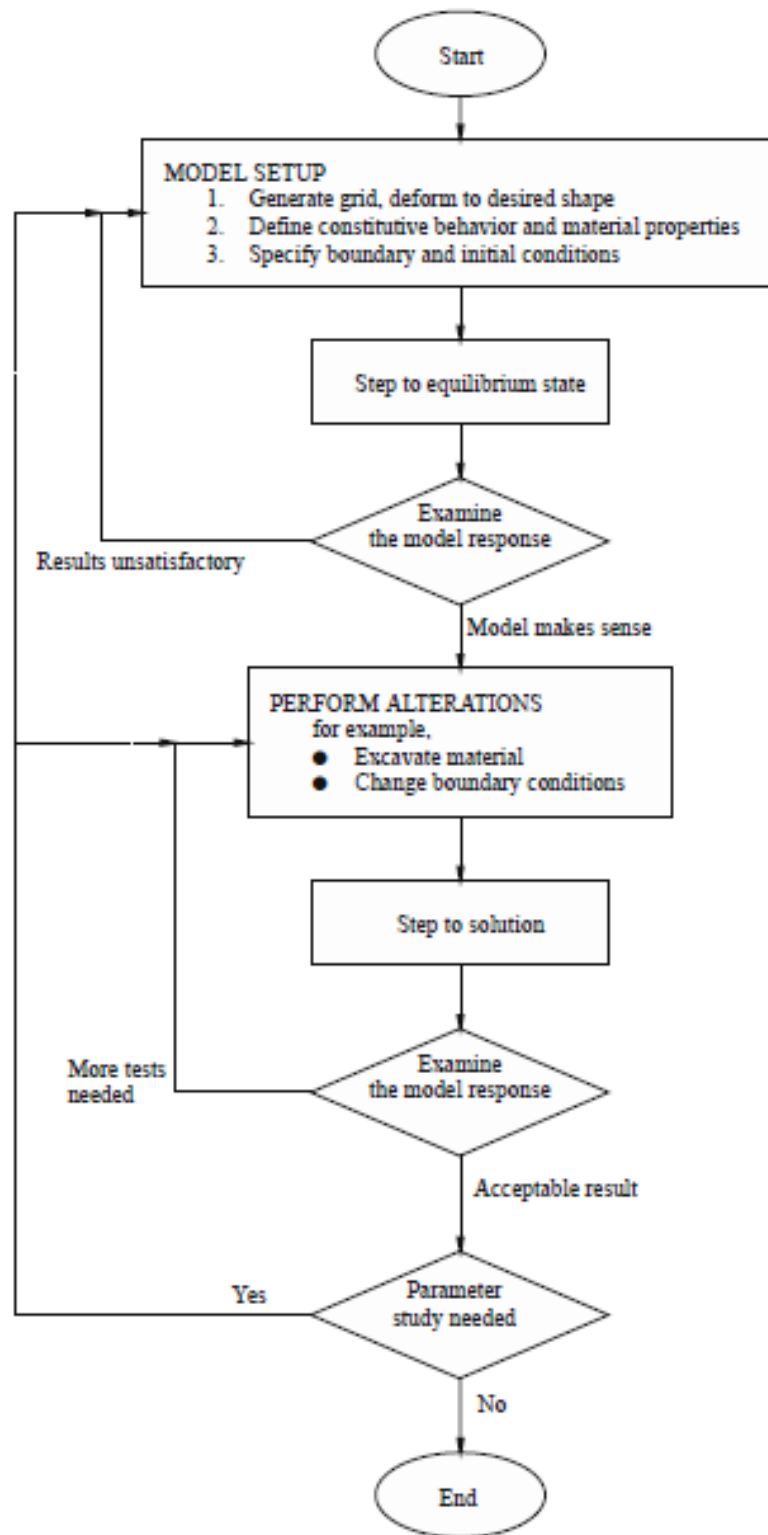


**Figure 4.1.** General solution procedure in *FLAC 3D* (FLAC 3D User's Manual, 2005).



### **4.3. Steps towards numerical models**

In order to simulate excavation steps at Necatibey Station and to discover resultant ground deformations 3-dimensional models were set up at this point. The steps followed to construct the models were itemized below.

#### **4.3.1. Grid generation**

Grid generation or the geometry of the problem is an important part of any numerical modeling. The purpose of the grid generation is to facilitate the creation of all required physical shapes in the model. Size of the grids is directly related with the accuracy of results and the solution time.

Sizing the grid for accurate results but with a reasonable number of zones can be complicated. Three factors should be kept in mind:

- (a) Finer meshes lead to more-accurate results in that they provide a better representation of high-stress gradients.
- (b) Accuracy increases as zone aspect ratios tend to unity.
- (c) If different zone sizes are needed, then the more-gradual the change from the smallest to the largest, the better the results (FLAC 3D User's Manuel, 2005).

When constructing geometry for Necatibey Station a region occupying two main tunnels and two connection tunnels (Figure 1.2) were considered due to the symmetry of the problem. That is why the model dimensions are 52 m, 60 m, and 32.60 m in x, y, z directions, respectively (Figure 4.2). Actually, symmetry of the problem just determines the length of the model (60 m). The total depth of the model (32.60 m) and the depth of different soil layers were determined by examining boring logs illustrated in Chapter 1 and geophysical investigation results illustrated in Chapter 3. As it can be seen from Figure 4.2 the model

consists of three layers namely fill (dm, 0-5.30 m), alluvium (qa, 5.30-17.30 m) and Ankara Clay (tg, 17.30-32.60 m) from top to bottom.

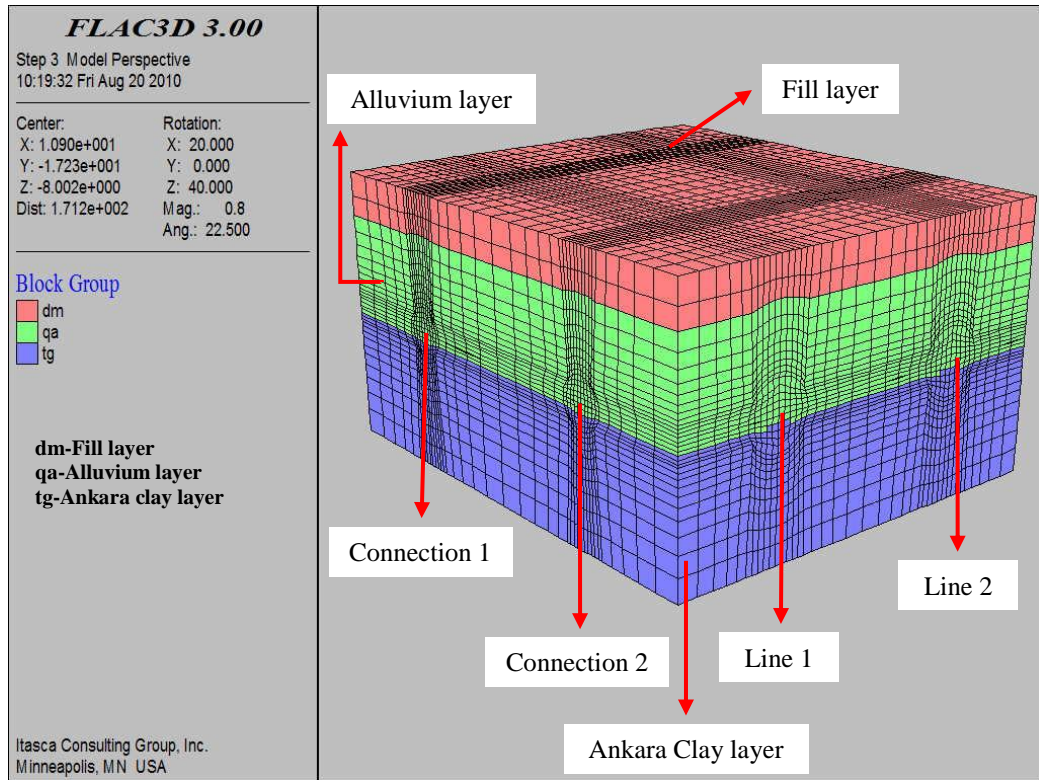


**Figure 4.2.** *FLAC 3D* grid showing the geometry of the problem.

Another important point need to be emphasized here is that the alluvium layer (green in color in Figure 4.2) was divided into three zones at every 20 m intervals along the y-direction in order to simulate lateral changes in soil properties. Resultant geometry of the model analyzed in this Chapter is shown in Figure 4.3. This final grid contains 51.200 zones and 56.841 gridpoints.

Sketch illustration of main tunnels 8 m in diameter (equivalent diameter circle) and connection tunnels 6 m in diameter (equivalent diameter circle) is also given in Figure 4.4 for further visualization.

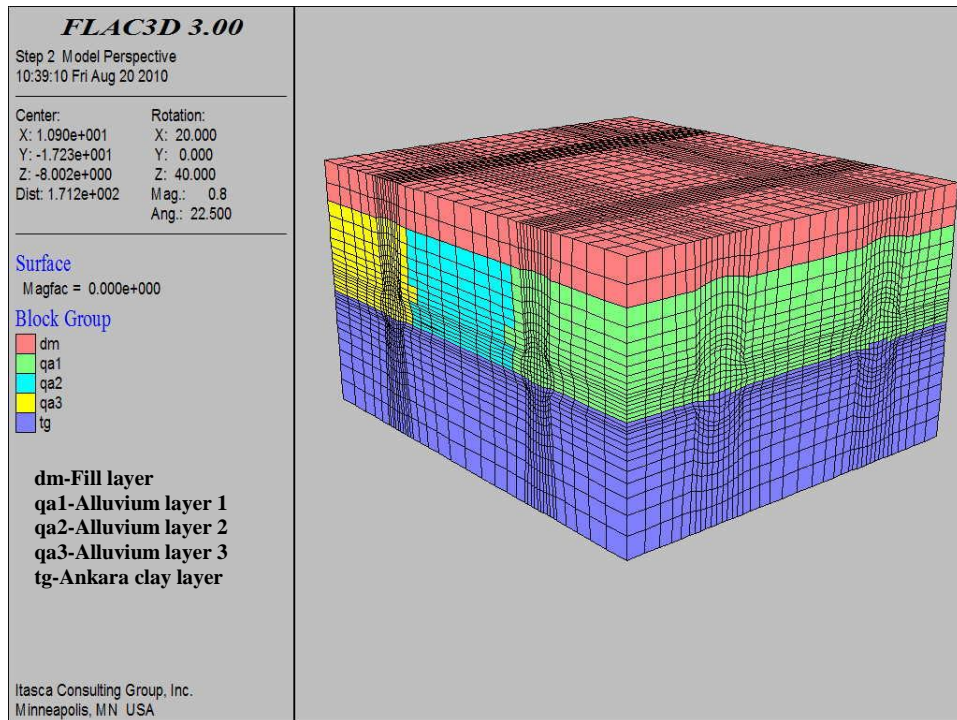


Figure 4.3. *FLAC 3D* grid showing the analyzed geometry of the problem.

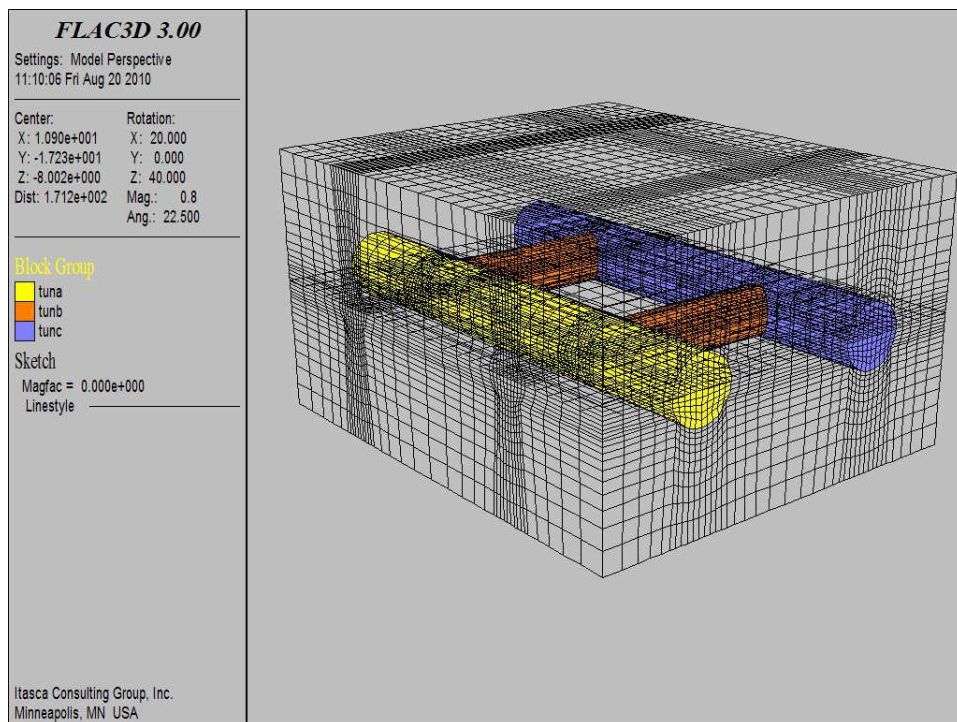


Figure 4.4. Sketch illustration of main tunnels and connection tunnels.

### 4.3.2. Constitutive behavior

Once the grid generation is completed, the material model and associated properties must be assigned to all zones in the model. The Mohr-Coulomb model is the most applicable for general engineering studies. Also, Mohr-Coulomb parameters for cohesion and friction angle are usually available more often than other properties for geo-engineering materials. Since it is suitable for loose and cemented granular materials and applicable for underground excavations, the Mohr-Coulomb material model was utilized throughout this study.

For the Mohr-Coulomb plasticity model, the required properties are: (1) bulk,  $K$ , and shear,  $G$ , moduli; (2) friction,  $\phi$ , and dilation,  $\psi$ , angles; (3) cohesion,  $c$ ; and (4) tensile strength,  $T$ . Bulk modulus,  $K$ , and shear modulus,  $G$ , are related to Young's modulus,  $E$ , and Poisson's ratio,  $\nu$ , by the following equations:

$$K = \frac{E}{3(1 - 2\nu)} \quad (4.1)$$

$$G = \frac{E}{2(1 + \nu)} \quad (4.2)$$

$$E = \frac{9KG}{3K + G} \quad (4.3)$$

$$\nu = \frac{3K - 2G}{2(3K + G)} \quad (4.4)$$

### 4.3.3. Material properties

The selection of material properties is often the most difficult element in the generation of a model because of the high uncertainty in the property database. It should be kept in mind when performing an analysis that the problem will always involve a data-limited system; the field data will never be known completely. That is why, in this study, considerable amount of model were run with different

material properties (K, G, c, etc.). The results were continuously correlated with recorded deformation measurements until a fairly well matching obtained. Soil properties at the instant of matching were accepted as real ones and used at the rest of the study.

The material properties required in *FLAC3D* are generally categorized in one of two groups: elastic deformability properties, and strength properties. This section provides an overview of the deformability and strength properties.

#### **4.3.3.1. Mass density**

The mass density is only required in a model if loading due to gravity is specified as it is in this study. The mass density is used to calculate the gravitational stresses within the model. Mass density has the units of mass divided by volume and does not include the gravitational acceleration. The following equation relates the total (saturated) density to the dry density:

$$\rho^{TOT} = \rho^{DRY} + n s \rho_w \quad (4.5)$$

where  $n$  is the porosity,  $s$  is the saturation, and  $\rho_w$  is the density of water.

#### **4.3.3.2. Deformability properties**

The Mohr-Coulomb material model assumes an isotropic material behavior in the elastic range described by two elastic constants namely bulk modulus (K) and shear modulus (G). The elastic constants, K and G, are used in *FLAC3D* rather than Young's modulus, E, and Poisson's ratio,  $\nu$ , because it is believed that bulk and shear moduli correspond to more fundamental aspects of material behavior than do Young's modulus and Poisson's ratio (FLAC 3D User's Manuel, 2005).

The equations to convert from (E,  $\nu$ ) to (K, G) were presented in Equation 4.1 and 4.2. Some typical values for elastic constants are summarized in Table 4.1 for selected soils.

**Table 4.1.** Selected elastic constants for soils (Das, 1994).

	<b>Unit Weight</b> <b>kN/m<sup>3</sup></b>	<b>Elastic</b> <b>Modulus (MPa)</b>	<b>Poisson's</b> <b>ratio</b>
Loose uniform sand	14.5	10-26	0.2-0.4
Dense uniform sand	18.2	34-69	0.3-0.45
Loose, angular-grained, silty sand	16.1		
Dense, angular-grained, silty sand	19.1		0.2-0.4
Stiff clay	17.1	6-14	0.2-0.5
Soft clay	11.5-14.7	2-3	0.15-0.25
Loess	13.6		
Soft organic clay	6-8.1		
Glacial till	21.2		

#### 4.3.3.3. Strength properties

The basic criterion for material failure is the Mohr-Coulomb relation, which is a linear failure surface corresponding to shear failure:

$$f_s = \sigma_1 - \sigma_3 N_\phi + 2c \sqrt{N_\phi} \quad (4.6)$$

where  $N_\phi = (1 + \sin \phi) / (1 - \sin \phi)$ ;

$\sigma_1$ : major principal stress (compressive stress is negative);

$\sigma_3$ : minor principal stress;

$\phi$ : friction angle; and

$c$ : cohesion.

Shear yield is detected if  $f_s < 0$ . The two strength constants,  $\phi$  and  $c$ , are conventionally derived from laboratory triaxial tests. Typical values of cohesion and friction angle values for soil specimens are given in Table 4.2. Strength is

often described in terms of the unconfined compressive strength,  $q_u$ . The relation between  $q_u$  and cohesion,  $c$ , and friction angle,  $\phi$ , is given by:

$$q_u = 2 c \tan(45 + \phi/2) \quad (4.7)$$

**Table 4.2.** Selected strength properties for soils (Ortiz et al., 1986).

	Cohesion (kPa)	Friction Angle (°)	
		Peak	Residual
Gravel	-	34	32
Sandy gravel with few fines	-	35	32
Sandy gravel with silty or clayey fines	1.0	35	32
Mixture of gravel and sand with fines	3.0	28	22
Uniform sand-fine	-	32	30
Uniform sand-coarse	-	34	30
Well-graded sand	-	33	32
Low plasticity silt	2.0	28	25
Medium- to high-plasticity silt	3.0	25	22
Low-plasticity clay	6.0	24	20
Medium-plasticity clay	8.0	20	10
High-plasticity clay	10.0	17	6
Organic silt or clay	7.0	20	15

#### 4.3.4. Boundary and initial conditions

The boundary conditions in a numerical model consist of the values of field variables (e.g., stress and displacement) that are prescribed at the boundary of the numerical grid. Boundaries are of two categories: real and artificial. Real boundaries exist in the physical object being modeled (e.g., a tunnel surface or the



ground surface). Artificial boundaries do not exist in reality, but they must be introduced in order to enclose the chosen number of zones (e.g., symmetry planes or boundary truncation).

Sometimes it is possible to take advantage of the fact that the geometry and loading in a system are symmetrical about one or more planes. For example, if everything is symmetrical about a vertical plane, then the horizontal displacements on that plane will be zero. When modeling infinite bodies (e.g., underground tunnels) or very large bodies, it may not be possible to cover the whole body with zones, due to constraints on memory and computer time. Artificial boundaries are placed sufficiently far away from the area of interest such that the behavior in that area is not greatly affected.

The boundary conditions for this problem were set as shown in Figure 4.5.

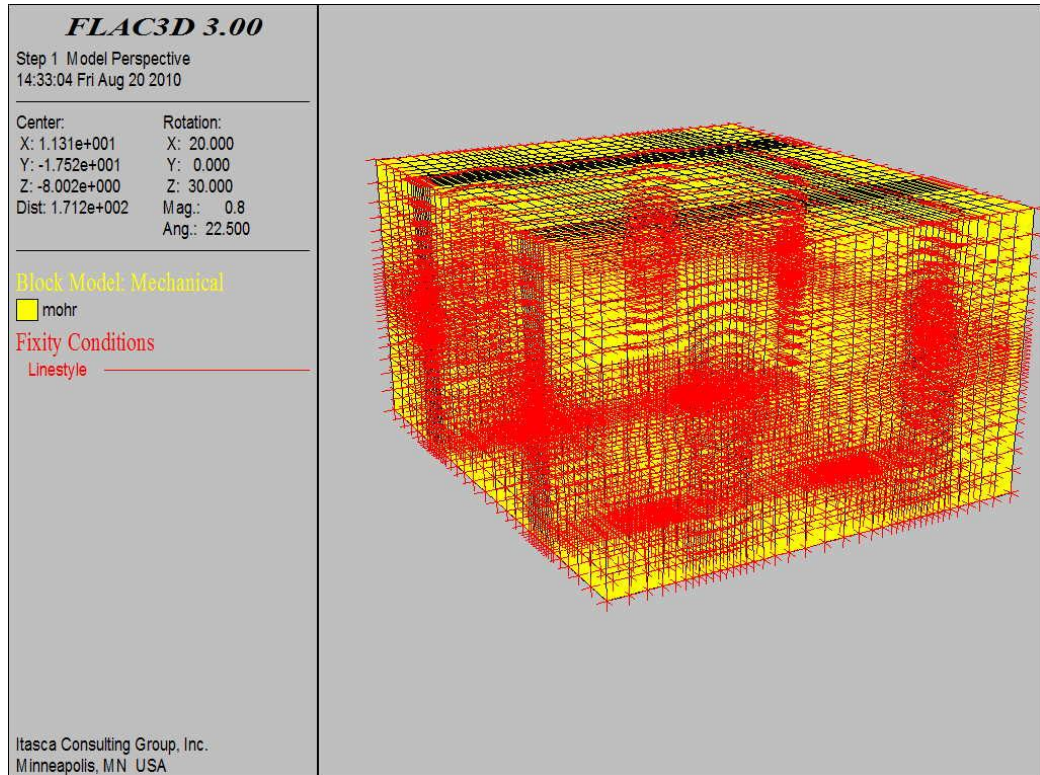


**Figure 4.5.** Boundary conditions for this study.



Roller boundaries were placed on four sides of the model. The boundaries are fixed only in the specified direction (i.e., no displacement or velocity is allowed). The following functions were performed:

- (i) The gridpoints along the boundary planes at  $x = 0$  and  $x = 52$  were fixed in the  $x$  and  $y$ -directions.
- (ii) The gridpoints along the boundary planes at  $y = 0$  and  $y = 60$  are fixed in the  $x$  and  $y$ -directions.
- (iii) The gridpoints along the bottom boundary ( $z = 0$ ) are fixed in the  $x$ ,  $y$ ,  $z$ -directions.

Since near the ground surface, the variation in stress with depth cannot be ignored, gravitational acceleration was operated on the grid. It is important to understand that the gravity does not directly cause stresses to appear in the grid; it simply causes body forces to act on all gridpoints. These body forces correspond to the weight of material surrounding each gridpoint. If no initial stresses are present, the forces cause the material to move (during stepping) in the direction of the forces until equal and opposite forces are generated by zone stresses. Given the appropriate boundary conditions (e.g., fixed bottom, roller side boundaries), the model generates its own gravitational stresses that are compatible with the applied gravity.

#### **4.4. Assumptions**

Several assumptions were adopted for improving the analysis by means of practicality, flexibility and precision. These are listed below:

- (a) The soil was represented by Mohr-Coulomb elastic-plastic material model. The use of a Mohr-Coulomb failure criterion assumes that the intermediate principle stress,  $\sigma_2$ , has no influence on the failure condition (Chen and Liu, 1990), and the failure is defined by:

$$\tau = c' + \sigma' \tan \phi' \tag{4.8}$$

where strength parameters  $c'$  and  $\phi$  represent the effective cohesion and angle of internal friction, respectively. The assumption of perfectly plastic behavior neglects any hardening response, and a nonassociative flow rule was assumed, with a dilation angle  $\psi=0$  corresponding to zero volume change during yield.

(b) Once the sub-layers are defined, they are all considered to be homogeneous elements on their own.

(c) Tunnel cross-sections were assumed to be equal diameter circles.

(d) Poisson's ratio was assumed to be 0.35 in all analyses.

(e) Since there is no data, lateral earth pressure was neglected and only gravitational loading was modeled.

(f) Investigation works conducted in the field were assumed to be by the standards with minimum error possible.

The above assumptions are typical of those employed in most geotechnical analyses, and are consistent with the uncertainty associated with the spatial variation of the material properties and depth to rock.

#### **4.5. Construction stages**

In this chapter, only ground deformations induced by mechanical excavation of main tunnels were considered. Deformations result from the excavation of connection tunnels and groundwater drainage will be presented in later chapters.

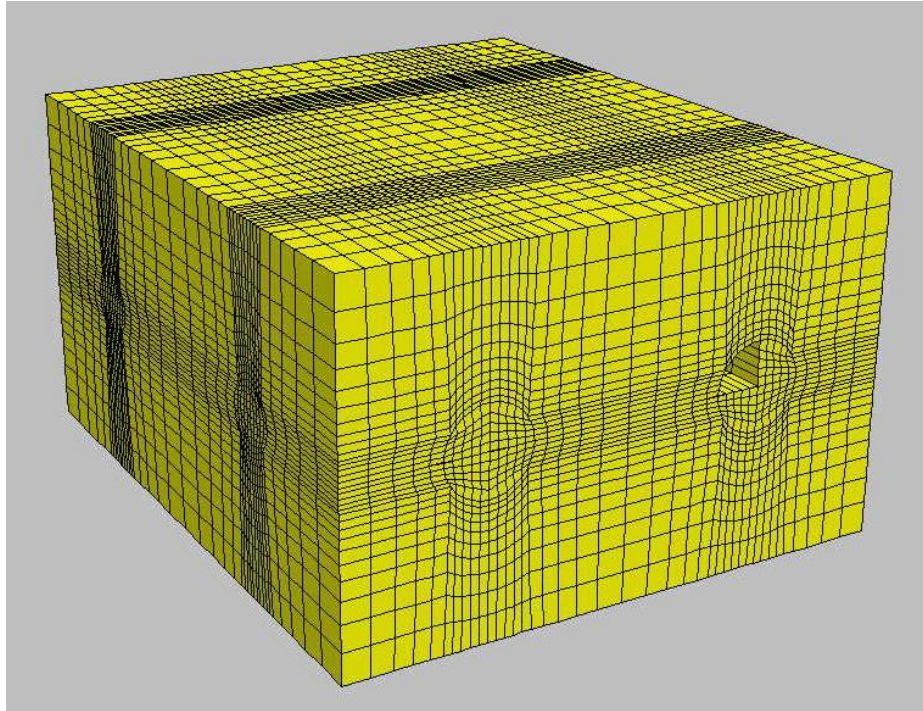
Main tunnels (Line 1 and Line 2, Figure 4.2) were excavated with a 10 m offset. In other words, Line 2 excavation was started firstly and carried forward till 15 m. Then Line 1 excavation was initiated and carried forward till 5 m. After that both tunnels were excavated step by step with a 5 m stage thickness keeping 10 m

offset between them. Table 4.3 summarizes excavation stages for all excavation processes conducted on main tunnels.

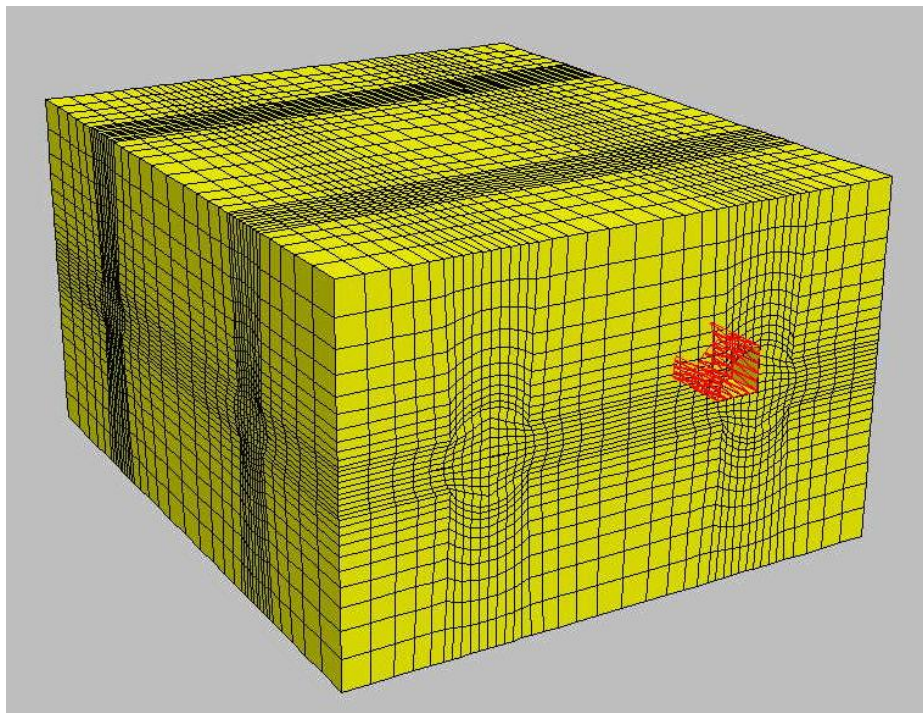
**Table 4.3.** Excavation stages for main tunnels.

<b>Stage</b>	<b>Line 1</b>	<b>Line 2</b>
1	-	5 m. excavation (60-55)
2	-	5 m. excavation (55-50)
3	-	5 m. excavation (50-45)
4	5 m. excavation (60-55)	-
5	-	5 m. excavation (45-40)
6	5 m. excavation (55-50)	-
7	-	5 m. excavation (40-35)
8	5 m. excavation (50-45)	-
9	-	5 m. excavation (35-30)
10	5 m. excavation (45-40)	-
11	-	5 m. excavation (30-25)
12	5 m. excavation (40-35)	-
13	-	5 m. excavation (25-20)
14	5 m. excavation (35-30)	-
15	-	5 m. excavation (20-15)
16	5 m. excavation (30-25)	-
17	-	5 m. excavation (15-10)
18	5 m. excavation (25-20)	-
19	-	5 m. excavation (10-5)
20	5 m. excavation (20-15)	-
21	-	5 m. excavation (5-0)
22	5 m. excavation (15-10)	-
23	5 m. excavation (10-5)	-
24	5 m. excavation (5-0)	-

Now, it is time to focus on excavation process in detail. While excavating main tunnels, partial face excavation has been modeled rather than full face excavation. Four different segments were adopted for each main tunnel and temporary and permanent shotcrete lining support was modeled. Excavation and support sequence mentioned via figures below (Figure 4.6 through Figure 4.9).



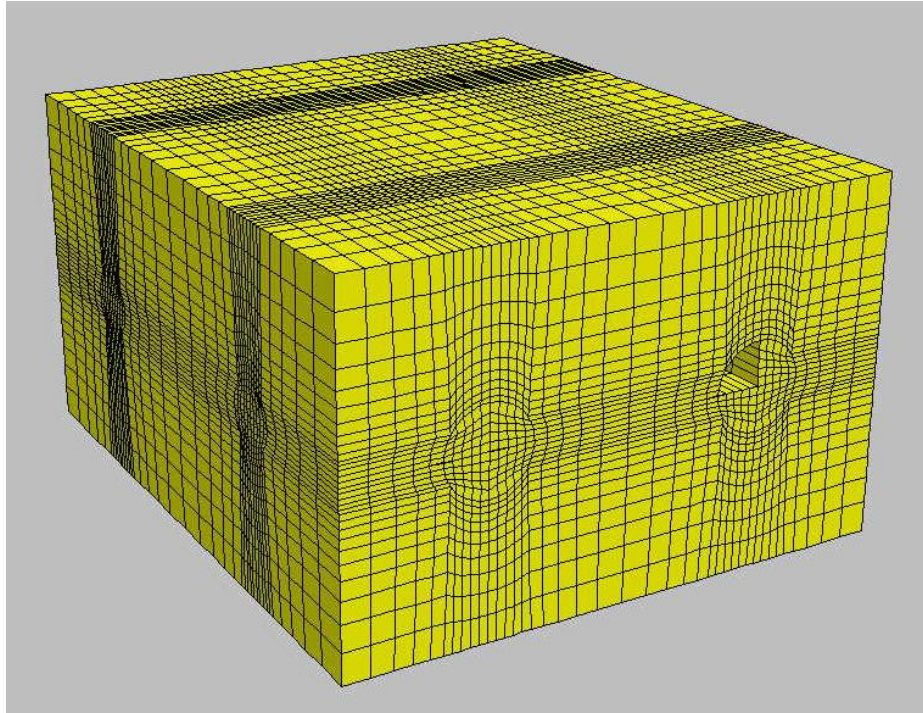
(a)



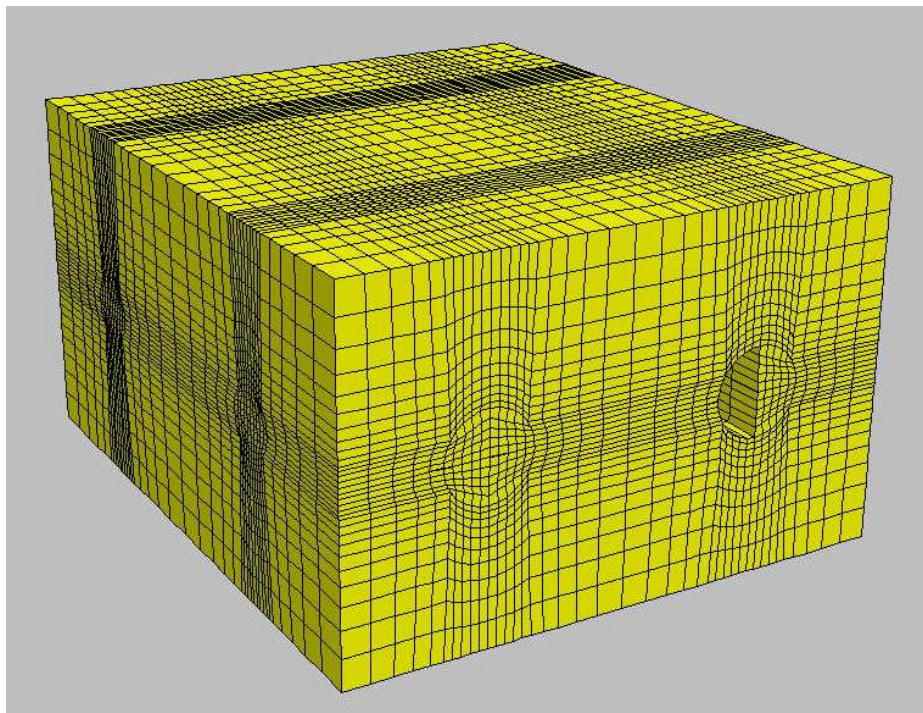
(b)

**Figure 4.6.** Step 1; a) excavation of segment 1, b) installation of temporary lining to segment 1.





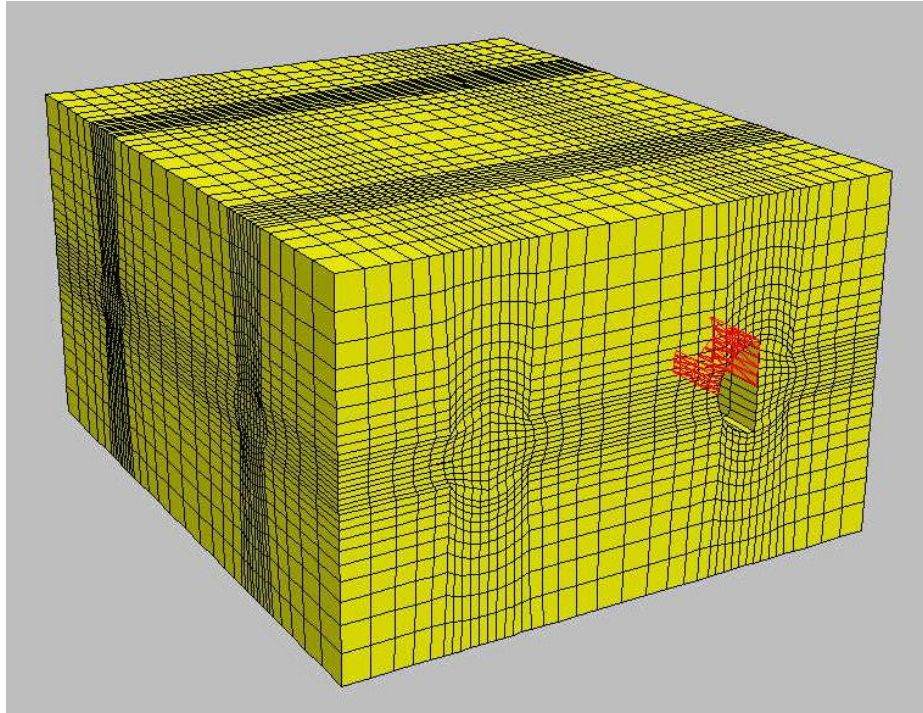
(a)



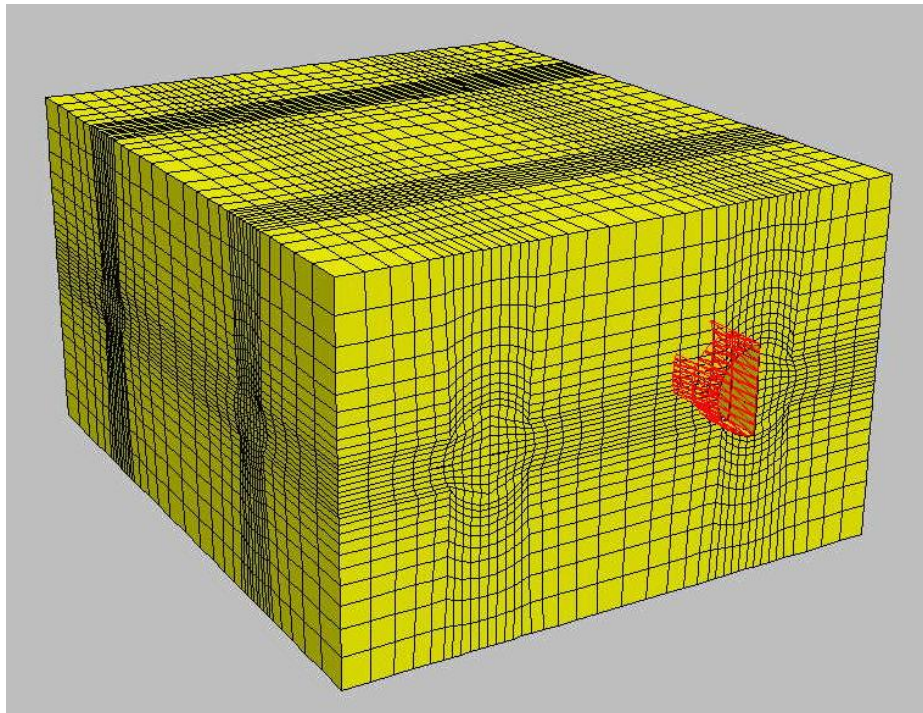
(b)

**Figure 4.7.** Step 2; a) removal of temporary lining at segment 1, b) excavation of segment 2,





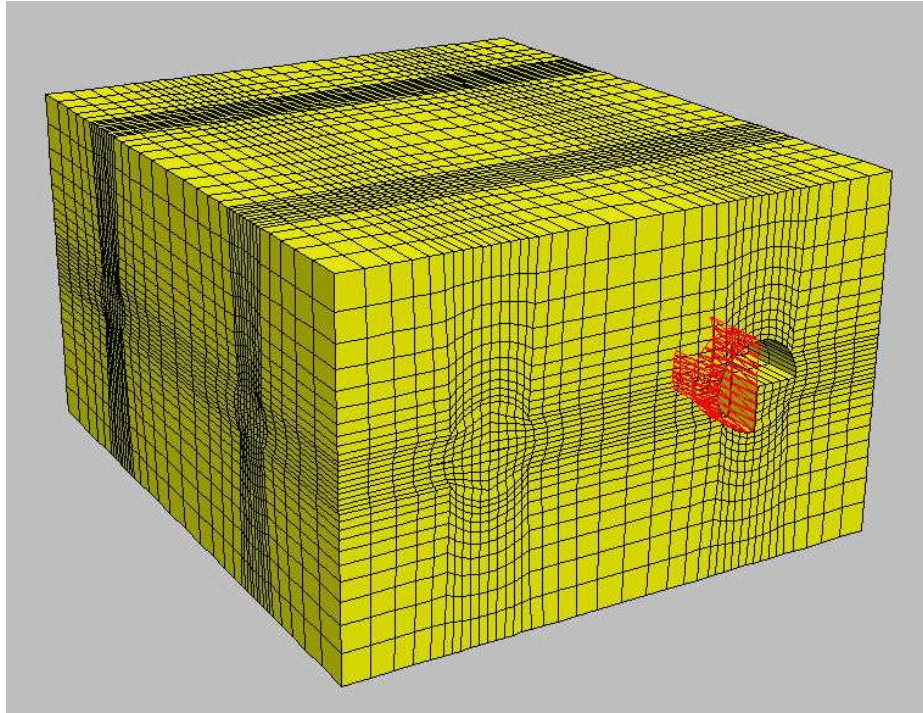
(c)



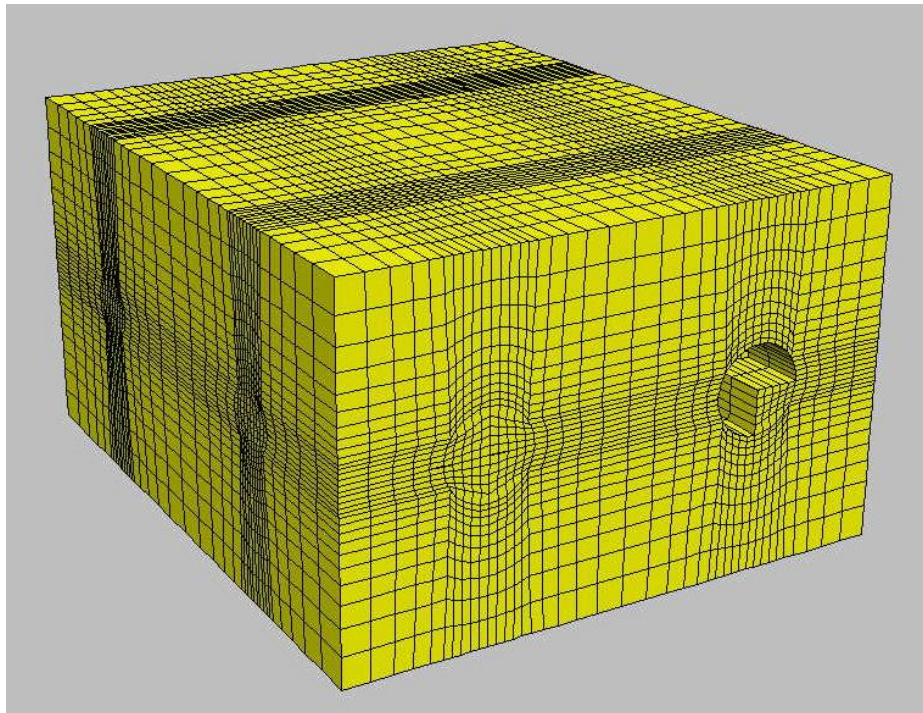
(d)

**Figure 4.7 cont'd.** c) installation of permanent lining at segment 1, d) installation of temporary lining at segment 2.





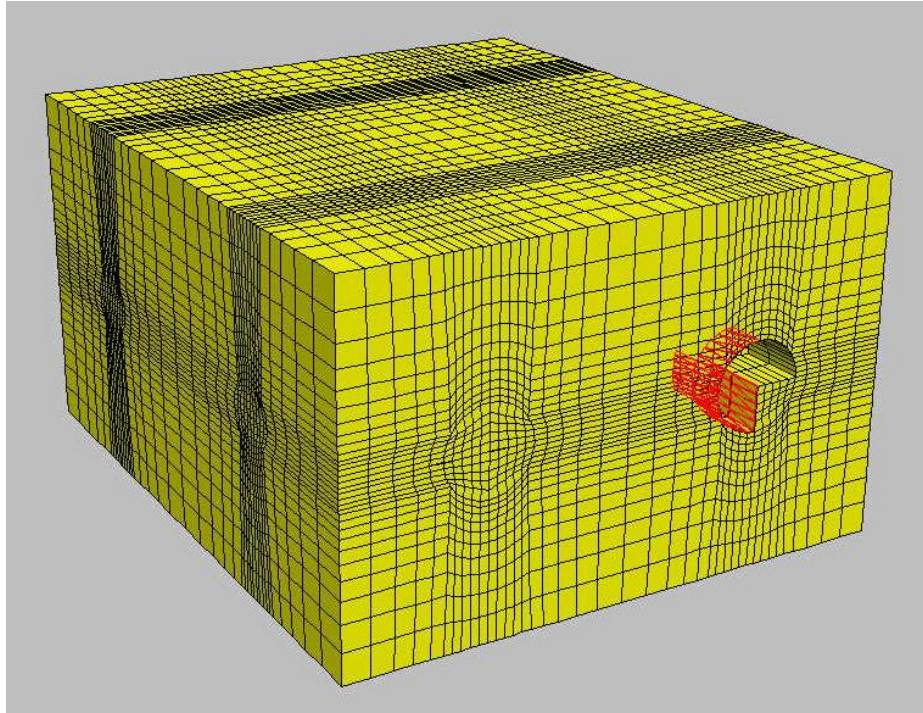
(a)



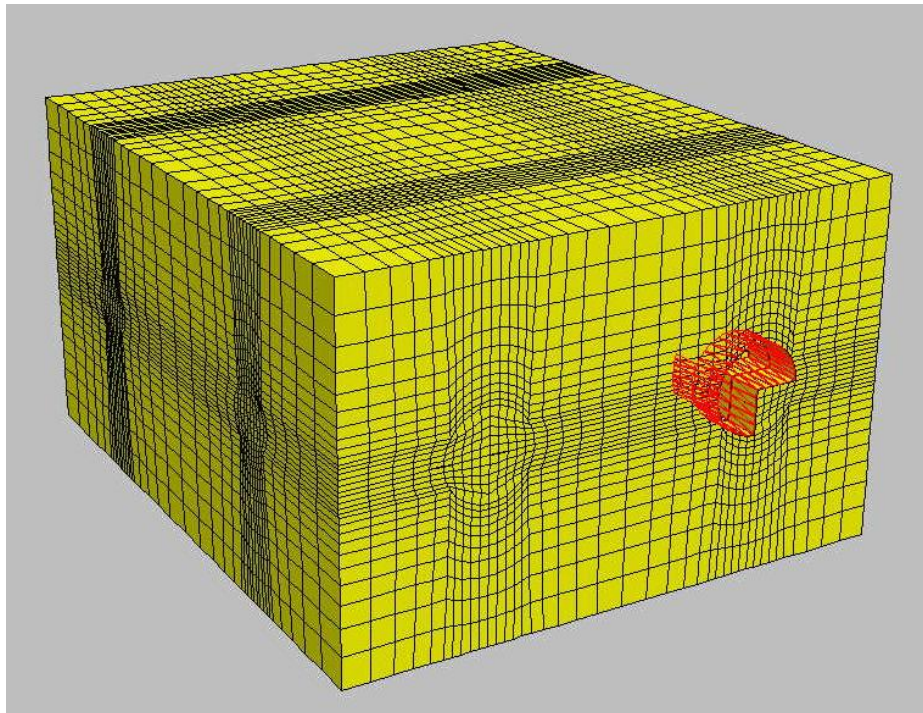
(b)

**Figure 4.8.** Step 3; a) excavation of segment 3, b) removal of permanent and temporary linings,





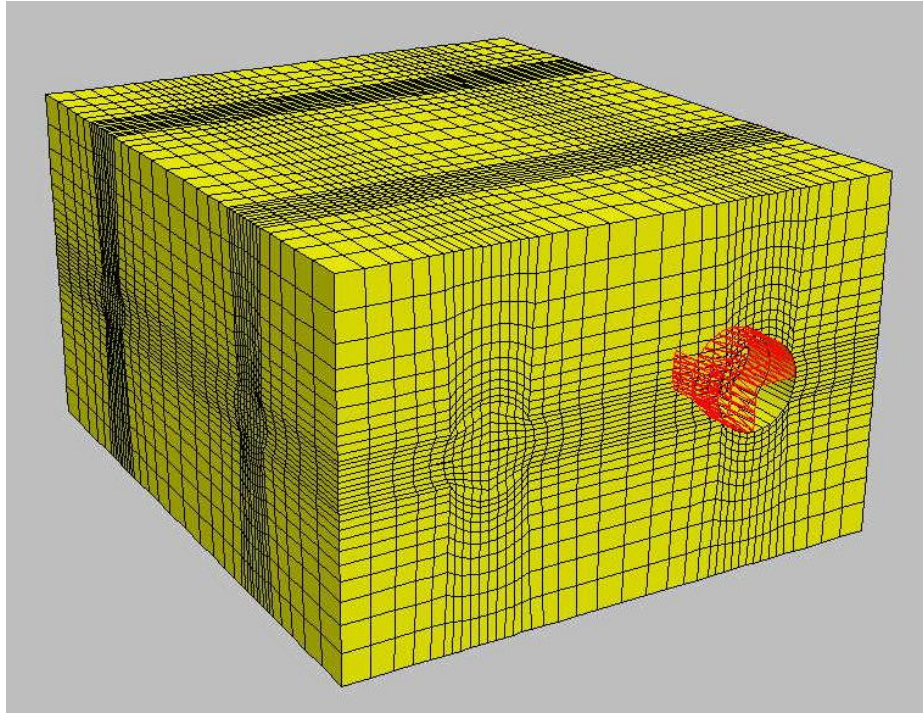
(c)



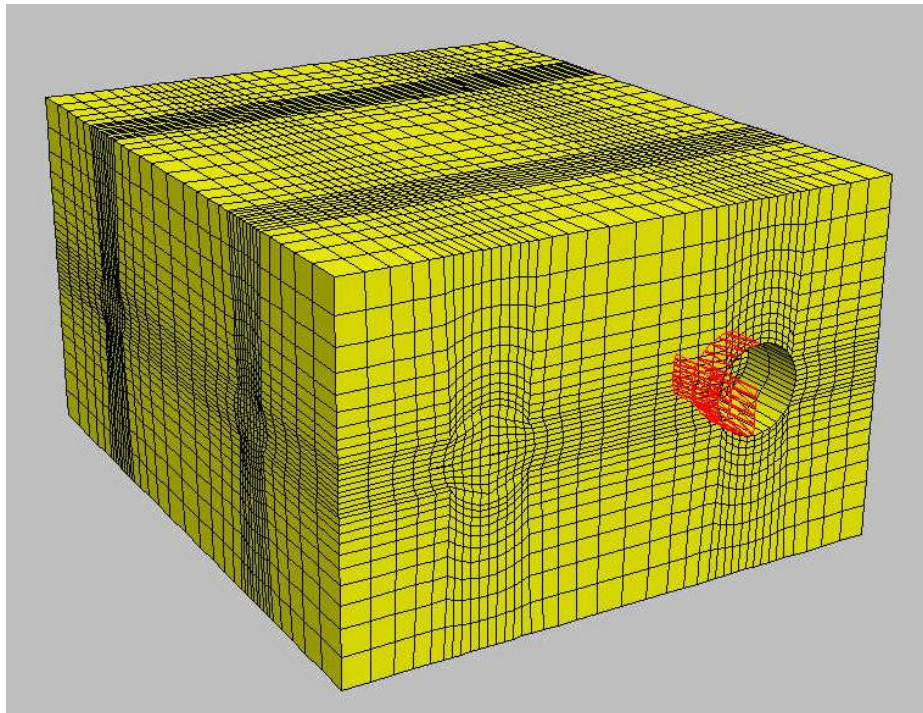
(d)

**Figure 4.8 cont'd.** c) installation of permanent linings at segment 1 and 2, d) installation of temporary lining at segment 3.





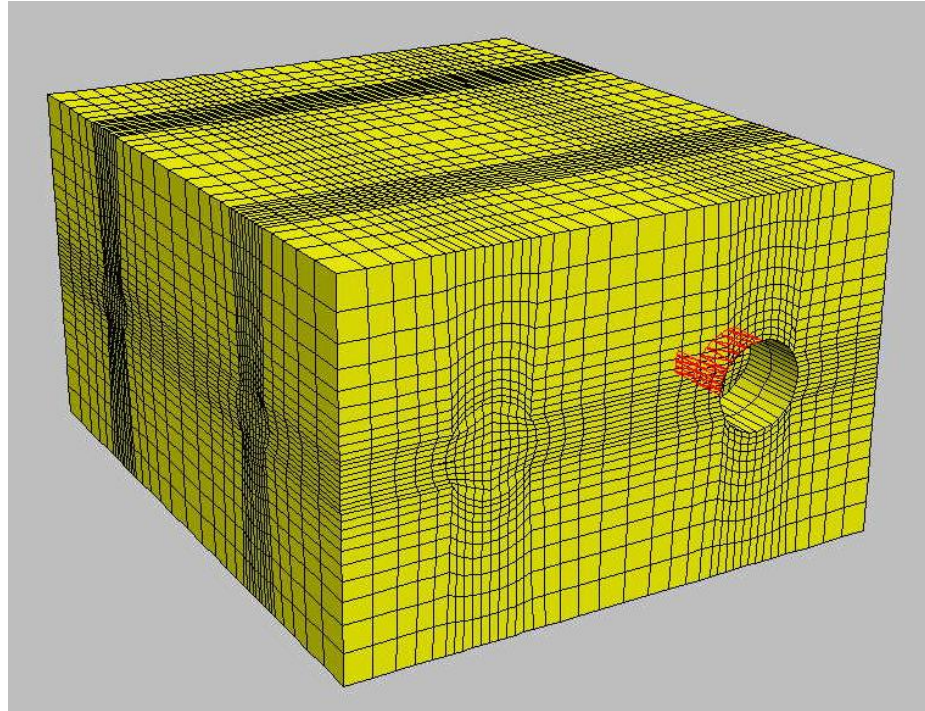
(a)



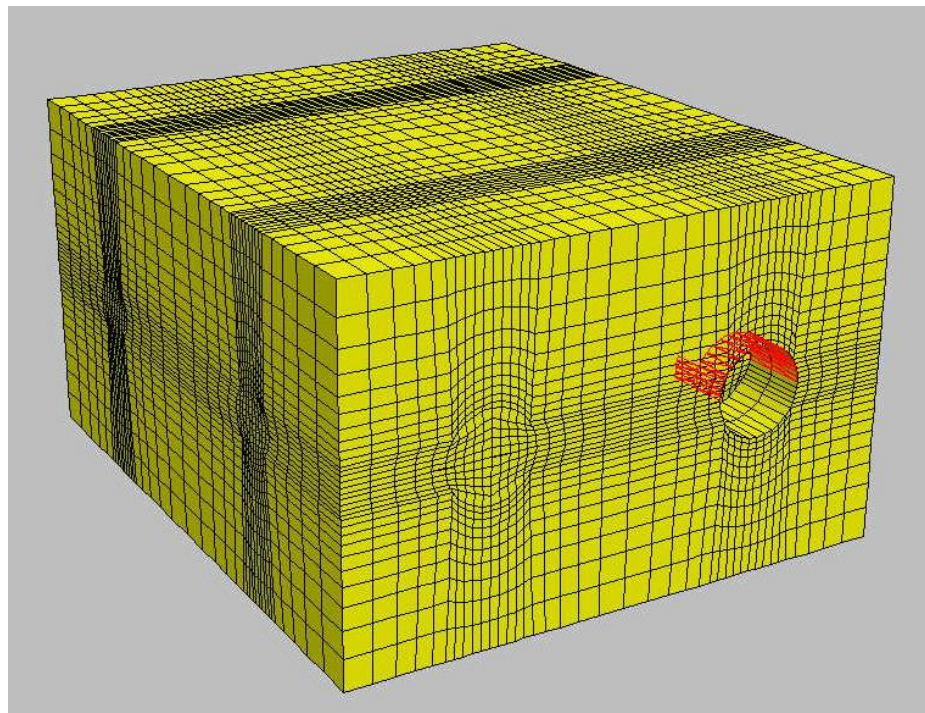
(b)

**Figure 4.9.** Step 4; a) excavation of segment 4, b) removal of temporary lining at segment 3,





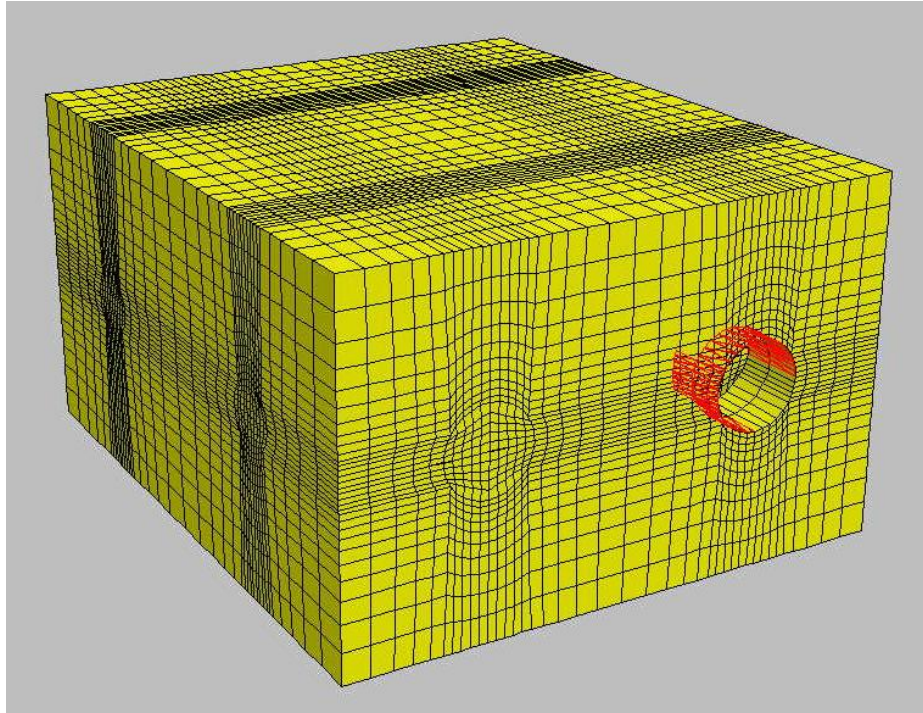
(c)



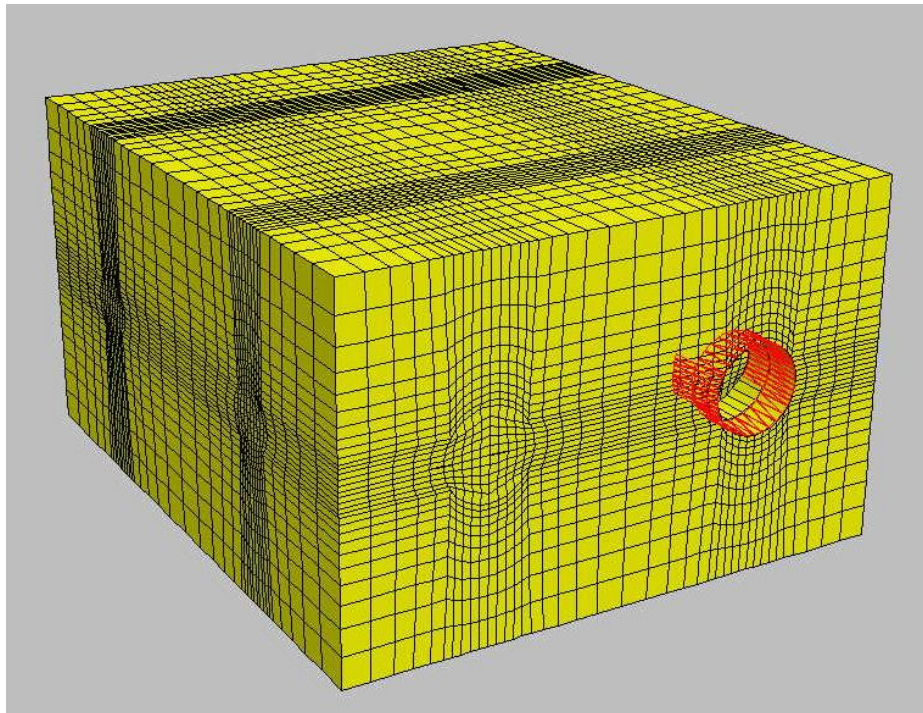
(d)

**Figure 4.9 cont'd.** c) removal of permanent lining at segment 2, d) installation of permanent lining at segment 3,





(e)

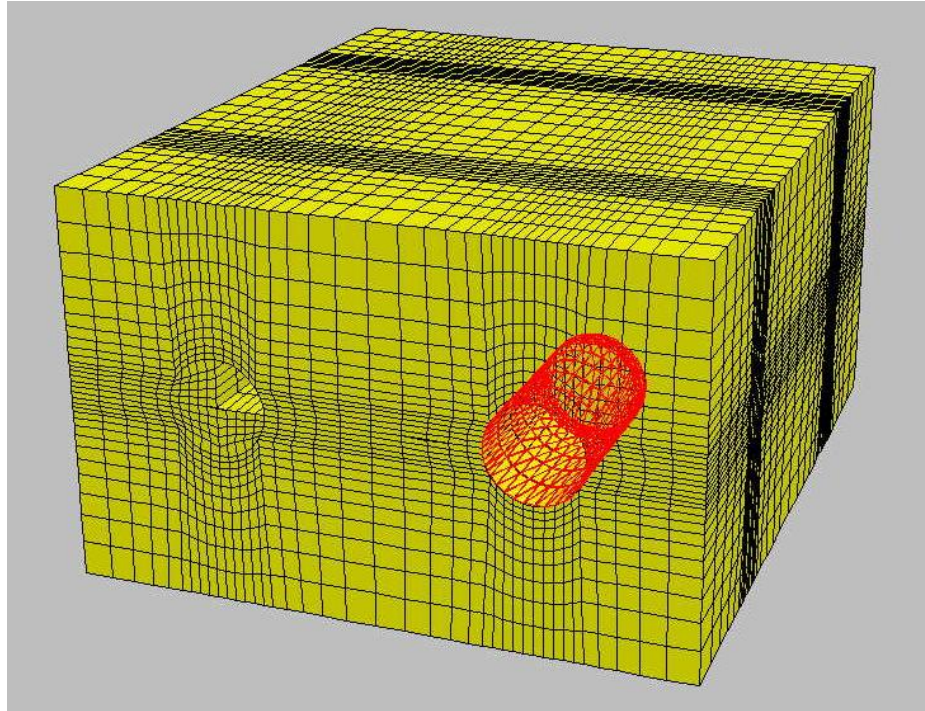


(f)

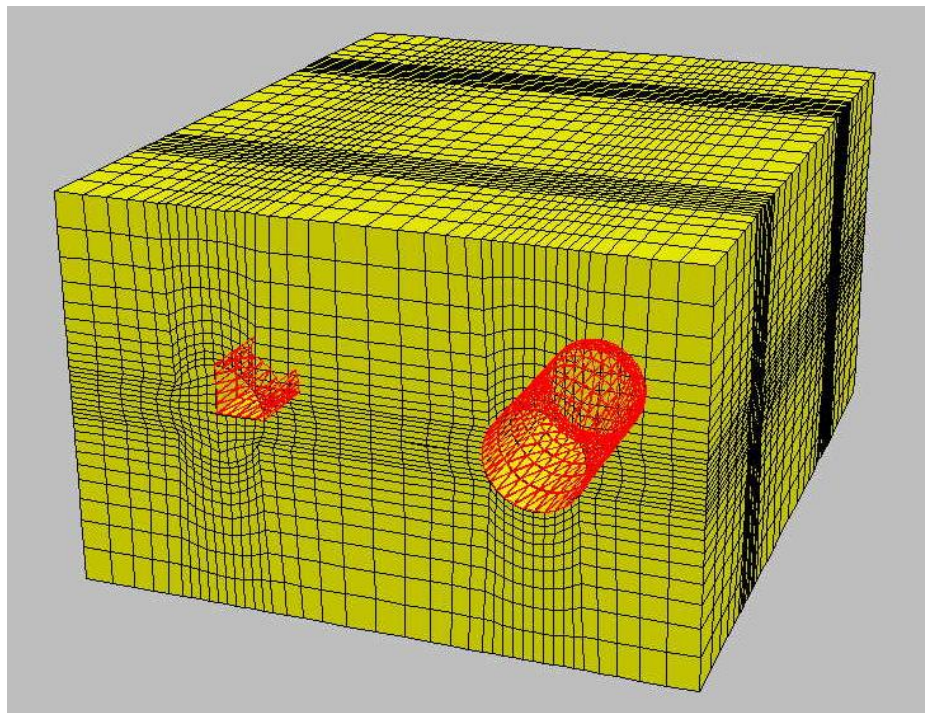
**Figure 4.9 cont'd.** e) installation of permanent lining at segment 2, f) installation of temporary lining at segment 4.

After 15 m excavation completed for Line 2, Line 1 excavation was initiated and carried forward with a 5 m stage advance. Excavation and support sequence for Line 1 tunnel mentioned via figures below (Figure 4.10 through Figure 4.13).





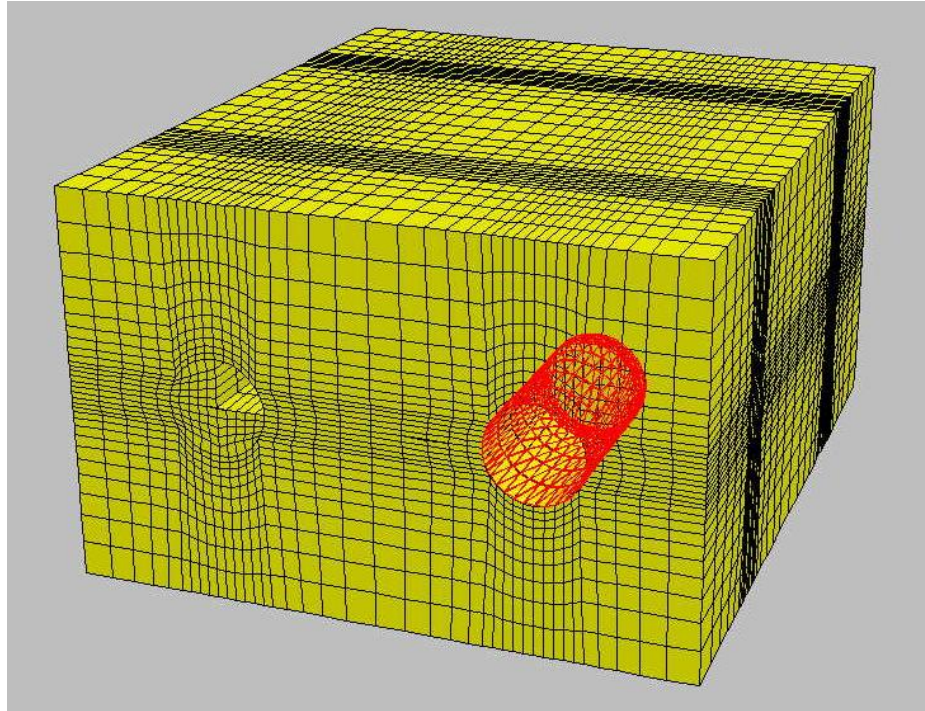
(a)



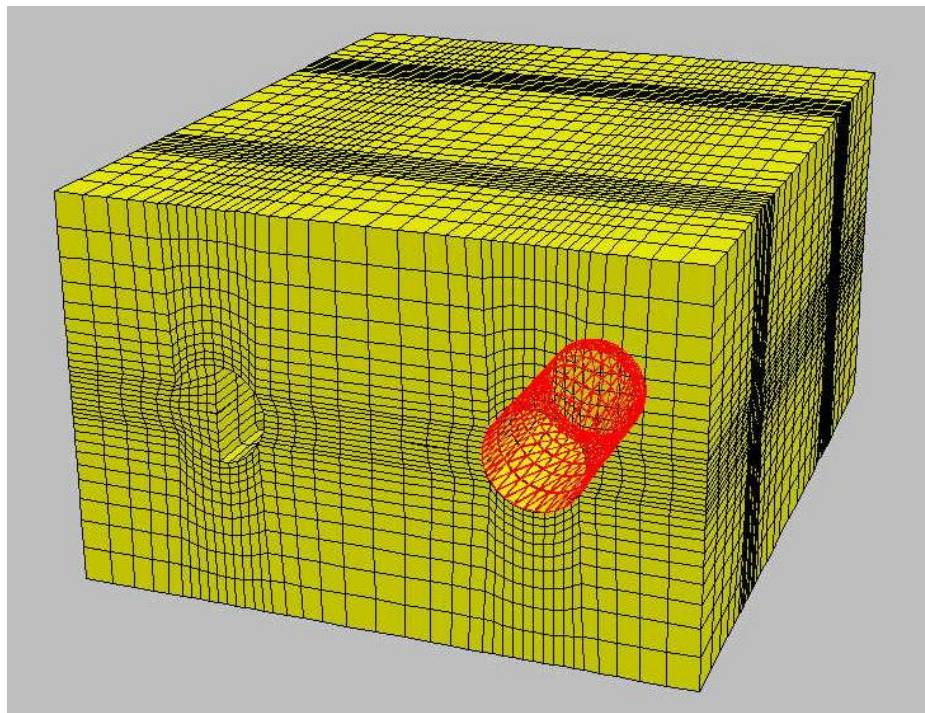
(b)

**Figure 4.10.** Step 1; a) excavation of segment 1, b) installation of temporary lining to segment 1.





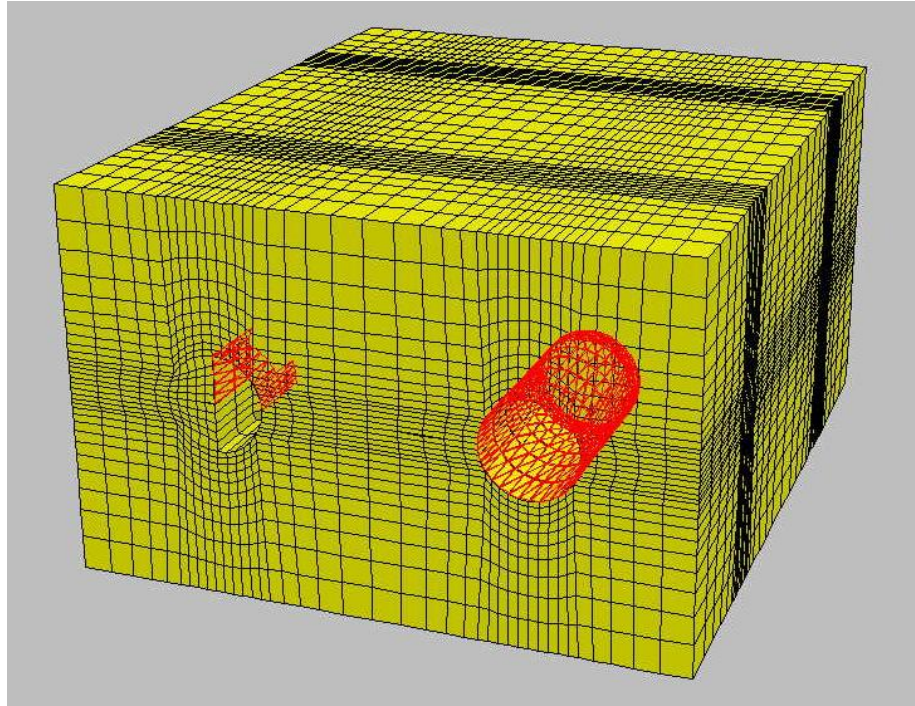
(a)



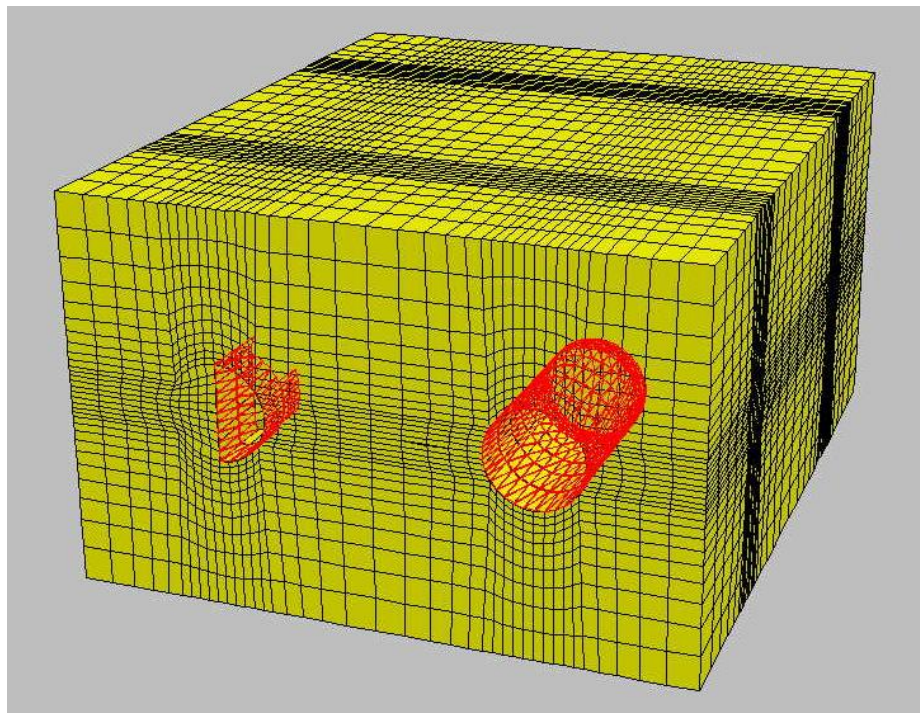
(b)

**Figure 4.11.** Step 2; a) removal of temporary lining at segment 1, b) excavation of segment 2,





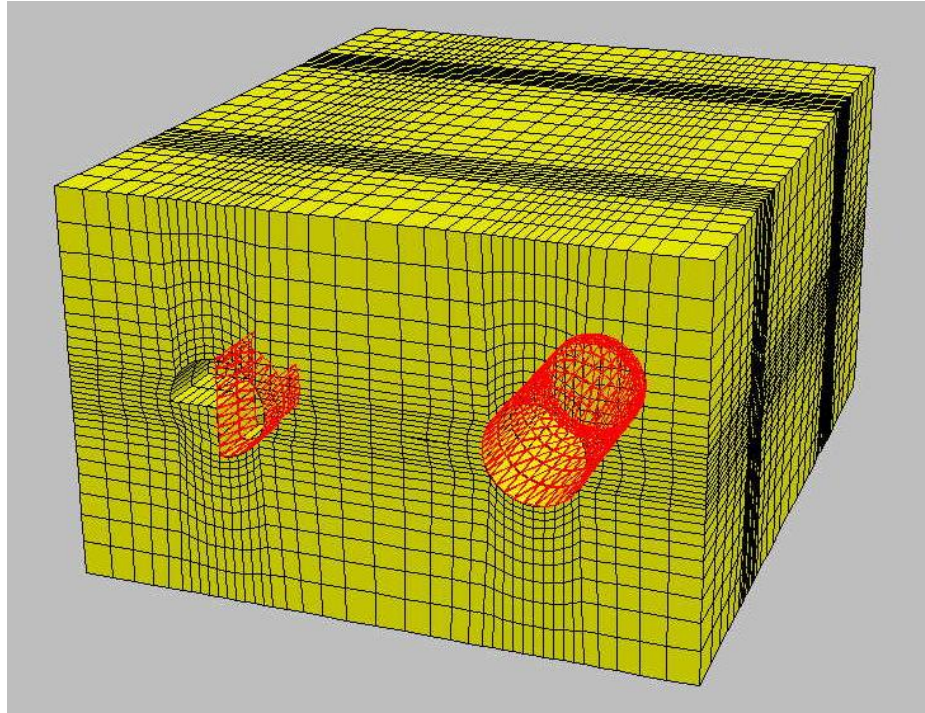
(c)



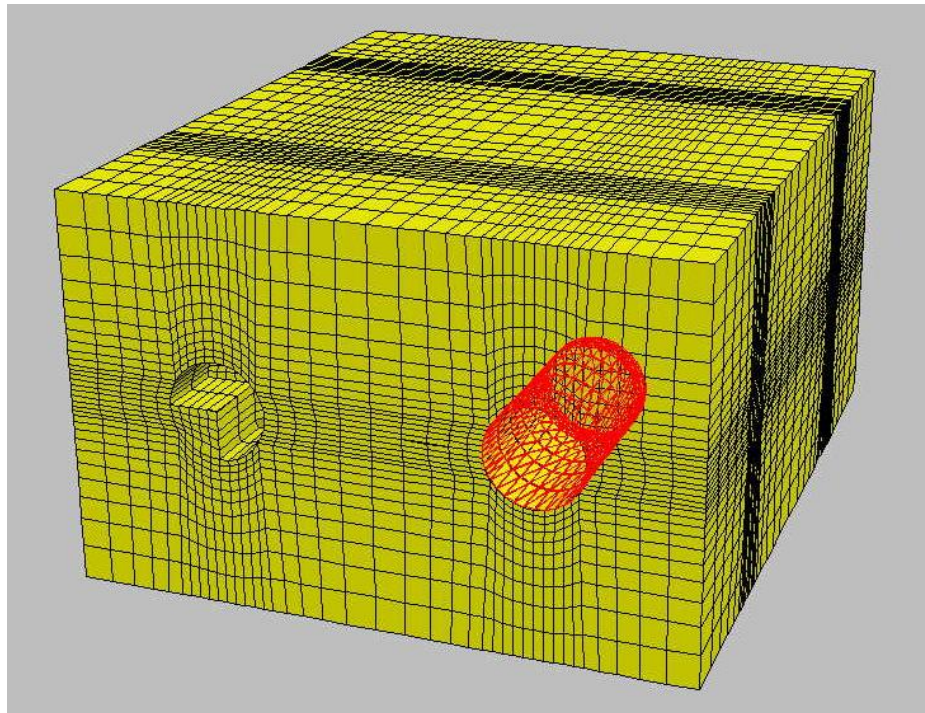
(d)

**Figure 4.11 cont'd.** c) installation of permanent lining at segment 1, d) installation of temporary lining at segment 2.





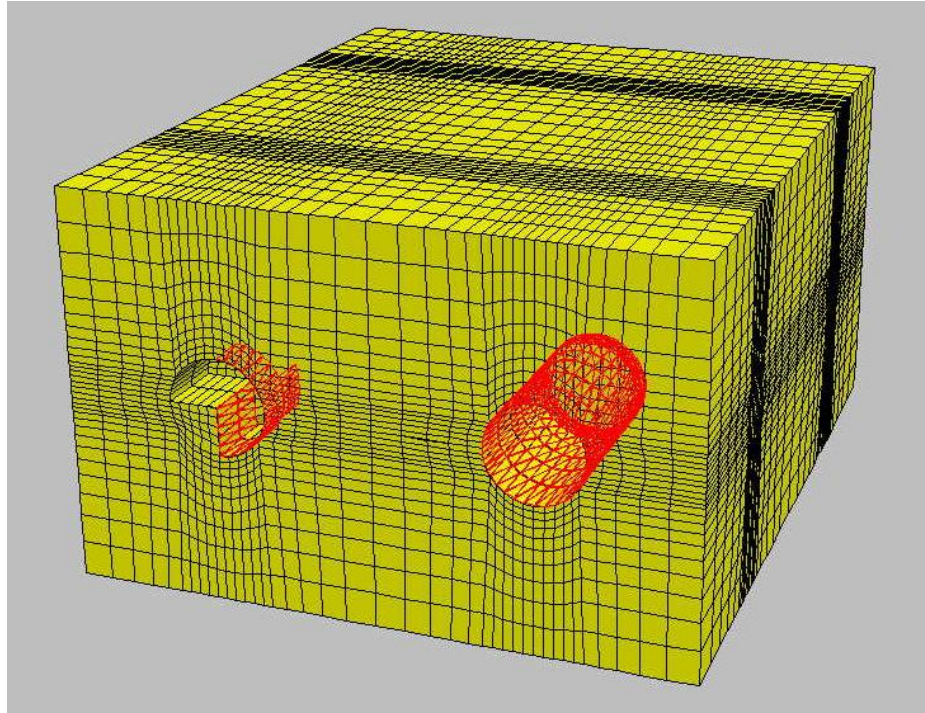
(a)



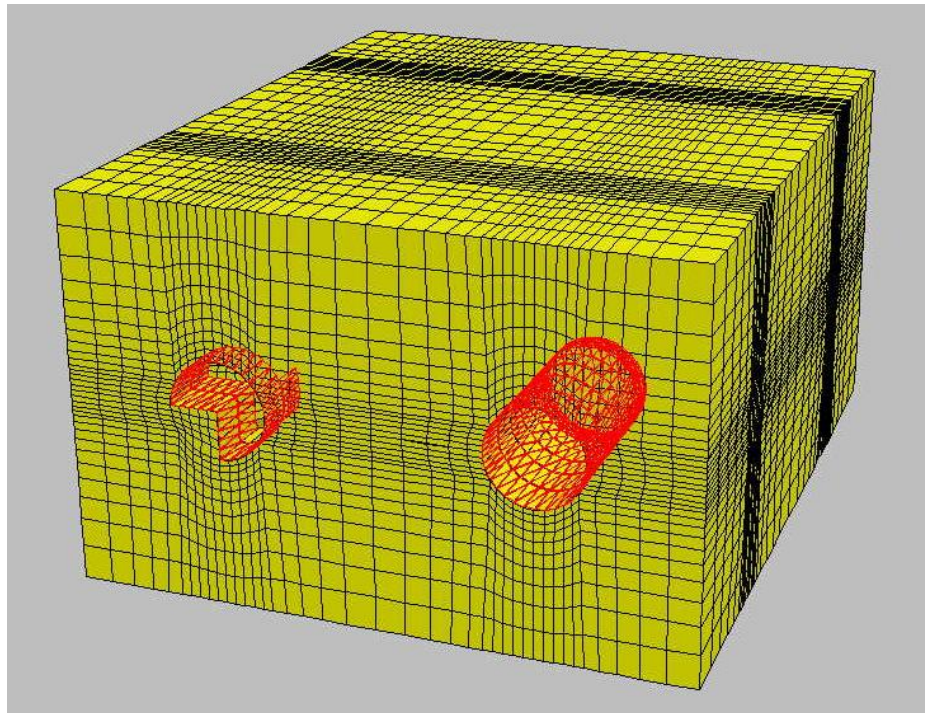
(b)

**Figure 4.12.** Step 3; a) excavation of segment 3, b) removal of permanent and temporary linings,





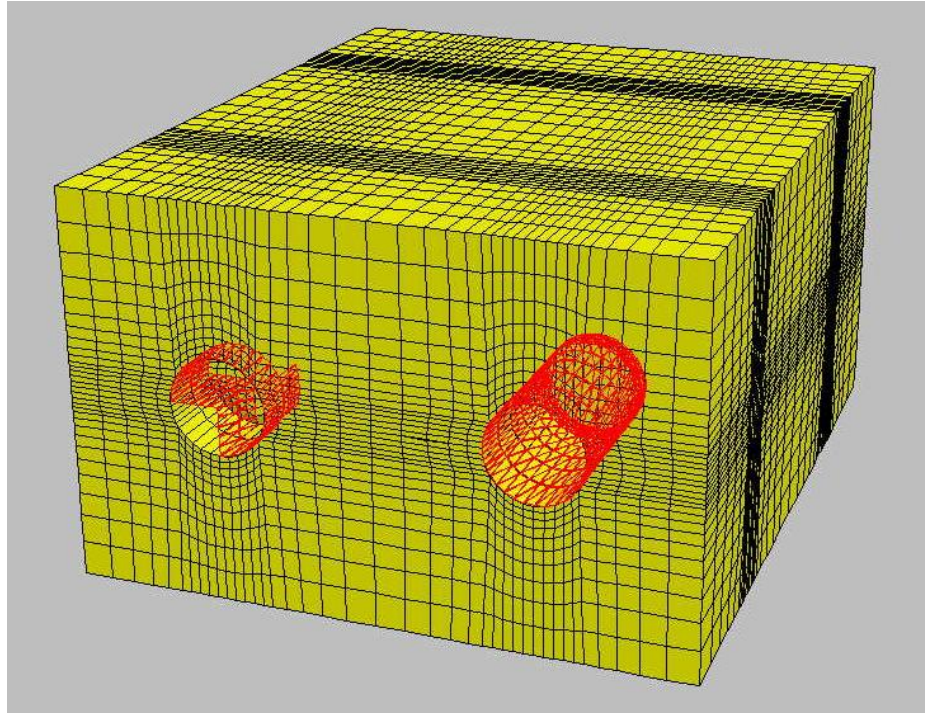
(c)



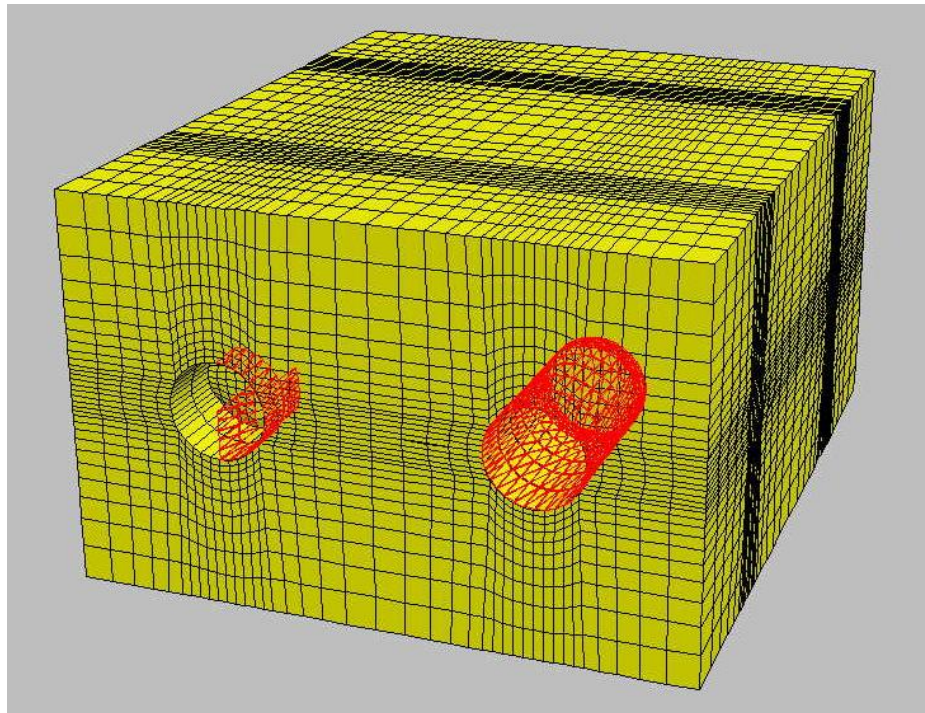
(d)

**Figure 4.12 cont'd.** c) installation of permanent linings at segment 1 and 2, d) installation of temporary lining at segment 3.





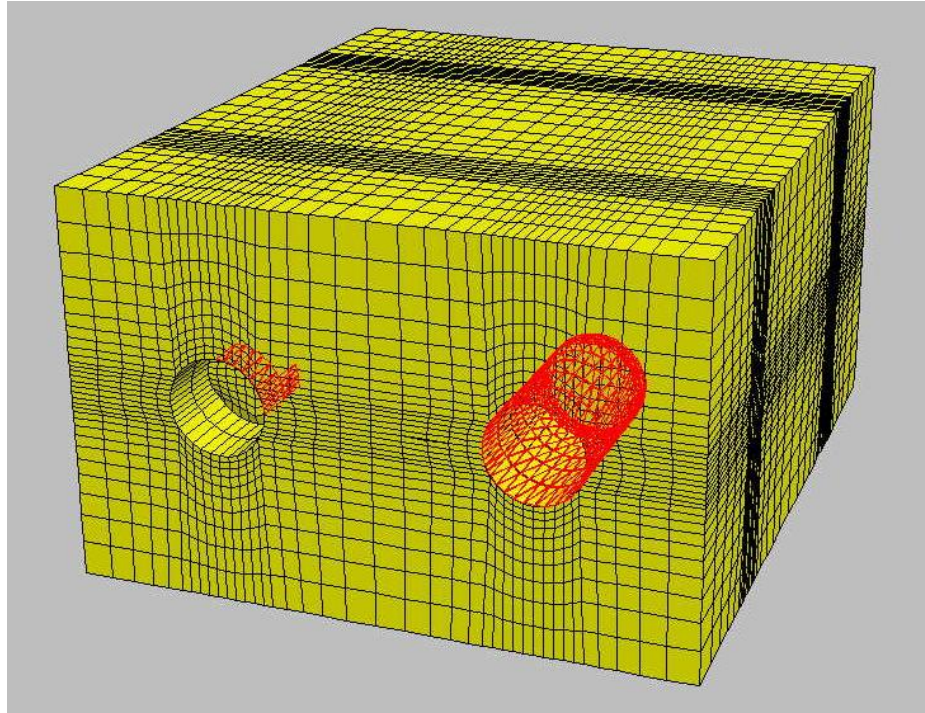
(a)



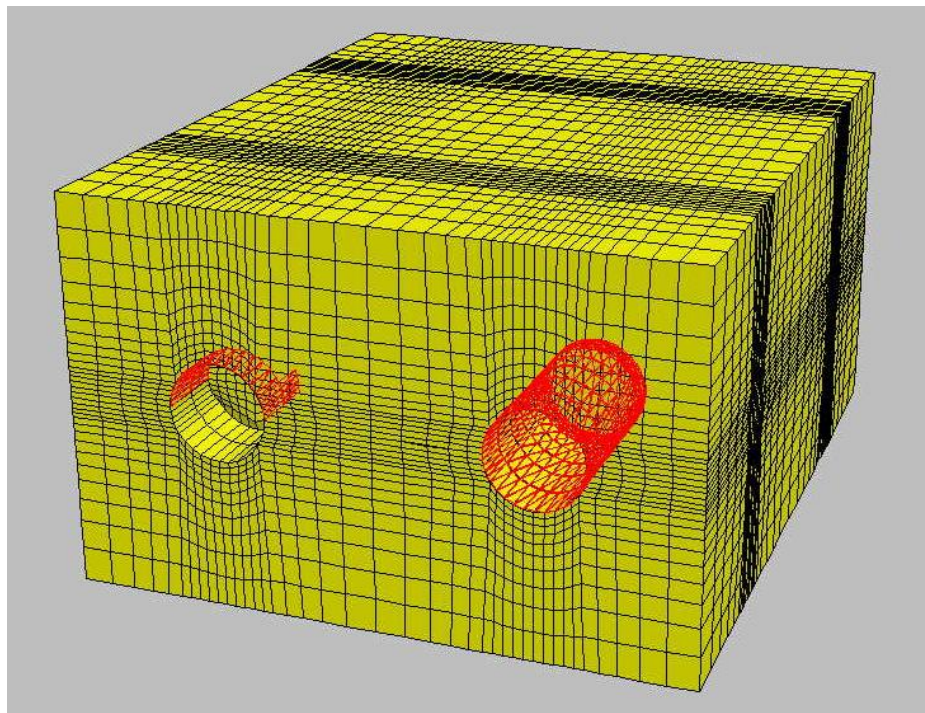
(b)

**Figure 4.13.** Step 4; a) excavation of segment 4, b) removal of temporary lining at segment 3,





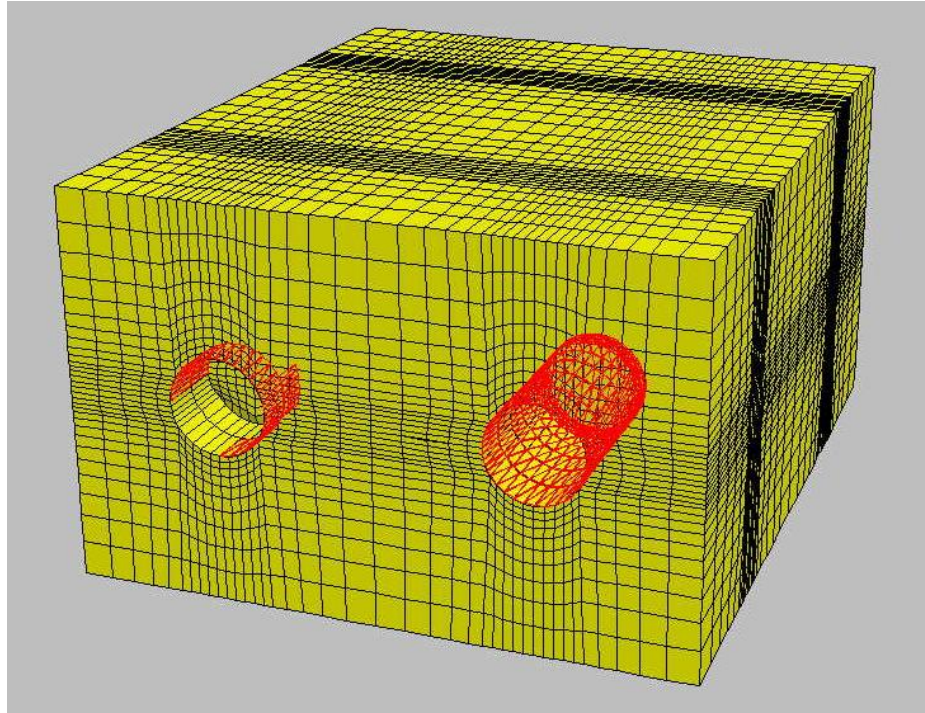
(c)



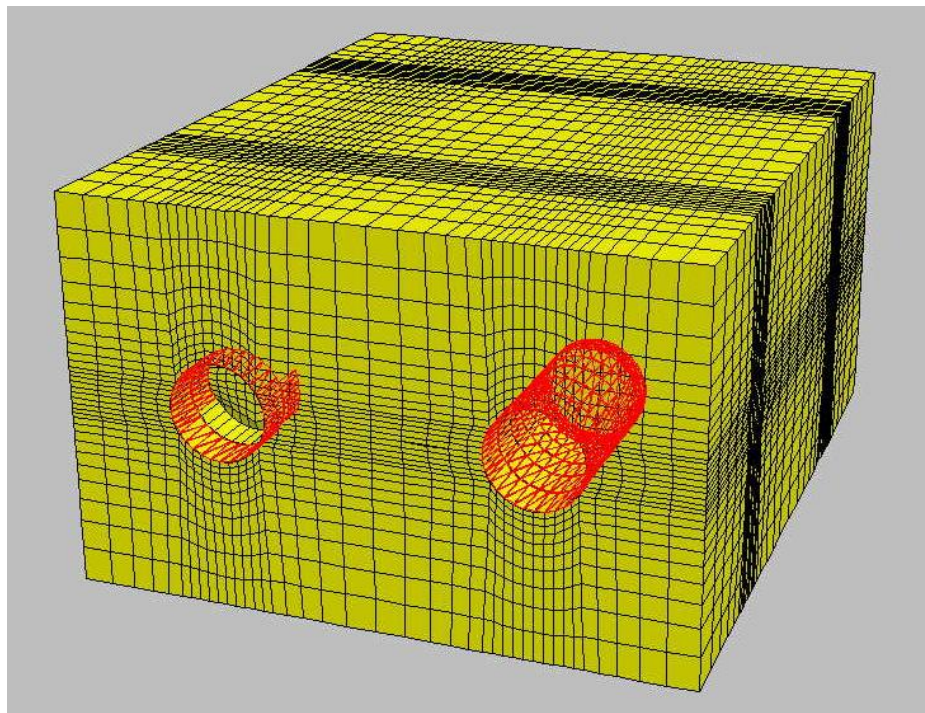
(d)

**Figure 4.13 cont'd.** c) removal of permanent lining at segment 2, d) installation of permanent lining at segment 3,





(e)



(f)

**Figure 4.13 cont'd.** e) installation of permanent lining at segment 2, f) installation of temporary lining at segment 4.

The pre-support concrete and shotcrete (temporary) and the concrete (permanent) tunnel linings are modeled with shell structural elements. The *FLAC 3D* zones provide a reasonable approximation for bending of thick liners, because each zone consists of two overlays of five tetrahedral sub-zones. The lining components are modeled as elastic materials with the following material properties:

(a) pre-support concrete and shotcrete (temporary)

Young's modulus,  $E = 7.1 \text{ GPa}$

Poisson's ratio,  $\nu = 0.15$

Thickness,  $t = 35 \text{ cm}$

(b) concrete liner (permanent)

Young's modulus,  $E = 28.5 \text{ GPa}$

Poisson's ratio,  $\nu = 0.15$

Thickness,  $t = 40 \text{ cm}$

A total of ninety nine sequential excavation and support steps were performed to simulate construction of main tunnels. Each construction step is run for 1000 cycles to reach an equilibrium state, and requires approximately 15 minutes to reach equilibrium. The total computation time was more than 24 hours for just one trial to simulate construction of main tunnels.

#### **4.6. Deformation measurements**

Recorded deformation measurements were supplied by GÜRİŞ Construction and Engineering Co. Inc. and illustrated in Appendix B. The locations of the surface deformation points are shown in Figure 4.14. Line 2 deformation points are considered for the purpose of correlation, since their measurement time range coincides with the exact construction time duration.

Maximum measured settlements above the tunnel axis at surface points 8, 9, 10, 11, 12, 13, 14, 15, 16, 17, 18, 19, 20 for line 2 tunnel were plotted against distance in Figure 4.15 and values were also tabulated in Table 4.4.

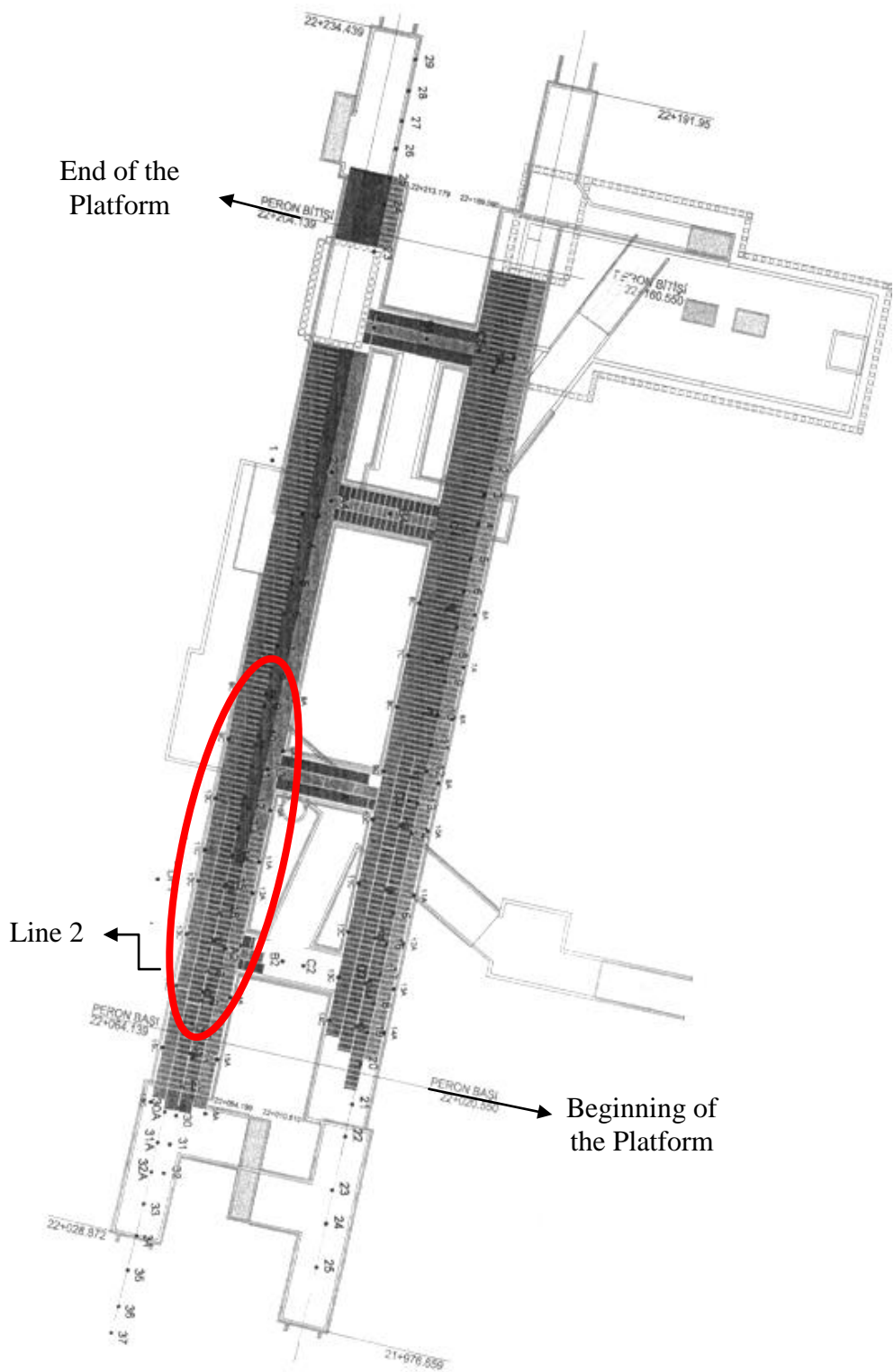


**Figure 4.14.** Locations of the surface deformation measurements points (red region includes surface deformation points 8 to 20 for Line 2 tunnel).



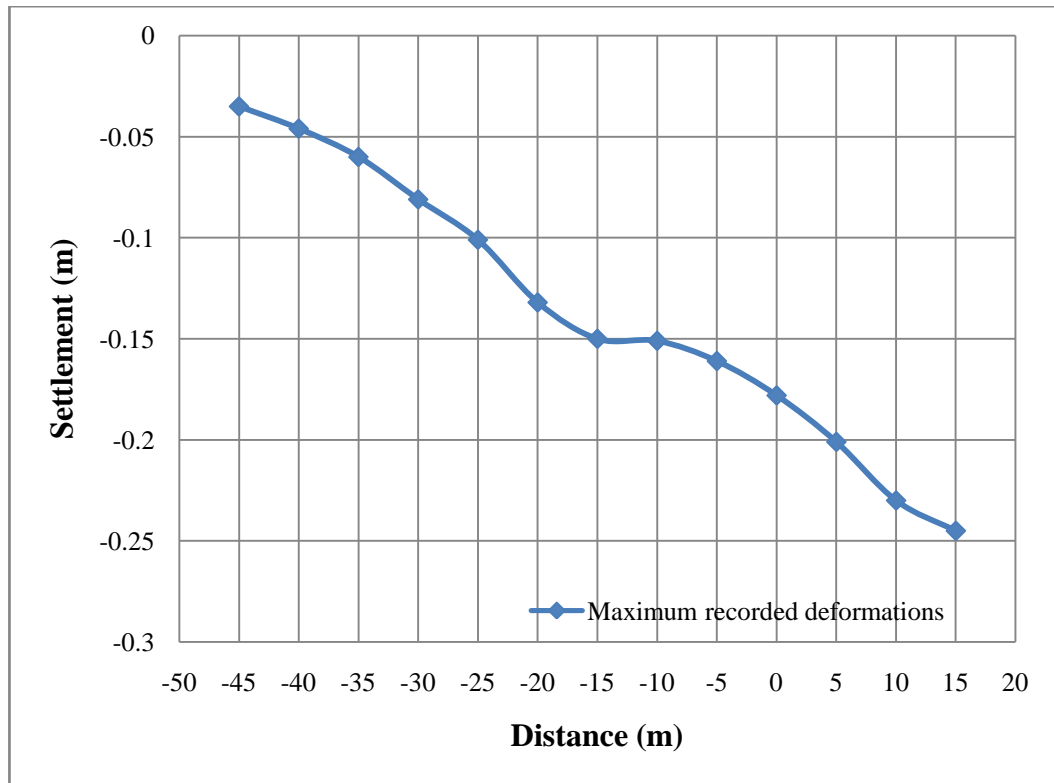


**Figure 4.15.** Maximum recorded settlements above the tunnel axis at surface points 8, 9, 10, 11, 12, 13, 14, 15, 16, 17, 18, 19, 20 for line 2 tunnel

**Table 4.4.** Maximum recorded settlement values above the Line 2 tunnel axis.

Settlement (m)	Distance (m)	Surface Point No.
-0,245	15	20
-0,23	10	19
-0,201	5	18
-0,178	0	17
-0,161	-5	16
-0,151	-10	15
-0,15	-15	14
-0,132	-20	13
-0,101	-25	12
-0,081	-30	11
-0,06	-35	10
-0,046	-40	9
-0,035	-45	8

#### 4.7. Results

Based on the maximum recorded deformation curves shown in Figure 4.15 numbers of numerical models were run using different material properties. The purpose was to obtain a fairly good matching curve with above one and to identify representative soil property values. Calibrated material properties were bulk modulus (K), shear modulus (G) and cohesion (c) for alluvium layers within the model. Although lots of curve were obtained during calibration phase the closest ones are shown in Figure 4.16 for Line 2 deformation values.

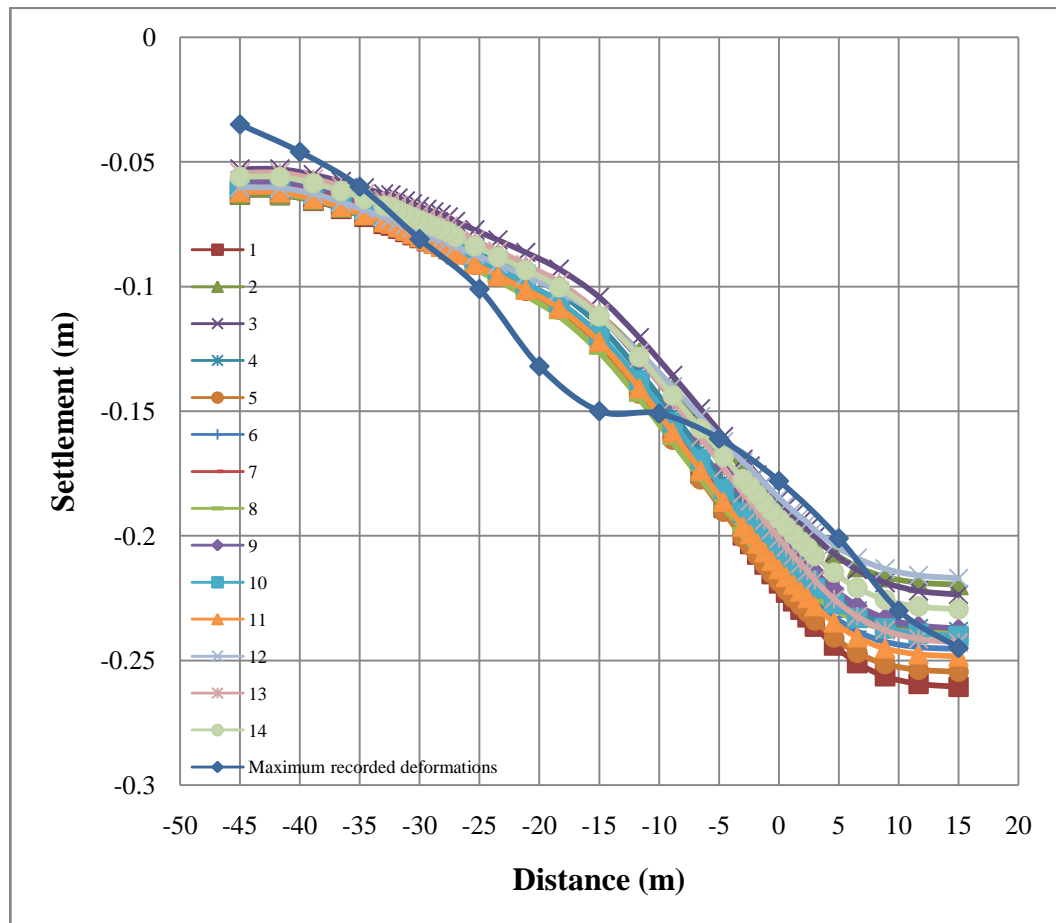


**Figure 4.16.** Different settlement curves obtained during calibration phase for Line 2 deformation values.

At this point, numerical results showed that changes in soil property values will not have significant effects on curve forms anymore since the value range permitting calibration is too small. That is why one of the curves should be selected at this point for the representative soil properties. By correlating closeness of the curves resulted from numerical analyses with recorded deformations measurement curve for Line 2 tunnel and considering their linear correlation curves it was decided to use curve number 8 presented in Figure 4.17.

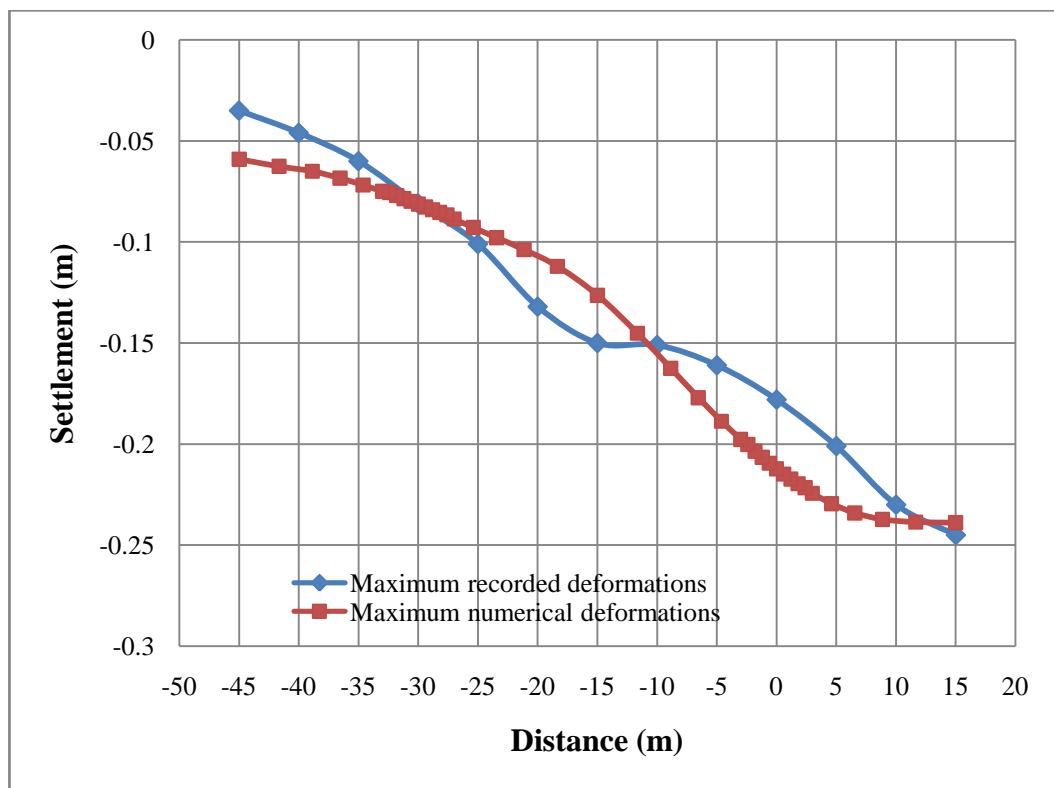


**Figure 4.17.** Correlation of recorded deformations and numerical analyses results for Line 2 tunnel.

This curve actually represents the numerical results run for representative construction stages to capture the maximum settlement values with the calibrated soil properties tabulated in Table 4.5.

**Table 4.5.** Calibrated soil properties used to obtain curve 8.

Property	Values				
	Fill	qa1	qa2	qa3	Tg
Bulk Modulus (kPa)	$12.5 \times 10^3$	$4.17 \times 10^6$	$3.77 \times 10^6$	$4.37 \times 10^6$	$64 \times 10^4$
Shear Modulus (kPa)	$6.0 \times 10^3$	$84 \times 10^3$	$76 \times 10^3$	$88 \times 10^4$	$16.6 \times 10^3$
Cohesion (kPa)	70	89.2	80.8	93.5	200
Friction angle (degree)	1	1	1	1	1
Density (kg/m <sup>3</sup> )	1800	1900	1900	1900	1900

Maximum vertical settlement values (z-displacements) along with distance in y-direction to form curve 8 were also tabulated in Table 4.6.

**Table 4.6.** Maximum z-displacement values along with distance in y-direction to form curve 8.

Settlement (m)	Distance (m)
-0,23884	15
-0,23859	11,656
-0,23725	8,8697
-0,23409	6,5476
-0,22952	4,6126
-0,22433	3
-0,2216	2,4
-0,21955	1,8
-0,21727	1,2
-0,21481	0,6
-0,21221	0
-0,20946	-0,6
-0,20656	-1,2
-0,2035	-1,8
-0,2002	-2,4
-0,1976	-3
-0,18869	-4,6126
-0,17707	-6,5476
-0,16248	-8,8697

**Table 4.6 cont'd**

-0,14514	-11,656
-0,12634	-15
-0,11204	-18,344
-0,10381	-21,13
-0,097855	-23,452
-0,092854	-25,387
-0,088601	-27
-0,08653	-27,6
-0,085327	-28,2
-0,08402	-28,8
-0,082665	-29,4
-0,081288	-30
-0,079902	-30,6
-0,078503	-31,2
-0,077072	-31,8
-0,075557	-32,4
-0,074891	-33
-0,071837	-34,613
-0,068405	-36,548
-0,065002	-38,87
-0,062583	-41,656
-0,059048	-45

Graphical numerical results were also represented in Figure 4.18 through Figure 4.39 for different construction stages. These graphs visualize the total displacement contours (in z-direction) due to the process of excavation. The variations in z-displacement (vertical) can be easily noticed with elapsed stages in these contour plots. In Figures, red crosses indicate support lining while colorful contours indicating z-displacement values. As shown from the figures maximum z-displacement is increasing continuously from  $2.1545 \times 10^{-2}$  m to  $3.500 \times 10^{-1}$  m because of proceeded excavation. It should also be stated that before excavation work started, the model was stepped to equilibrium under gravitational loading and then displacements in all directions were set to zero.

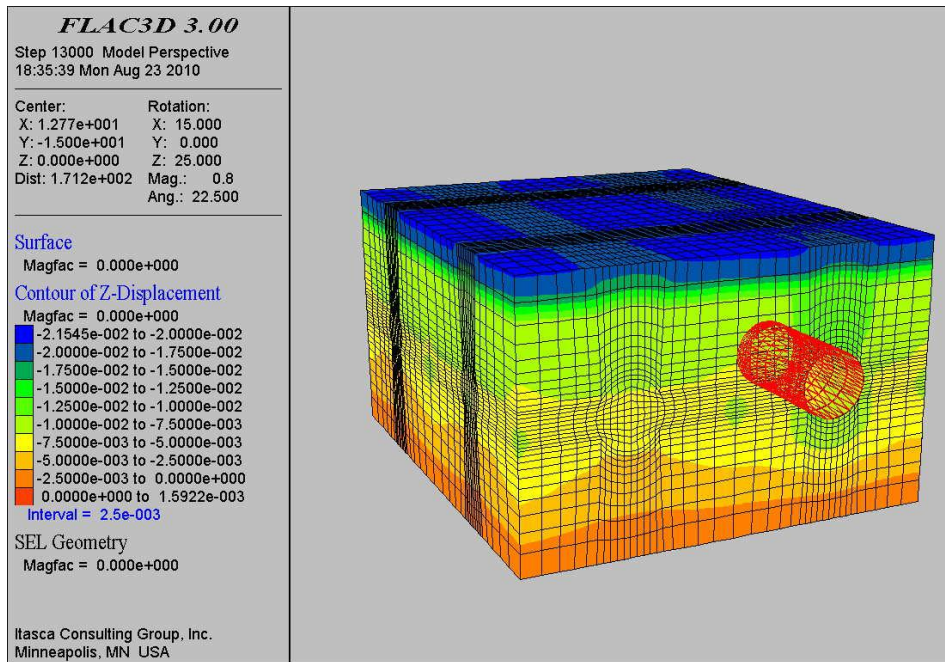


**Figure 4.18.** 15 m excavation and support of Line 2 tunnel.

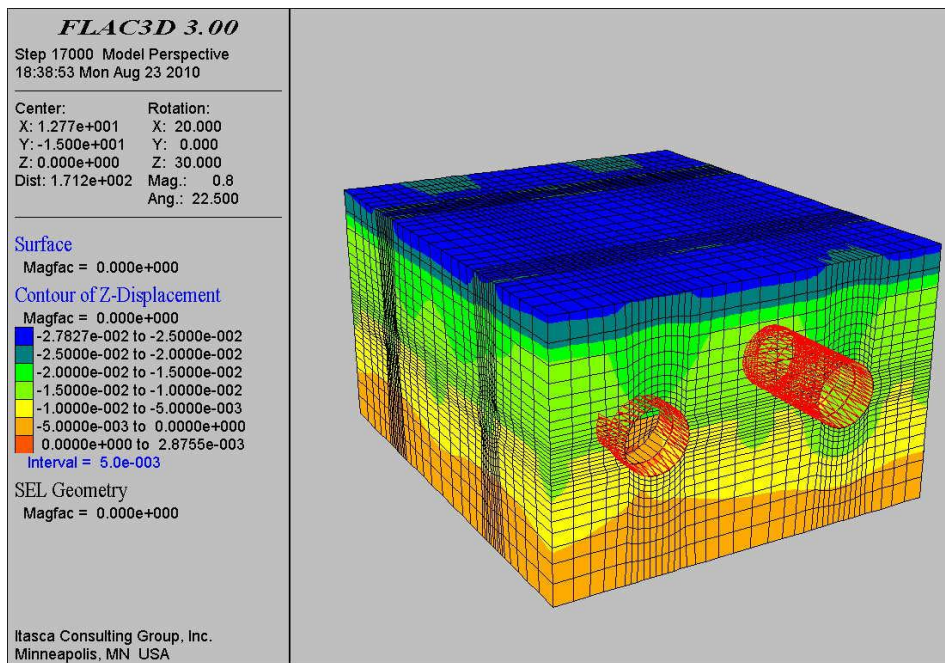


**Figure 4.19.** 15 m excavation and support of Line 2 tunnel, 5 m excavation and support of Line 1 tunnel.

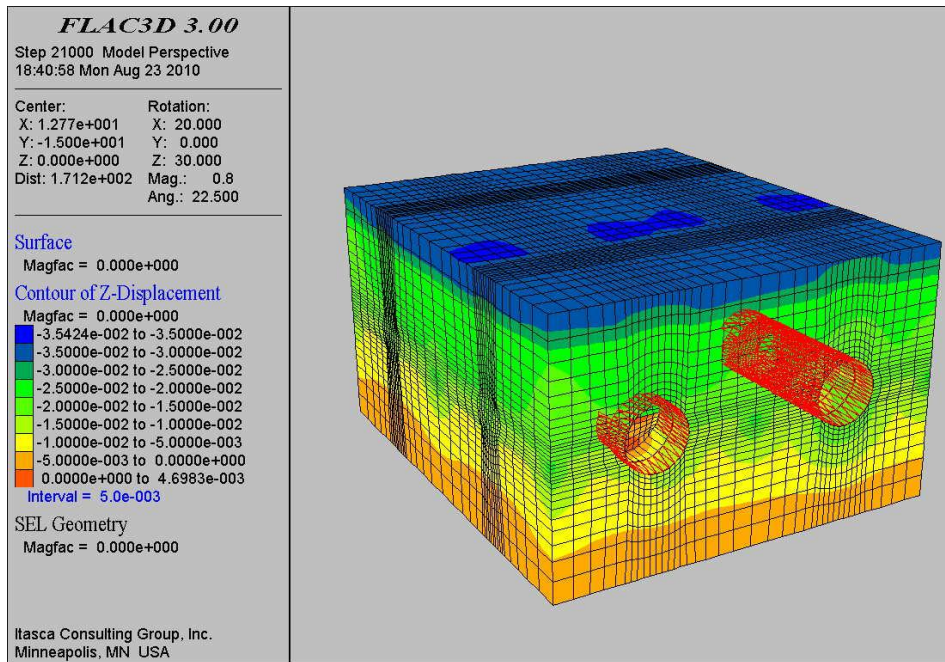


**Figure 4.20.** 20 m excavation and support of Line 2 tunnel, 5 m excavation and support of Line 1 tunnel.

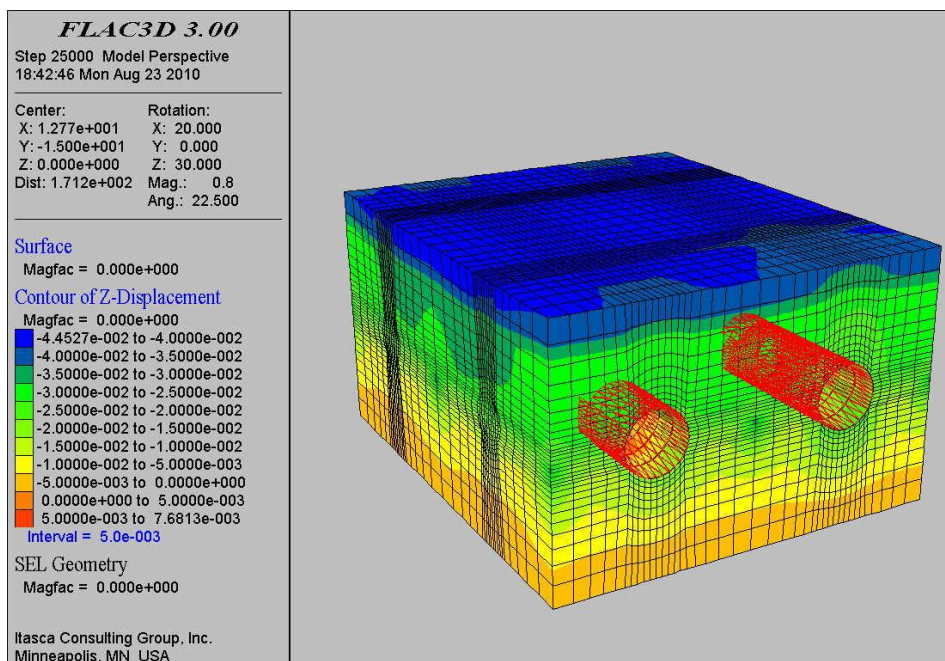


**Figure 4.21.** 20 m excavation and support of Line 2 tunnel, 10 m excavation and support of Line 1 tunnel.



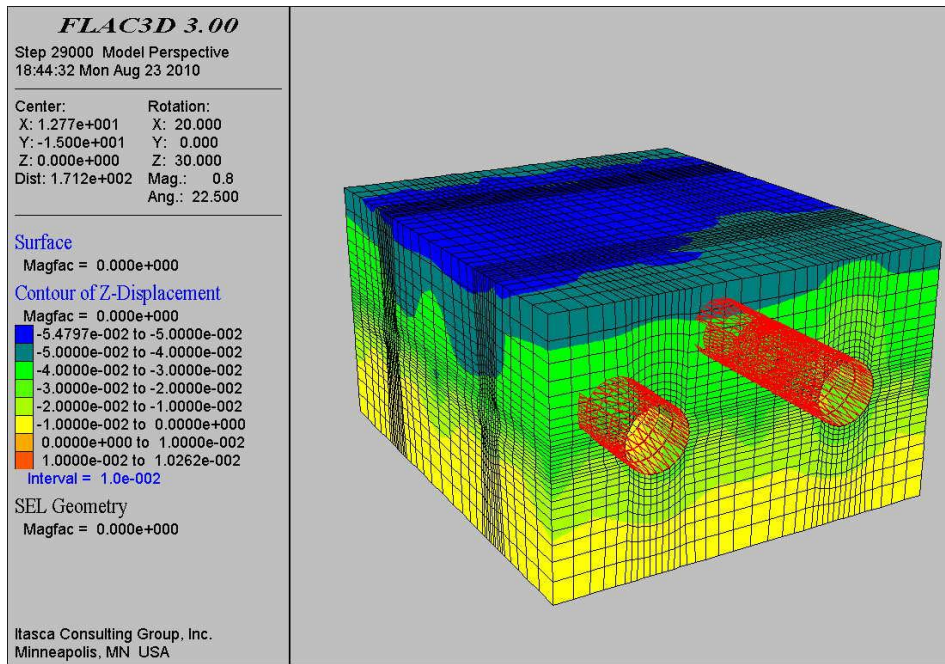


**Figure 4.22.** 25 m excavation and support of Line 2 tunnel, 10 m excavation and support of Line 1 tunnel.

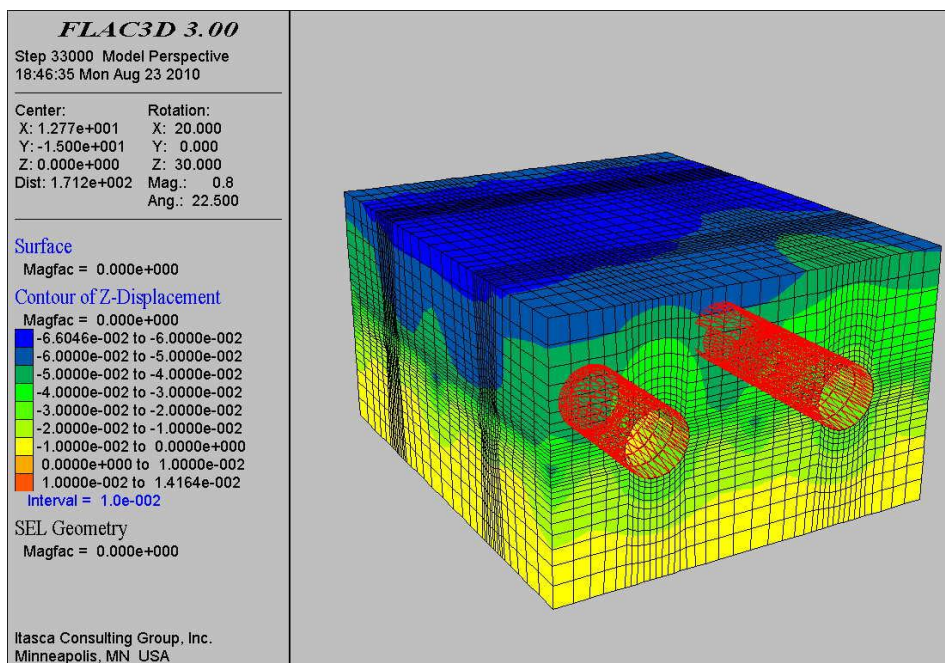


**Figure 4.23.** 25 m excavation and support of Line 2 tunnel, 15 m excavation and support of Line 1 tunnel.

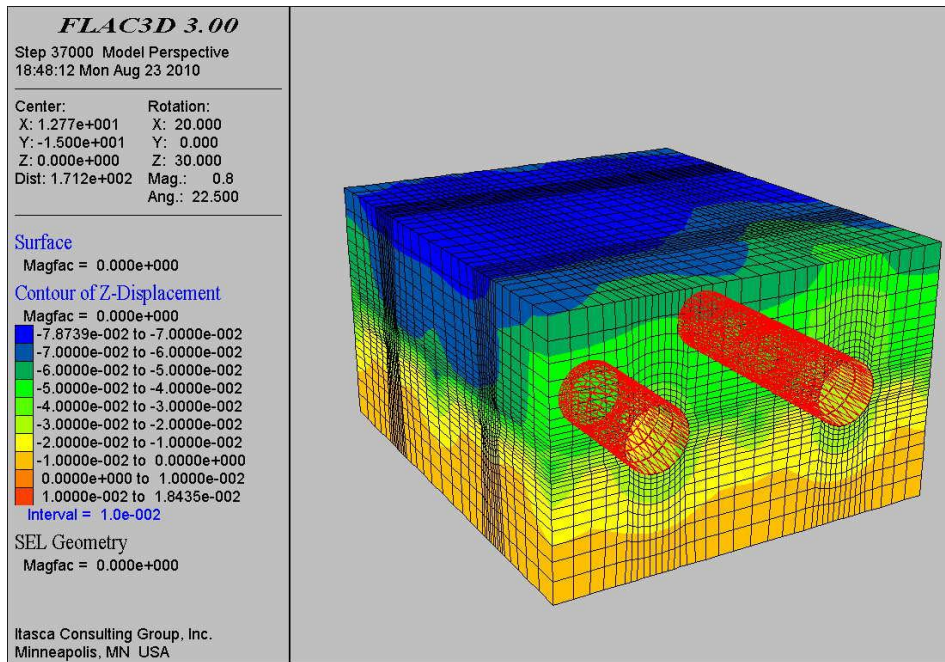


**Figure 4.24.** 30 m excavation and support of Line 2 tunnel, 15 m excavation and support of Line 1 tunnel.

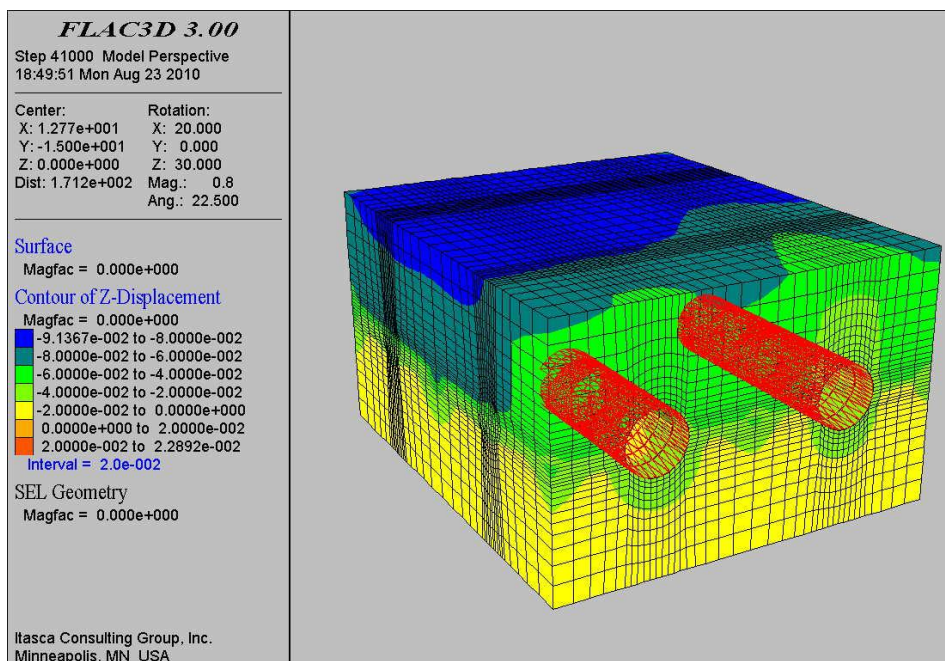


**Figure 4.25.** 30 m excavation and support of Line 2 tunnel, 20 m excavation and support of Line 1 tunnel.



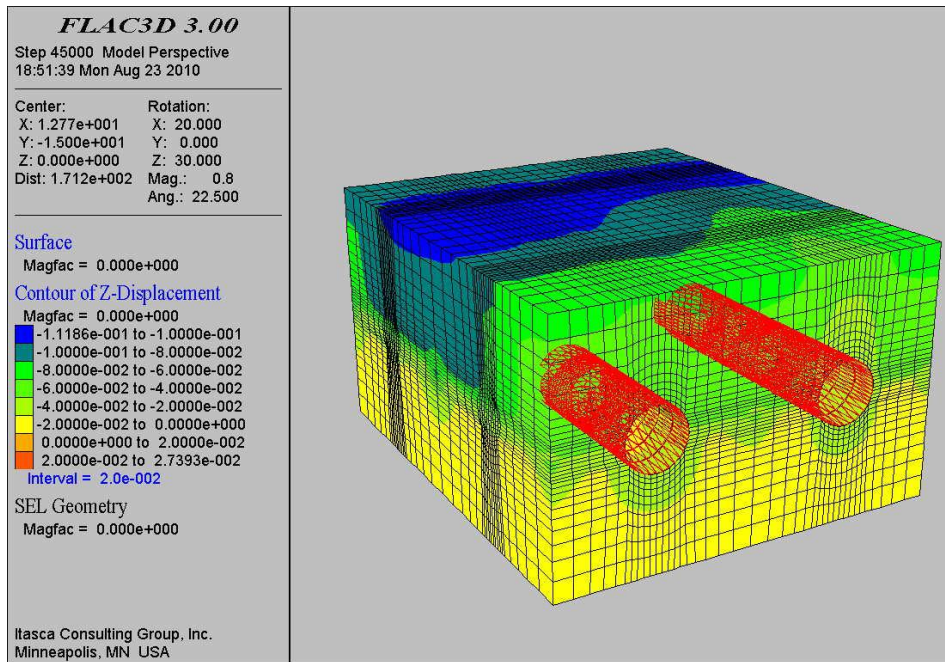


**Figure 4.26.** 35 m excavation and support of Line 2 tunnel, 20 m excavation and support of Line 1 tunnel.

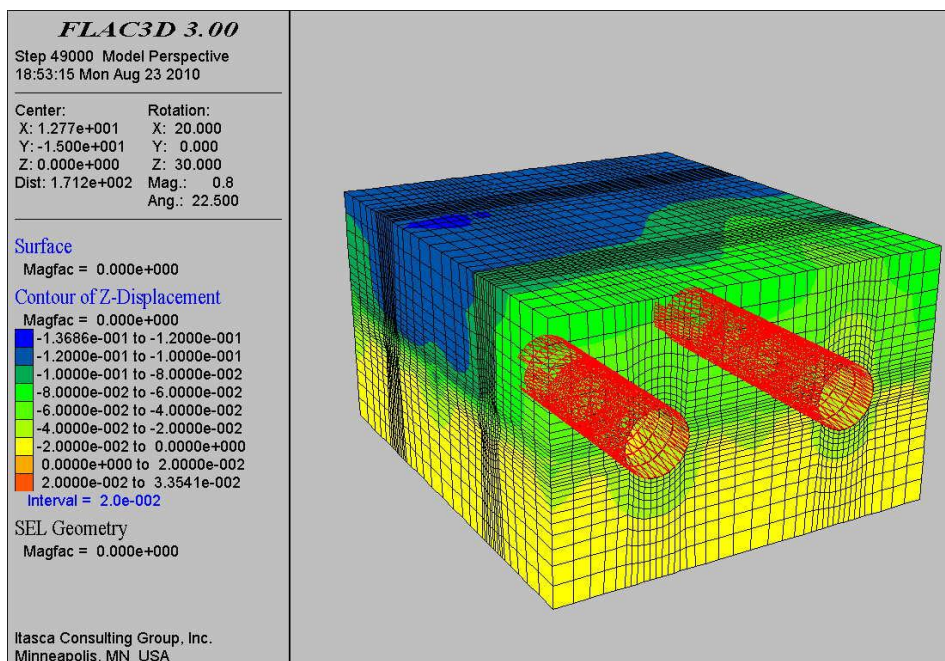


**Figure 4.27.** 35 m excavation and support of Line 2 tunnel, 25 m excavation and support of Line 1 tunnel.

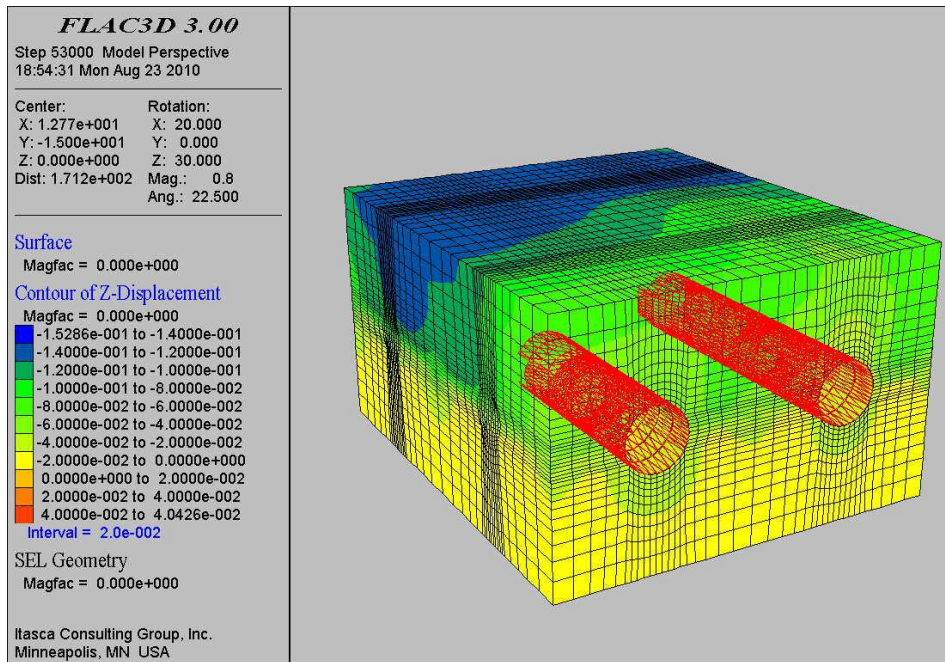


**Figure 4.28.** 40 m excavation and support of Line 2 tunnel, 25 m excavation and support of Line 1 tunnel.

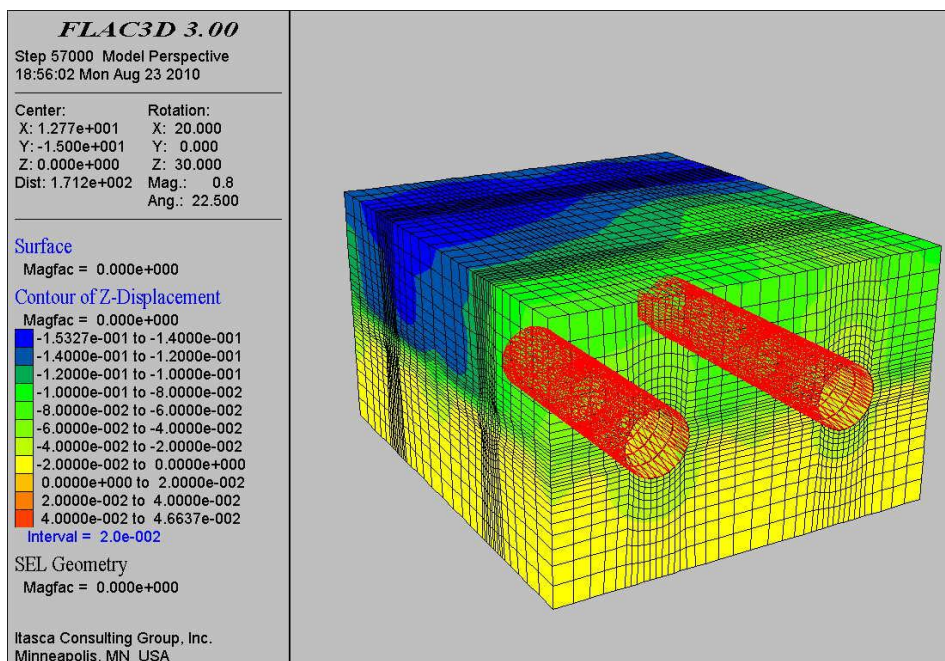


**Figure 4.29.** 40 m excavation and support of Line 2 tunnel, 30 m excavation and support of Line 1 tunnel.



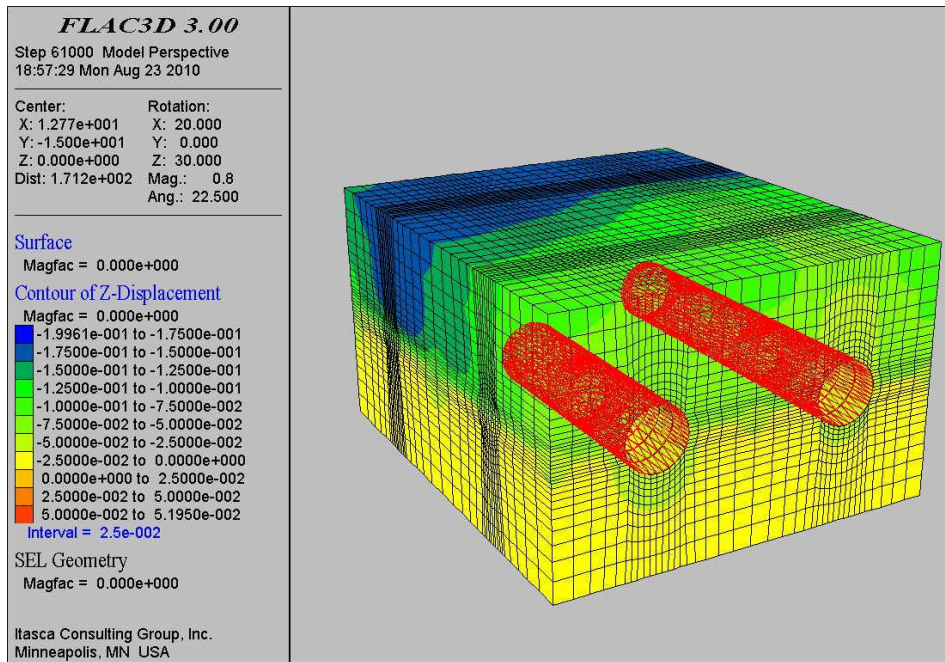


**Figure 4.30.** 45 m excavation and support of Line 2 tunnel, 30 m excavation and support of Line 1 tunnel.

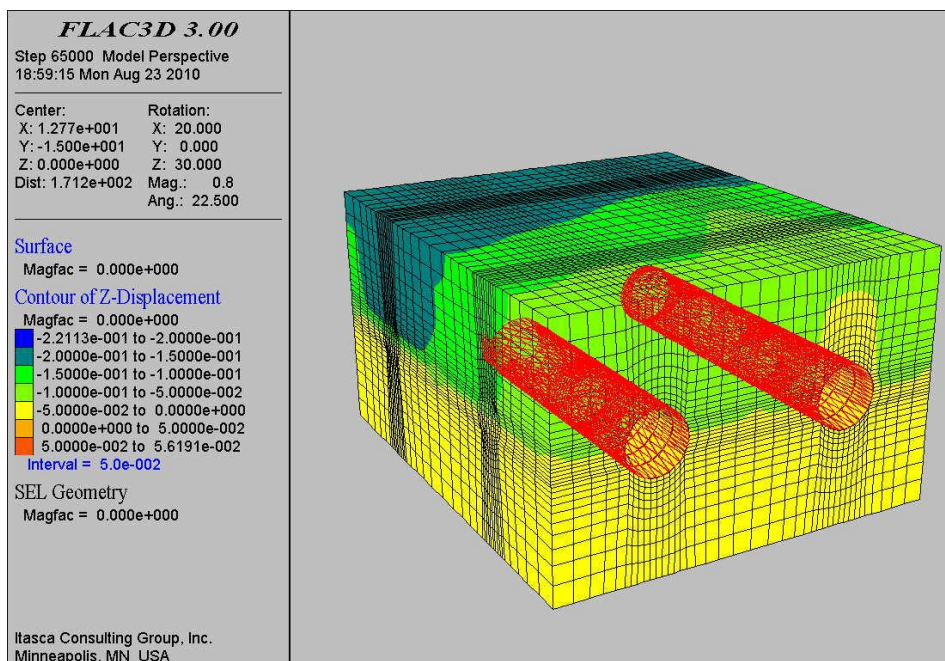


**Figure 4.31.** 45 m excavation and support of Line 2 tunnel, 35 m excavation and support of Line 1 tunnel.

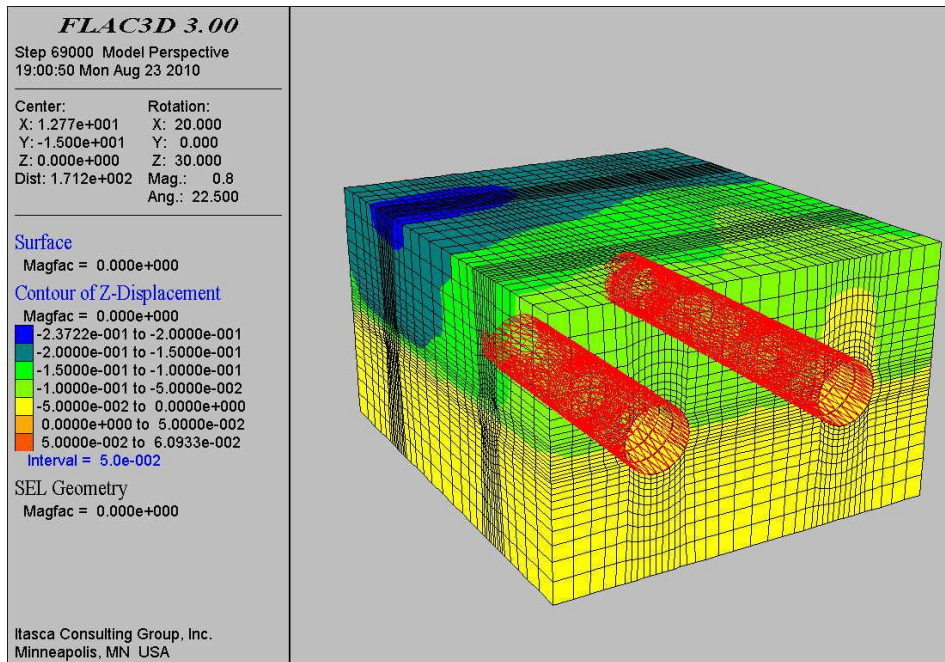


**Figure 4.32.** 50 m excavation and support of Line 2 tunnel, 35 m excavation and support of Line 1 tunnel.

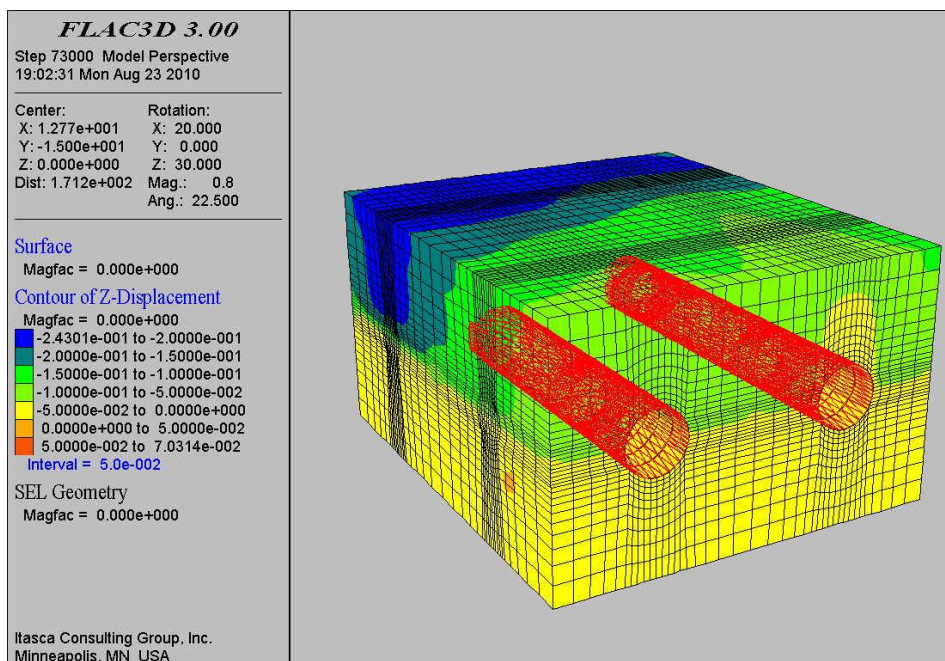


**Figure 4.33.** 50 m excavation and support of Line 2 tunnel, 40 m excavation and support of Line 1 tunnel.



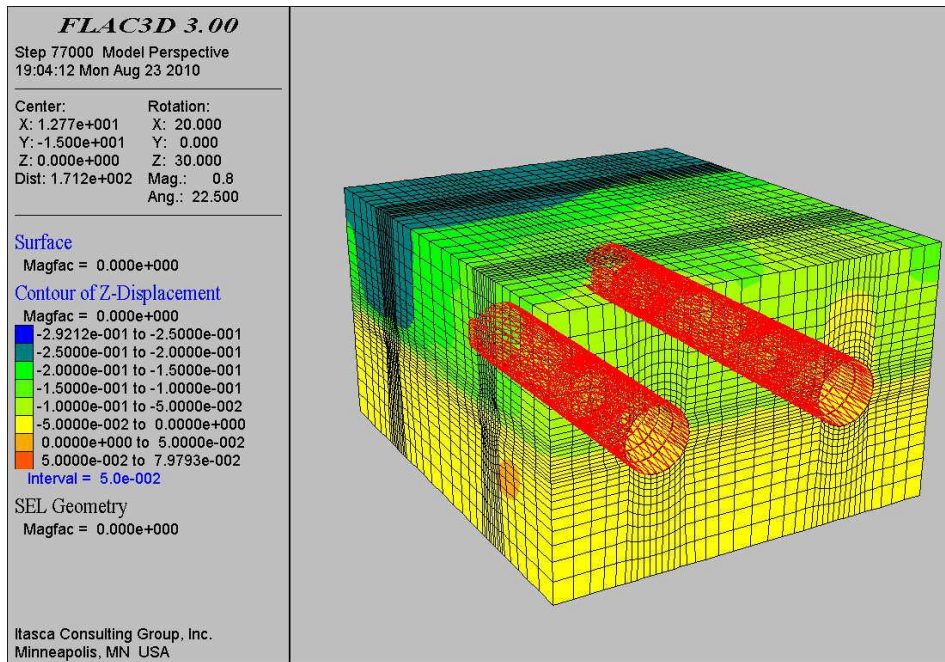


**Figure 4.34.** 55 m excavation and support of Line 2 tunnel, 40 m excavation and support of Line 1 tunnel.

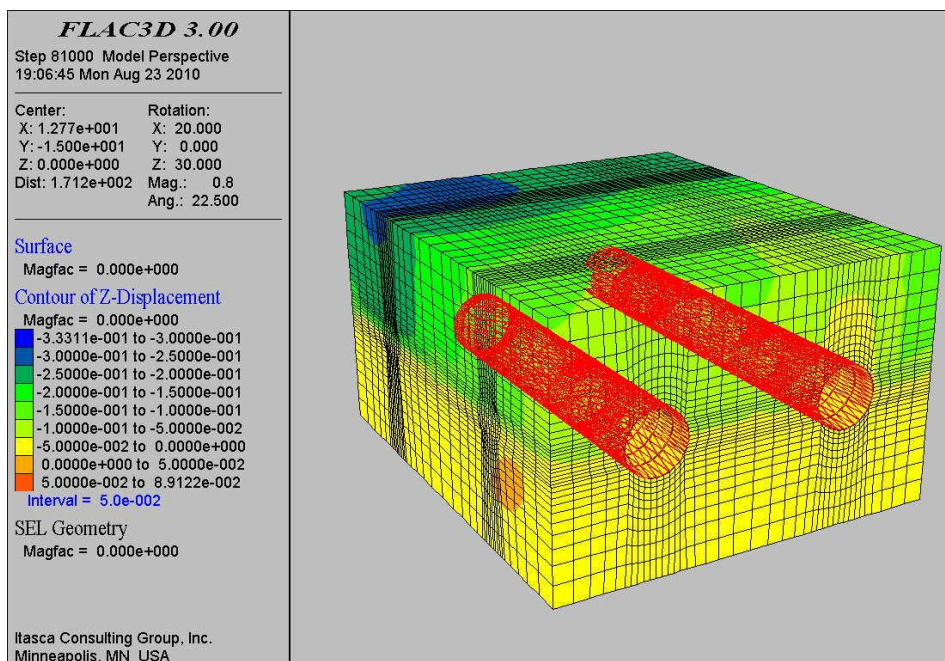


**Figure 4.35.** 55 m excavation and support of Line 2 tunnel, 45 m excavation and support of Line 1 tunnel.



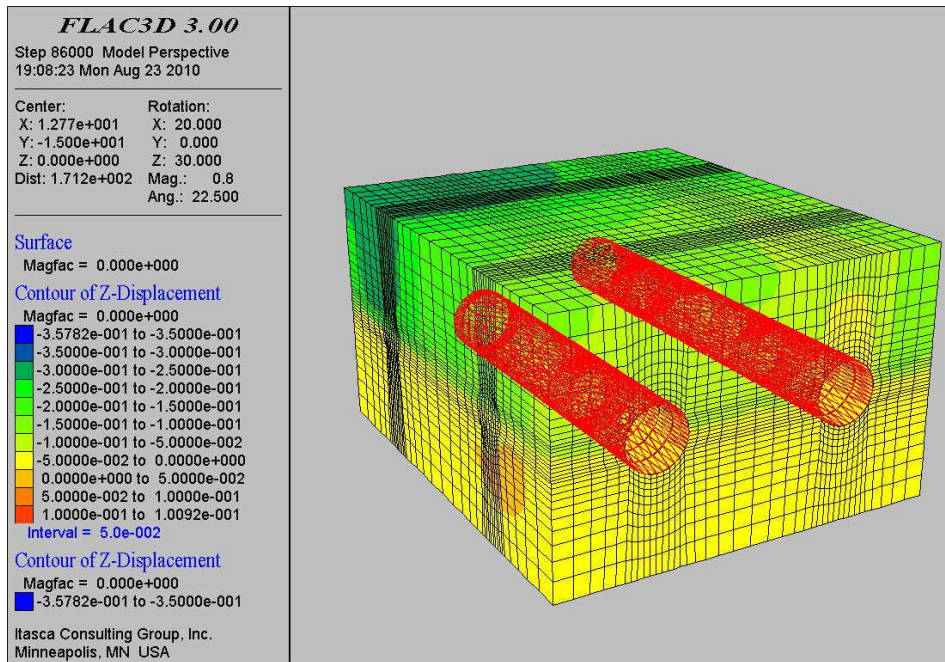


**Figure 4.36.** 60 m excavation and support of Line 2 tunnel, 45 m excavation and support of Line 1 tunnel.

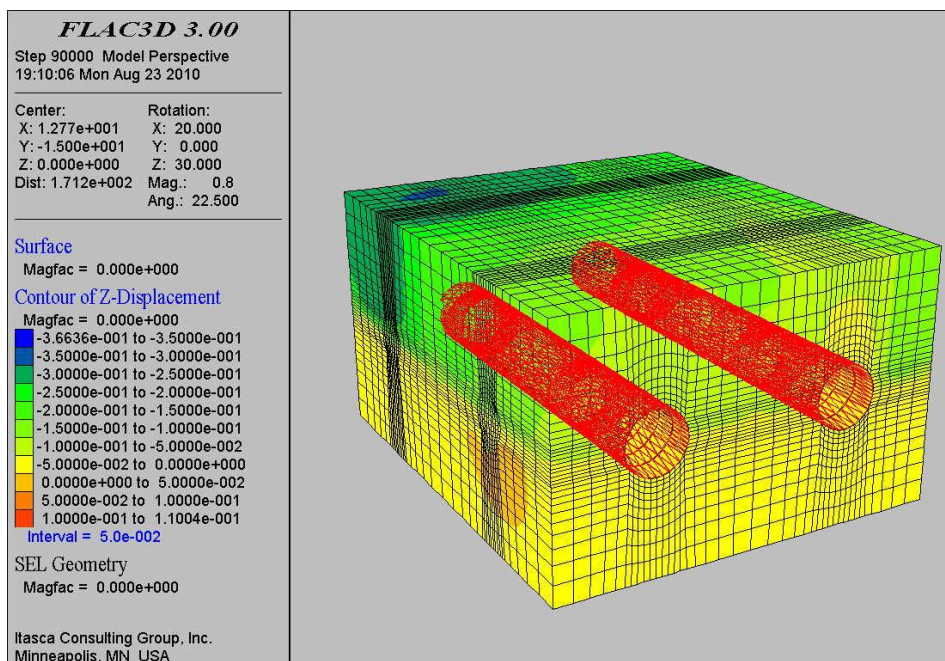


**Figure 4.37.** 60 m excavation and support of Line 2 tunnel, 50 m excavation and support of Line 1 tunnel.

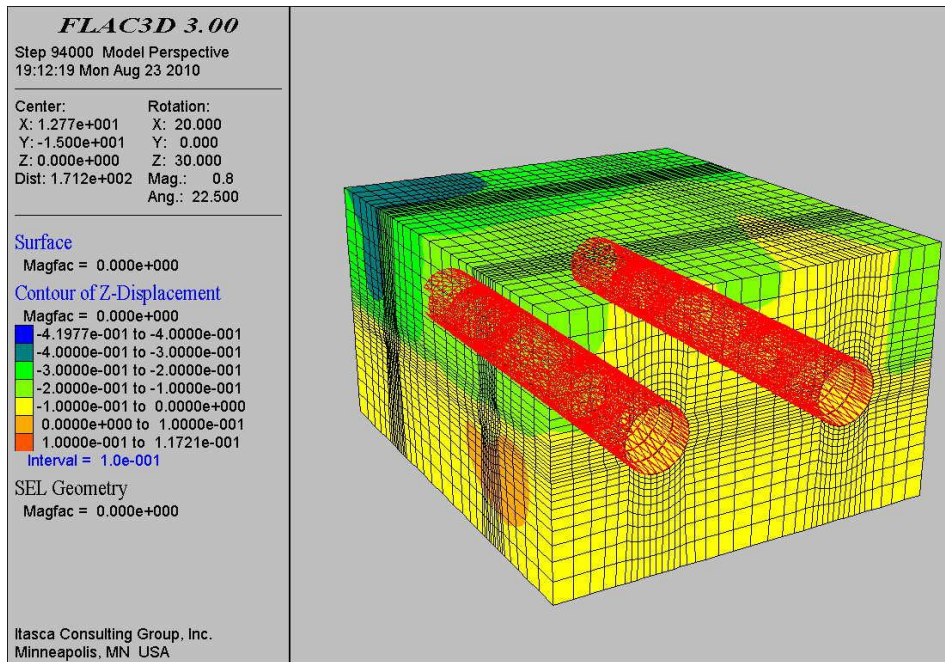


**Figure 4.38.** 60 m excavation and support of Line 2 tunnel, 55 m excavation and support of Line 1 tunnel.

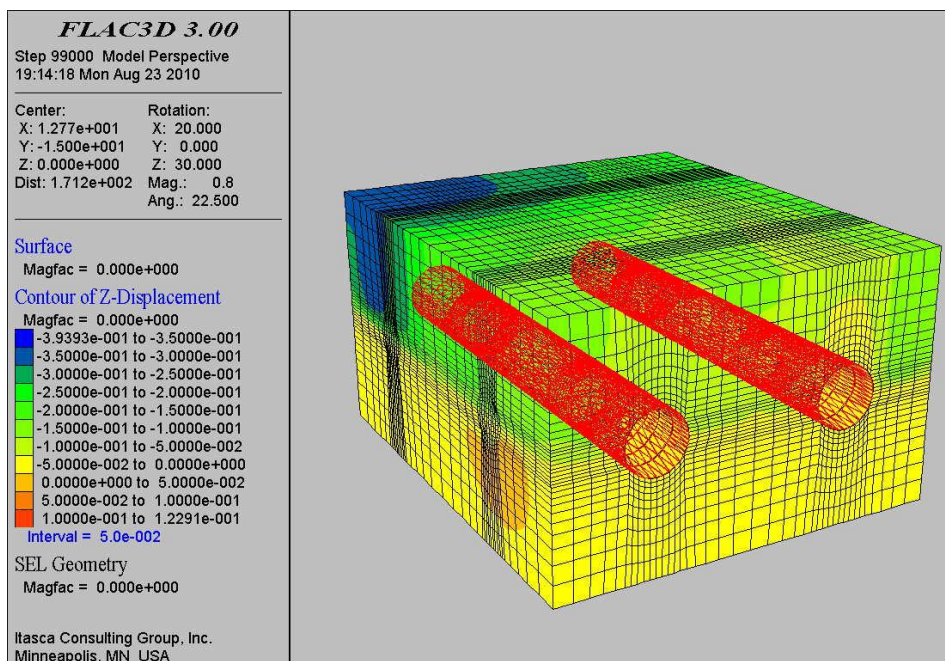


**Figure 4.39.** 60 m excavation and support of Line 2 tunnel, 60 m excavation and support of Line 1 tunnel.

## CHAPTER 5

### EFFECTS OF CONNECTION TUNNEL EXCAVATIONS ON GROUND DEFORMATIONS

#### 5.1. Introduction

In this chapter, the ground deformations at the Ankara Subway System of Necatibey Station and its close vicinity due to the mechanical excavation of connection tunnels have been investigated by utilizing 3-dimensional numerical models.

It is, actually, a follow up study to previous chapter. That is why 3-dimensional numerical modeling concept is the same as described in the previous chapter. In this chapter primary aim is to discover effects of excavation of connection tunnels on each other and also on the newly excavated and supported main tunnels.

In order to simulate mechanical excavation of connection tunnels the same models used in Chapter 4 were further run and resultant ground deformations were considered. Deformations occurred on connection tunnel axes after each connection tunnel excavation were investigated firstly. Effects of connection tunnel excavations on each other in terms of deformations were also correlated. Then deformations taking place on main tunnel axes because of connection tunnels excavations were investigated. Correlations between the effects of connection 1 tunnel excavation on main tunnels and the effects of connection 2 tunnel excavation on main tunnels were also supplied.

Firstly, very short information about step by step procedure will be mentioned about numerical modeling concept, then, construction stages will be illustrated

using screen captures from the *FLAC 3D* code. Finally, in the results section numerical model results and graphs showing correlation between deformations occurred on different tunnel axes due to the connection tunnel excavations will be given.

## **5.2. Steps towards numerical models**

For the geometry of the problem Figures 4.2, 4.3 and 4.4 can be referred. From those figures position of the connection tunnels and their configuration with main tunnels can be easily seen. There is about 30 m distance between the two connection tunnel axes and each tunnel is 6 m in diameter.

Constitutive behavior is still the same as the Mohr-Coulomb model. For the Mohr-Coulomb plasticity model, the required properties are: bulk,  $K$ , and shear,  $G$ , moduli; friction angles,  $\phi$ , and cohesion,  $c$ . Table 4.5 can be reviewed for the value of these parameters.

Real and artificial boundaries can be deduced from Figure 4.5. As seen, roller boundaries were placed on four sides of the model while bottom boundary is fixed in all directions.

Several assumptions adopted for improving the analysis by means of practicality, flexibility and precision were listed in section 4.4 and there is no additional assumption is required.

## **5.3. Construction stages**

This chapter investigates only ground deformations induced by mechanical excavation of connection tunnels. That is why the deformations result from the excavation of main tunnels were set to zero just before the excavations of connection tunnels started.

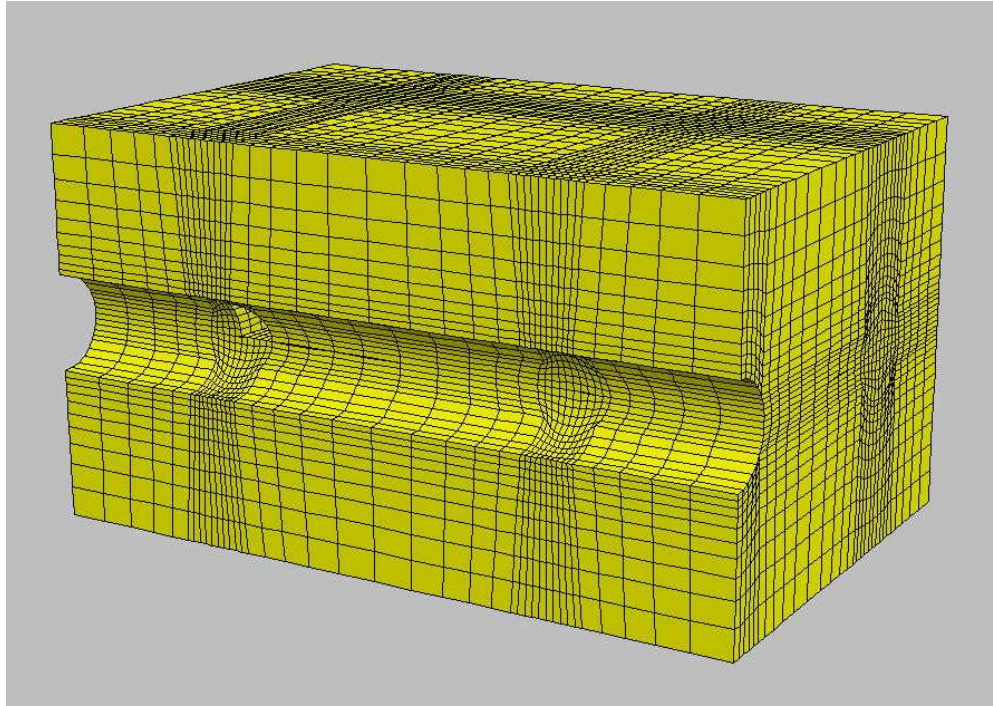
Connection tunnels were excavated in the direction from Line 1 tunnel to Line 2 tunnel and Table 5.1 summarizes excavation stages for all excavation processes conducted on connection tunnels.

**Table 5.1.** Excavation stages for connection tunnels.

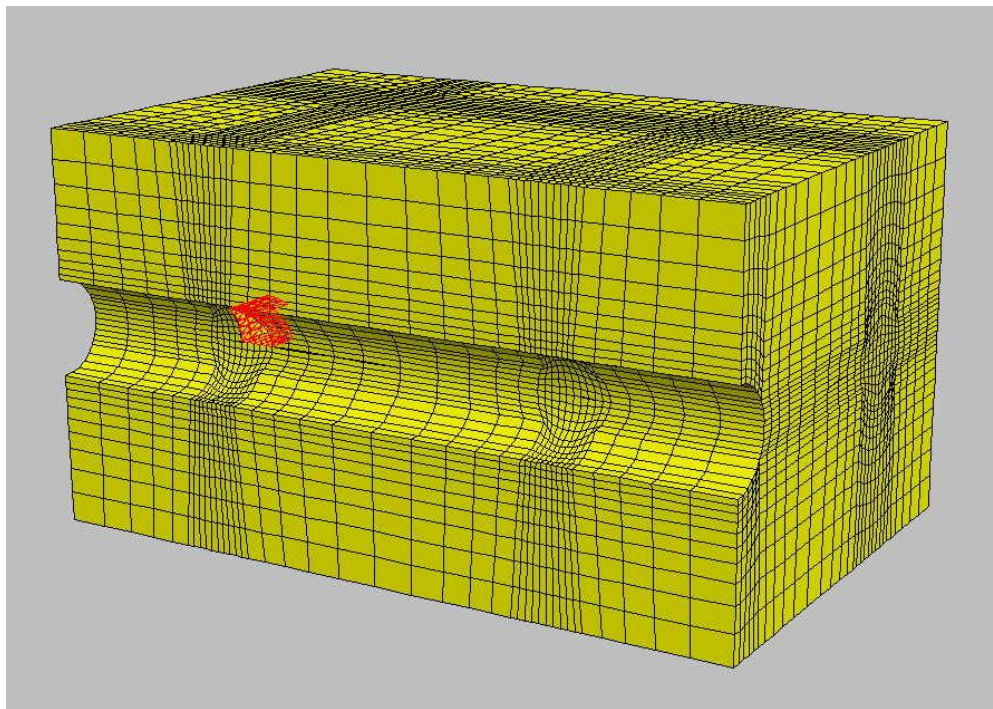
<b>Stage</b>	<b>Connection 1</b>	<b>Connection 2</b>
1	7 m excavation (0-7)	7 m excavation (0-7)
2	4 m excavation (7-11)	4 m excavation (7-11)
3	4 m excavation (11-15)	4 m excavation (11-15)
4	4 m excavation (15-19)	4 m excavation (15-19)
5	4.5 m excavation (19-23.5)	4.5 m excavation (19-23.5)

When excavating connection tunnels, partial face excavation has been modeled rather than full face excavation. Three different segments were adopted for each connection tunnel and temporary and permanent shotcrete lining support was modeled. Excavation and support sequence are shown in Figure 5.1 through Figure 5.4. The section given in the figures crosses Line 1 tunnel axis.





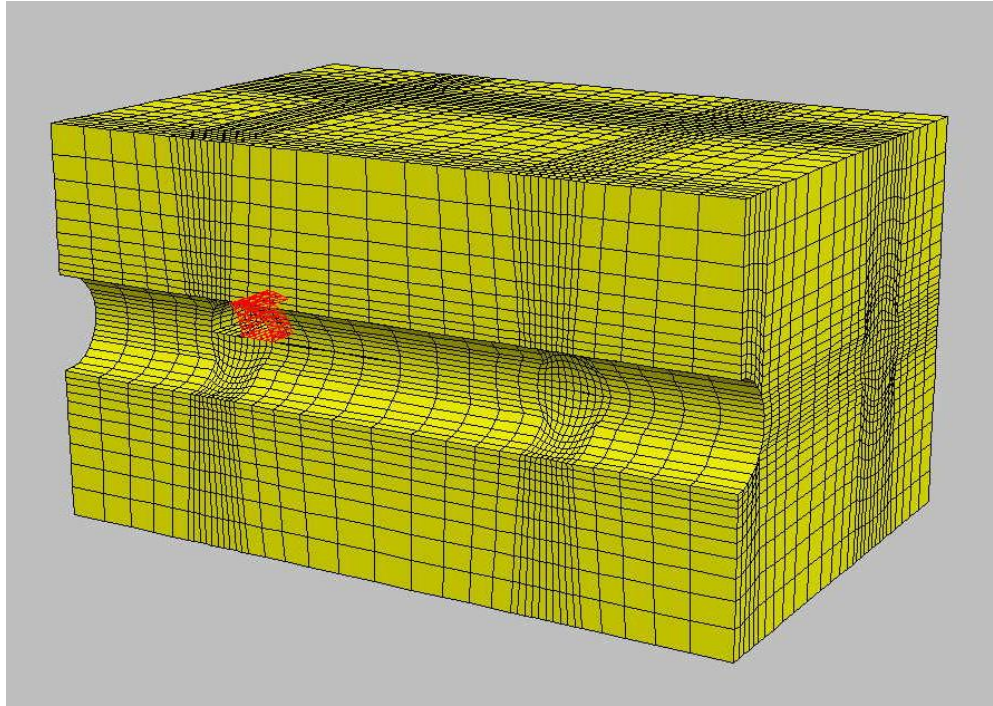
(a)



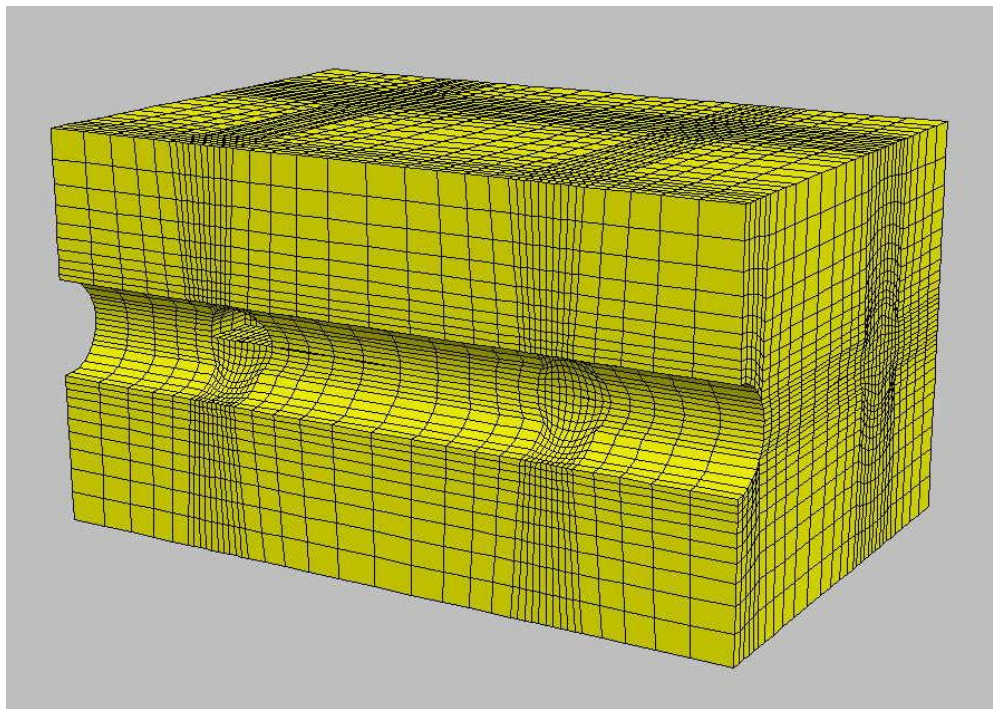
(b)

**Figure 5.1.** Step 1; a) excavation of upper inner part, b) installation of temporary lining to upper inner part.





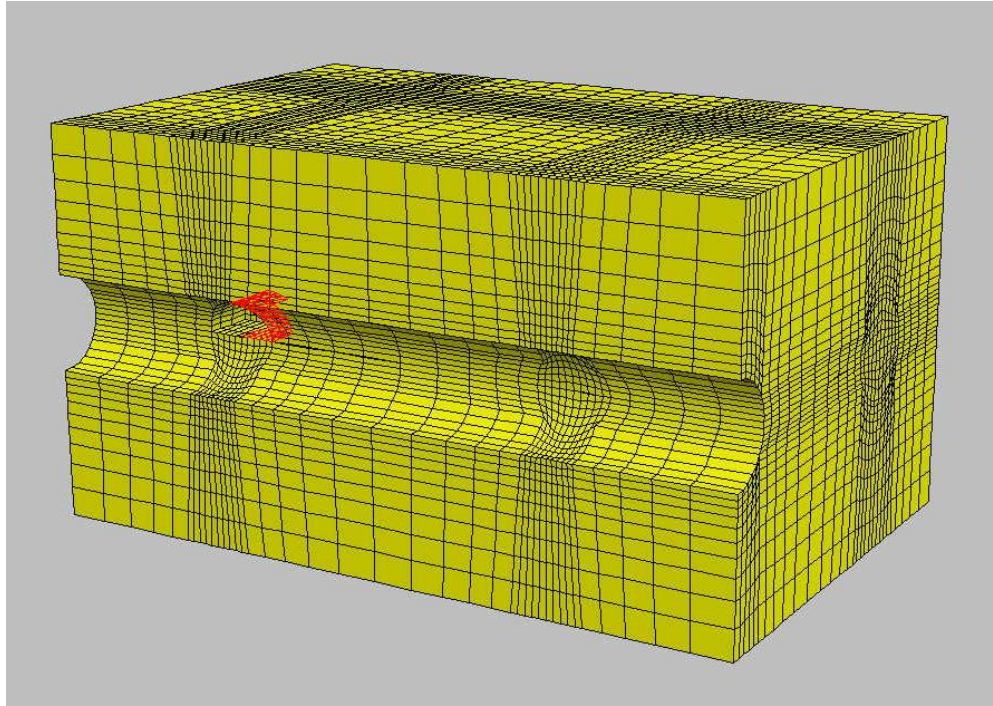
(a)



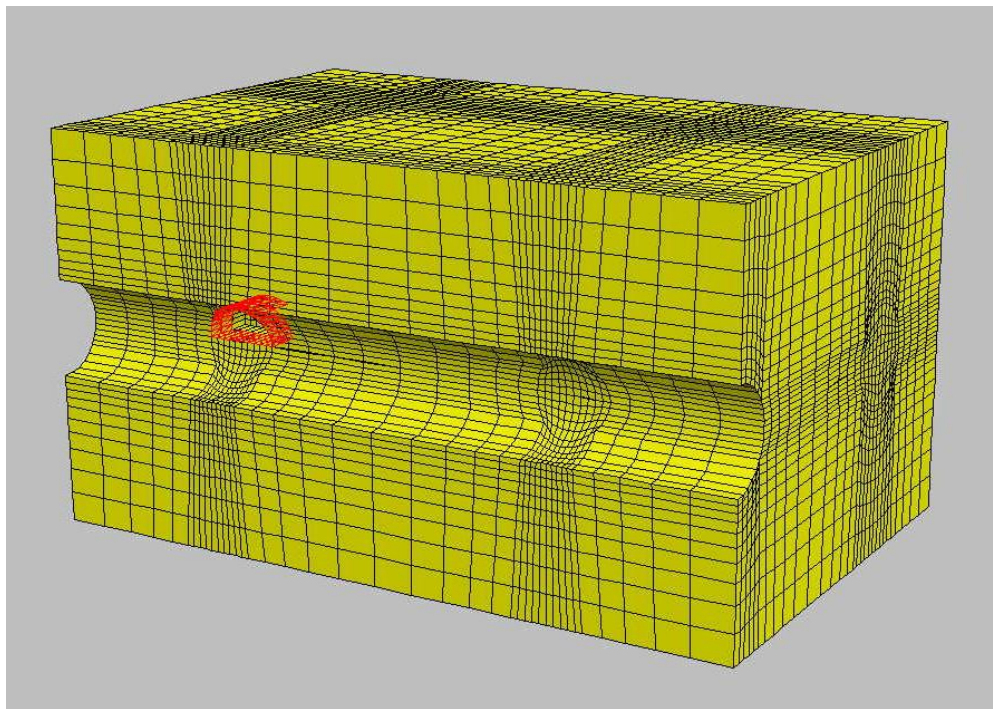
(b)

**Figure 5.2.** Stage 2; a) excavation of upper outer part, b) removal of temporary lining from upper inner part,





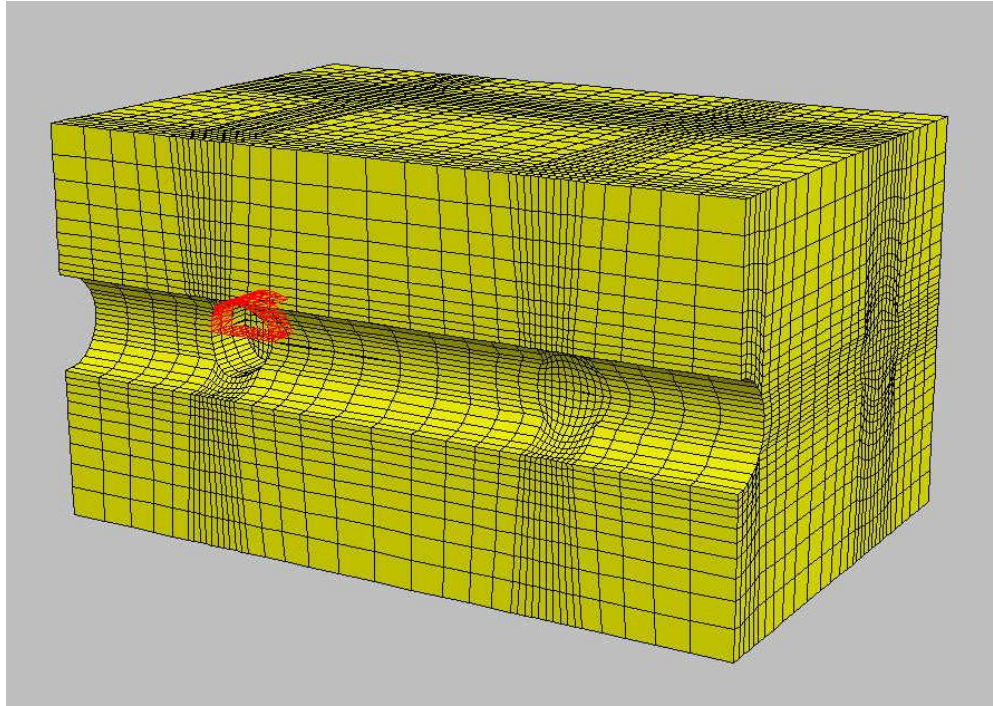
(c)



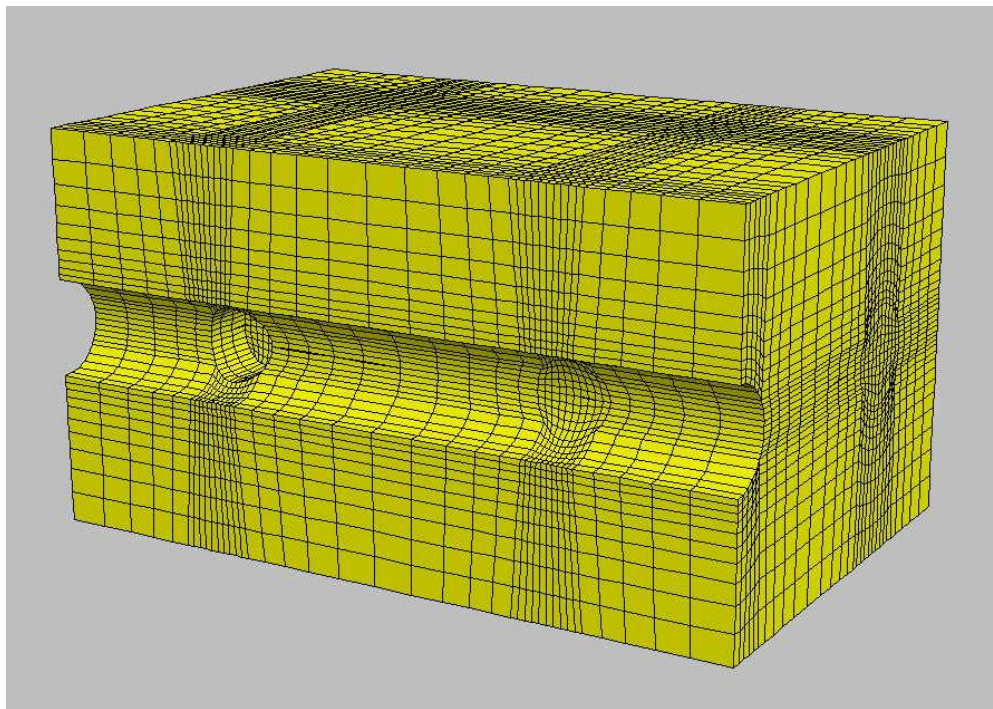
(d)

**Figure 5.2 cont'd.** c) installation of permanent lining to upper inner part, d) installation of temporary lining to upper outer part.





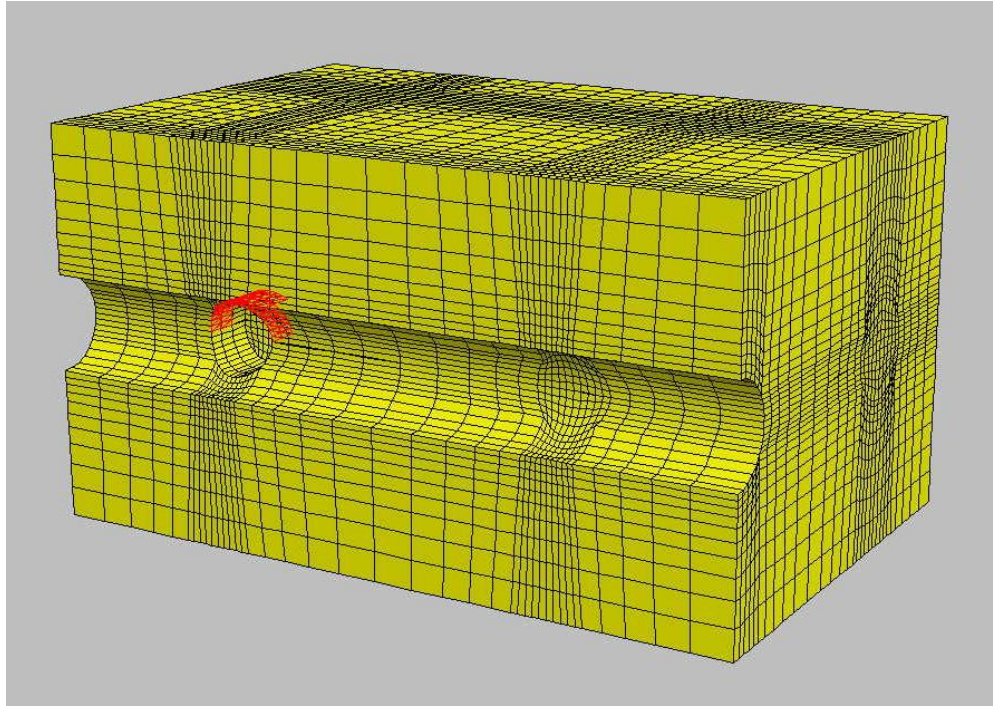
(a)



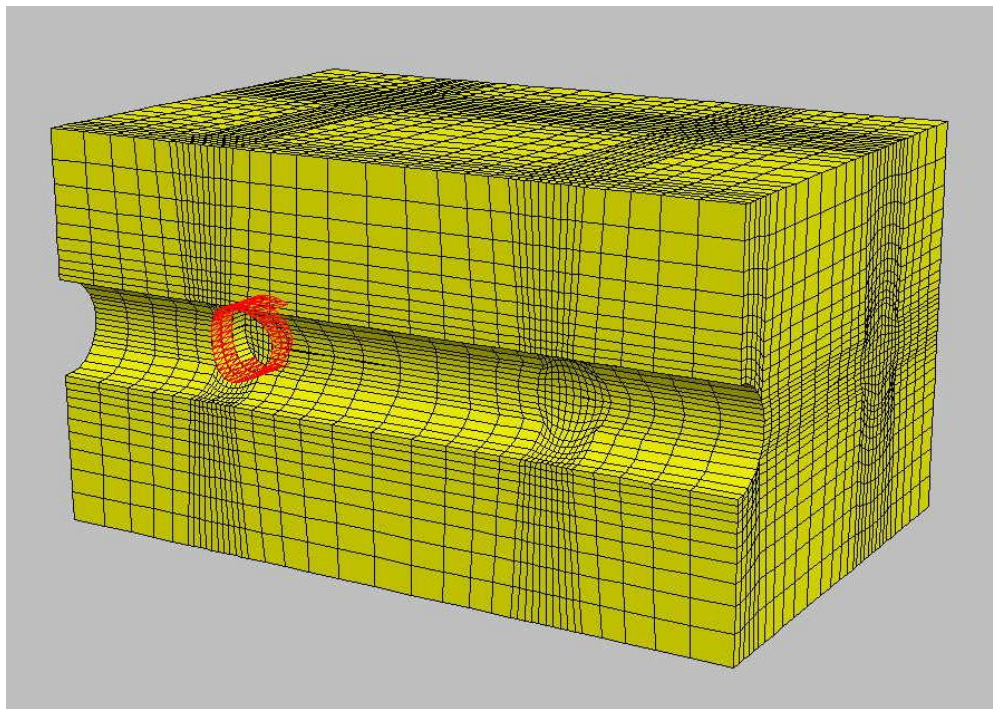
(b)

**Figure 5.3.** Stage 3; a) excavation of lower half part, b) removal of all linings,





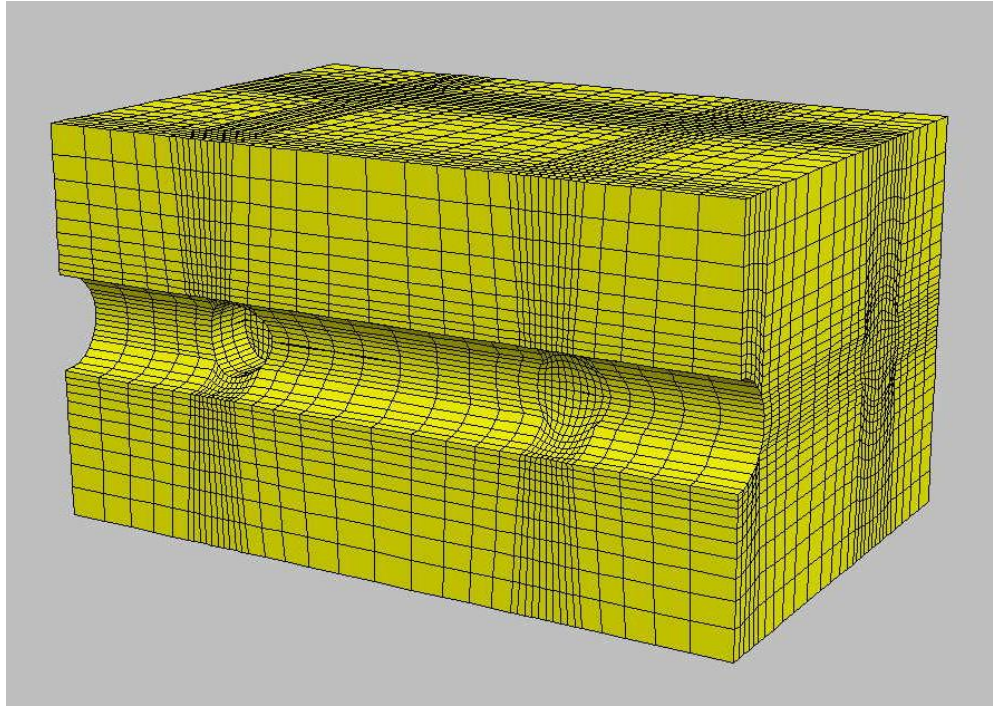
(c)



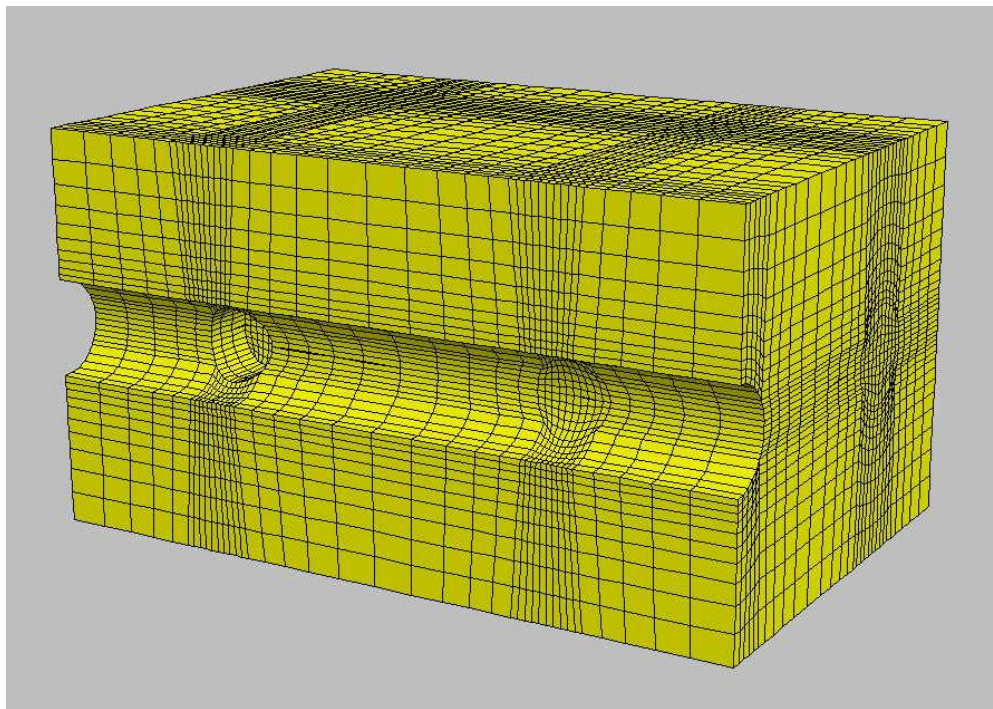
(d)

**Figure 5.3 cont'd.** c) installation of permanent linings to upper inner and upper outer parts, d) installation of temporary lining to lower half part.





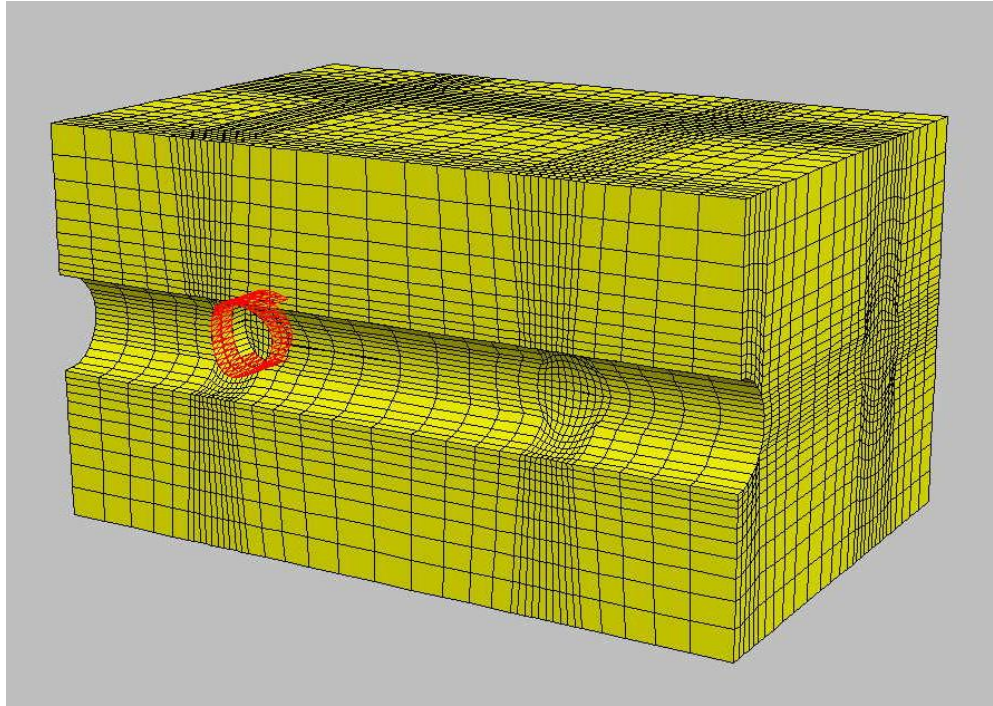
(a)



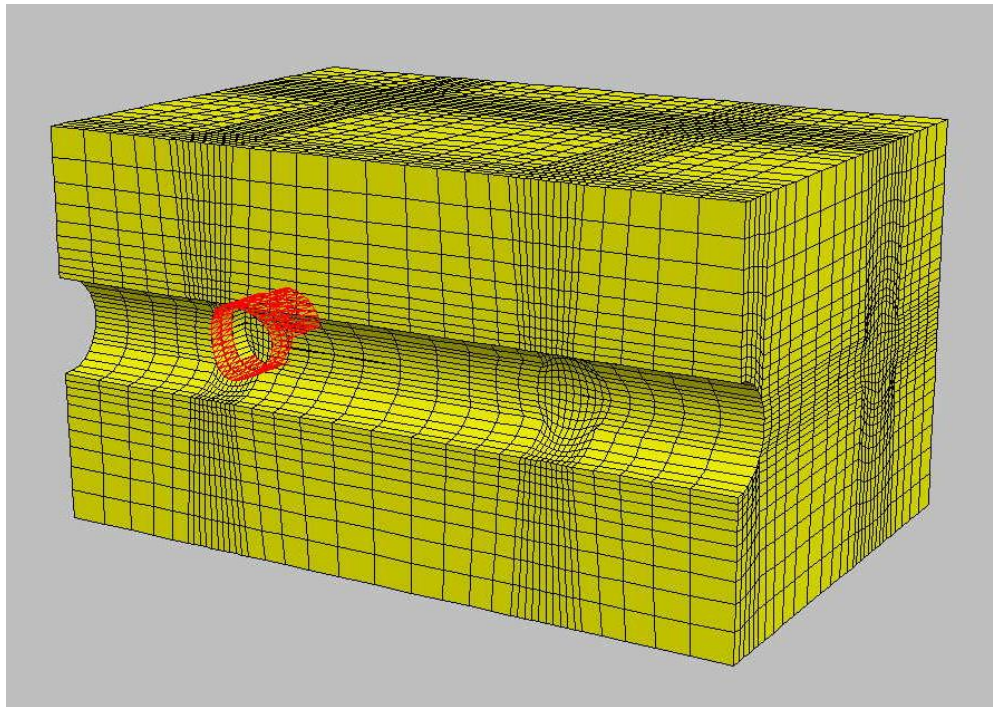
(b)

**Figure 5.4.** Stage 4; a) removal of all linings, b) excavation of second upper inner part,





(c)

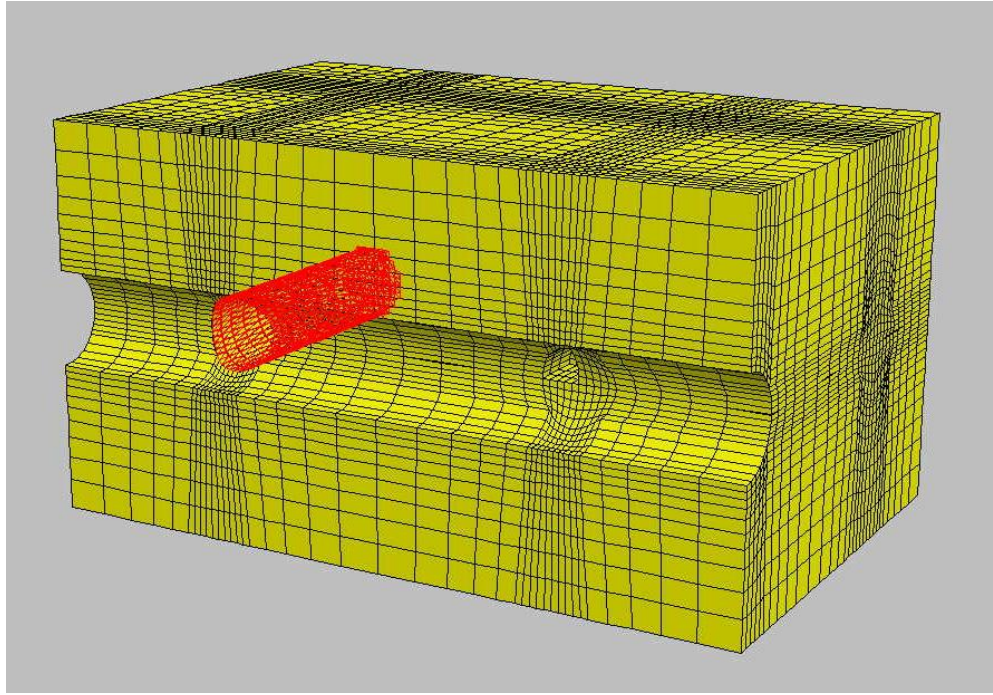


(d)

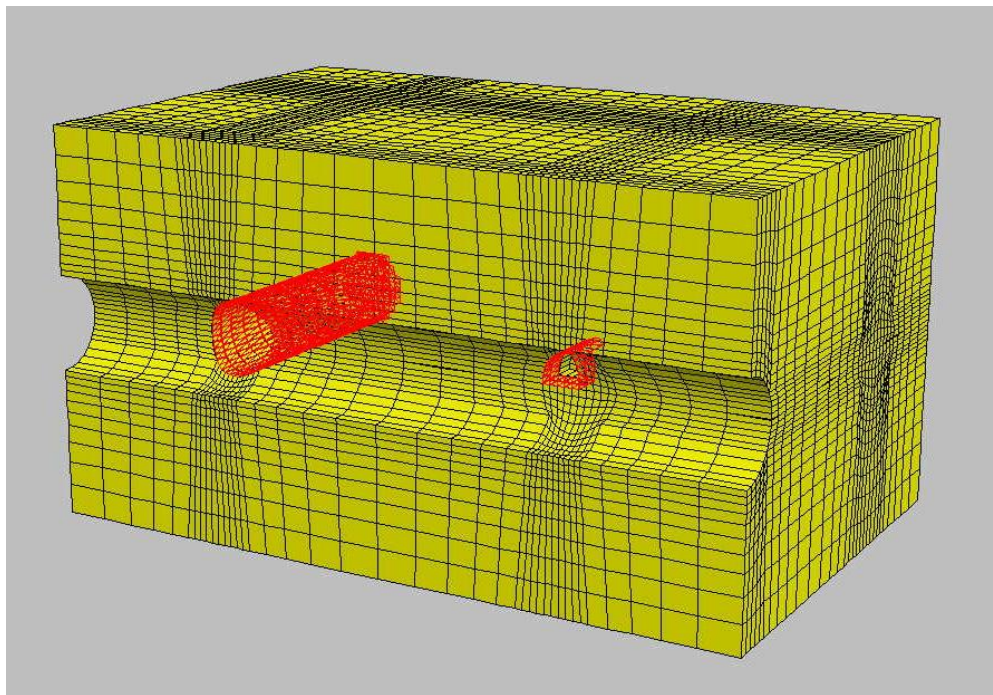
**Figure 5.4 cont'd.** c) installation of permanent linings to upper inner, upper outer and lower half parts, d) installation of temporary lining to second upper inner part.



After first connection tunnel excavation completed, second connection tunnel excavation was initiated and carried forward with a 7 m first stage advance. Excavation and support sequence for the second connection tunnel is given in Figure 5.5 through Figure 5.8.

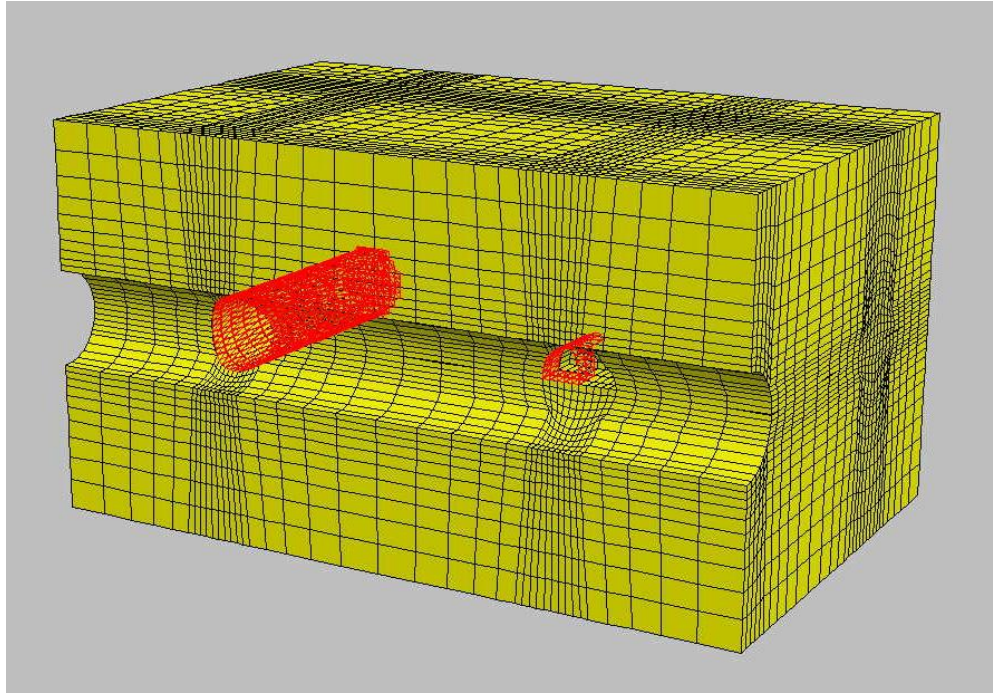


(a)

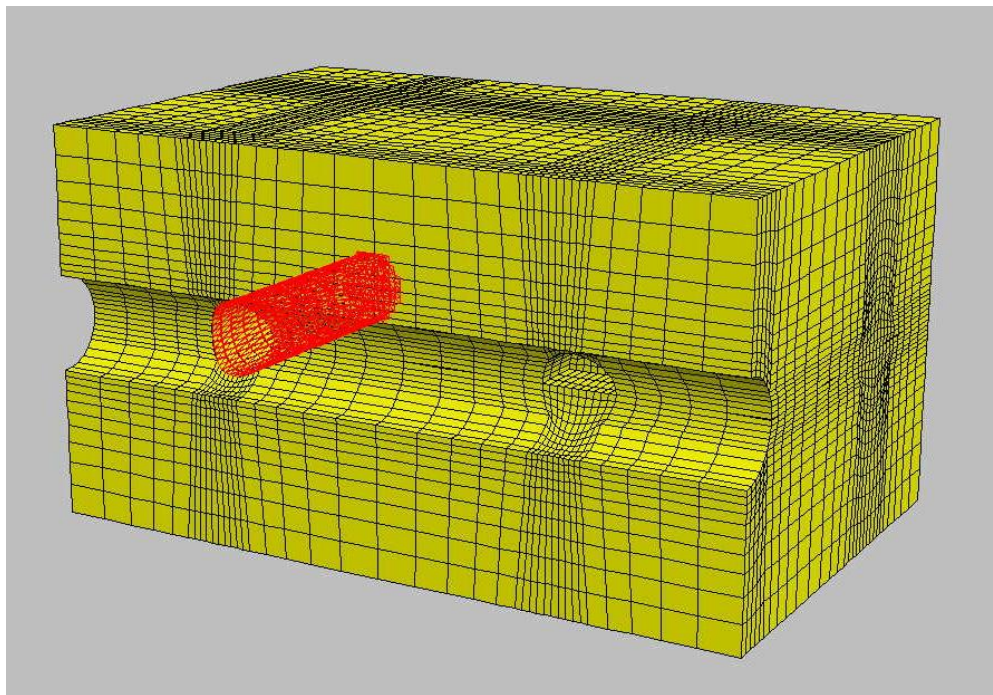


(b)

**Figure 5.5.** Step 1; a) excavation of upper inner part, b) installation of temporary lining to upper inner part.



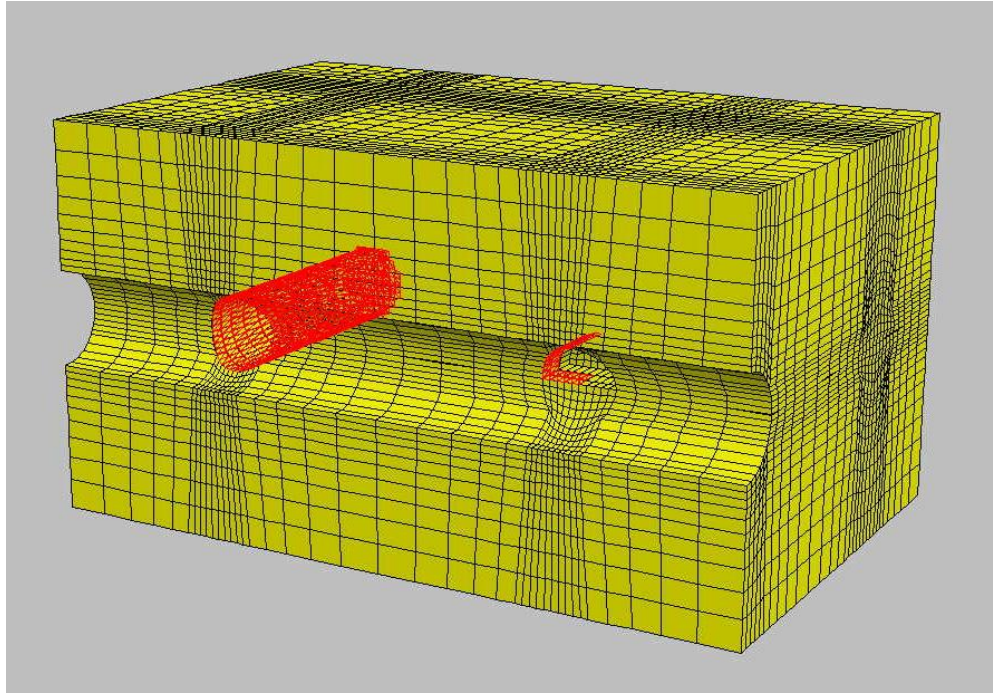
(a)



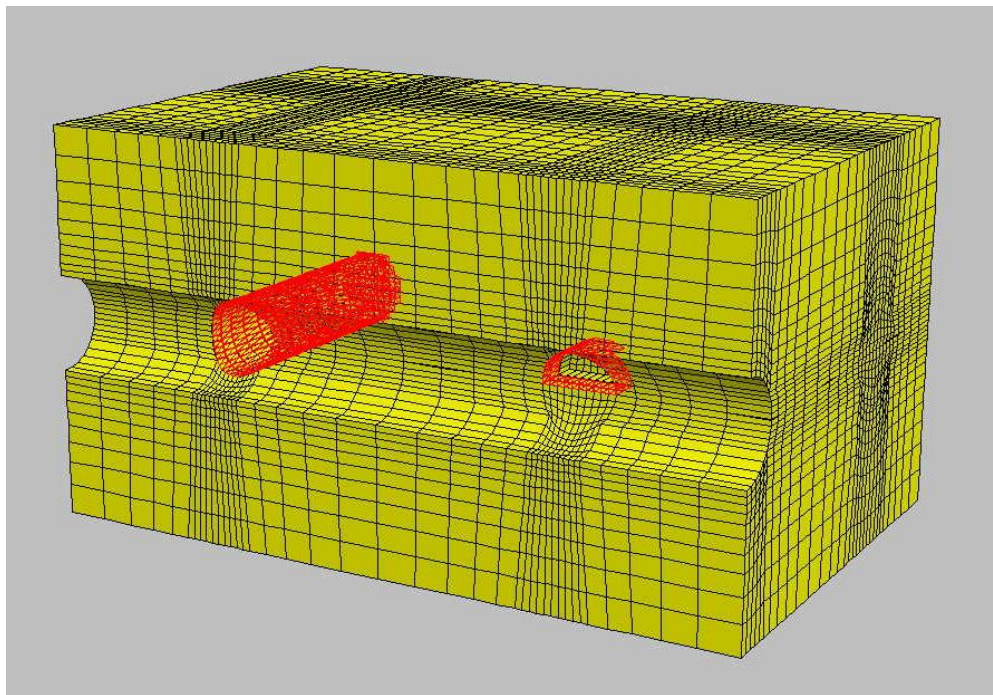
(b)

**Figure 5.6.** Stage 2; a) excavation of upper outer part, b) removal of temporary lining from upper inner part,



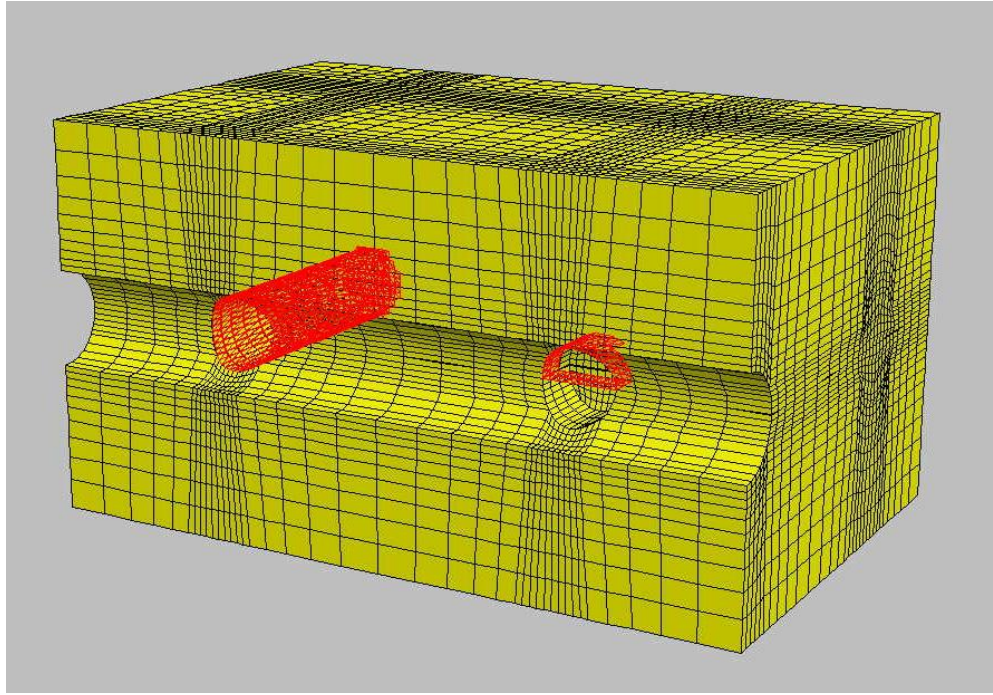


(c)

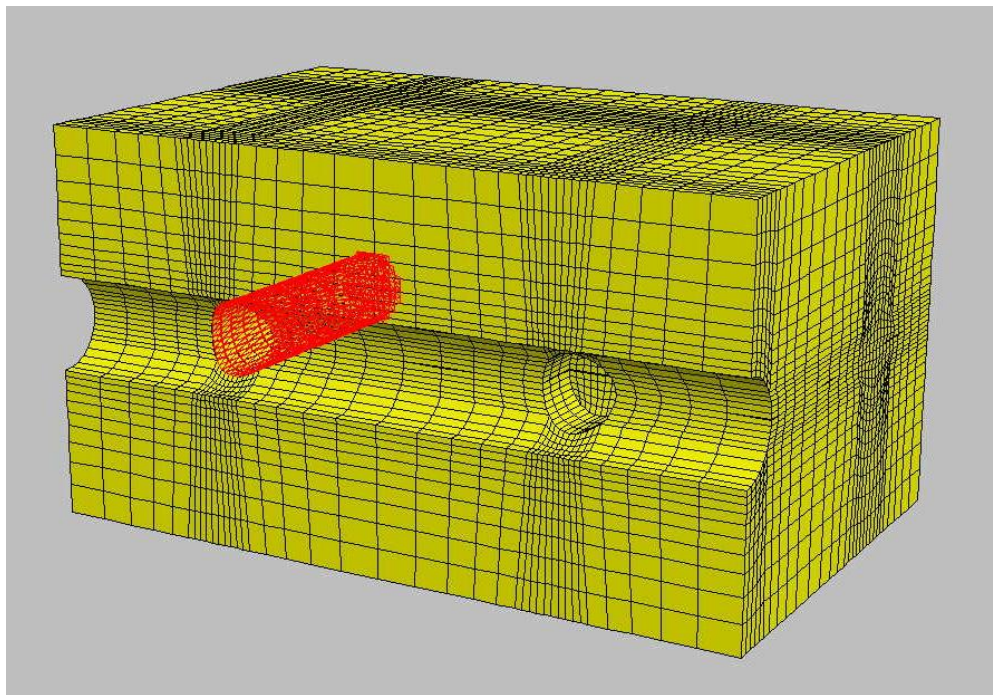


(d)

**Figure 5.6 cont'd.** c) installation of permanent lining to upper inner part, d) installation of temporary lining to upper outer part.



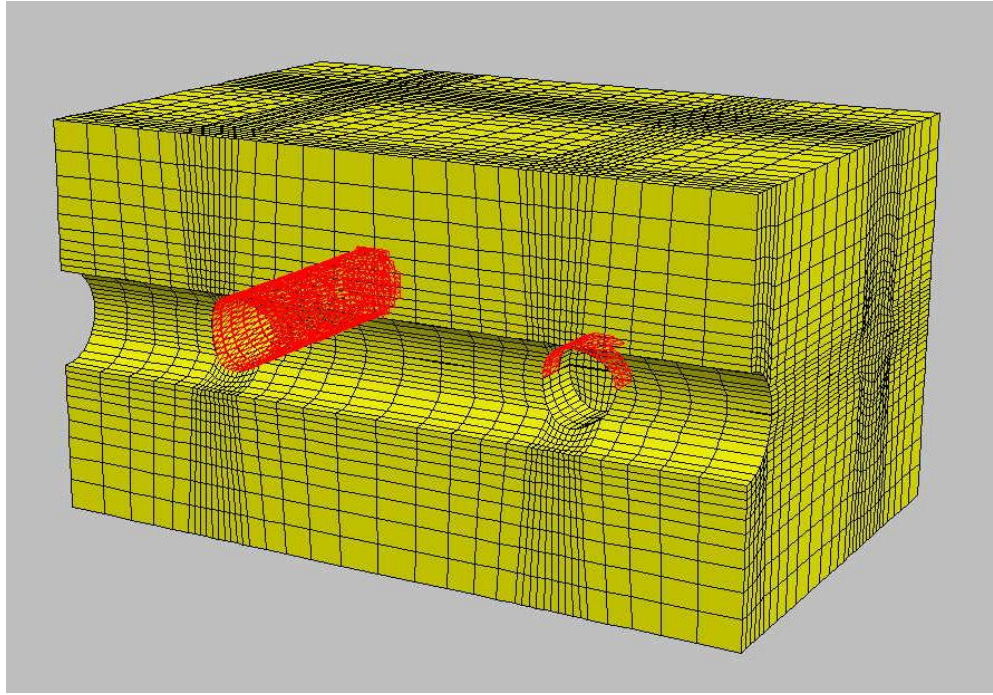
(a)



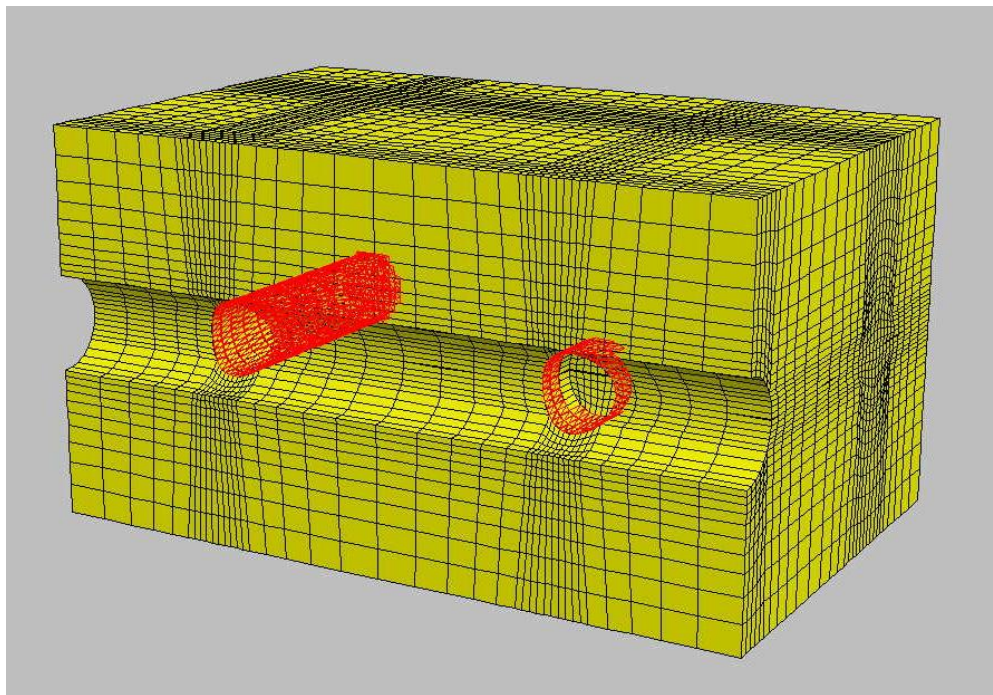
(b)

**Figure 5.7.** Stage 3; a) excavation of lower half part, b) removal of all linings,





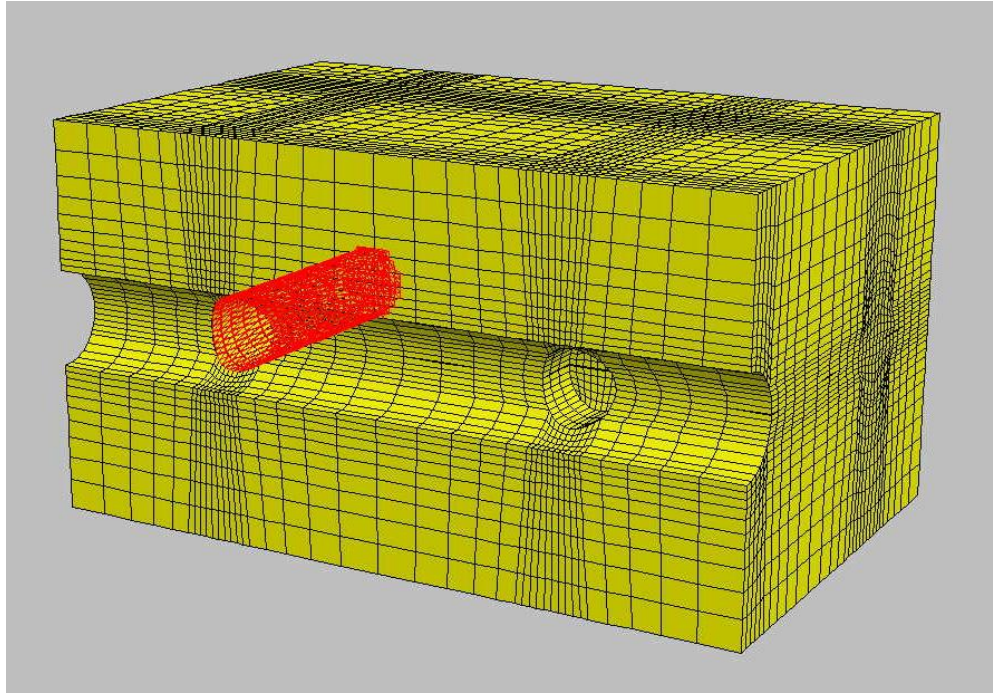
(c)



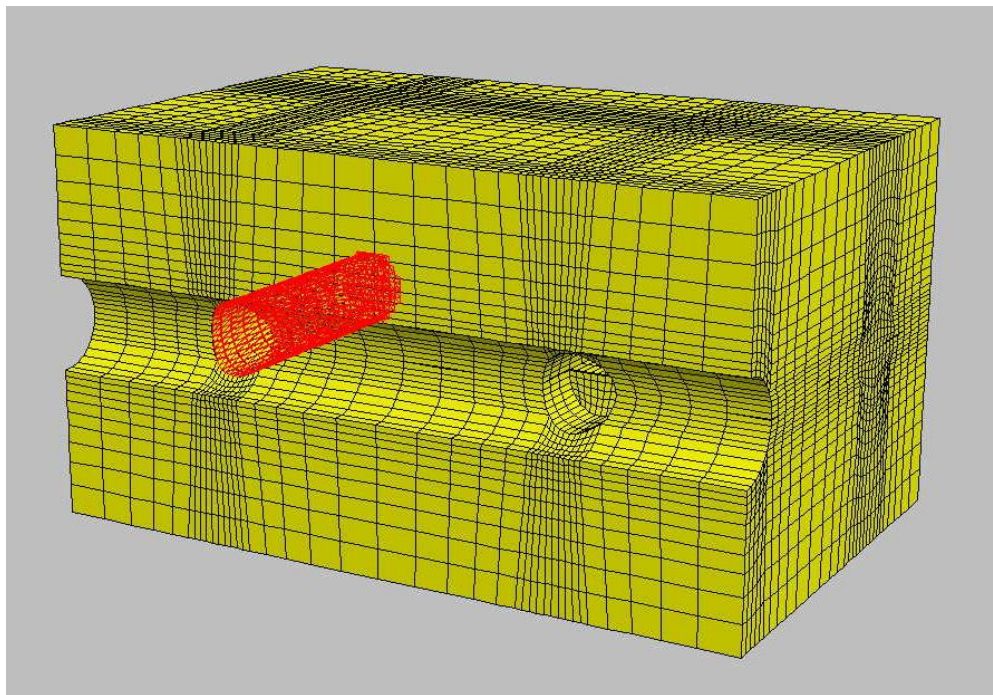
(d)

**Figure 5.7 cont'd.** c) installation of permanent linings to upper inner and upper outer parts, d) installation of temporary lining to lower half part.



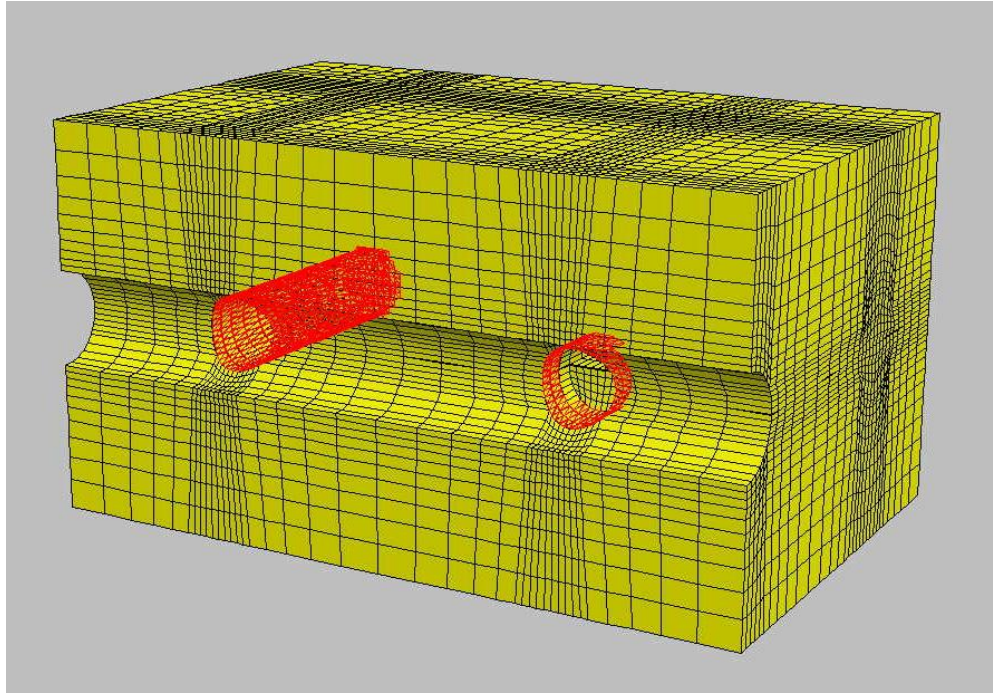


(a)

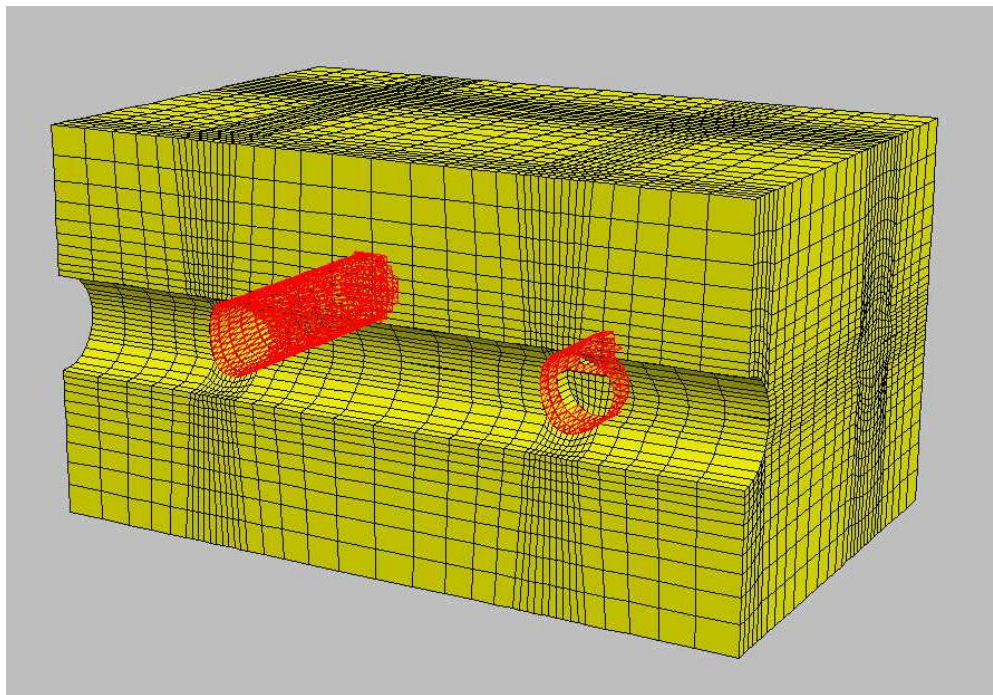


(b)

**Figure 5.8.** Stage 4; a) removal of all linings, b) excavation of second upper inner part,



(c)



(d)

**Figure 5.8 cont'd.** c) insatallatin of permanent linings to upper inner, upper outer and lower half parts, d) installation of temporary lining to second upper inner part.



As it was mentioned in Chapter 4, the pre-support concrete and shotcrete (temporary) and the concrete (permanent) tunnel linings are modeled with shell structural elements. The lining components are modeled as elastic materials with the following material properties:

(a) pre-support concrete and shotcrete (temporary)

Young's modulus,  $E = 7.1 \text{ GPa}$

Poisson's ratio,  $\nu = 0.15$

Thickness,  $t = 35 \text{ cm}$

(b) concrete liner (permanent)

Young's modulus,  $E = 28.5 \text{ GPa}$

Poisson's ratio,  $\nu = 0.15$

Thickness,  $t = 40 \text{ cm}$

A total of thirty two sequential excavation and support steps were performed to simulate construction of connection tunnels. Each construction step is run for 1000 cycles to reach an equilibrium state, and requires approximately 15 minutes to reach equilibrium. The total computation time was more than 8 hours to simulate construction of connection tunnels.

#### **5.4. Results**

The results in terms of deformations (z-displacements) were plotted against distance and illustrated in Figure 5.9 through Figure 5.16. Figure 5.9 shows connection 1 tunnel axis deformations after its excavation. As seen from the figure connection 1 tunnel excavation does not cause significant deformation on its axis. Maximum z-displacement is about 9 mm and occurred at the Line 1 tunnel side.

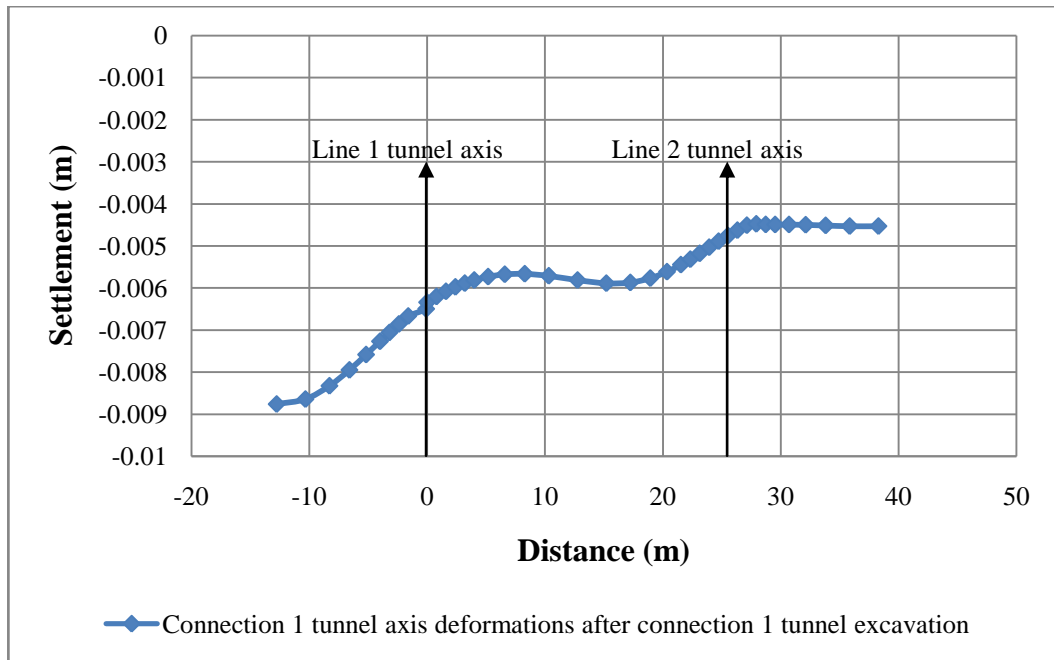
Figure 5.10 and Figure 5.11 illustrate effects of connection 1 tunnel excavation on Line 1 and Line 2 tunnels, respectively. It seems that maximum z-displacement is about 6.5 mm on Line 1 tunnel axis and about 5 mm on Line 2 tunnel axis.

Figure 5.12 represents connection 2 tunnel axis deformations induced by its excavation. Maximum deformations take place at both sides of the model and are about 1.5 cm. Another point to be paid attention in this figure is that deformations are decreasing significantly at main tunnel axes.

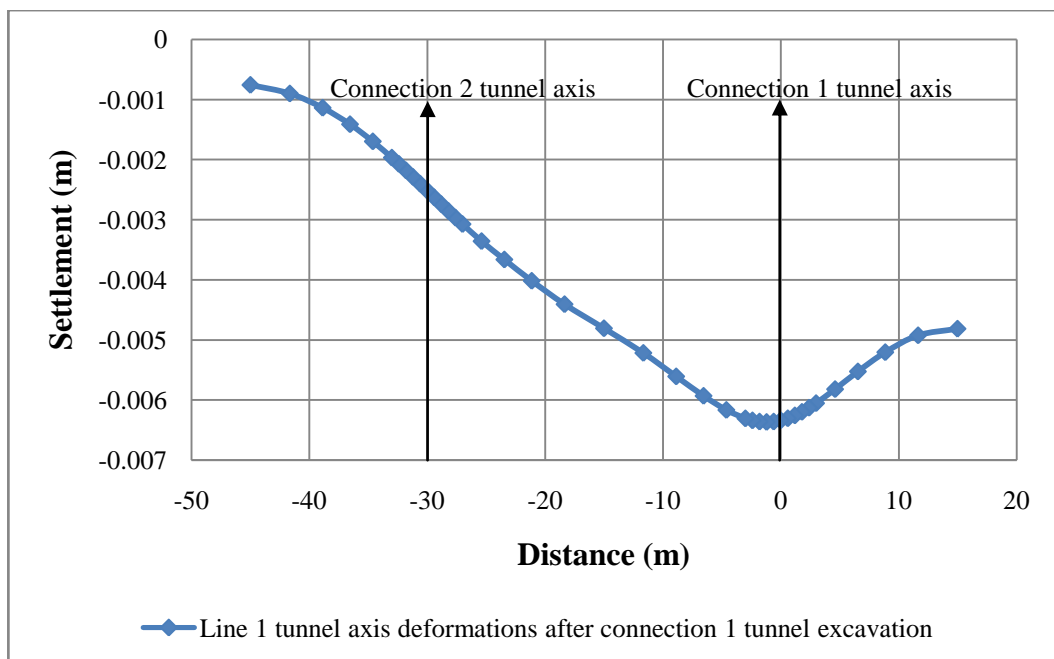
Figure 5.13 can be viewed for the correlation between connection 1 tunnel axis deformations and connection 2 tunnel axis deformations due to their excavations. Connection 2 tunnel excavation can cause deformations on its axis almost two times more than that of connection 1 tunnel excavation can do on its axis in terms of maximum z-displacements.

Figure 5.14 shows correlation of connection 1 tunnel axis deformations after connection 1 and 2 tunnel excavations. Maximum deformation would be around 1.7 cm on connection 1 tunnel axis after connection 2 tunnel excavation.

Figure 5.15 illustrates correlation of Line 1 tunnel axis deformations after connection 1 and 2 tunnel excavations and Figure 5.16 illustrates correlation of Line 2 tunnel axis deformations after connection 1 and 2 tunnel excavations. Both Figures show that connection 2 tunnel excavation can affect the main tunnels more than connection 1 tunnel excavation and Line 1 tunnel can be affected by excavations more than Line 2 tunnel.



**Figure 5.9.** Connection 1 tunnel axis deformations after connection 1 tunnel excavation.



**Figure 5.10.** Line 1 tunnel axis deformations after connection 1 tunnel excavation.



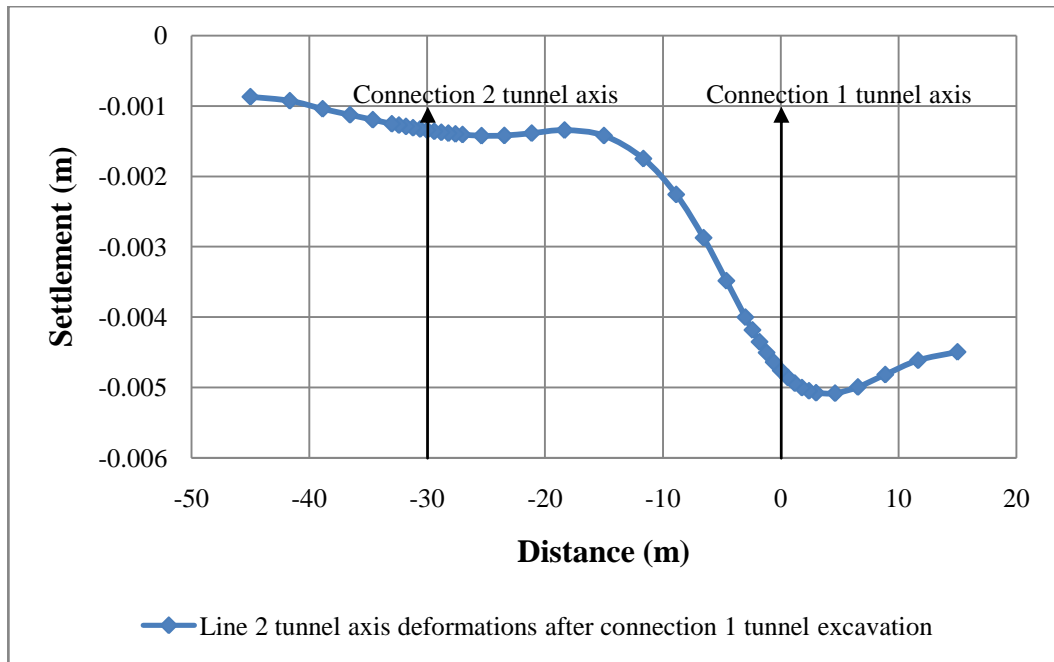


**Figure 5.11.** Line 2 tunnel axis deformations after connection tunnel 1 excavation.

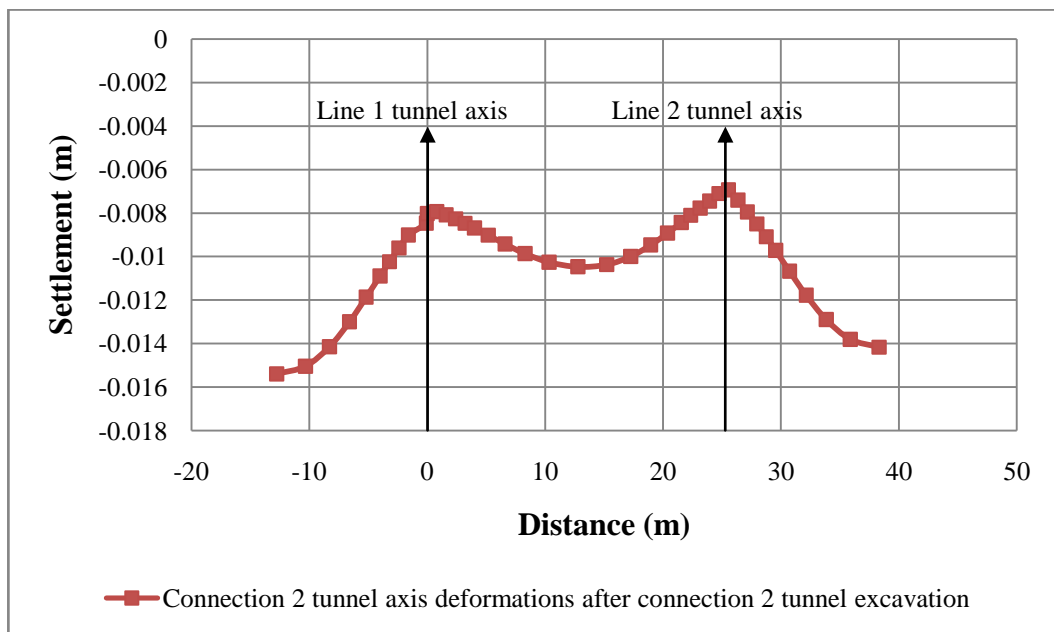


**Figure 5.12.** Connection 2 tunnel axis deformations after connection 2 tunnel excavation.

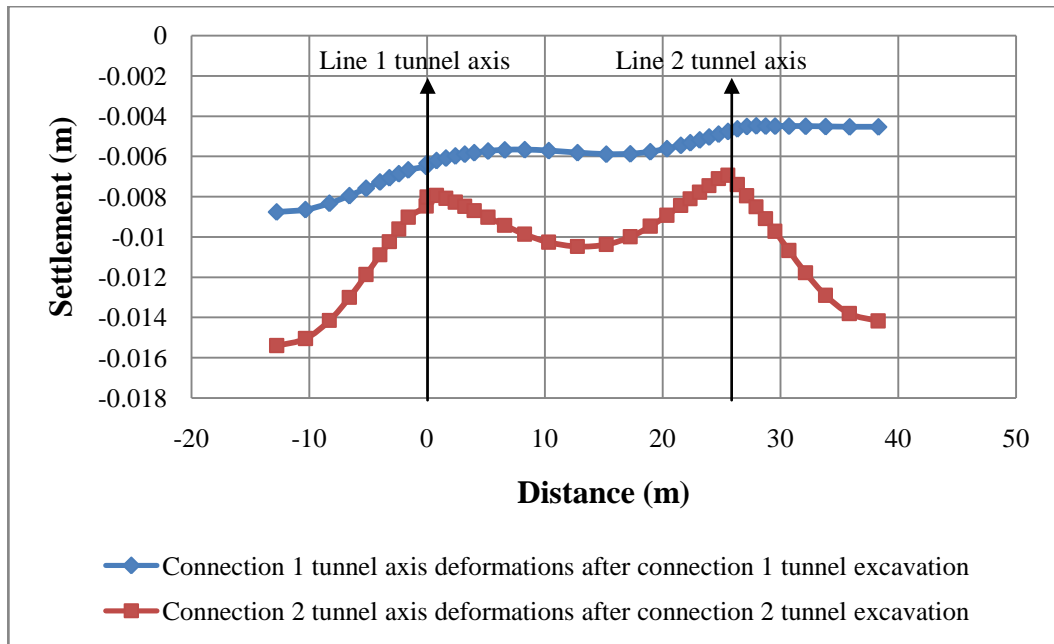


**Figure 5.13.** Correlation of connection 1 tunnel axis deformations and connection 2 tunnel axis deformations after their excavations.

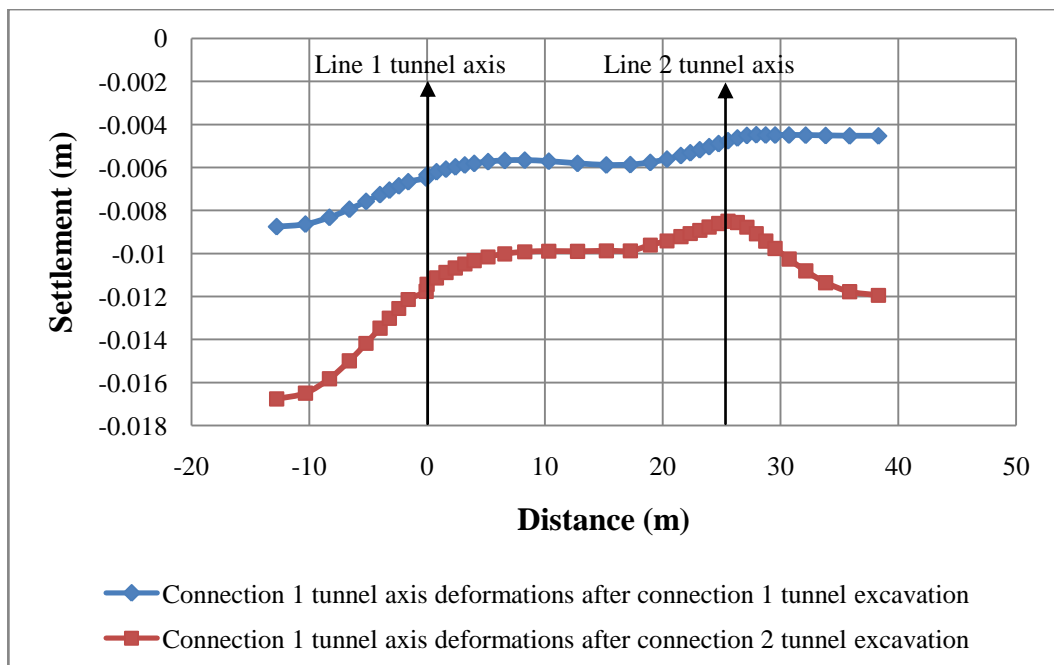


**Figure 5.14.** Correlation of connection 1 tunnel axis deformations after connection 1 and 2 tunnel excavations.

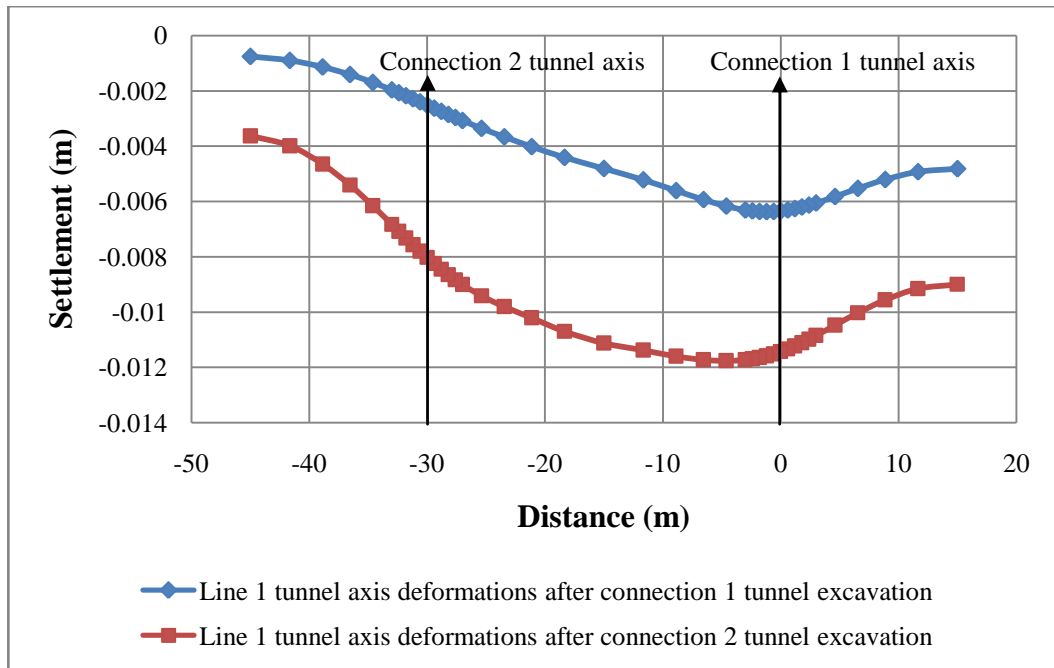


**Figure 5.15.** Correlation of Line 1 tunnel axis deformations after connection 1 and 2 tunnel excavations.

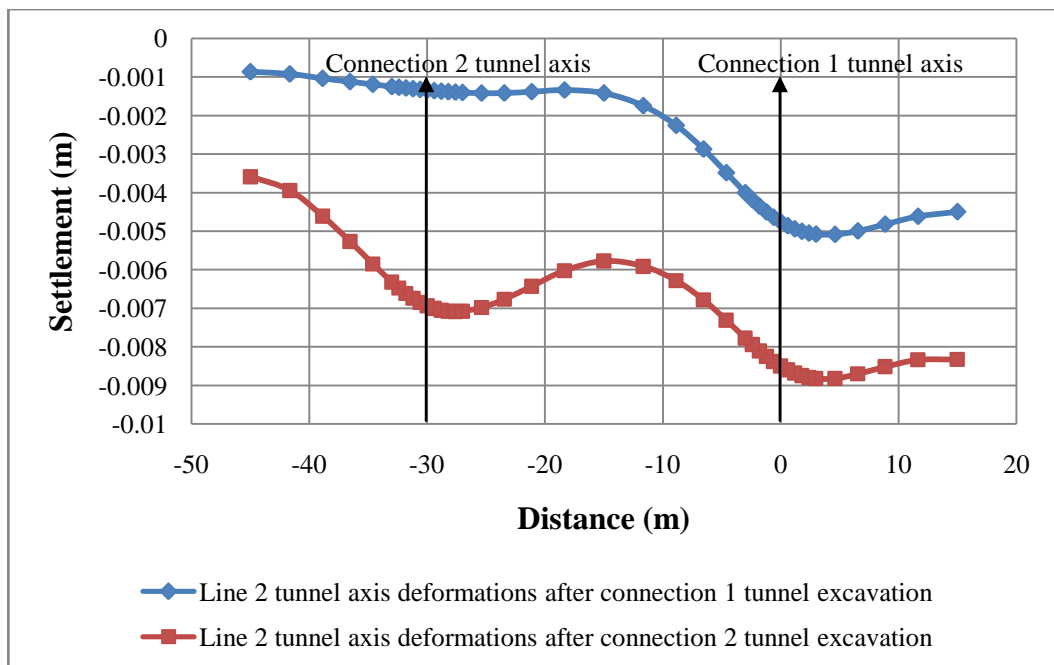


**Figure 5.16.** Correlation of Line 2 tunnel axis deformations after connection 1 and 2 tunnel excavations.

The values plotted in above figures were tabulated in Table 5.2 thru Table 5.5 below.

**Table 5.2.** Line 1 tunnel axis deformations.

	<b>Line 1 after Connection 1</b>	<b>Line 1 after Connection 2</b>
<b>Distance (m)</b>	<b>z-displacemnts (m)</b>	<b>z-displacements (m)</b>
15	-0,0048156	-0,0089962
11,656	-0,0049253	-0,0091479
8,8697	-0,0052063	-0,0095566
6,5476	-0,005527	-0,010024
4,6126	-0,0058214	-0,01047
3	-0,0060547	-0,010846
2,4	-0,0061312	-0,010979
1,8	-0,0062	-0,011106
1,2	-0,0062585	-0,011224
0,6	-0,0063062	-0,011333
0	-0,0063402	-0,011429
-0,6	-0,006361	-0,011512
-1,2	-0,0063677	-0,011583
-1,8	-0,0063609	-0,011642
-2,4	-0,0063412	-0,011689
-3	-0,0063078	-0,011723
-4,6126	-0,0061676	-0,01176
-6,5476	-0,0059325	-0,011723
-8,8697	-0,0056089	-0,011598
-11,656	-0,0052184	-0,011376
-15	-0,0048086	-0,01112
-18,344	-0,0044077	-0,010696
-21,13	-0,0040183	-0,010207
-23,452	-0,003664	-0,009801
-25,387	-0,0033585	-0,0094116
-27	-0,0030747	-0,0090016
-28,2	-0,0028563	-0,0086466
-28,8	-0,0027437	-0,0084484
-29,4	-0,0026297	-0,0082394
-30	-0,0025156	-0,0080212
-30,6	-0,0024025	-0,0077948
-31,2	-0,0022908	-0,0075609
-31,8	-0,0021809	-0,0073204
-32,4	-0,0020735	-0,007075
-33	-0,0019687	-0,0068268
-34,613	-0,0016983	-0,0061527
-36,548	-0,0014132	-0,005402
-38,87	-0,0011392	-0,0046457
-41,656	-0,0009017	-0,0039792
-45	-0,00075837	-0,0036214



**Table 5.3.** Line 2 tunnel axis deformations.

	<b>Line 2 after Connection 1</b>	<b>Line 2 after Connection 2</b>
<b>Distance (m)</b>	<b>z-displacements (m)</b>	<b>z-displacements (m)</b>
15	-0,0044948	-0,008327
11,656	-0,0046141	-0,0083361
8,8697	-0,0048173	-0,0085162
6,5476	-0,004994	-0,0087015
4,6126	-0,005082	-0,0088221
3	-0,0050764	-0,0088238
2,4	-0,0050485	-0,0087949
1,8	-0,0050033	-0,0087478
1,2	-0,00494	-0,0086829
0,6	-0,0048581	-0,0086
0	-0,004758	-0,0084995
-0,6	-0,0046399	-0,0083818
-1,2	-0,0045044	-0,0082486
-1,8	-0,0043517	-0,0081084
-2,4	-0,0041831	-0,0079426
-3	-0,0040016	-0,0077747
-4,6126	-0,0034836	-0,0073083
-6,5476	-0,0028723	-0,006782
-8,8697	-0,0022569	-0,006282
-11,656	-0,0017473	-0,0059106
-15	-0,0014201	-0,005774
-18,344	-0,0013424	-0,0060251
-21,13	-0,0013857	-0,0064292
-23,452	-0,0014188	-0,006766
-25,387	-0,001422	-0,0069823
-27	-0,0014054	-0,0070754
-28,2	-0,0013862	-0,0070792
-28,8	-0,0013737	-0,0070509
-29,4	-0,0013595	-0,0070028
-30	-0,001344	-0,0069349
-30,6	-0,0013272	-0,0068473
-31,2	-0,0013092	-0,00674
-31,8	-0,0012902	-0,0066143
-32,4	-0,0012716	-0,0064734
-33	-0,001253	-0,0063188
-34,613	-0,0011947	-0,0058497
-36,548	-0,0011249	-0,0052655
-38,87	-0,0010399	-0,0046105
-41,656	-0,00092511	-0,0039428
-45	-0,00086825	-0,0035842

**Table 5.4.** Connection 1 tunnel axis deformations.

	<b>Connect. 1 after Connect. 1</b>	<b>Connect. 1 after Connect. 2</b>
<b>Distance (m)</b>	<b>z-displacements (m)</b>	<b>z-displacements (m)</b>
-12,77	-0,0087576	-0,016761
-10,326	-0,0086401	-0,01649
-8,2898	-0,0083236	-0,015817
-6,5927	-0,0079477	-0,014992
-5,1785	-0,0075819	-0,014178
-4	-0,0072676	-0,013472
-3,2	-0,007059	-0,013006
-2,4	-0,0068576	-0,012556
-1,6	-0,0066679	-0,012139
-0,08	-0,0064962	-0,011763
0	-0,0063402	-0,011429
0,8	-0,0062034	-0,011139
1,6	-0,0060811	-0,010886
2,4	-0,0059761	-0,01067
3,2	-0,0058872	-0,010488
4	-0,0058133	-0,010336
5,1785	-0,0057318	-0,010161
6,5927	-0,0056761	-0,010018
8,2898	-0,005664	-0,0099244
10,326	-0,0057121	-0,009891
12,77	-0,0058135	-0,0098997
15,214	-0,0058883	-0,0098768
17,25	-0,0058708	-0,0098768
18,947	-0,0057681	-0,0096117
20,361	-0,0056151	-0,009416
21,54	-0,0054476	-0,0092207
22,34	-0,0053187	-0,0090767
23,14	-0,0051795	-0,0089258
23,94	-0,0050344	-0,0087689
24,74	-0,0048915	-0,0086083
25,54	-0,004758	-0,0084995
26,34	-0,0046297	-0,0085662
27,14	-0,0045122	-0,0087775
28,74	-0,0044933	-0,0094276
29,54	-0,0044947	-0,0097672
30,719	-0,0044949	-0,010258
32,133	-0,0045009	-0,010811
33,83	-0,0045158	-0,011357
35,866	-0,0045326	-0,011776
38,31	-0,0045328	-0,011944

**Table 5.5.** Connection 2 tunnel axis deformations.

	<b>Connect. 2 after Connect. 2</b>
<b>Distance (m)</b>	<b>z-displacements (m)</b>
-12,77	-0,015399
-10,326	-0,015046
-8,2898	-0,014146
-6,5927	-0,013003
-5,1785	-0,01187
-4	-0,010891
-3,2	-0,010239
-2,4	-0,0096089
-1,6	-0,0090159
-0,08	-0,0084633
0	-0,0080212
0,8	-0,0079389
1,6	-0,0080827
2,4	-0,0082694
3,2	-0,0084749
4	-0,0086919
5,1785	-0,0090201
6,5927	-0,0094235
8,2898	-0,0098672
10,326	-0,010259
12,77	-0,010473
15,214	-0,010373
17,25	-0,0099951
18,947	-0,0094699
20,361	-0,0089244
21,54	-0,0084393
22,34	-0,0081079
23,14	-0,0077772
23,94	-0,0074535
24,74	-0,0071062
25,54	-0,0069349
26,34	-0,0074037
27,14	-0,0079517
28,74	-0,0090932
29,54	-0,0097171
30,719	-0,010679
32,133	-0,011781
33,83	-0,012899
35,866	-0,013805
38,31	-0,014169

Graphical numerical results were also represented in Figure 5.17 through Figure 5.26 for different construction stages for connection tunnels. These graphs visualize the total displacement contours (in z-direction) due to the process of excavation. The variations in z-displacement (vertical) can be easily noticed with elapsed stages in these contour plots. In figures, red crosses indicate support lining while colorful contours indicate z-displacement values. As shown in the figures maximum z-displacement is increasing continuously from  $4.8731 \times 10^{-3}$  m to  $2.1609 \times 10^{-2}$  m in the model because of proceeded excavation. It should also be stated that before excavation work started, the model was stepped to equilibrium under gravitational loading and then displacements in all directions were set to zero.

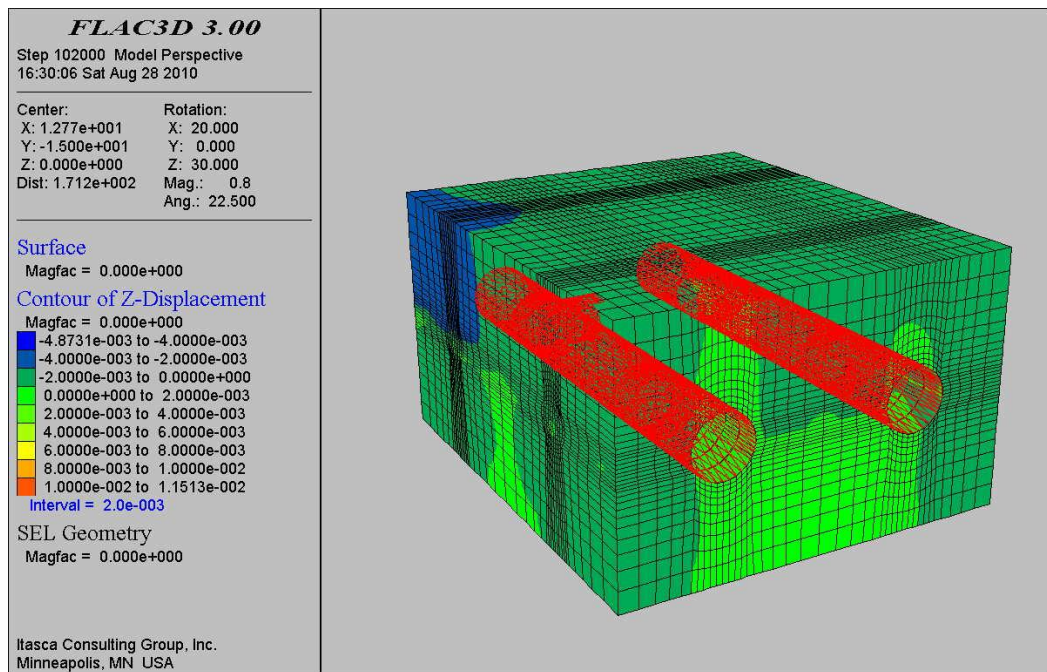


**Figure 5.17.** 7 m excavation and support of connection 1 tunnel.

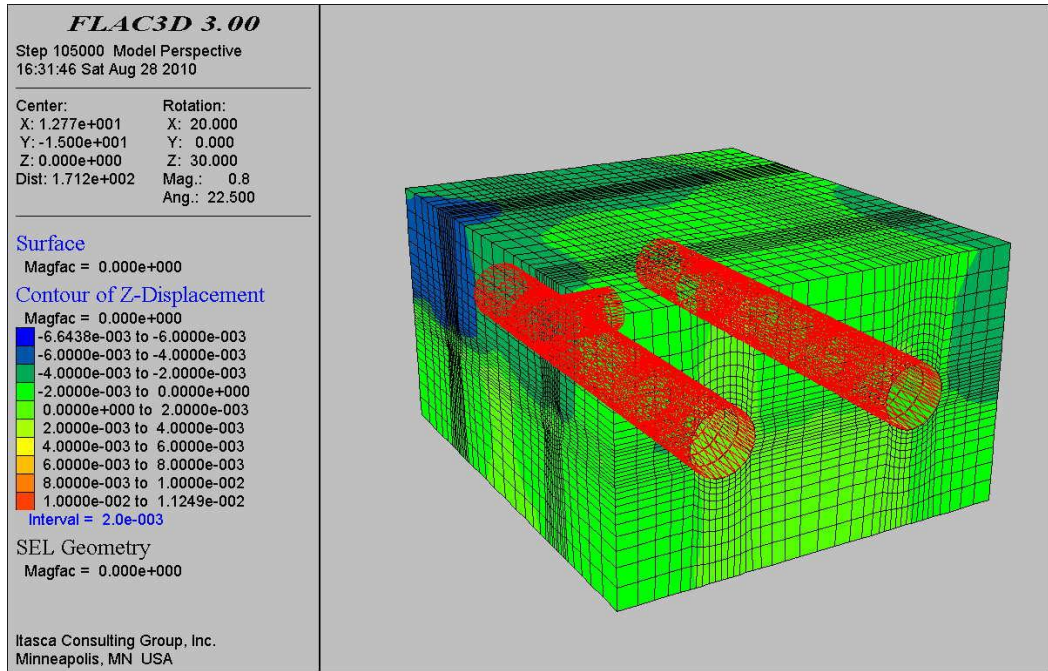


**Figure 5.18.** 11 m excavation and support of connection 1 tunnel.

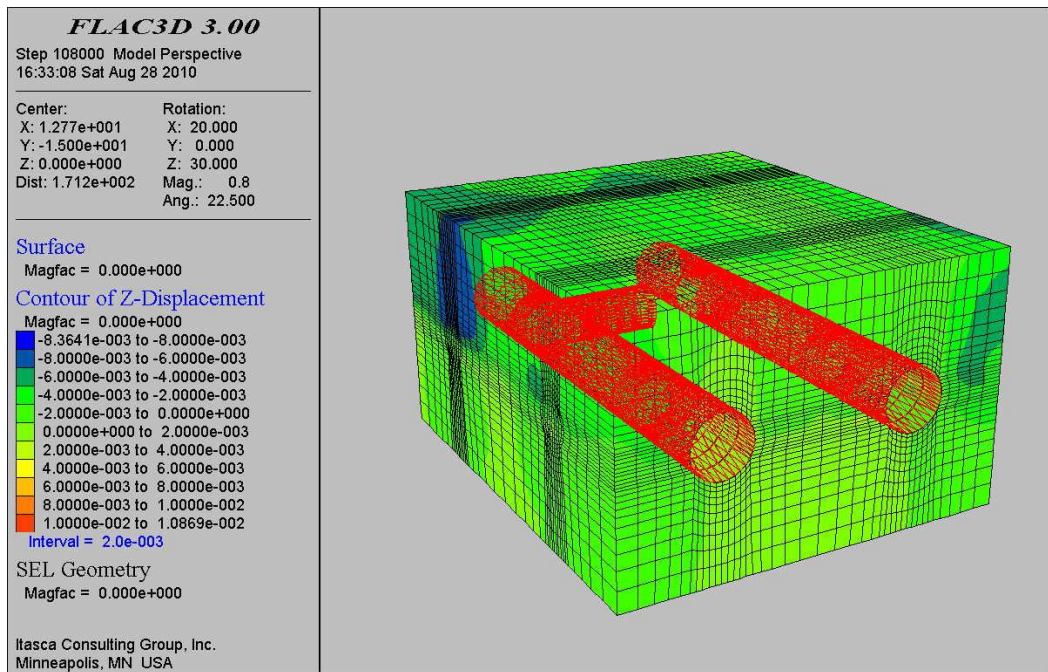


**Figure 5.19.** 15 m excavation and support of connection 1 tunnel.



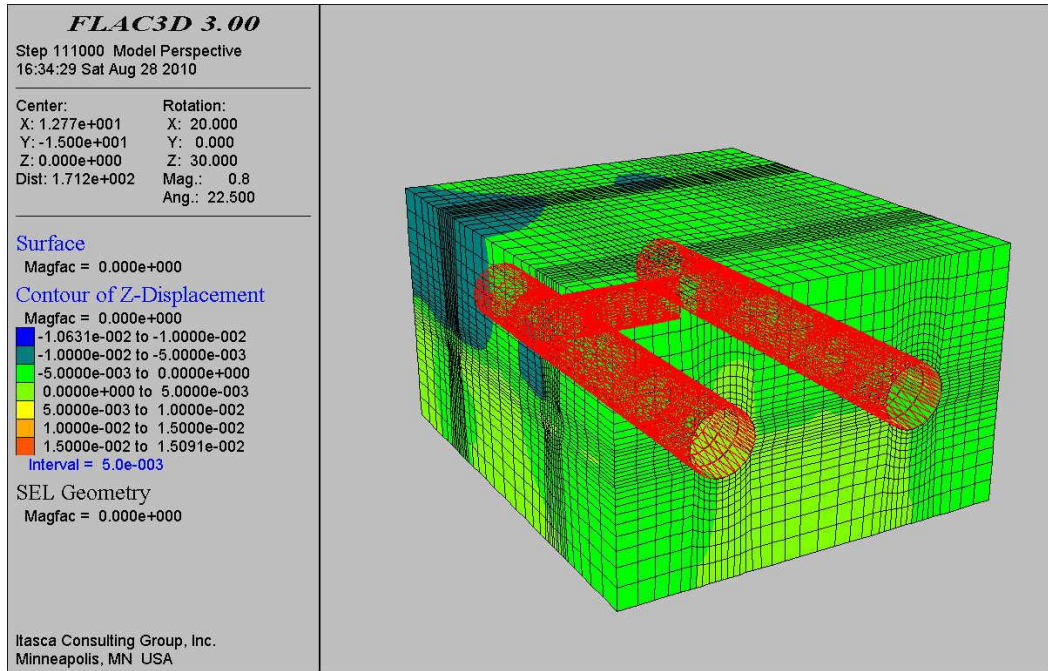


**Figure 5.20.** 19 m excavation and support of connection 1 tunnel.

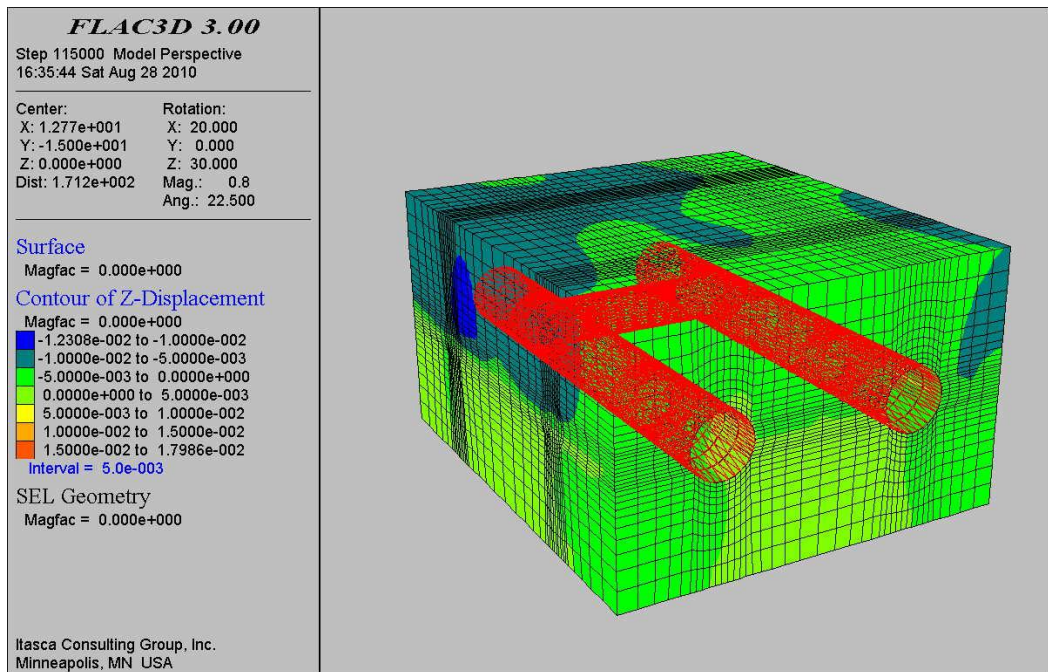


**Figure 5.21.** 23.5 m excavation and support of connection 1 tunnel.

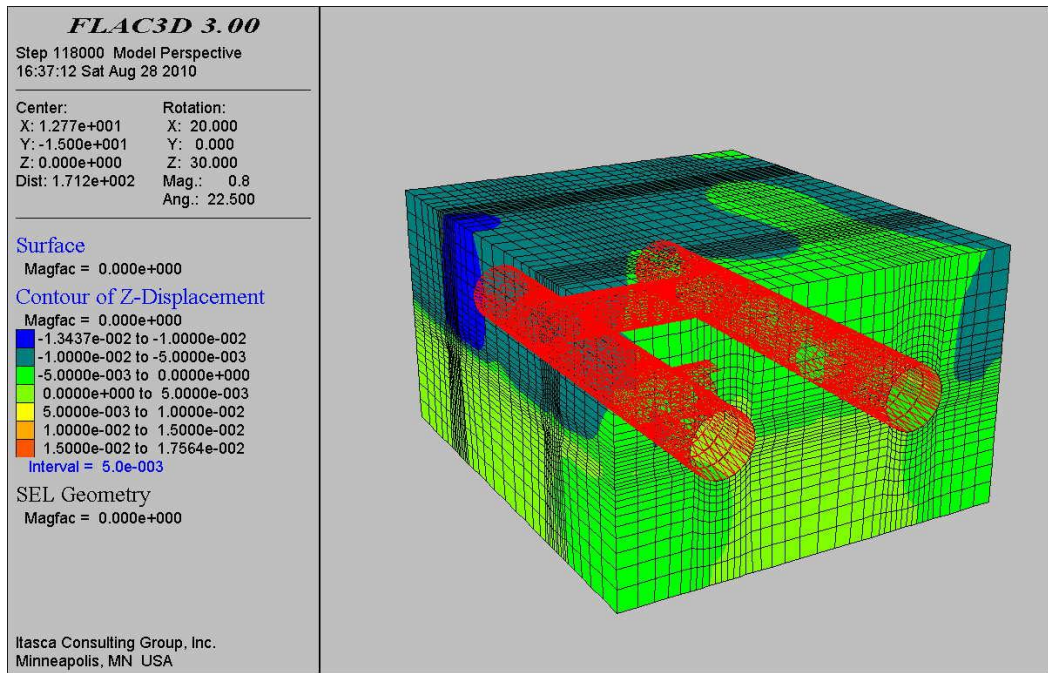


**Figure 5.22.** 7 m excavation and support of connection 2 tunnel.

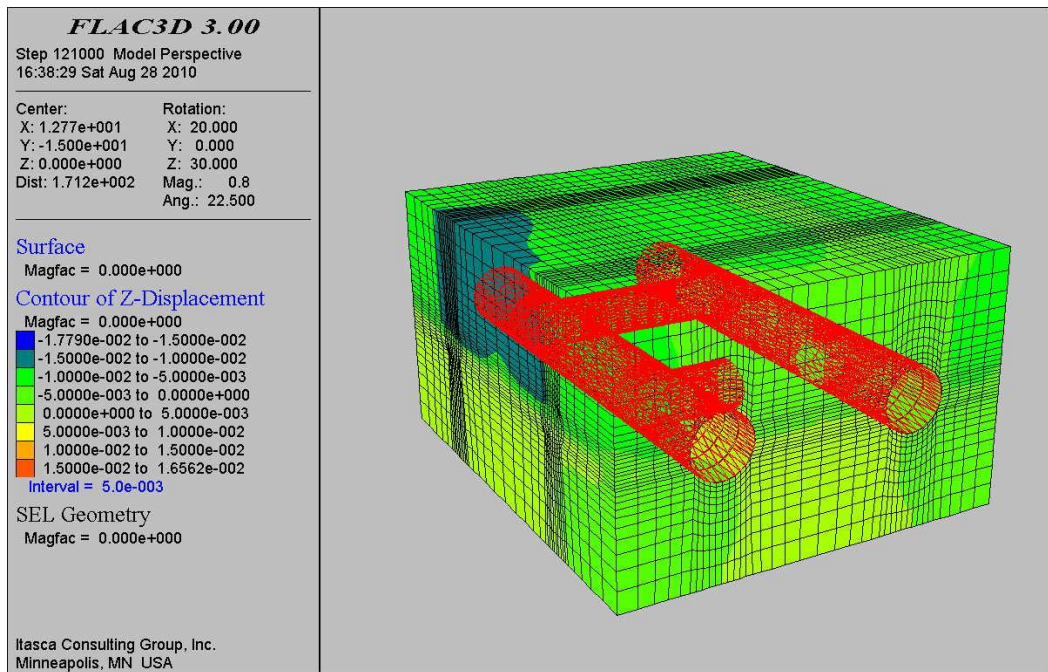


**Figure 5.23.** 11 m excavation and support of connection 2 tunnel.



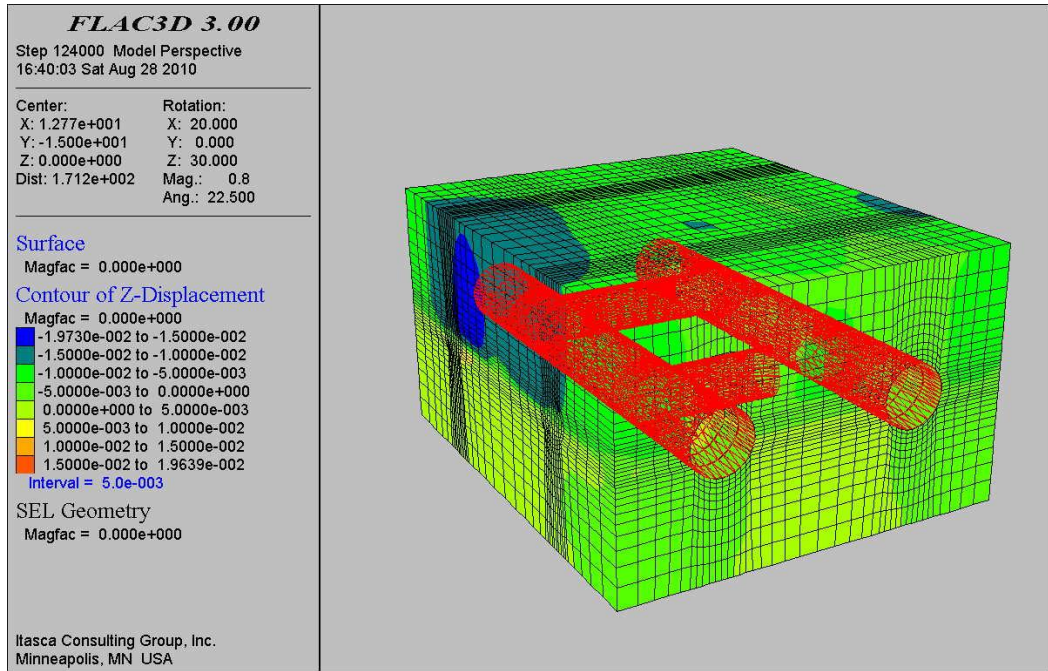


**Figure 5.24.** 15 m excavation and support of connection 2 tunnel.

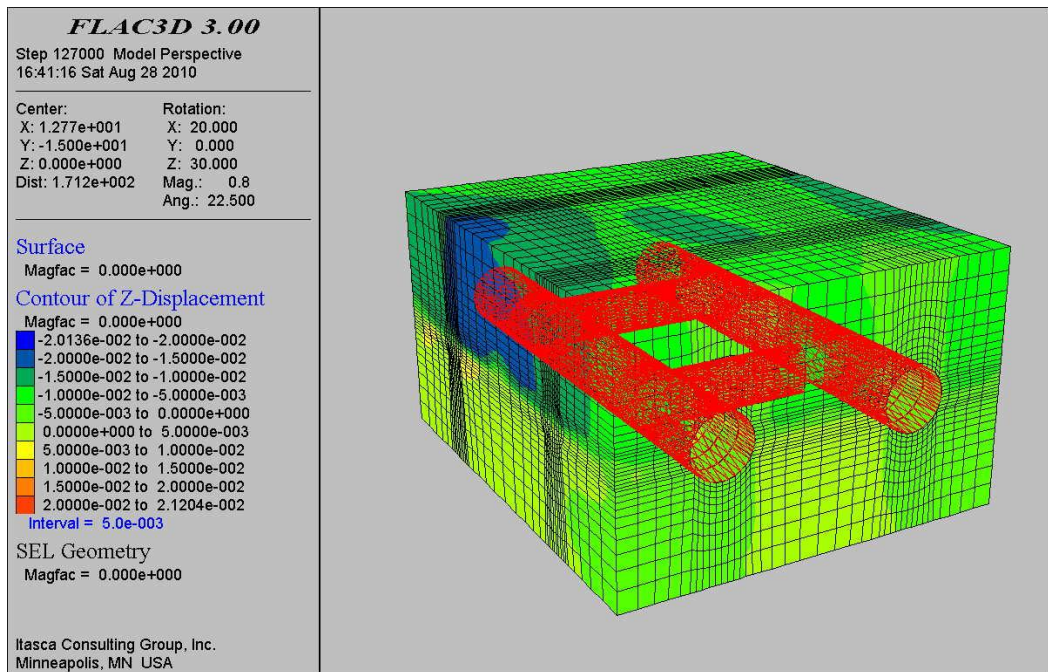


**Figure 5.25.** 19 m excavation and support of connection 2 tunnel.

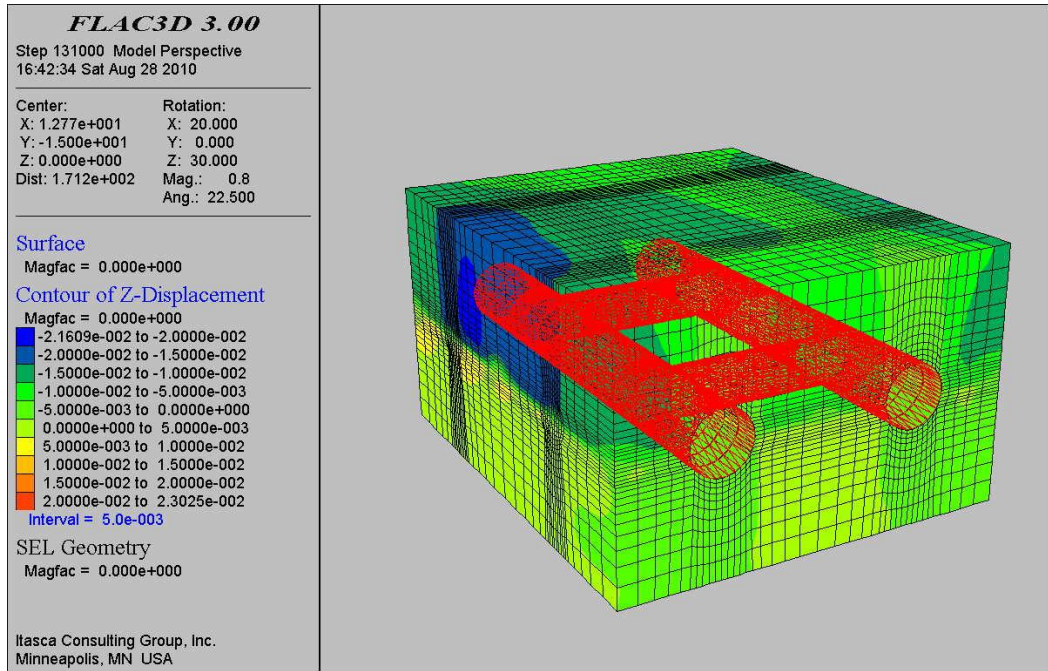


**Figure 5.26.** 23.5 m excavation and support of connection 2 tunnel.

## CHAPTER 6

### EFFECTS OF GROUNDWATER DRAINAGE ON GROUND DEFORMATIONS

#### 6.1. Introduction

3-dimensional fully coupled (fluid-mechanical) numerical models created to estimate the consolidation settlements taking place at the Ankara Subway System Necatibey Station and its close vicinity due to the groundwater drainage in this chapter.

The alluvium of Dikmen Valley crosses Necatibey Station almost perpendicularly. It is composed of clay, silty clay and gravelly sand units. This alluvium aquifer was the only source of high rate (8 l/sec) and continuous groundwater inflow during construction of main tunnels (Doyuran, 2006). To avoid flooding of the tunnel excavation work was stopped and three pumping wells were installed to drain groundwater at the site.

Pumping groundwater causes lowering of hydraulic head of the aquifer, and hence, reduction of the pore water pressure within the alluvium. In this chapter it is aimed to simulate induced surface settlement due to groundwater withdrawal at the site.

In order to simulate this phenomenon the critical soil profile used in Chapter 4 was adopted to set off a basis for numerical models. Calibrated soil properties (e.g., bulk modulus, shear modulus, cohesion, etc.) in Chapter 4 were also used in the models to simulate groundwater drainage wells at the site. To do this, 3-



dimensional fully coupled (fluid-mechanical) numerical models were run using different time durations (1, 2, 3, 4, 5, 6, 7, 14, 28, 60, 90, 120, 150, 180 days).

Information about *FLAC 3D* code's fluid-mechanical coupling option and step by step procedure about numerical modeling concept will be mentioned at the same time in this chapter. Itemized assumptions made to improve numerical models quality and results part illustrating graphical plots and numerical model outputs will also be represented.

## **6.2. Fluid-mechanical coupling**

*FLAC3D* is capable of modeling the flow of fluid through a permeable solid, such as soil, in order to capture the effects of fluid/solid interaction. One type of fluid/solid interaction is consolidation, in which the slow dissipation of pore pressure causes displacements to occur in the soil. This type of behavior involves two mechanical effects. First, changes in pore pressure cause changes in effective stress, which affect the response of the solid (for example, a reduction in effective stress may induce plastic yield). Second, the fluid in a zone reacts to mechanical volume changes by a change in pore pressure (FLAC 3D User's Manuel, 2005).

### **6.2.1. Properties and units for fluid flow analysis**

The properties that relate to fluid flow in *FLAC3D* are the permeability coefficient,  $k$ , the fluid mass density,  $\rho_f$ , and either the Biot coefficient,  $\alpha$ , and Biot modulus,  $M$ , for flow through a material with compressible grains, or the fluid bulk modulus,  $K_f$ , and porosity,  $n$ , for flow through a material with incompressible grains only.

#### **6.2.1.1. Permeability coefficient**

The isotropic permeability coefficient,  $k$  (e.g.,  $\text{m}^2/(\text{Pa}/\text{sec})$  in SI units), used in *FLAC3D* is also referred to in the literature as the mobility coefficient. It is the

coefficient of the pressure term in Darcy's law and is related to the hydraulic conductivity,  $k_h$  (e.g., m/s), by the expression:

$$k_h = k g \rho_f \quad (6.1)$$

where  $g$  is the gravitational acceleration.

The following conversion may be given to calculate  $k$  in SI units for water in *FLAC3D*:

$$k \text{ (in SI units)} \equiv k_h \text{ (in cm/sec)} \times 1.02 \times 10^{-6}$$

### 6.2.1.2. Mass density

If *FLAC3D* is configured for fluid flow, then the dry density of the solid material must be used. *FLAC3D* will compute the saturated density of each element using the known density of the fluid, the porosity,  $n$ , and the saturation,  $s$ :  $\rho_s = \rho_d + ns\rho_f$ . All densities are zone variables in *FLAC3D* and are mass densities (e.g., kg/m<sup>3</sup> in SI units).

### 6.2.1.3. Fluid bulk modulus

In analyses where the grain compressibility can be neglected, fluid bulk modulus,  $K_f$ , can be utilized. The bulk modulus,  $K_f$ , is defined as:

$$K_f = \frac{\Delta P}{\Delta V_f / V_f} \quad (6.2)$$

where  $\Delta P$  is the change in pressure for a volumetric strain of  $\Delta V_f / V_f$ .

In real soils, pore water may contain some dissolved air or air bubbles, which substantially reduce its apparent bulk modulus.

#### **6.2.1.4. Porosity**

Porosity,  $n$ , is a dimensionless number defined as the ratio of void volume to total volume of an element. It is related to the void ratio,  $e$ , by:

$$n = \frac{e}{1 + e} \quad (6.3)$$

Porosity is used by *FLAC3D* to calculate the saturated density of the medium and evaluate Biot modulus in the case when the fluid bulk modulus is given as an input.

#### **6.2.1.5. Saturation**

Saturation,  $s$ , is defined as the ratio of pore volume occupied by fluid to total pore volume. Although the initial saturation assumed as 1 in the model, it is also updated during *FLAC3D*'s calculation cycle as necessary to preserve the mass balance.

#### **6.2.1.6. Fluid tension limit**

In fine soils, the pore water may be able to sustain a significant tension. In *FLAC3D*, negative pore pressures can develop, by default, up to a limit beyond which desaturation will take place. It should be noted that a negative pore pressure is not the same as “tension” due to capillary.

In considerations of the information above, properties of fluid-flow analysis and physical soil parameters were tabulated in Table 6.1. It should be noted that physical soil parameters are the same parameters used in Chapter 4 since the aim of this Chapter is to investigate the contribution of groundwater drainage on ground deformations at the same site.

**Table 6.1.** Properties of fluid-flow analysis and physical soil parameters.

Property	Values			
	Fill	qa1	qa2	qa3
Bulk Modulus (kPa)	$12.5 \times 10^3$	$4.17 \times 10^6$	$3.77 \times 10^6$	$4.37 \times 10^6$
Shear Modulus (kPa)	$6.0 \times 10^3$	$84 \times 10^3$	$76 \times 10^3$	$88 \times 10^4$
Cohesion (kPa)	70	89.2	80.8	93.5
Friction angle (degree)	1	1	1	1
Density ( $\text{kg/m}^3$ )	1800	1900	1900	1900
Porosity	-	0.35	0.35	0.35
Permeability ( $\text{m}^2/(\text{Pa} \cdot \text{sec.})$ )	-	$1 \times 10^{-12}$	$1 \times 10^{-11}$	$1 \times 10^{-12}$
Fluid Modulus (kPa)	$1 \times 10^5$			
Fluid density ( $\text{kg/m}^3$ )	1000			
Fluid tensile strength (kPa)	0			

### 6.2.2. Fluid-flow boundary conditions

Boundaries are impermeable and this is the default condition in *FLAC3D*. That means there is no exchange between the grid and the outside world. Pressure and saturation changes are computed depending on the current value of saturation and whether the fluid has fallen below the tensile limit or not. Boundaries may also be fixed indicating permeable boundaries across which fluid flows to and from the outside world. But, in this situation, saturation is forced to be one by the code. This was not the case for this study since pumping wells were also modeled.

At Necatibey Station, groundwater inflow has occurred during face excavation. This was the reason to stop excavation work between August 14<sup>th</sup>, 2006 and November 21<sup>st</sup>, 2006. Three pumping wells were immediately installed and groundwater drainage work started. During three months, only water drainage work was undertaken. Then excavation work was started again and both drainage

and excavation were carried on together for an additional three months until February 18<sup>th</sup>, 2007. These three pumping wells whose locations indicated in Figure 1.2 as Kuyu 1, Kuyu 2 and Kuyu 3 were included in the models with a total rate of pumping of 8 l/sec. for current study.

### **6.2.3. Coupled fluid-mechanical calculations**

By default, *FLAC3D* can do a coupled fluid flow and mechanical calculation if the grid is configured suitable for this and if the Biot modulus, or fluid bulk modulus, and permeability are set to realistic values.

The relative time scales associated with consolidation and mechanical loading should be appreciated. Mechanical effects occur almost instantaneously (on the order of seconds or fractions of seconds). However, fluid flow is a long process: the dissipation associated with consolidation takes place over hours, days or weeks.

In most modeling situations, the initial mechanical conditions correspond to a state of equilibrium must first be achieved before the coupled analysis is started. Typically, a certain number of mechanical steps must be taken for each fluid step to allow the system to adjust according to the different time scales involved. A corresponding numerical simulation was generated in combination with appropriate settings. Firstly a mechanical force limit was set to limit the out of balance force under which mechanical equilibrium would be assumed. Secondly, certain substeps were introduced to the code to be taken by mechanical and fluid modules. Finally, the computation was maintained until the fluid-flow time (6 months) is reached.

### **6.3. Steps towards numerical models**

In order to simulate groundwater drainage at Necatibey Station and to estimate resultant ground deformations fully coupled 3 dimensional models were set up at this stage. The steps followed to construct the models were itemized below.



### 6.3.1. Grid generation

The same grid (geometry) used in Chapter 4 was utilized here for the basis of numerical models. As remembered, the model dimensions were 52 m, 60 m, and 32.60 m in x, y, z directions respectively (Figure 6.1). As it can be seen from Figure 6.1 the model consists of three layers namely fill (dm, 0-5.30 m), alluvium (qa, 5.30-17.30 m) and Ankara Clay (Tg, 17.30-32.60 m) from top to bottom.

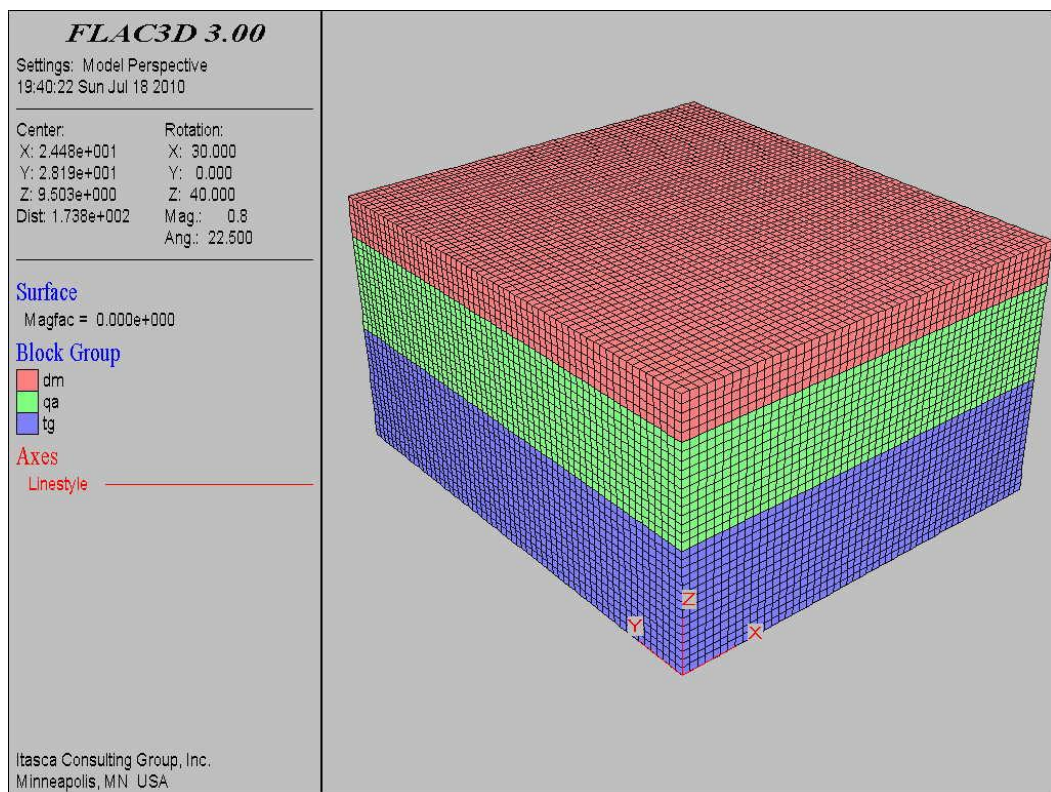


**Figure 6.1.** *FLAC 3D* grid showing the geometry of fluid-flow analysis.

The other steps for setting up the model is going to be discussed under following subtitles, but it is a good point to state that the clay layer (light blue in color in Figure 6.1) occupying bottom of the model was omitted during analyses to reduce run times. It has been thought that settlements due to the groundwater drainage

would be negligible in the lower clay layer and thus this layer was omitted in the model. Therefore, following figures in this chapter will not include the clay layer at all. Another important point need to be emphasized here is that the alluvium layer (green in color in Figure 6.1) was divided into three zones at every 20 m intervals along the y-direction in order to simulate lateral changes in soil properties as it was in Chapter 4. Resultant geometry of the model analyzed in this chapter is shown in Figure 6.2. This final grid contains 56.160 zones and 61.427 gridpoints.

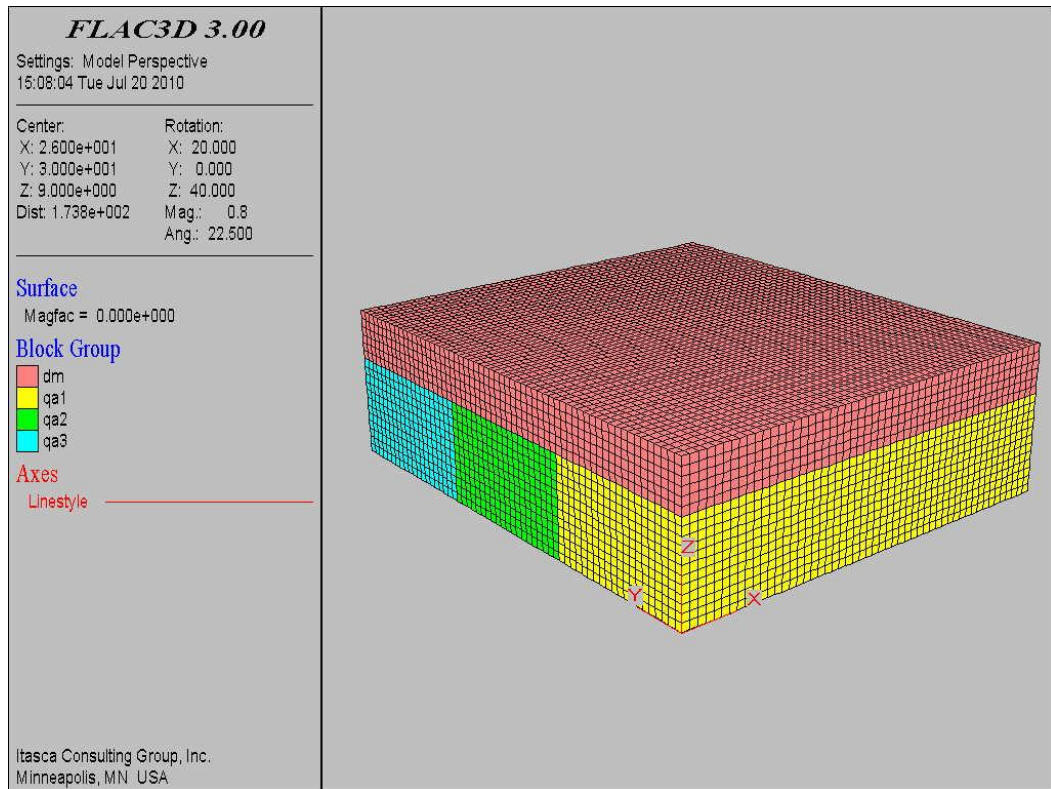


**Figure 6.2.** *FLAC 3D* grid showing the analyzed geometry of the problem.

Once the grid generation is completed, material model and associated properties must be assigned to all zones in the model. Constitutive behavior (the Mohr-Coulomb) and physical material properties (mass density, deformability properties

(K, G), strength properties ( $c$ ,  $\phi$ ) were kept the same with their values used in Chapter 4.

### 6.3.2. Boundary and initial conditions

The boundary conditions for fluid-flow analysis were set up as shown in Figure 6.3.

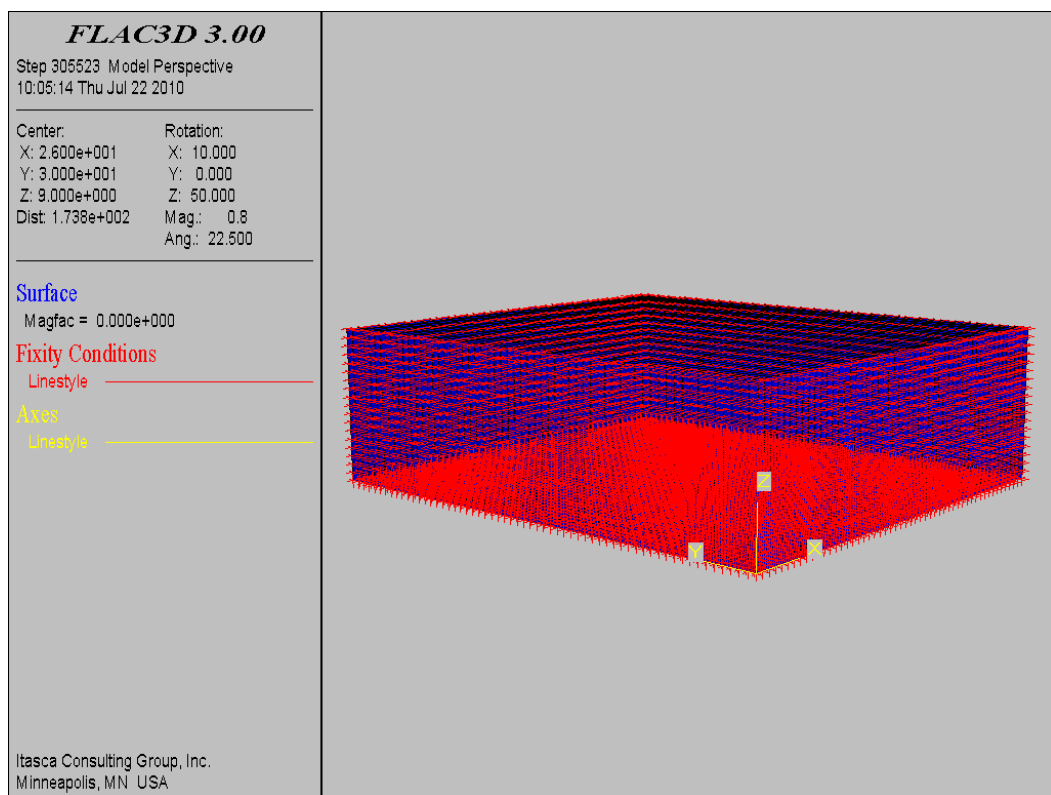


**Figure 6.3.** Boundary conditions for fluid-flow analysis.

Roller boundaries were placed on four sides of the model. The boundaries are fixed only in the specified direction (i.e., no displacement or velocity is allowed). The following functions were performed:

- (i) The gridpoints along the boundary planes at  $x = 0$  and  $x = 52$  were fixed in the  $x$  and  $y$ -directions.
- (ii) The gridpoints along the boundary planes at  $y = 0$  and  $y = 60$  are fixed in the  $x$  and  $y$ -directions.
- (iii) The gridpoints along the bottom boundary ( $z = 0$ ) are fixed in the  $x$ ,  $y$ ,  $z$ -directions.

Since near the ground surface, the variation in stress with depth cannot be ignored, gravitational acceleration was operated on the grid. It is important to understand that the gravity does not directly cause stresses to appear in the grid; it simply causes body forces to act on all gridpoints. These body forces correspond to the weight of material surrounding each gridpoint. If no initial stresses are present, the forces cause the material to move (during stepping) in the direction of the forces until equal and opposite forces are generated by zone stresses. Given the appropriate boundary conditions (e.g., fixed bottom, roller side boundaries), the model generates its own gravitational stresses that are compatible with the applied gravity.

Pore pressures were also initialized in the same way as stresses to the alluvium layer. The gridpoint pore pressures are initialized rather than the zone pore pressures. Zone pore pressures are derived from gridpoint pore pressures by averaging and then are used to calculate effective stresses needed by the constitutive models.

#### **6.4. Assumptions**

In addition to the assumptions made in Chapter 4, following three assumptions were considered for fluid-flow couple analysis:

- (a) Poisson's ratio was assumed to be 0.35 in all analyses.
- (b) Alluvium layer was assumed as fully saturated.
- (c) Total rate of groundwater drainage was kept constant during analyses and it was 8 l/sec.

## 6.5. Deformation measurements

Recorded deformation measurements were supplied by GÜRIŞ Construction and Engineering Co. Inc. and illustrated in Appendix D. As mentioned before, at Necatibey Station, groundwater inflow has occurred during face excavation and excavation work was stopped for a three months period between August 14<sup>th</sup>, 2006 and November 21<sup>st</sup>, 2006. Three pumping wells were immediately installed and groundwater drainage work started with a total rate of pumping of 8 l/sec. During three months only water drainage work was undertaken. Then excavation work was started again and both drainage with a low rate (about 3.5 l/sec) and excavation were carried on together for an additional three months until February 18<sup>th</sup>, 2007. Maximum deformation measurements caused only by drainage work between August 14<sup>th</sup>, 2006 and November 21<sup>st</sup>, 2006 were plotted in Figure 6.4.

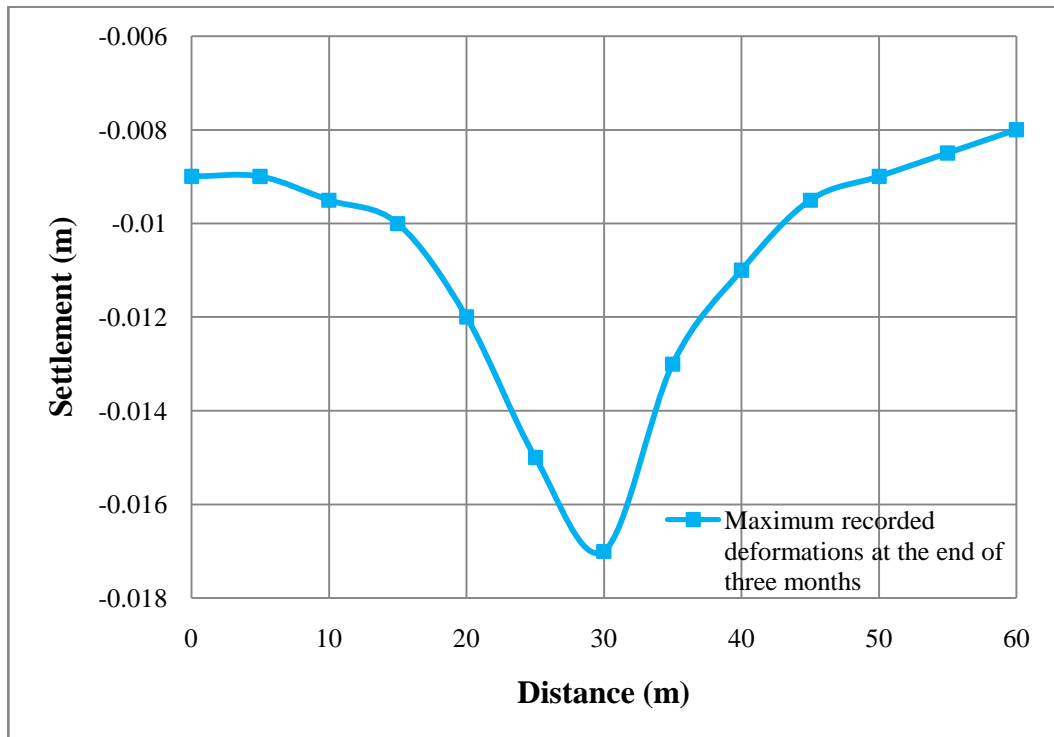


**Figure 6.4.** Maximum recorded deformations at the end of three months period for Line 2 surface points 8, 9, 10, 11, 12, 13, 14, 15, 16, 17, 18, 19, 20.



Although it seems there is a dramatic change in the values, the curve is actually varying from 8 mm to 17 mm.

## 6.6. Results

Based on the fluid-flow properties and calibrated physical soil properties tabulated in Table 6.1 coupled analysis were run to estimate ground deformations caused by pumping of groundwater. Although different time scales (1, 2, 3, 4, 5, 6, 7, 14, 28, 60, 90, 120, 150, 180 days) were introduced to the code, the results obtained at three months (between August 14<sup>th</sup>, 2006 and November 21<sup>st</sup>, 2006) were considered to simulate only drainage effects. The numerically obtained maximum settlement values were plotted below in Figure 6.5 along with distance.

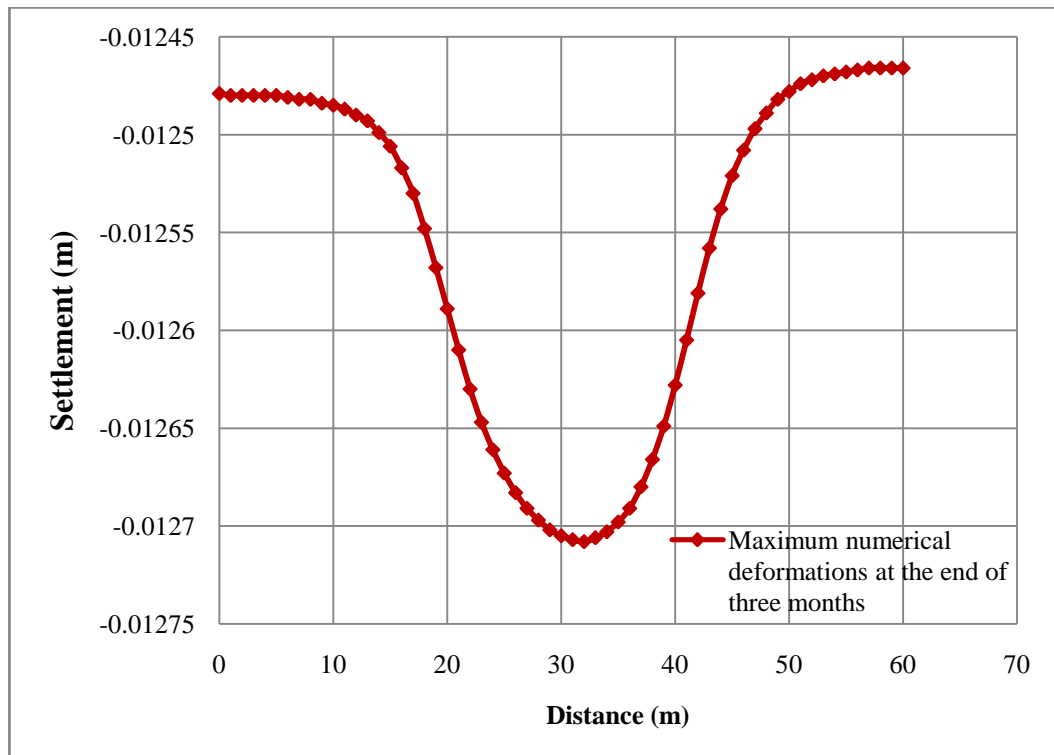


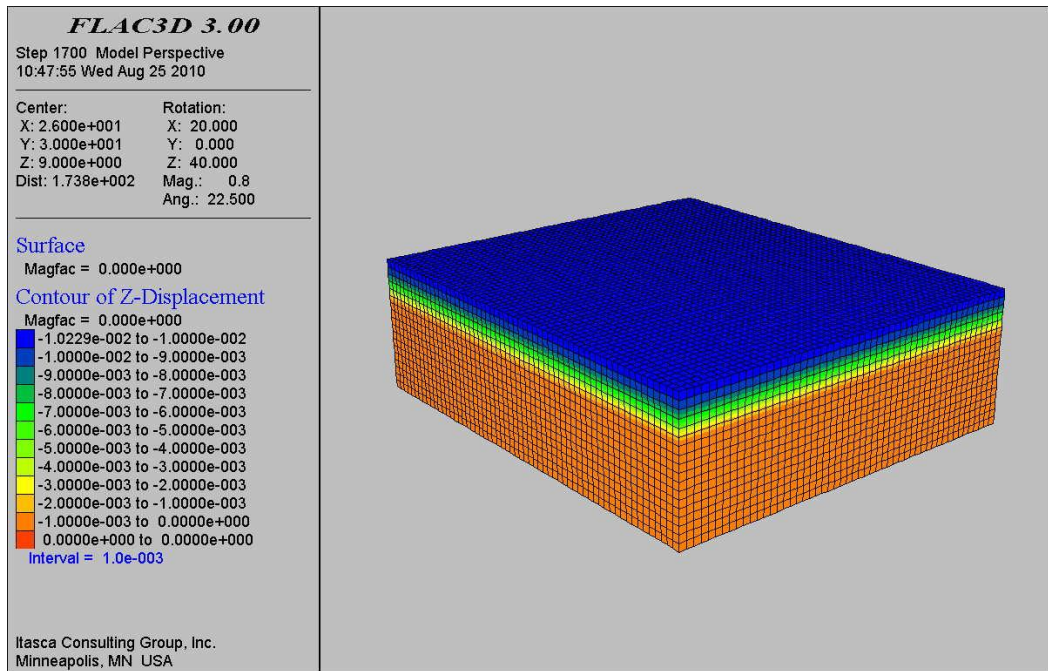
**Figure 6.5.** Maximum numerical deformations at the end of three months period for Line 2 surface points 8, 9, 10, 11, 12, 13, 14, 15, 16, 17, 18, 19, 20.

The curve illustrated in Figure 6.5 actually represents the numerical results run for a six month period to capture the maximum settlement values with the calibrated soil properties tabulated in Table 6.1. The results show that groundwater drainage at the site can cause about 1.3 cm maximum settlement and this value is a kind of average value of recorded deformation values.

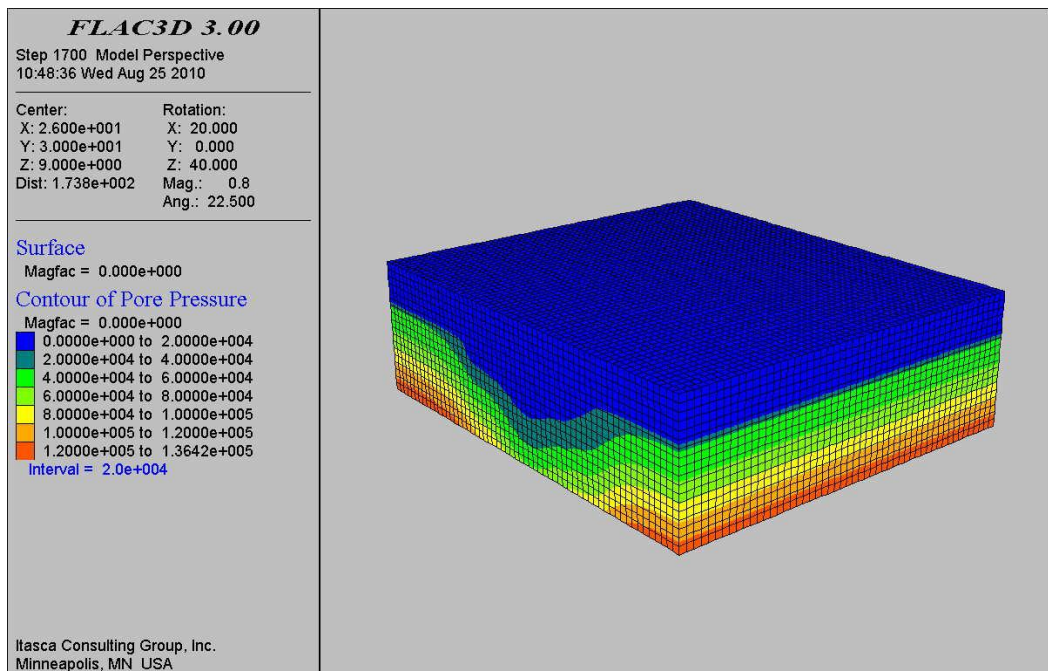
Graphical numerical results were also represented in Figure 6.6 through Figure 6.19. These graphs visualize the pore pressure contours after the drainage of groundwater as well as the total displacement contours due to the process of consolidation. The variations in z-displacement (vertical) and pore pressure can be easily noticed with elapsed time in these contour plots. Figures were arranged in the order of time taken (1, 2, 3, 4, 5, 6, 7, 14, 28, 60, 90, 120, 150, 180 days). As shown from the figures, maximum z-displacement is varying from  $1.0229 \times 10^{-2}$  m for one day to  $1.2774 \times 10^{-2}$  m for 180 days with a small variation. Maximum pore pressure is increasing slightly due to the effect of gravitational loading and then decreasing with the effect of pumping work. Both z-displacement and pore pressure values with time are tabulated in Table 6.2.

**Table 6.2.** Maximum z-displacement and maximum pore pressure values with varying time.

<b>Time (day)</b>	<b>z_displacement (m)</b>	<b>Pore pressure (Pa)</b>
1	$1.0229 \times 10^{-2}$	$1.3642 \times 10^5$
2	$1.5242 \times 10^{-2}$	$1.4414 \times 10^5$
3	$1.2343 \times 10^{-2}$	$1.4448 \times 10^5$
4	$1.2723 \times 10^{-2}$	$1.4406 \times 10^5$
5	$1.2825 \times 10^{-2}$	$1.4331 \times 10^5$
6	$1.2806 \times 10^{-2}$	$1.4195 \times 10^5$
7	$1.2801 \times 10^{-2}$	$1.4040 \times 10^5$
14	$1.2795 \times 10^{-2}$	$1.2850 \times 10^5$
28	$1.2796 \times 10^{-2}$	$1.1841 \times 10^5$
60	$1.2796 \times 10^{-2}$	$1.1758 \times 10^5$
90	$1.2787 \times 10^{-2}$	$1.1758 \times 10^5$
120	$1.2779 \times 10^{-2}$	$1.1758 \times 10^5$
150	$1.2776 \times 10^{-2}$	$1.1758 \times 10^5$
180	$1.2774 \times 10^{-2}$	$1.1758 \times 10^5$

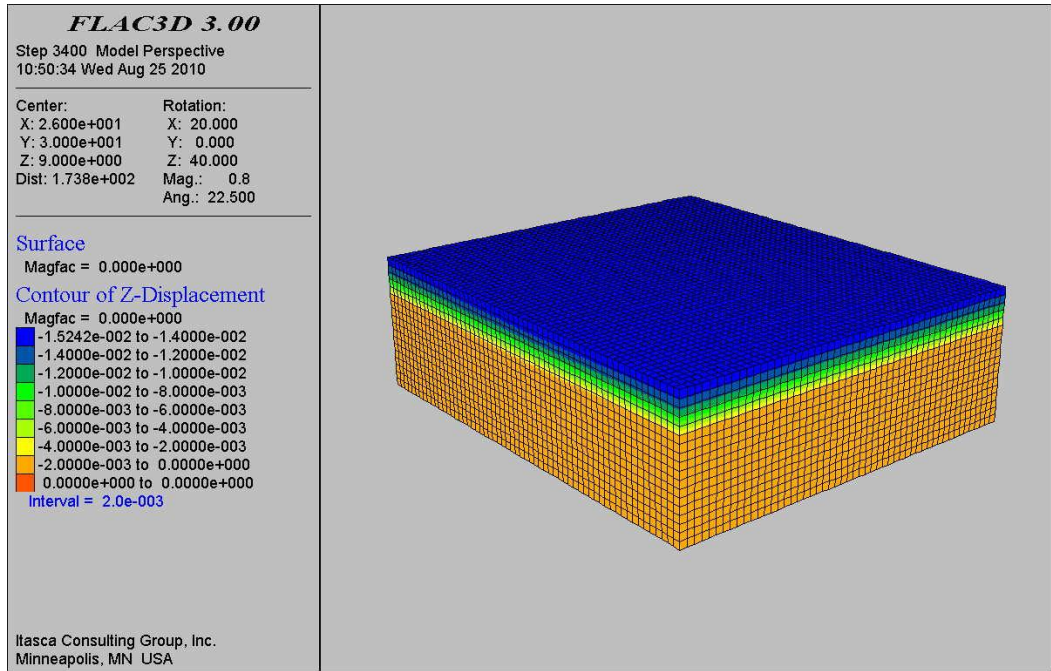


(a)

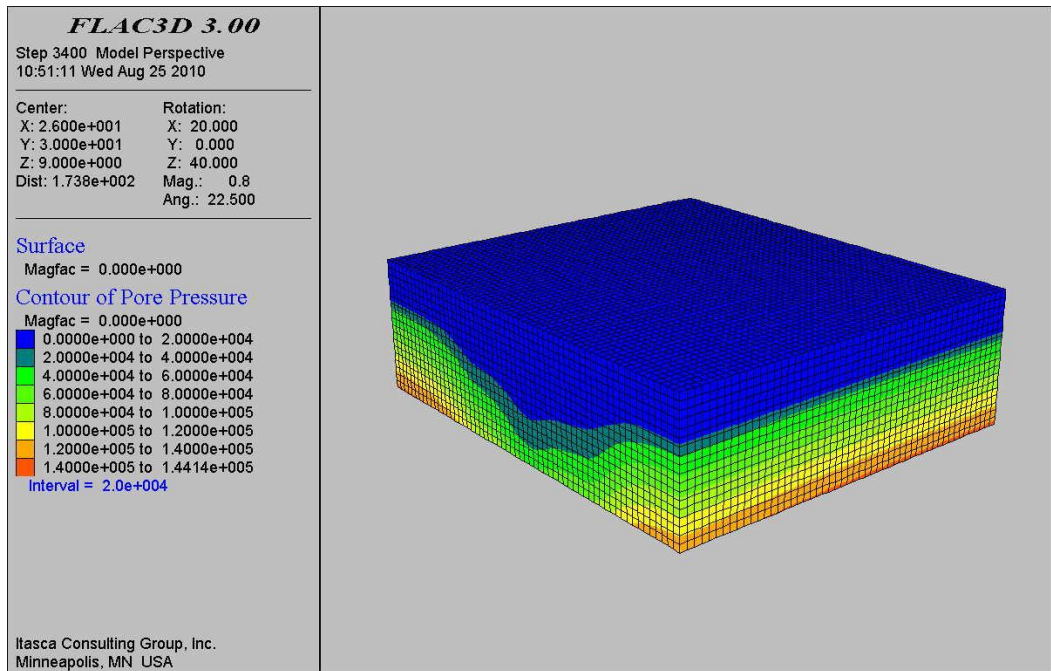


(b)

**Figure 6.6.** Contour plot of a) z-displacement, b) pore pressure for 1 day.



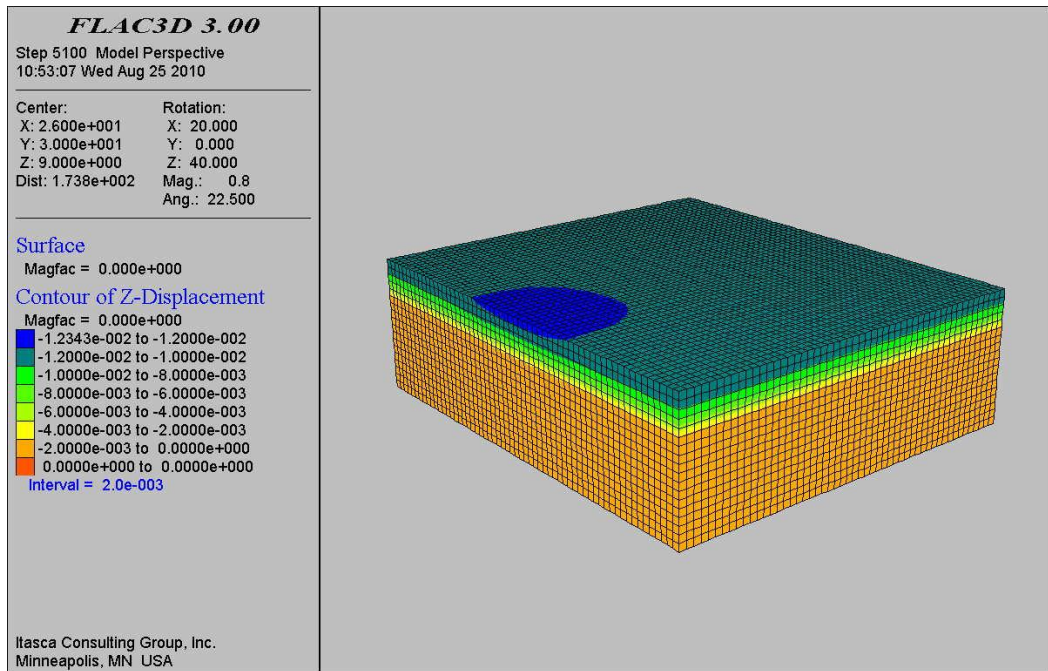
(a)



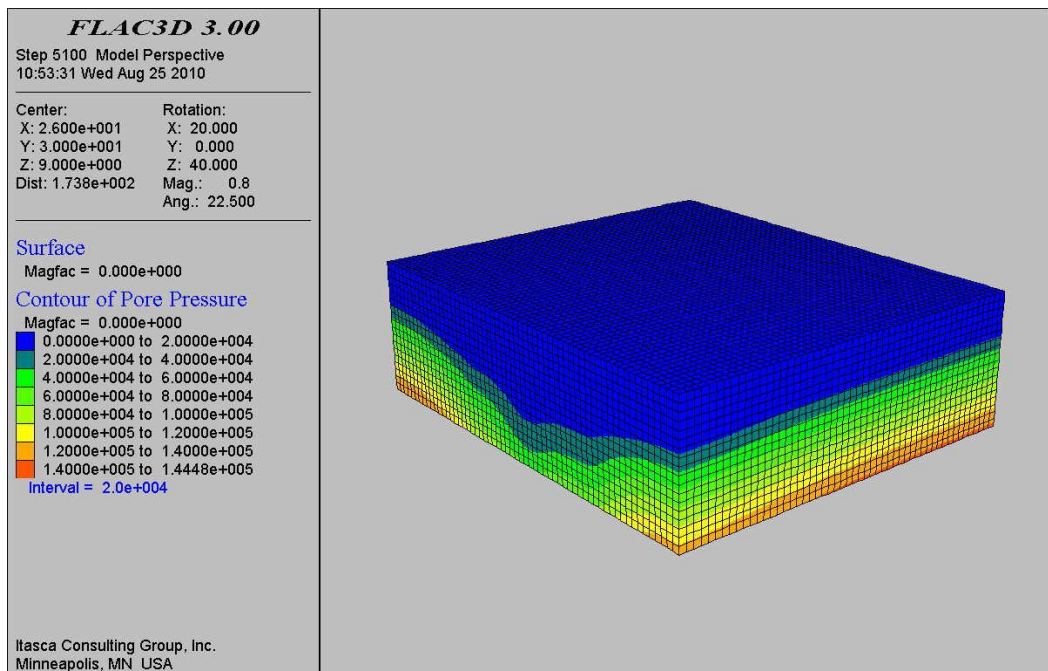
(b)

**Figure 6.7.** Contour plot of a) z-displacement, b) pore pressure for 2 days.



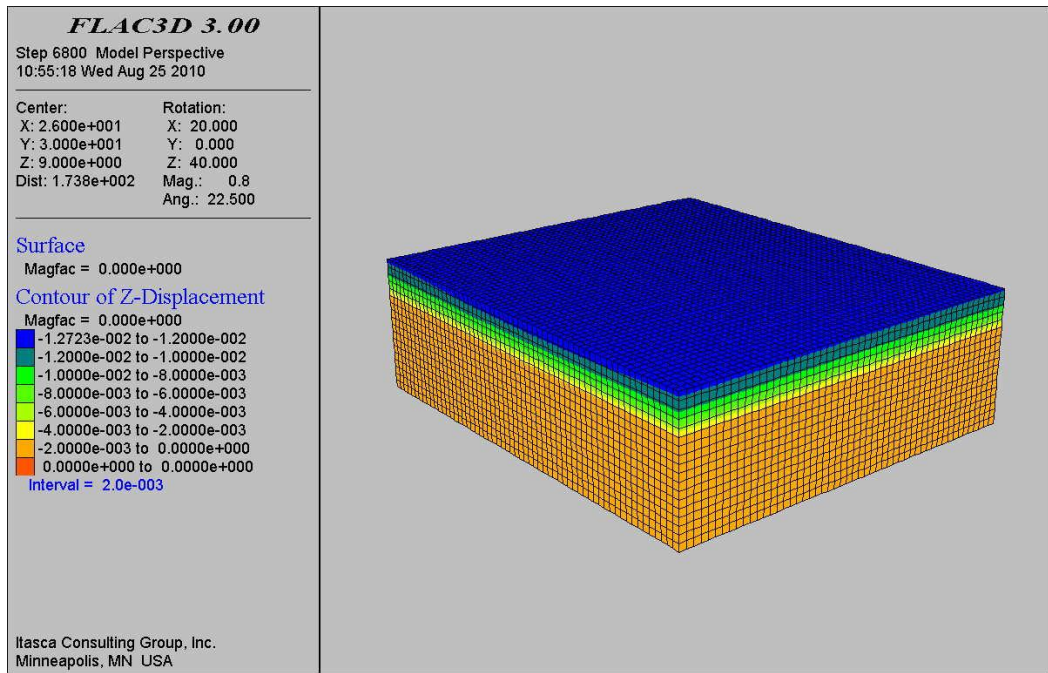


(a)

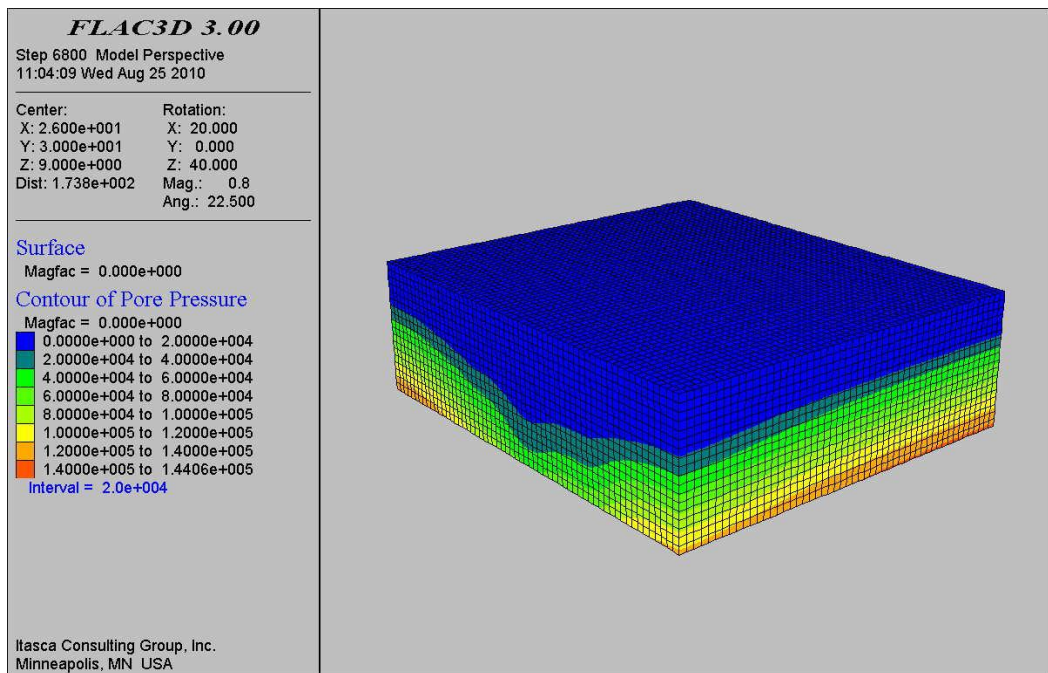


(b)

**Figure 6.8.** Contour plot of a) z-displacement, b) pore pressure for 3 days.

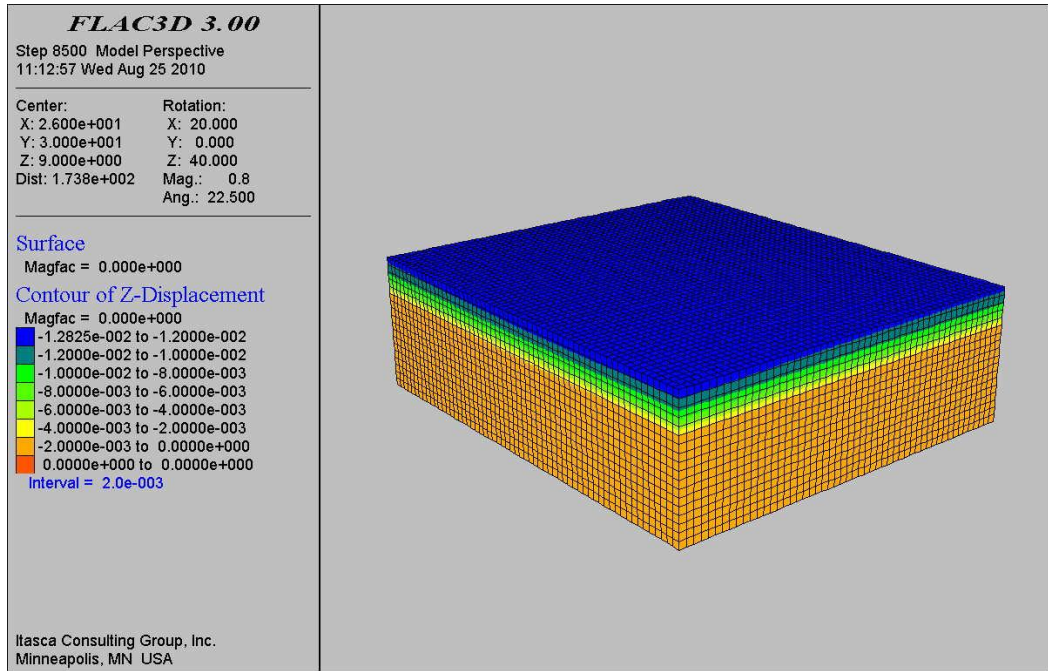


(a)

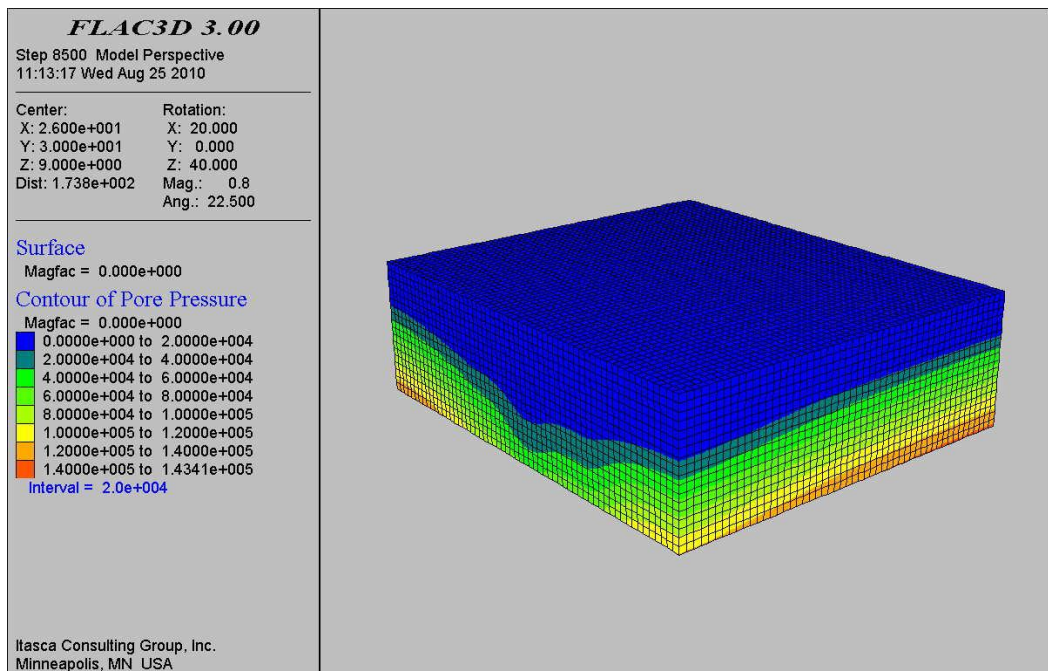


(b)

**Figure 6.9.** Contour plot of a) z-displacement, b) pore pressure for 4 days.



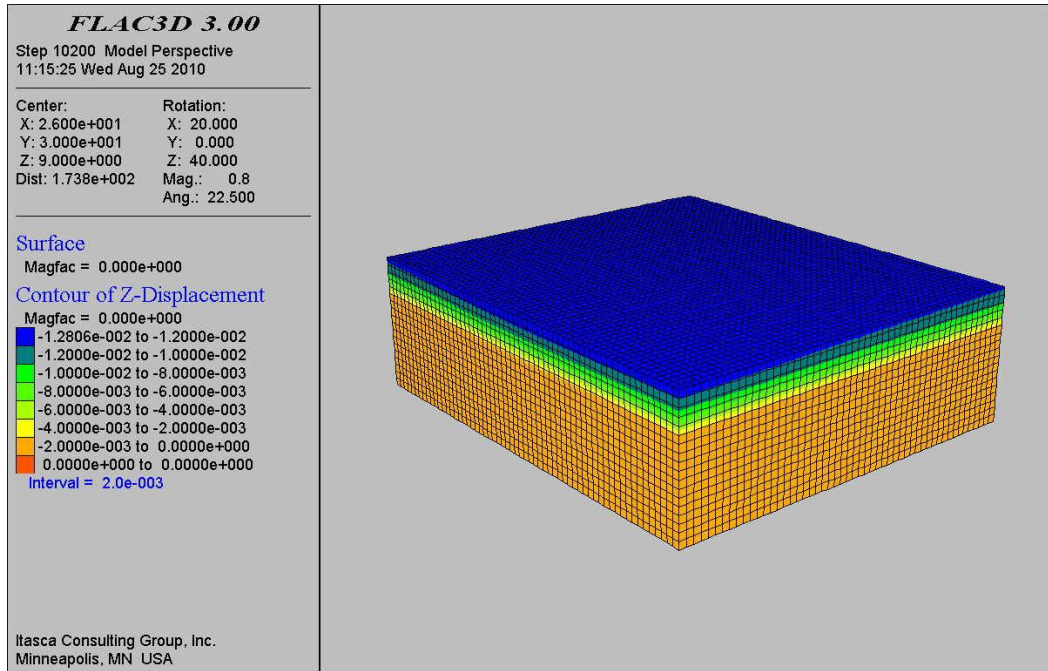
(a)



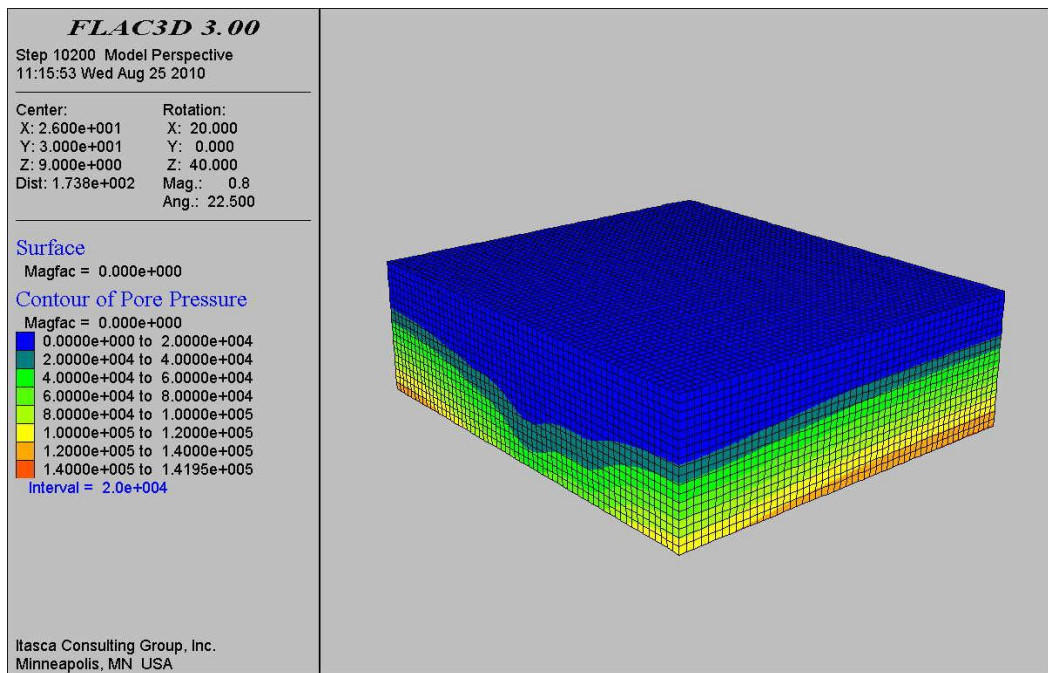
(b)

**Figure 6.10.** Contour plot of a) z-displacement, b) pore pressure for 5 days.



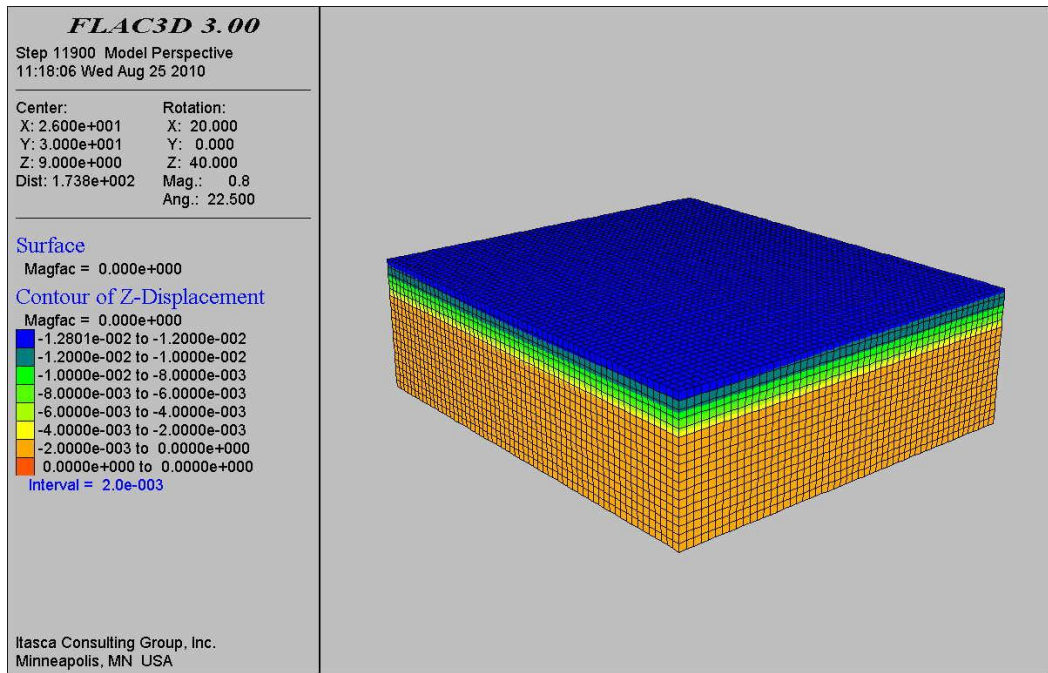


(a)

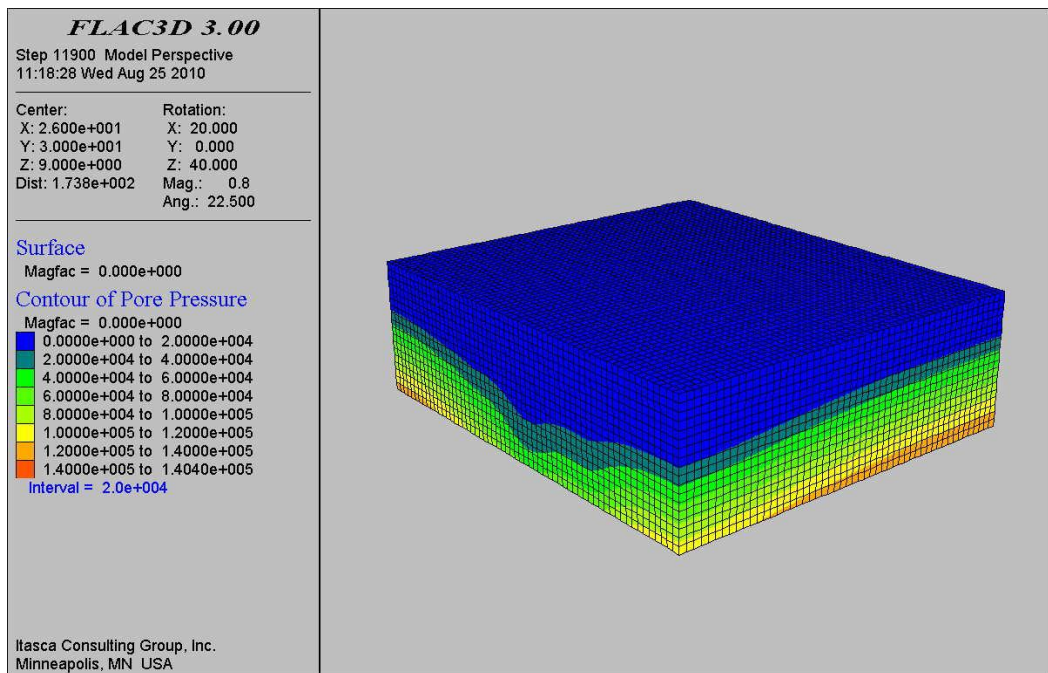


(b)

**Figure 6.11.** Contour plot of a) z-displacement, b) pore pressure for 6 days.



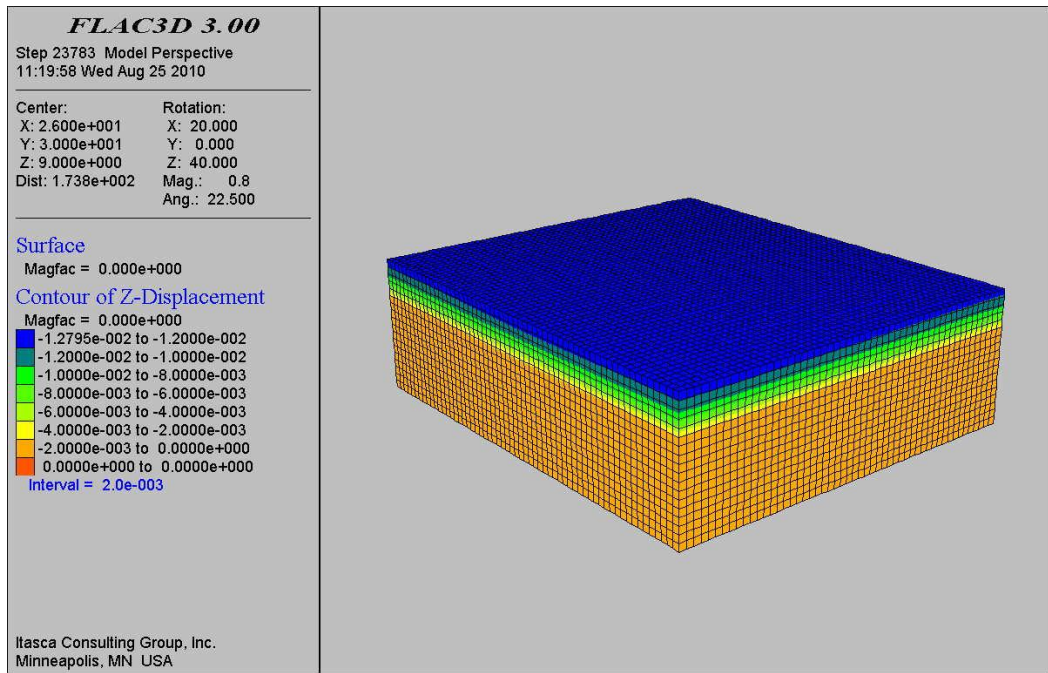
(a)



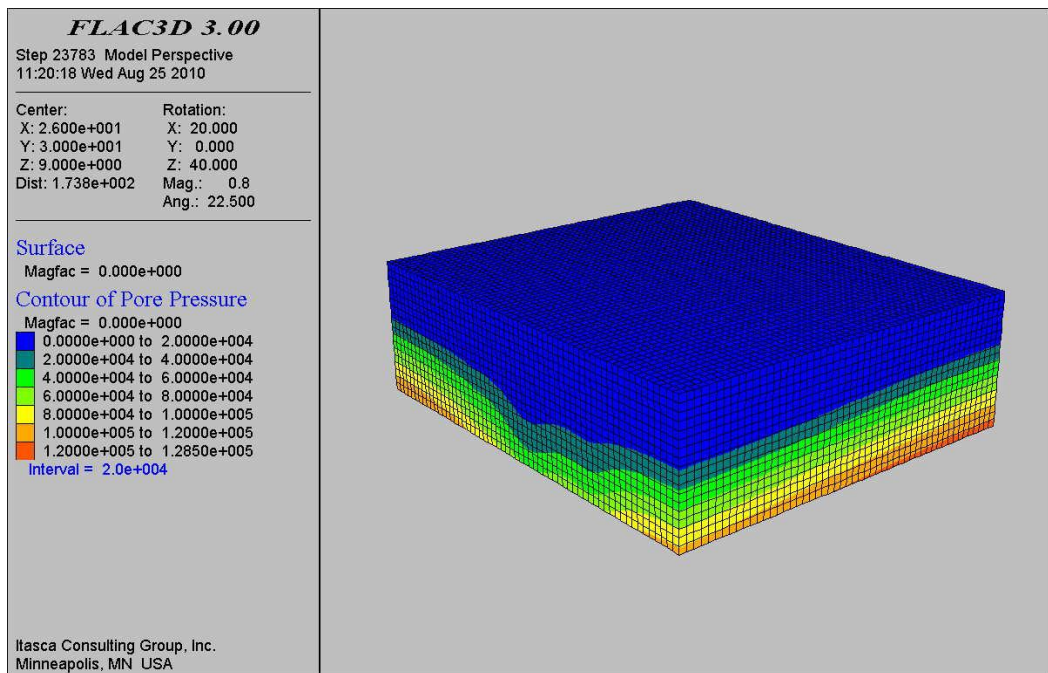
(b)

**Figure 6.12.** Contour plot of a) z-displacement, b) pore pressure for 7 days.



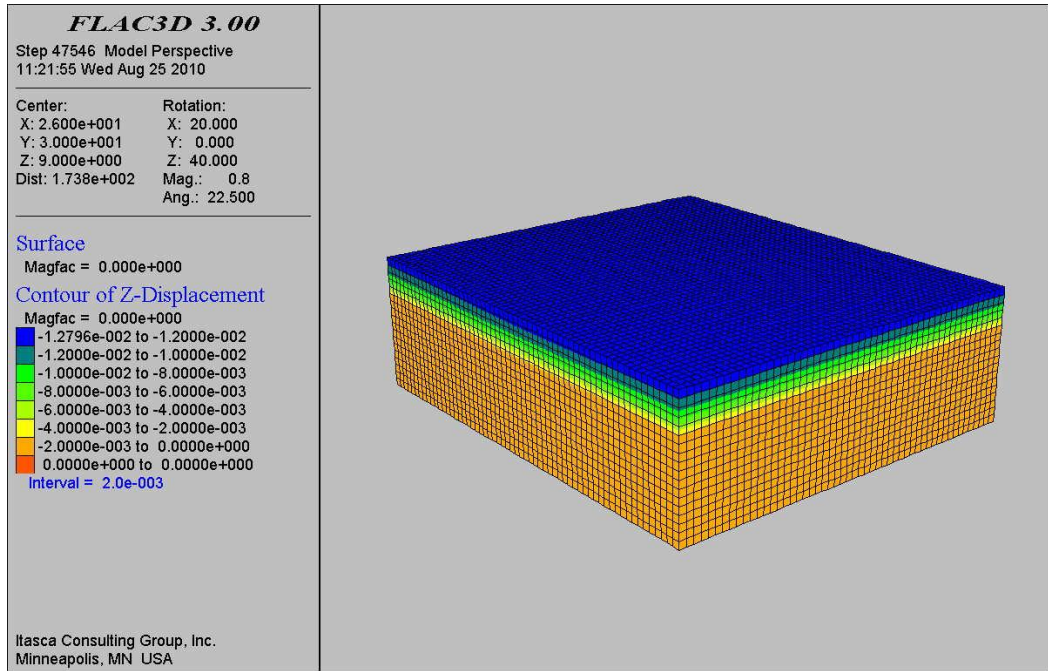


(a)

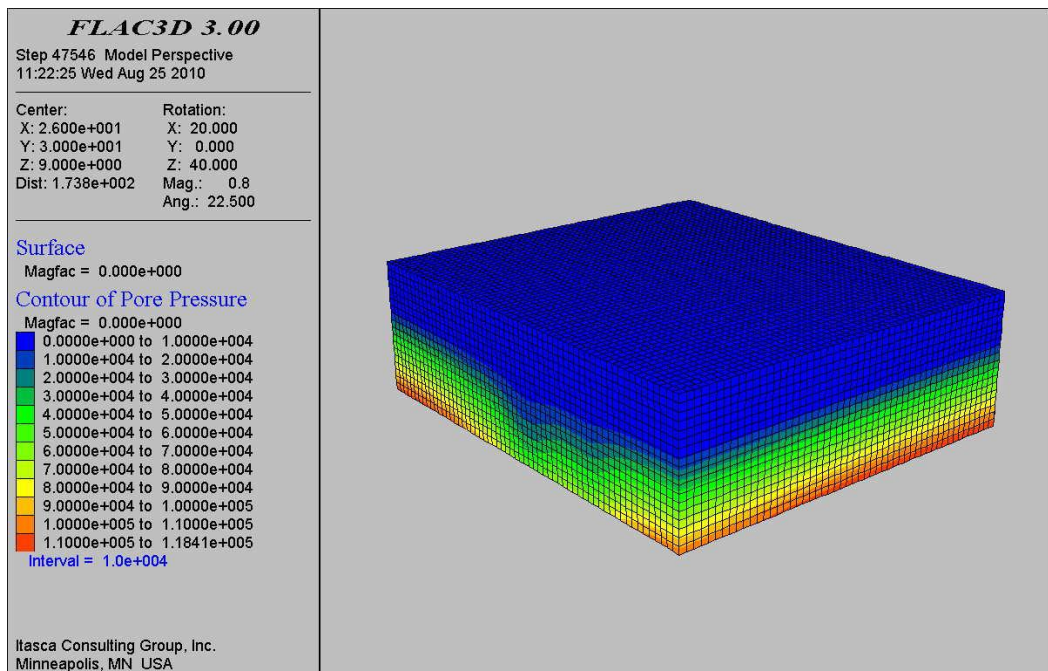


(b)

**Figure 6.13.** Contour plot of a) z-displacement, b) pore pressure for 14 days.

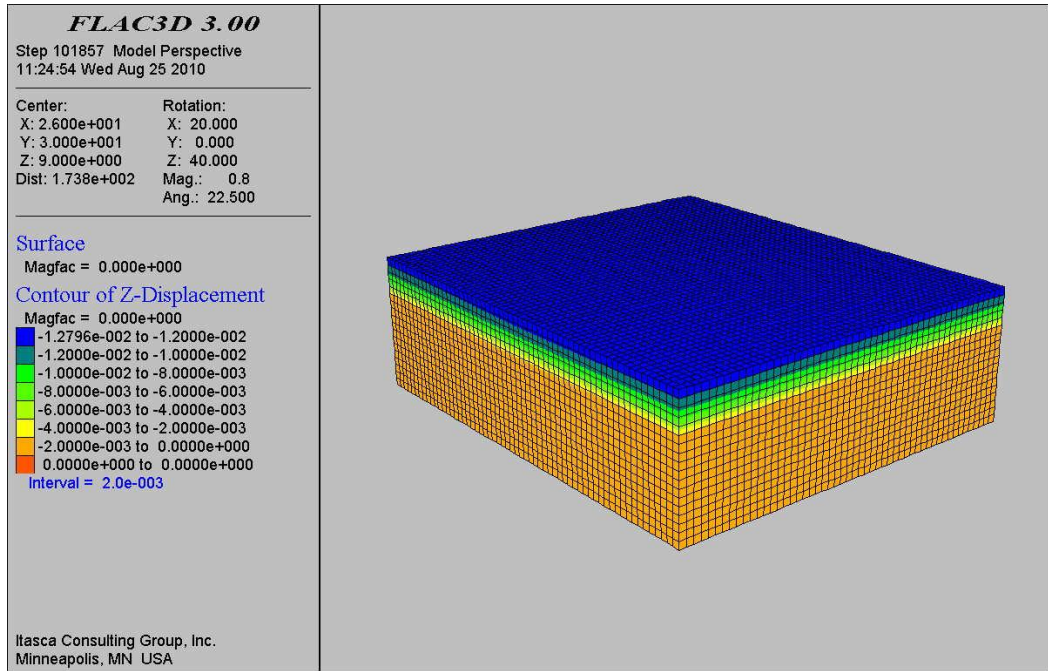


(a)

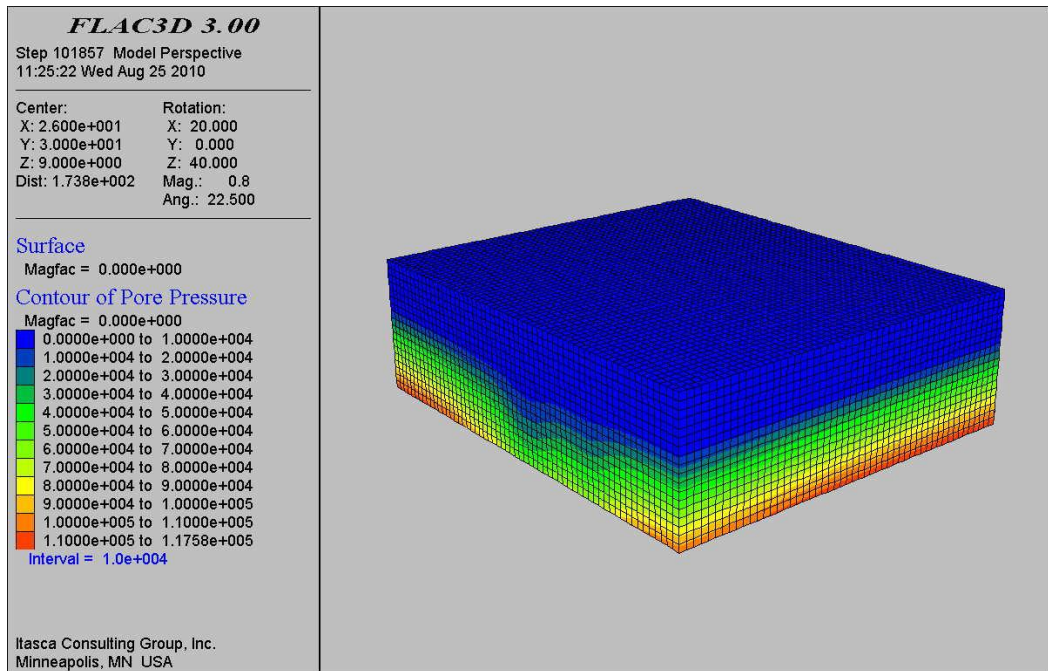


(b)

**Figure 6.14.** Contour plot of a) z-displacement, b) pore pressure for 28 days.



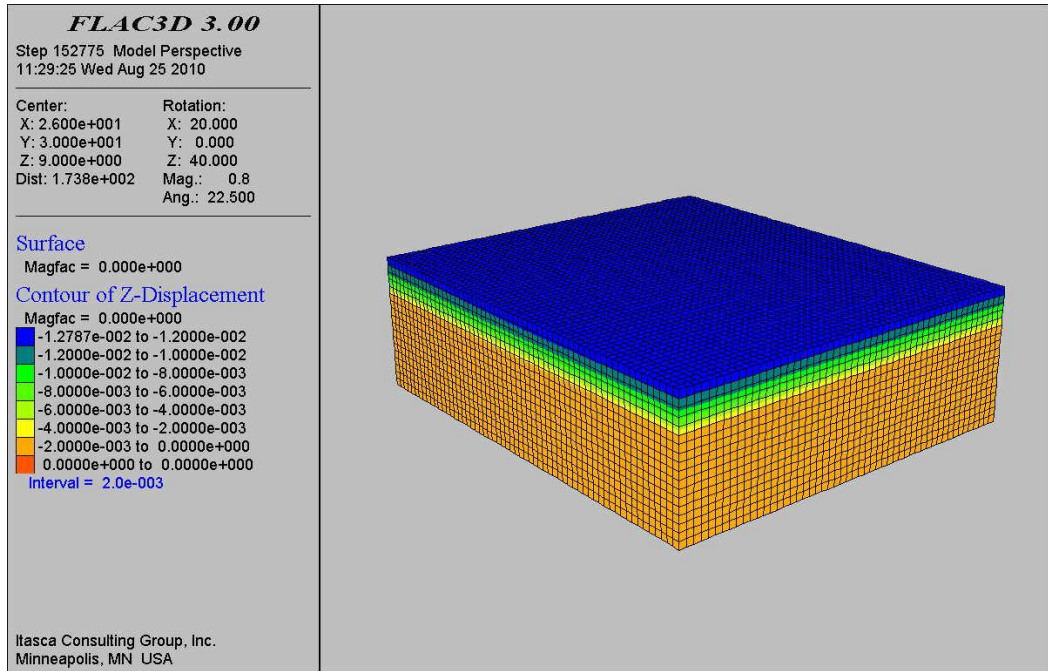
(a)



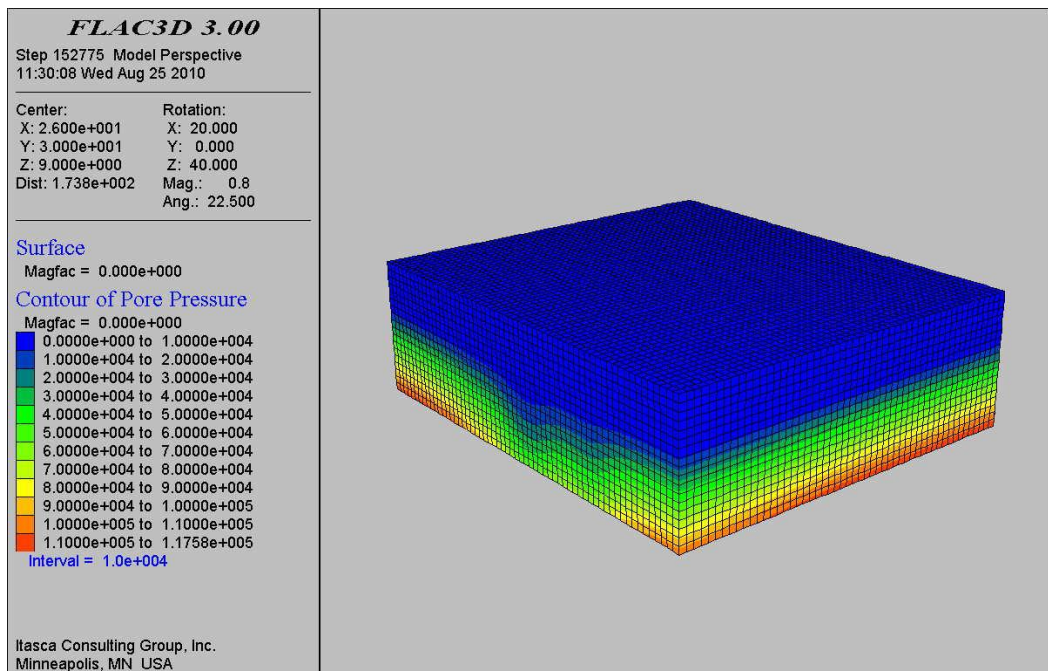
(b)

Figure 6.15. Contour plot of a) z-displacement, b) pore pressure for 60 days.



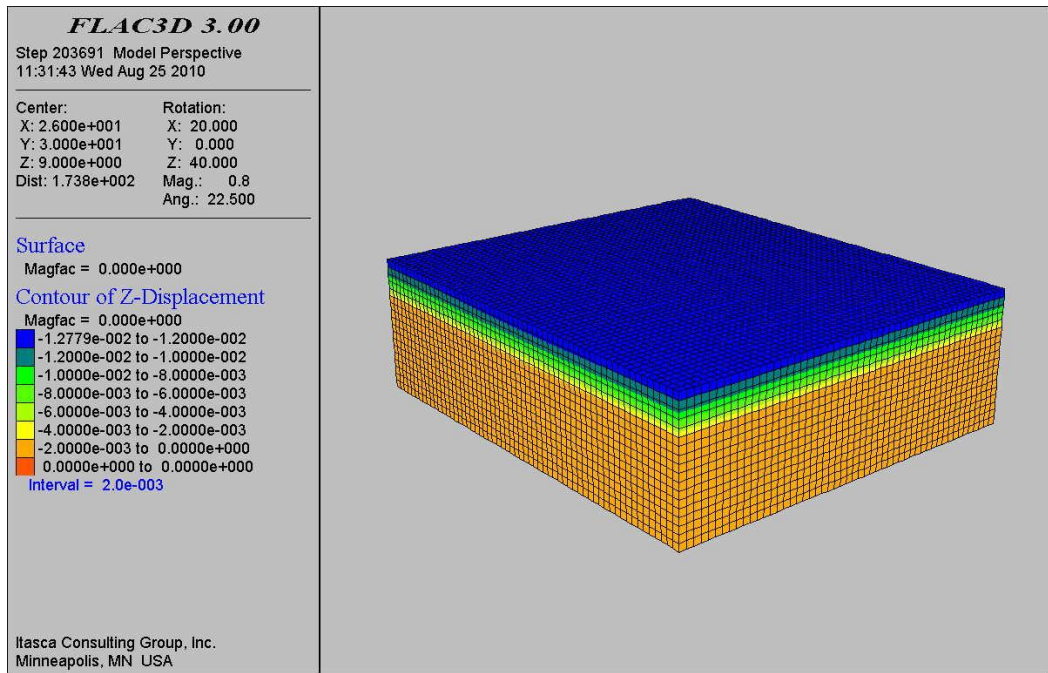


(a)

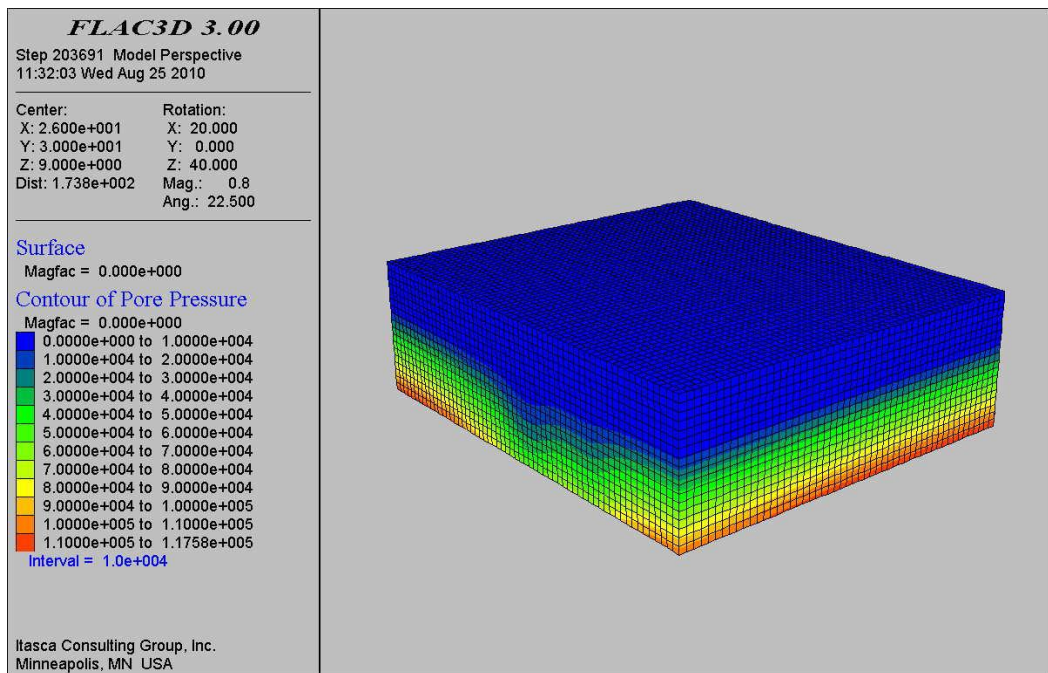


(b)

**Figure 6.16.** Contour plot of a) z-displacement, b) pore pressure for 90 days.



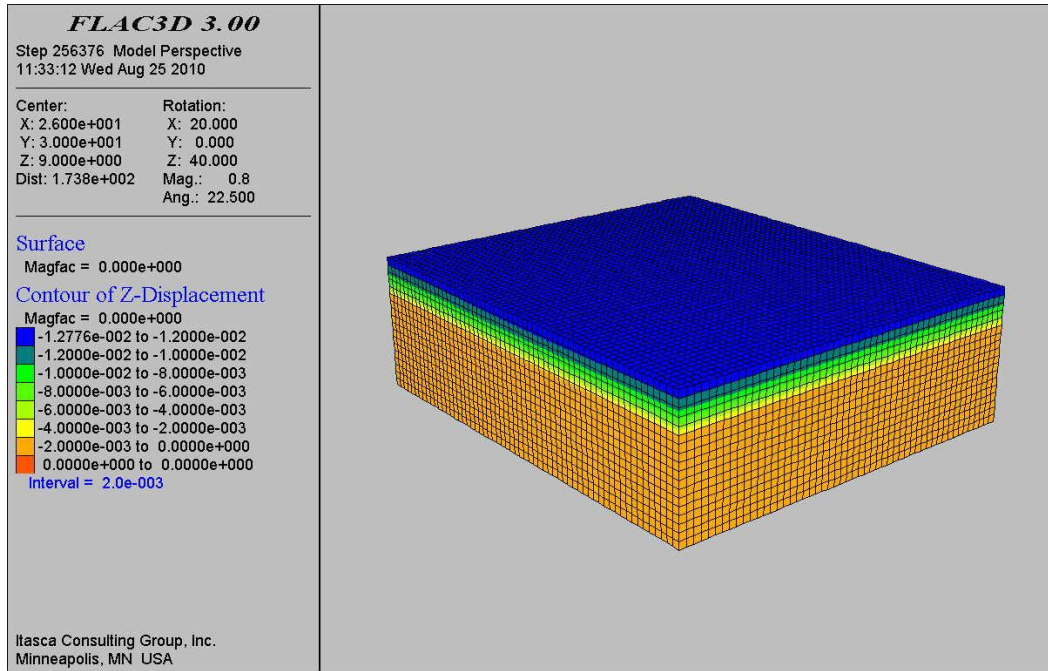
(a)



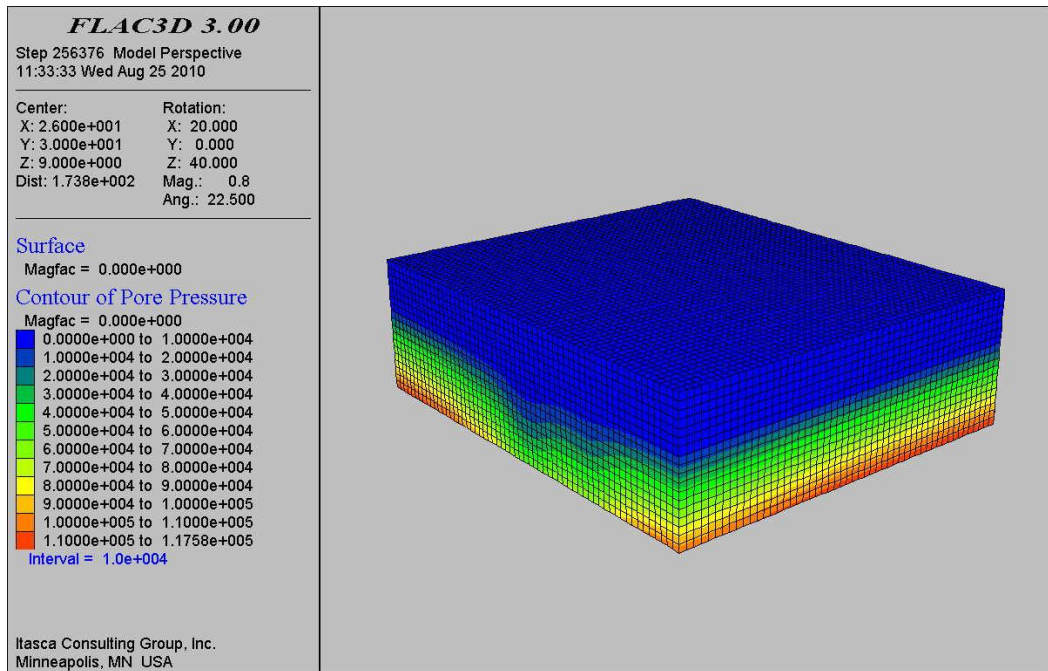
(b)

**Figure 6.17.** Contour plot of a) z-displacement, b) pore pressure for 120 days.



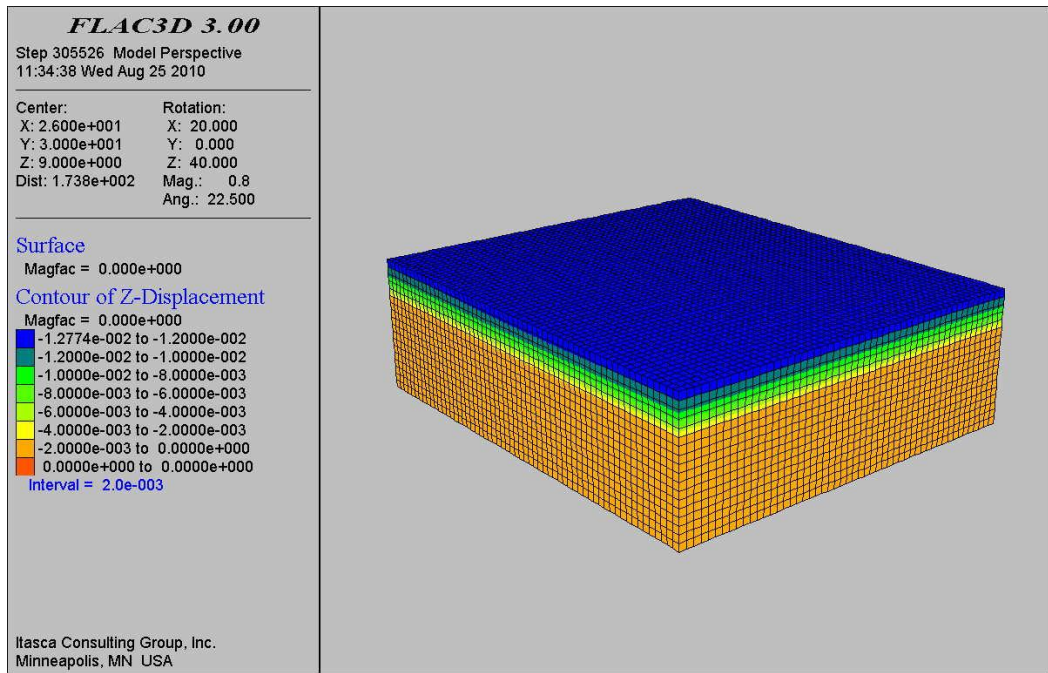


(a)

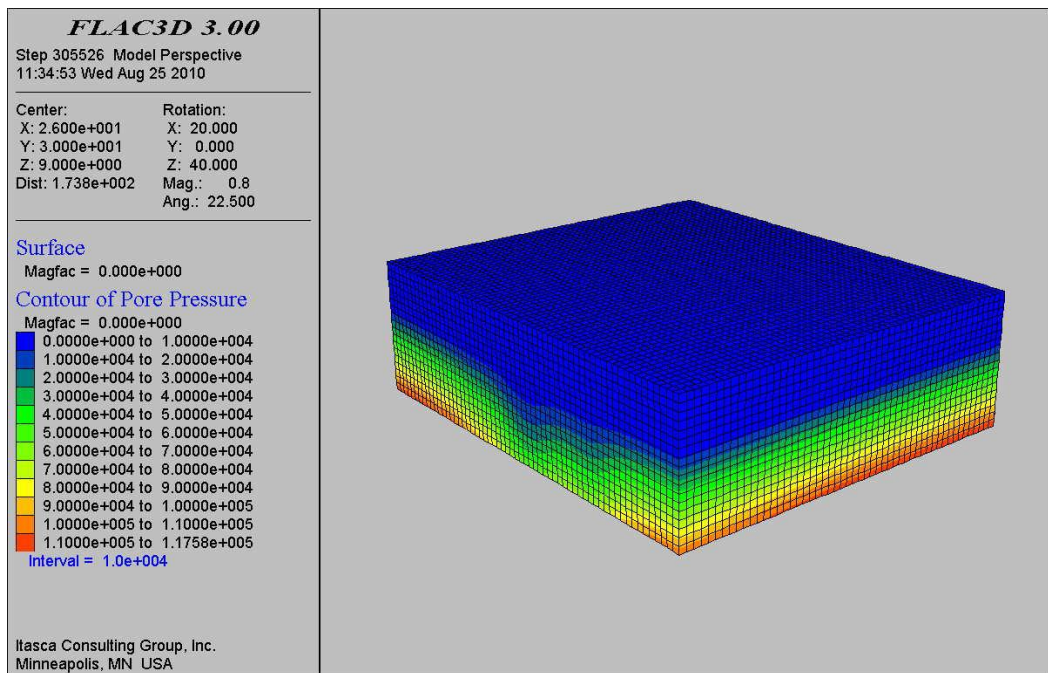


(b)

**Figure 6.18.** Contour plot of a) z-displacement, b) pore pressure for 150 days.



(a)



(b)

Figure 6.19. Contour plot of a) z-displacement, b) pore pressure for 180 days.

## **CHAPTER 7**

### **DISCUSSIONS**

The aim of this chapter is to evaluate the problems faced during the geophysical and numerical modeling studies with discussions. This chapter is divided into two main sections in order to interpret the step by step procedures.

#### **7.1. Geophysical studies**

In this study, one of the effective difficulties associated with Electrical Resistivity Imaging (ERI) was finding sufficient space for the layout of the cables. The study area is located among the buildings of Turkish General Staff, Turkish Air Force and General Directorate of Highways. Due to dense settlement and restrictions imposed by the military buildings available space was highly limited for the layout of the intelligent cables. This was the main reason for limited depth of penetration. Another challenge is that highly conductive surface fill material would confine the current follow in the top layer, and therefore, would limit the amount of information coming from deeper layers.

The resistivity contrast between Ankara clay and the Dikmen Valley alluvium was not significantly high because of high clayey content of the alluvium as well. The sandy and gravelly lenses within the Ankara clay would also respond similarly to those of alluvium.

From the resistivity profile it is confirmed that the foundation soil of the metro station is highly heterogeneous. In the model this heterogeneity is smoothed out by defining a transition zone between the Ankara clay and the alluvial deposits.

GPR results are very site-specific because of the limited depth of penetration in conductive environments, such as in clay and water bearing sediments. The amplitude of EM fields decreases exponentially with depth. In most materials, energy is lost to scattering from material variability. The signal propagates well in sand and gravel while conductive soils such as clay or fill saturated with conductive groundwater cause GPR signal attenuation and loss of target resolution. Because of high clay content of the foundation soils penetration depth of GPR was rather limited.

## **7.2. Numerical modeling studies**

Considering the heterogeneous nature of the foundation material of the construction site the model is modified by considering a transition zone between clay dominant Ankara clay and granular material dominant stream channel deposits. During simulation runs it was aimed to obtain a good match between measured and computed deformations. Various factors, however, affect the shape of the deformation measurements. These are the heterogeneity of the foundation material, excavation-related problems, temporary support systems and delays in their application, hardening of shotcrete, traffic vibrations, and groundwater conditions.

The mechanical behavior of a shotcrete layer, which is often used as a first support in tunneling, varies over time as a result of concrete hardening. This phenomenon should be taken into account in tunneling design because the stress release around the tunnel depends on the distance from tunnel face (Panet and Guenet, 1982) and, thus, on excavation rate and time. For this reason, the global behavior of a supported tunnel (e.g., ground deformations) is influenced by both the increase in stresses related to the tunnel advancement and the increase in mechanical properties of the shotcrete as it hardens. Therefore, the most critical conditions may occur before the full strength of the shotcrete is reached. Although beyond the scope of current study, this effect can be studied by using complex 3-dimensional numerical analyses that are able to model the tunnel excavation advance and the progressive hardening of the concrete or by using 2-dimensional

numerical models that can evaluate the stress release caused by the distance between the tunnel face and the studied section, and consider the corresponding shotcrete properties by referring to its life time (Oreste and Pella, 1997).

Traffic-induced vibrations are a common source of environmental nuisance as they may cause malfunctioning of sensitive equipment, discomfort to people and damage to buildings and underground structures (e.g., tunnels). They are mainly due to heavy lorries that pass at relatively high speed on a road with an uneven surface. Interaction between the wheels and the road surface causes a dynamic excitation, which generates waves that propagate in the soil and impinge on the foundations of nearby structures. Wave propagation is of great importance as it couples the source and the receiver (Lombaert et al., 2000). Therefore, traffic-induced vibrations should be predicted since they may have extra effects on ground deformations during tunneling.

Because deformation curves obtained by numerical modeling tend to be a Gaussian curve, expected fit with recorded deformation curve could not be attained. Thus, rather than seeking the curve match, linear fit lines of both measured and computed deformation data were considered. Figure 7.1 depicts the linear trends of measured and computed data. As seen from the figure, there is a good correlation between the two. The deviation remains within  $\pm 1-2$  cm.

In these model studies, tunnel cross-sections were assumed as circular shape rather than horse-shoe shape due to the difficulties in grid generation option in *FLAC 3D* code especially in simulating tunnel connections. This may also have some effect on the results but it is a preferred assumption in numerical modeling.

It is possible to take advantage of the fact that the geometry and loading in a system are symmetrical about one or more planes. For example, if everything is symmetrical about a vertical plane, then the horizontal displacements on that plane should be zero. When modeling infinite bodies (e.g., underground tunnels) or very large bodies, it may not be possible to cover the whole body with zones, due to constraints on memory and computer time. Artificial boundaries are placed



sufficiently far away from the area of interest such that the behavior in that area is not greatly affected. Boundaries, in this study, might be extended to minimize their effects on the area of interest but it was not possible since the whole grid was constructed by reflecting twelve small bricks. Very long run time was also considered.

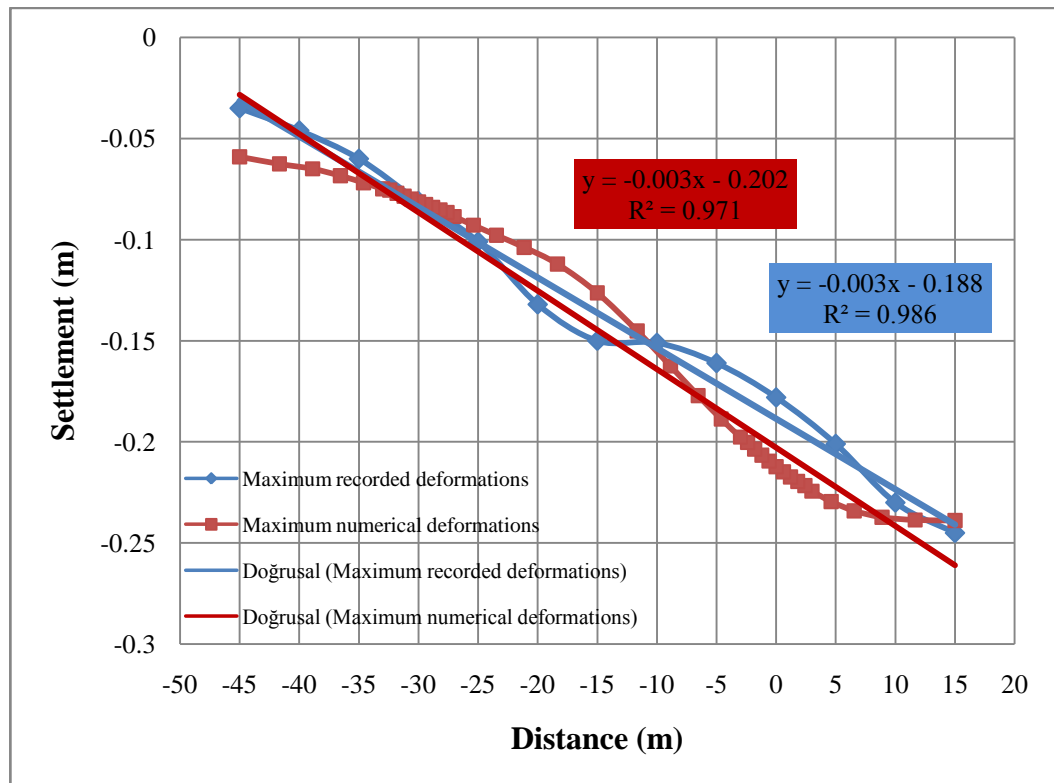


**Figure 7.1.** Correlation of linear trends of measured and computed data.

## CHAPTER 8

### CONCLUSIONS AND RECOMMENDATIONS

This study mainly aims to investigate the efficiency of numerical models for calculating settlements caused by main tunnel excavations, connection tunnel excavations and groundwater drainage at the Necatibey Station of the Ankara Subway System.

Ground movements in response to the tunnel excavations and groundwater drainage will be transmitted to the surface. In order to estimate those movements (deformations) numerically, soil profile has to be constructed precisely. Identifying critical soil profile at the working area is the basis of any numerical modeling.

The Necatibey Station of the Ankara Subway System is located within the alluvial deposits of Dikmen Creek and the so-called Ankara clay. At the subway station a number of boreholes were drilled. However, due to the spacing of the boreholes the boundary between alluvium and Ankara clay deposits could not be separated precisely. Thus, geophysical studies have been planned for the delineation of the boundaries of the two deposits.

Two geophysical methods were used in this thesis, namely Electrical Resistivity Imaging (ERI) and Ground Penetrating Radar (GPR). These two methods are among the most popular near-surface geophysical methods, especially with the advancement in equipment and computing technology. Generally they are time and cost effective and relatively easy to execute. They share a significant physical parameter namely electrical conductivity. This physical parameter provides the means with which the methods are to be integrated as it is the main parameter that

governs the ERI technique and it highly affects the propagation of the GPR signals.

The results of geophysical investigations are presented as 2D images to interpret subsurface profile and results were correlated with boring logs. Using 2D geophysical images and borehole logs 3D subsurface panel diagrams were constructed.

By examining these 3-dimensional subsurface panel diagrams a critical soil profile was chosen in order to construct a basis for the numerical models that utilized to estimate the ground deformations taking place at the Necatibey Station site of the Ankara Subway System and its close vicinity in response to tunnel excavations and groundwater drainage.

After the critical soil profile was identified, numerical modeling studies were initiated to investigate ground deformations caused by main tunnel excavations, connection tunnel excavations and groundwater drainage. With this scope 3-dimensional numerical analyses were performed to investigate mechanical effects of main and connection tunnel excavations on the amount of deformations firstly. Then 3-dimensional coupled analyses were generated to simulate removal of groundwater. Results were then verified by recorded deformation measurements at the site.

In fact, the soil profile used for the numerical models consists of three layers namely artificial fill, alluvium and Ankara clay from the youngest to oldest. Both Ankara clay and alluvium show lateral lithological variation. Therefore, the primary aim of the numerical model was to calibrate soil properties (e.g., bulk modulus, shear modulus, cohesion, etc.) for alluvium layer by modeling sequential excavation steps of main tunnels.

During the model studies first the effect of Necatibey Station tunnels construction on the surface deformations were studied. As expected, majority of surface deformations had occurred in response to the excavation of large diameter station

tunnels. This has contributed more than 90% of the total measured surface deformation of 24.5 cm.

The effects of connection tunnel excavations on ground deformations were also investigated. In order to simulate mechanical excavation of connection tunnels the same models used for the main tunnels were further run with calibrated soil parameters and resultant ground deformations were considered. Deformations occurred on connection tunnel axes after each connection tunnel excavation were investigated firstly. Effects of connection tunnel excavations on each other in terms of deformations were also correlated. Finally, deformations taking place on the main tunnel axes because the excavation of the connection tunnels were investigated. Correlations between the effects of connection 1 tunnel excavation on main tunnels and the effects of connection 2 tunnel excavation on main tunnels were also supplied.

The results of modeling of connection tunnel excavations have shown that connection 1 tunnel excavation does not cause significant deformation on its axis. Maximum z-displacement is about 9 mm and occurred at the Line 1 tunnel side. Connection 1 tunnel excavation can also cause z-displacement about 6.5 mm on Line 1 tunnel axis and about 5 mm on Line 2 tunnel axis. Maximum deformations take place at both sides of the model because of the excavation of connection 2 tunnel and are about 1.5 cm. Excavation of the Connection 2 tunnel may cause deformations on its axis almost two times more than that of Connection 1 tunnel excavation may do on its axis in terms of maximum z-displacements. Maximum deformation would be around 1.7 cm on connection 1 tunnel axis after connection 2 tunnel excavation. Also it can be concluded that connection 2 tunnel excavation may affect the main tunnels more than connection 1 tunnel excavation and Line 1 tunnel can be affected by excavations more than Line 2 tunnel.

In order to simulate induced surface settlement due to groundwater withdrawal at the site 3-dimensional fully coupled (fluid-mechanical) numerical models were run using different time durations (1, 2, 3, 4, 5, 6, 7, 14, 28, 60, 90, 120, 150, 180 days) based on the fluid-flow properties and calibrated physical soil properties.

Although different time scales were introduced to the code, results obtain at three months (between August 14<sup>th</sup>, 2006 and November 21<sup>st</sup>, 2006) were considered to simulate only the drainage effects. Numerically obtained maximum settlement values show that groundwater drainage at the site may cause about 1.3 cm maximum settlement and this value is a kind of average value of recorded deformation values.

In an overall sense, numerical model results reveal that ground deformations recorded at the study area results from the main tunnel excavations rather than connection tunnel excavations or groundwater drainage work.

It should also be kept in mind that in addition to the factors modeled in this study various other factors may also contribute to ground deformations. These include the heterogeneity of the foundation material, excavation-related problems, temporary support systems and delays in their application, hardening of shotcrete, traffic vibrations, and groundwater conditions.

The work presented in this study has helped to provide a better understanding of the mechanisms which control the tunnel-soil interaction problems. In the light of this understanding following recommendations can be made for future studies:

- 1) 3-dimensional numerical models should be constructed to investigate tunnel-soil-structure interactions. Identifying effects of tunnel induced deformations on surrounding buildings would be helpful for future projects.
- 2) In the metro projects it is highly important to monitor groundwater levels before, during and after construction operations. Hydraulic conductivities of the foundation materials should also be provided for better evaluation of the groundwater-related problems during and after construction works.
- 3) Improving greenfield settlement predictions for high  $K_0$  situations should be the focus of future research. This would favorably affect the shape of deformation curve and the model outcomes.



4) Long term analyses should be run by using appropriate drained soil parameters to consider deformations that would take place after finalizing the construction work.

5) This study reveals that connection tunnel excavations also impose extra deformations on those of main tunnels. Lining properties should also be considered at especially intersection areas between connection and main tunnels.

6) Within the project frame, a pedestrian tunnel has planned above the station floor and effects of excavation of this pedestrian tunnel on connection and main tunnels should also be investigated.

7) It is obvious that stair tunnels between connection tunnels and upper pedestrian tunnel will impose an additional effect on the ground deformations. Thus, provided that required data are made available the effects of such auxiliary structures may also be considered in the model studies.

## REFERENCES

- Abidin, H. Z., Djaja, R., Darmawan, D., Hadi, S., Akbar, A., Rajiyowiryo, H., Sudibyo, Y., Meilano, I., Kasuma, M. A., Kahar, J., Subarya, C., 2001. Land subsidence of Jakarta (Indonesia) and its geodetic monitoring system. *Natural Hazards*, Vol. 23 (2-3), pp. 365-387.
- Alshuhail, A. A., 2006. Integration of 3D Resistivity Imaging and Ground Penetrating Radar Surveys in Characterizing Near-Surface Fluvial Environment. University of Calgary, Department of Geology and Geophysics, Alberta. Master Thesis, Unpublished.
- Annan, A. P., 1999. Practical Processing of GPR Data. Proceeding of the Second Government Workshop on Ground Penetrating Radar, Mississauga, ON, 16pp.
- Annan, A. P., 2002. The History of Ground Penetrating Radar. *Subsurface Sensing Technologies and Applications*, Vol. 3, No. 4, October 2002, pp. 303-320.
- Annan, A. P., 2003. *Ground Penetrating Radar Principles, Procedures and Applications*. Sensor and Software.
- Attewell, P. B. and Selby, A. R., 1989. Tunneling in compressible soils: Large ground movements and structural implications. *Tunneling and Underground Space Technology*, 4 (4).
- Attewell, P. B. and Woodman, J. P., 1982. Predicting the dynamics of ground settlement and its derivatives caused by tunneling in soil. *Ground Engineering*, 15 (8), 13-22.

- Bell, F. G., Cripps, J.C., Culshaw, M. G., 1986. A review of the engineering behavior of soils and rocks with respect to groundwater. In: Cripps, J.C., Bell, F.G. & Culshaw, M.G. (eds) *Groundwater in Engineering Geology*. Geological Society Engineering Geology Special Publications, 3, 1–23.
- Broms, B. B. and Bennermark, H., 1967. Stability of clay in vertical openings. *Journal of Soil Mechanics and Foundations*, ASCE, 193, 71-94.
- Chen, C., Pei, S., and Jiao, J. J., 2003. Land Subsidence caused by Groundwater Exploitation in Suzhou City, China, in *Hydrogeology Journal*, No: 11, pp. 275-287.
- Chen, W. F., and Liu, X. L., 1990. *Limit analysis in soil mechanics*, Elsevier Science, New York.
- Chow, L., 1994. Prediction of surface settlement due to tunneling in soft ground. Unpublished Thesis (MSc), University of Oxford.
- Collins, I. F. and Houlby, G. T., 1997. Application of thermomechanical principles to the modeling of geotechnical materials. *Proc. Royal Society, Series A*, 453, 1975-2001.
- Conyers, L. B., and Goodman, D., 1997. *Ground Penetrating Radar. An Introduction for Archaeologist*. Altamira Press.
- Cristallini, E., and Almendinger, R., 2001. Pseudo 3D Modeling of Trishear Fault-Propagation Folding. *Journal of Structural Geology*, 23, 1883-1899.
- Dahlin, T., and Loke, M. H., 1998. Resolution of 2D Wenner Resistivity Imaging as Assessed by Numerical Modeling. *Journal of Applied Geophysics*, 38, 237-249.

- Daniels, F., and Alberty, R. A., 1966. *Physical Chemistry*. John Wiley and Sons, Inc.
- Daniels, D. J. (ed.), 2004. *Ground Penetrating Radar, Radar, Sonar, Navigation and Avionics Series 15*, The Institute of Electrical Engineers, London, UK.
- Daniels, D., J., Gunton, D. J., and Scott, H. F., 1988. Introduction to Subsurface Radar: *IEEE Proc. F*, 135, 278-320.
- Das, B. M., 1994. *Principles of Geotechnical Engineering*, 3rd Ed. Boston: PWS Publishing Company.
- Davis, E. H., Gunn, M.J., Mair, R. J. and Seneviratne, H. N., 1980. The stability of shallow tunnels and underground openings in cohesive material. *Géotechnique*, 30 (4), 397-416.
- Davis, J. L., and Annan, A. P., 1989. Ground Penetrating Radar for High Resolution Mapping of Soil and Rock Stratigraphy: *Geophysical Prospecting*, 37, 531-551.
- deGroot-Hedlin, C., and Constable, S., 1990. Occam's Inversion to Generate Smooth, Two-dimensional Models Form Magnetotelluric Data. *Geophysics*, 55, 1613-1624.
- De Moor, E.K. and Taylor, R.N., 1989. Model studies of the behavior of deep tunnels in clay. In: *Proc. 12th ICSMFE*, Vol. 2, Rio de Janeiro, 13-18 August. Rotterdam: Balkema, 909-912.
- Dey, A., and Morrison, H. F., 1979a. Resistivity Modeling for Arbitrary Shaped Two-dimensional Structures. *Geophysical Prospecting* 27, 1020-1036.
- Dey, A., and Morrison, H. F., 1979b. Resistivity Modeling for Arbitrarily Shaped Three-dimensional Shaped Structures. *Geophysics* 44, 753-780.

- Doyuran, V., 2006. Necatibey İstasyonu Hat 2 Peron Tüneli Hidrojeolojik Değerlendirme Raporu, ODTÜ, Jeoloji Mühendisliği Bölümü (in Turkish).
- Edwards, L. S., 1977. A Modified Pseudosection for Resistivity and Induced Polarization. *Geophysics*, 42, 1020-1036.
- El Nahhas, F., El Kadi, F. and Ahmed, A., 1992. Interaction of tunnel linings and soft ground. *Tunneling and Underground Space Technology*, 7 (1).
- Erol, O., 2006. Ankara Metrosu Kızılay Söğütözü Hattı Projesi Km: 23+600-25+580 Arası Geoteknik Raporu (in Turkish).
- Erol, O., and Çetin, K. Ö., 2006. Ankara Raylı Ulaşım Sistemi Kızılay Milli Kütüphane Hattı Necatibey İstasyonu Püskürtme Beton Kaplamalı Peron Tünellerinin Tasarıma Esas Sayısal Modellenmesi, ODTÜ, İnşaat Mühendisliği Bölümü (in Turkish).
- Finno, R. J. and Clough, G. W., 1985. Evaluation of soil response to EPB shield tunneling. *Journal of Geotechnical Engineering, ASCE*, 111 (2), 155-173.
- FLAC3D, 2005, "User's Manual-Fast Lagrangian Analysis of Continua in 3-Dimensions", Itasca Consulting Group, Minnesota.
- GoogleEarth, 2007. Version 4.2.0180.1134 (beta). <http://earth.google.com>
- Grant, R. J. and Taylor, R. N., 2000. Evaluating plasticity solutions for the response of clay around tunnels. In: *Proc. Int. Sympos. on Geotechnical Aspects of Underground Construction in Soft Ground*, Tokyo, 21-23 July 1999. Rotterdam: Balkema, 373-378.
- Grasmueck, M., and Weger, R., 2003. How Dense is Dense Enough for a Real 3D GPR Survey? *Society of Exploration Geophysics, Expanded Abstracts*, 1180-1183.



- Grasmueck, M., Weger, R., and Heinrich, H., 2005. Full Resolution 3D GPR Imaging . *Geophysics*, 70, K12-K19.
- Griffiths, D. H., and Barker, R. D., 1993. Two-dimensional Resistivity Imaging and Modeling in Areas of Complex Geology. *Journal of Applied Geophysics*, 29, 211-226.
- Guy, E., Daniel, J., and Radzevicius, S., 1999. Demonstration of Using Crossed Dipole GPR Antenna for Site Characterization. *Geophysical Research Letters*, 26, 3421-3424.
- Houlsby, G. T., 1999. A model for the variable stiffness of undrained clay. In: *Proc. Int. Symposium on Pre-failure Deformation Characteristics of Geomaterials*, Torino, September. Rotterdam: Balkema.
- Irving, J. D., and Knight, R. J., 2003. Removal of Wavelet Dispersion from Ground Penetrating Radar Data. *Geophysics*, 68, 960-970.
- Jardine, R. J., Potts, D. M., Fourie, A. B. and Burland, J. B., 1986. Studies of the influence of non-linear stress-strain characteristics in soil-structure interaction. *Géotechnique*, 36 (3), 377-396.
- Jol, H. M., 2009. *Ground Penetrating Radar: Theory and Applications*. Elsevier B.V.
- Jol, H. M., and Kaminsky, G., 2000. High Resolution 2D and 3D Ground Penetrating Radar Datasets. U.S. Geological Survey, Open-File Report, 99-104.
- Karlsruud, K., 2001. Control of water leakage when tunneling under urban areas in the Oslo Region: Norwegian Tunneling Society, Pub. 12, pp. 27-33.

- Keller, G. V., and Frischknecht, F. C., 1966. *Electrical Methods in Geophysical Prospecting*. Pergamon Press Inc., Oxford.
- Kim, S. H., Burd, H. J. and Milligan, G. W. E., 1996. Interaction between closely spaced tunnels in clay. In: *Proc. Int. Sympos. on Geotechnical Aspects of Underground Construction in Soft Ground*, London, April. Rotterdam: Balkema, 543-548.
- Kimura, T. and Mair, R. J., 1981. Centrifugal testing of model tunnels in soft clay. In: *Proc. 10th ICSMFE, Vol. 1*, Stockholm, 15-19 June. Rotterdam: Balkema, 319-322.
- Loke, M. H., 2001. *Tutorial: 2D and 3D Electrical Imaging Surveys*. Geotomo Software, Malaysia.
- Loke, M. H., 2004. *Tutorial: 2D and 3D Electrical Imaging Surveys. Revised Copy*. Geotomo Software, Malaysia.
- Loke, M. H., and Barker, R. D., 1995. Least-Squares Deconvolution of Apparent Resistivity Pseudosections: *Geophysics*, 60, 1682-1690.
- Loke, M. H., and Barker, R. D., 1996. Rapid Least Squares inversion of apparent resistivity pseudosections by a quasi-Newton method. *Geophysical Prospecting*, 44, 131-152.
- Lombaert, G., Degrandea, G. and Clouteaub, D., 2000. Numerical modeling of free field traffic-induced vibrations. *Soil Dynamics and Earthquake Engineering*, Volume 19, Issue 7, pp. 473-488
- Macklin, S. R. and Field, G. R., 1999. The response of London clay to full-face TBM tunneling at West Ham, London. In: *Proc. Int. Conf. On Urban Ground Engineering*, Hong Kong, 11-12 November 1998. London: Thomas Telford.

- Mair, R. J., 1979. Centrifugal modeling of tunnel construction in soft clay. Thesis (PhD). University of Cambridge.
- Mair, R. J., Gunn, M. J. and O'Reilly, M. P., 1981. Ground movements around shallow tunnels in soft clay. Proc. 10th ICSMFE, Vol. 1, Stockholm, 15-19 June. Rotterdam: Balkema, 323-328.
- Mair, R. J. and Taylor, R. N., 1993. Prediction of clay behavior around tunnels using plasticity solutions. In: Predictive Soil Mechanics: Proc. Wroth Memorial Symposium, Oxford, 27-29 July 1992. London: Thomas Telford, 449-463.
- Mair, R. J., Taylor, R. N. and Bracegirdle, A., 1993. Subsurface settlement profiles above tunnels in clays. Géotechnique, 43 (2), 315-320.
- Marti, J., and Cundall, P. A., 1982. "Mixed Discretization Procedure for Accurate Solution of Plasticity Problems," Int. J. Num. Methods and Anal. Methods in Geomech., 6, 129-139.
- McCaul, C., O'Reilly, M. P. and Crabb, G. I., 1986. Settlements over a small diameter tunnel driven by hand and machine in London clay. Municipal Engineer (ICE), 3 (6), 311-322.
- McMechan, G., Gaynor, G., and Szerbiak, R., 1997. Use of Ground Penetrating Radar for 3D Sedimentological Characterization of Clastic Reservoir Analogs. Geophysics, 62, 786-796.
- Milsom, J., 2000. Field Geophysics. 2<sup>nd</sup> Ed.: John Wiley and Sons Inc.
- Mitchell, J. K., Baxter, C. D. P. and Soga, K., 1997. Time effects on the stress-deformation behavior of soils. In: Proc. Sakuro Murayama Memorial Symposium, Kyoto, April.

- Morton, K. and Au, E., 1975. Settlement observations on eight structures in London. In: Proc. Conf. Settlement of Structures, Cambridge, April 1974. London: Pentech Press, 183-203.
- Nakai, T. Farias, M. M., Matsubara, H. and Kusunoki, S., 2000. Effects of excavation sequence on the 3D settlement of shallow tunnels. In: Proc. Int. Sympos. on Geotechnical Aspects of Underground Construction in Soft Ground, Tokyo, 21-23 July 1999. Rotterdam: Balkema, 403-408.
- Olhoeft, G. R., Powers, M. H., and Capron, D. E., 1994. Buried object Detection with Ground Penetrating Radar. Proceeding of Unexploded Ordance Detection and Range Remediation Conference, 207-233.
- O'Reilly, M. P., 1988. Evaluating and predicting ground settlements caused by tunneling in London clay. In: Proc. Int. Symposium Tunneling '88, London 18-21 April. London: Institution of Mining and Metallurgy, 231-241.
- O'Reilly, M. P. and New, B., 1982. Settlement above tunnels in the United Kingdom- their magnitude and prediction. In: Proc. Int. Symposium Tunneling '82, London, 7-11 June. London: Institution of Mining and Metallurgy, 173-181.
- Oreste, P. P. and Pella, D., 1987. Modelling progressive hardening of shotcrete in convergence-confinement approach to tunnel design. Tunneling and Underground Space Technology, Volume 12, Issue 3, pp. 425-431
- Ortiz, J. M. R., Serra, J. and Oteo, C., 1986. Curso Aplicado de Cimentaciones, 3rd Ed. Madrid: Colegio Oficial de Arquitectos de Madrid.
- Panet, M. and Guenot, A., 1982. Analysis of convergence behind the face of a tunnel. Proc. Tunneling '82, Brighton, England, 197-204. London: IMM.

- Peck, R. B., 1969. Deep excavations and tunneling in soft ground. In: Proc. 7th ICSMFE, State-of-the-art Volume, Mexico City. Mexico: Sociedad Mexicana de Mecánica de Suelos, 225-290.
- Poland, J. F. and Davis, G. H., 1969. Land Subsidence due to withdrawal of Fluids, Reviews in Engineering Geology II: Geological Society of America, pp. 187-269.
- Potts, D. M., 1976. Behavior of lined and unlined tunnels in sand. Thesis (PhD). University of Cambridge.
- Pratt, W. E., and Johnson, D. W., 1926. Local subsidence of the Goose Creek oil field, J. Geol., 34 (7), 577-590.
- RES2DINV, 2004. Version 3.54. Rapid 2D Resistivity and IP inversion using the Least Square Method. Geotomo Software, [www.geoelectrical.com](http://www.geoelectrical.com).
- Reynolds, J. M., 1997. An Introduction to Applied and Environmental Geophysics. John Wiley and Sons, Chichester, England.
- Reynolds, J. M., 2000. An Introduction to Applied and Environmental Geophysics: John Wiley and Sons Inc.
- Rowe, R. K. and Lee, K. M., 1989. Parameters for predicting deformations due to tunneling. In: Proc. 12th ICSMFE, Vol. 2, Rio de Janeiro, 13-18 August. Rotterdam: Balkema, 793-796.
- Rowe, R. K., Lo, K. J. and Kack, G. J., 1983. A method of estimating surface settlement above tunnels constructed in soft clay. Canadian Geotechnical Journal, 20 (1), 11-22.
- Schmidt, B., 1969. Settlements and ground movements associated with tunneling in soil. Unpublished Thesis (PhD). University of Illinois.



- Sharma, P. V., 1997. Environmental and Engineering Geophysics: Cambridge University Press.
- Sheriff, R. E., 1999. Encyclopedic Dictionary of Exploration Geophysics. 3<sup>rd</sup> Ed.: Society of Exploration Geophysics.
- Silvester, P. P., and Ferrari, R. L., 1990. Finite Elements for Electrical Engineers. 2<sup>nd</sup> Ed.: Cambridge University Press.
- Simons, N. E. and Som, N. N., 1970. Settlement of structures on clay with particular emphasis on London clay. CIRIA Report 22.
- Smith, D., and Jol, H., 1995. Ground Penetrating Radar: Antenna Frequencies and Maximum Probable Depths of Penetration in Quaternary Sediments. Journal of Applied Geophysics, 33, 93-100.
- Stallebrass, S. E. and Taylor, R. N., 1997. The development and evaluation of a constitutive model for the prediction of ground movements in overconsolidated clay. Géotechnique, 47 (2), 235-253.
- Telford, W. M., Geldart, L. P., Sheriff, R. E., 1990. Applied Geophysics. 2<sup>nd</sup> Ed.: Cambridge University Press.
- TOKER Drilling and Construction Co., 2003. Ankara Rail Transit System Kızılay Söğütözü Line Construction Works, Soil Investigations Factual Report.
- Tsoflias, G. P., Gestel, J. P. V., Stoffa, P. L., Blankenship, D. D., and Sen, M., 2004. Vertical Fracture Detection by Exploiting the Polarization Properties of Ground Penetrating Radar Signals. Geophysics, 69, 803-810.
- Van Overmeeren, R. A., 1998. Radar Facies of Unconsolidated Sediments in the Netherlands. A Radar Stratigraphy Interpretation Method for Hydrogeology. Journal of Applied Geophysics, 40, 1-18.

Verruijt, A. and Booker, J. R., 1996. Surface settlements due to deformation of a tunnel in an elastic half plane. *Géotechnique*, 46 (4), 753-75.

Yilmaz, O., 2001., *Seismic Data Analysis: Processing, Inversion and Interpretation of Seismic Data*. Society of Exploration Geophysics.

Young, R., Zhenghan, D., and Sun, J., 1995. Interactive Processing of GPR Data. *The Leading Edge*, 14, 175-280.

## APPENDIX A

### MEASURED RESISTIVITY DATA

**Table A.1.** Measured resistivity data of Schlumberger N6 Dipole Dipole N4 electrode configuration for profile 1.

<b>Profile #1, Schl. N6 DD N4</b>			
Electrode spacing 2 m			
Total # of data level is 7			
Total # of datum point is 49			
	<b>Spacing (m)</b>	<b>Level</b>	<b>Resistivity (<math>\Omega\text{m}</math>)</b>
0	2	1	7,21
2	2	1	6,37
4	2	1	5,98
6	2	1	6,85
8	2	1	7,81
10	2	1	8,81
12	2	1	9,15
14	2	1	9,18
16	2	1	7,94
18	2	1	8,83
20	2	1	9,04
22	2	1	12,78
24	2	1	41,48
0	2	2	5,59
2	2	2	4,62
4	2	2	6,08
6	2	2	6,73
8	2	2	6,59
10	2	2	8,59
12	2	2	6,93
14	2	2	7,52
16	2	2	10,33

**Table A.1 cont'd**

18	2	2	7,88
20	2	2	14,72
0	2	3	4,55
2	2	3	5,42
4	2	3	5,83
6	2	3	6,51
8	2	3	8,01
10	2	3	6,59
12	2	3	6,7
14	2	3	8,64
16	2	3	8,77
0	2	4	5,12
2	2	4	5,65
4	2	4	5,79
6	2	4	8,13
8	2	4	6,42
10	2	4	6,35
12	2	4	8,35
0	2	5	5,45
2	2	5	5,72
4	2	5	8,14
6	2	5	6,76
8	2	5	5,78
0	2	6	5,79
2	2	6	7,81
4	2	6	6,84
0	6	2	7,02

**Table A.2.** Measured resistivity data of Dipole Dipole N6 S1 electrode configuration for profile 1.

<b>Profile #1, DD N6 S1</b>			
Electrode spacing 2 m			
Total # of data level is 3			
Total # of datum point is 84			
	<b>Spacing (m)</b>	<b>Level</b>	<b>Resistivity (<math>\Omega</math>m)</b>
0	2	1	5,97
2	2	1	5,85
4	2	1	7,58
6	2	1	7,5
8	2	1	6,9
10	2	1	9,3
12	2	1	12,89
14	2	1	9,34
16	2	1	8,09
18	2	1	7
20	2	1	7,97
22	2	1	12,62
24	2	1	15,64
0	2	2	5,04
2	2	2	6,1
4	2	2	7,25
6	2	2	4,23
8	2	2	7,38
10	2	2	7,96
12	2	2	9,27
14	2	2	11,6
16	2	2	6,51
18	2	2	7,32
20	2	2	12,35
22	2	2	7,56
0	2	3	5,49
2	2	3	6,15
4	2	3	4,27
6	2	3	5,47
8	2	3	6,25
10	2	3	5,94
12	2	3	10,17
14	2	3	10
16	2	3	7,26

**Table A.2 cont'd**

18	2	3	7,74
20	2	3	7,62
0	2	4	5,33
2	2	4	4,19
4	2	4	5,63
6	2	4	3,58
8	2	4	5,31
10	2	4	7,05
12	2	4	7,86
14	2	4	10,61
16	2	4	8,1
18	2	4	9,97
0	2	5	3,17
2	2	5	3,86
4	2	5	3,96
6	2	5	3,33
8	2	5	4,63
10	2	5	5,88
12	2	5	7,92
14	2	5	13,46
16	2	5	9,35
0	2	6	4,71
6	2	6	5,94
8	2	6	5,41
10	2	6	6,03
12	2	6	8,91
14	2	6	7,37
0	4	2,5	4,22
2	4	2,5	4,15
4	4	2,5	3,69
6	4	2,5	5
8	4	2,5	5,74
10	4	2,5	7,49
12	4	2,5	10,18
0	4	3	3,98
2	4	3	3,19
4	4	3	4,81
6	4	3	4,29
8	4	3	6,42
10	4	3	7,74



**Table A.2 cont'd**

0	4	3,5	2,68
2	4	3,5	2,49
4	4	3,5	2,72
6	4	3,5	4,06
8	4	3,5	5,64
2	4	4	3,68
6	4	4	3,77
2	4	4,5	5,02
4	4	4,5	3,19
2	4	5	3,63

**Table A.3.** Measured resistivity data of Schlumberger N6 electrode configuration for profile 1.

<b>Profile #1, Schl. N6</b>			
Electrode spacing 2 m			
Total # of data level is 7			
Total # of datum point is 49			
	<b>Spacing (m)</b>	<b>Level</b>	<b>Resistivity (<math>\Omega\text{m}</math>)</b>
0	2	1	7,21
2	2	1	6,35
4	2	1	5,98
6	2	1	6,82
8	2	1	7,76
10	2	1	8,78
12	2	1	9,13
14	2	1	9,27
16	2	1	7,95
18	2	1	8,82
20	2	1	9,16
22	2	1	12,82
24	2	1	41,56
0	2	2	5,58
2	2	2	4,6
4	2	2	6,09
6	2	2	6,7
8	2	2	6,57
10	2	2	8,68
12	2	2	6,9
14	2	2	7,49
16	2	2	10,34
18	2	2	7,9
20	2	2	14,71
0	2	3	4,52
2	2	3	5,44
4	2	3	5,84
6	2	3	6,44
8	2	3	7,92
10	2	3	6,56
12	2	3	6,67
14	2	3	8,73
16	2	3	8,74
0	2	4	5,18

**Table A.3 cont'd**

2	2	4	5,69
4	2	4	5,76
6	2	4	8,07
8	2	4	6,41
10	2	4	6,3
12	2	4	8,36
0	2	5	5,45
2	2	5	5,69
4	2	5	8,13
6	2	5	6,65
8	2	5	5,72
0	2	6	5,74
2	2	6	7,85
4	2	6	6,75
0	6	2	6,88

**Table A.4.** Measured resistivity data of Wenner Alpha electrode configuration for profile 1.

<b>Profile #1, Wenner Alpha</b>			
Electrode spacing 2 m			
Total # of data level is 1			
Total # of datum point is 35			
	<b>Spacing (m)</b>	<b>Level</b>	<b>Resistivity (<math>\Omega</math>m)</b>
0	2	2	7,2
2	2	2	6,34
4	2	2	5,98
6	2	2	6,83
8	2	2	7,76
10	2	2	8,79
12	2	2	9,13
14	2	2	9,27
16	2	2	7,94
18	2	2	8,82
20	2	2	9,14
22	2	2	12,8
24	2	2	41,57
0	2	4	4,73
2	2	4	5,39
4	2	4	6,1
6	2	4	6,81
8	2	4	7,38
10	2	4	7,15
12	2	4	6,95
14	2	4	8,65
16	2	4	9
18	2	4	12,61
0	2	6	5,16
2	2	6	6,1
4	2	6	6,87
6	2	6	6,66
8	2	6	6,82
10	2	6	6,97
12	2	6	7,5
0	2	8	6,59
2	2	8	6,73
4	2	8	6,66
6	2	8	7,28

**Table A.5.** Measured resistivity data of Schlumberger N6 Dipole Dipole N4 electrode configuration for profile 2.

<b>Profile #2, Schl. N6 DD N4</b>			
Electrode spacing 3,5 m			
Total # of data level is 7			
Total # of datum point is 46			
	<b>Spacing (m)</b>	<b>Level</b>	<b>Resistivity (<math>\Omega</math>m)</b>
0	3,5	1	108,63
3,5	3,5	1	15,73
7	3,5	1	48,3
10,5	3,5	1	38,87
14	3,5	1	37,01
17,5	3,5	1	57,38
21	3,5	1	68,55
24,5	3,5	1	58,75
28	3,5	1	70,09
31,5	3,5	1	51,94
35	3,5	1	68,15
38,5	3,5	1	83,73
42	3,5	1	66,63
0	3,5	2	7,61
3,5	3,5	2	5,72
7	3,5	2	16,96
10,5	3,5	2	18,21
14	3,5	2	17,77
17,5	3,5	2	19,69
21	3,5	2	20,65
24,5	3,5	2	22,7
28	3,5	2	25,83
31,5	3,5	2	38,74
35	3,5	2	25,1
0	3,5	3	3,22
3,5	3,5	3	4,27
7	3,5	3	6,94
10,5	3,5	3	6,03
14	3,5	3	7,34
17,5	3,5	3	8,25
21	3,5	3	9,85
24,5	3,5	3	12,33
28	3,5	3	11,21
0	3,5	4	1,87

**Table A.5 cont'd**

3,5	3,5	4	1,56
7	3,5	4	2,82
10,5	3,5	4	3,96
14	3,5	4	4,1
17,5	3,5	4	4,99
21	3,5	4	4,2
3,5	3,5	5	1,13
7	3,5	5	2,21
10,5	3,5	5	2,37
14	3,5	5	2,05
3,5	3,5	6	1,1
7	3,5	6	1,11



**Table A.6.** Measured resistivity data of Dipole Dipole N6 S1 electrode configuration for profile 2.

<b>Profile #2, DD N6 S1</b>			
Electrode spacing 3,5 m			
Total # of data level is 3			
Total # of datum point is 57			
	<b>Spacing (m)</b>	<b>Level</b>	<b>Resistivity (<math>\Omega</math>m)</b>
0	3,5	1	1,71
3,5	3,5	1	109,35
7	3,5	1	37,66
10,5	3,5	1	30,12
14	3,5	1	61,73
17,5	3,5	1	63,36
21	3,5	1	92,39
24,5	3,5	1	121,86
28	3,5	1	63,44
31,5	3,5	1	67,4
35	3,5	1	67,5
38,5	3,5	1	100,1
42	3,5	1	161,29
3,5	3,5	2	29,43
7	3,5	2	20,4
10,5	3,5	2	15,86
14	3,5	2	30,02
17,5	3,5	2	38,63
21	3,5	2	43,47
24,5	3,5	2	34,18
28	3,5	2	27,45
31,5	3,5	2	27,74
35	3,5	2	44,81
38,5	3,5	2	105,01
3,5	3,5	3	14
7	3,5	3	10
10,5	3,5	3	9,39
14	3,5	3	15,22
17,5	3,5	3	16,17
21	3,5	3	11,86
24,5	3,5	3	14,96
28	3,5	3	13,78
31,5	3,5	3	18,31
35	3,5	3	37,35

**Table A.6 cont'd**

3,5	3,5	4	5,83
7	3,5	4	6,28
10,5	3,5	4	5,51
14	3,5	4	7,01
17,5	3,5	4	5,16
21	3,5	4	6,14
24,5	3,5	4	8,38
28	3,5	4	9,11
31,5	3,5	4	14,58
3,5	3,5	5	6,39
7	3,5	5	4,37
24,5	3,5	5	5,2
28	3,5	5	7,65
24,5	3,5	6	8,68
0	7	2,5	3,69
3,5	7	2,5	3,34
7	7	2,5	2,79
10,5	7	2,5	1,94
14	7	2,5	2,22
17,5	7	2,5	2,35
21	7	2,5	4,12
3,5	7	3	2,28
7	7	4,5	65,39

**Table A.7.** Measured resistivity data of Schlumberger N6 electrode configuration for profile 2.

<b>Profile #2, Schl. N6</b>			
Electrode spacing 3,5 m			
Total # of data level is 7			
Total # of datum point is 45			
	<b>Spacing (m)</b>	<b>Level</b>	<b>Resistivity (<math>\Omega\text{m}</math>)</b>
0	3,5	1	90,03
3,5	3,5	1	15,72
7	3,5	1	50,78
10,5	3,5	1	38,79
14	3,5	1	36,99
17,5	3,5	1	57,12
21	3,5	1	68,24
24,5	3,5	1	58,71
28	3,5	1	70,17
31,5	3,5	1	51,96
35	3,5	1	67,91
38,5	3,5	1	83,67
42	3,5	1	66,51
0	3,5	2	7,52
3,5	3,5	2	5,76
7	3,5	2	17,41
10,5	3,5	2	18,28
14	3,5	2	17,84
17,5	3,5	2	19,72
21	3,5	2	20,69
24,5	3,5	2	22,78
28	3,5	2	25,9
31,5	3,5	2	38,76
35	3,5	2	25,23
0	3,5	3	3,23
3,5	3,5	3	4,28
7	3,5	3	7,09
10,5	3,5	3	6,05
14	3,5	3	7,35
17,5	3,5	3	8,26
21	3,5	3	9,88
24,5	3,5	3	12,38
28	3,5	3	11,27
0	3,5	4	1,88

**Table A.7 cont'd**

3,5	3,5	4	1,56
7	3,5	4	2,9
10,5	3,5	4	3,96
14	3,5	4	4,1
17,5	3,5	4	5,03
21	3,5	4	4,22
3,5	3,5	5	1,1
7	3,5	5	2,18
10,5	3,5	5	2,33
14	3,5	5	2,06
7	3,5	6	1,18

**Table A.8.** Measured resistivity data of Wenner Alpha electrode configuration for profile 2.

<b>Profile #2, Wenner Alpha</b>			
Electrode spacing 3,5 m			
Total # of data level is 1			
Total # of datum point is 34			
	<b>Spacing (m)</b>	<b>Level</b>	<b>Resistivity (<math>\Omega</math>m)</b>
0	3,5	3,5	90,06
3,5	3,5	3,5	15,73
7	3,5	3,5	50,84
10,5	3,5	3,5	38,84
14	3,5	3,5	37,05
17,5	3,5	3,5	57,17
21	3,5	3,5	68,26
24,5	3,5	3,5	58,77
28	3,5	3,5	70,26
31,5	3,5	3,5	52,02
35	3,5	3,5	68,1
38,5	3,5	3,5	83,81
42	3,5	3,5	66,52
0	3,5	7	5,36
3,5	3,5	7	7,64
7	3,5	7	15,45
10,5	3,5	7	14,99
14	3,5	7	12,79
17,5	3,5	7	14,78
21	3,5	7	17,14
24,5	3,5	7	22,11
28	3,5	7	30,99
31,5	3,5	7	20,56
0	3,5	10,5	3,02
3,5	3,5	10,5	2,46
7	3,5	10,5	4,91
10,5	3,5	10,5	5,05
14	3,5	10,5	5,94
17,5	3,5	10,5	8,48
21	3,5	10,5	7,44
0	3,5	14	1,47
3,5	3,5	14	1,69
7	3,5	14	2,79
10,5	3,5	14	2,72

**Table A.9.** Measured resistivity data of Schlumberger N6 Dipole Dipole N4 electrode configuration for profile 3.

<b>Profile #3, Schl. N6 DD N4</b>			
Electrode spacing 5 m			
Total # of data level is 7			
Total # of datum point is 49			
	<b>Spacing (m)</b>	<b>Level</b>	<b>Resistivity (<math>\Omega</math>m)</b>
0	5	1	5931,15
5	5	1	3279,22
10	5	1	2615,13
15	5	1	1741,45
20	5	1	380,28
25	5	1	1503,08
30	5	1	1551,12
35	5	1	1995,54
40	5	1	1738,8
45	5	1	1302,3
50	5	1	1533,07
55	5	1	1541,12
60	5	1	628,16
0	5	2	3502,52
5	5	2	3381,36
10	5	2	2728,24
15	5	2	629,87
20	5	2	1878,54
25	5	2	1635,48
30	5	2	1539,64
35	5	2	1774,51
40	5	2	1697,11
45	5	2	3061,08
50	5	2	1957,72
0	5	3	3160,88
5	5	3	2346,22
10	5	3	546,12
15	5	3	1489,02
20	5	3	1218,98
25	5	3	833,56
30	5	3	709,82
35	5	3	1265,47
40	5	3	2329,19
0	5	4	1825,71



**Table A.9 cont'd**

5	5	4	363,3
10	5	4	933,63
15	5	4	712,77
20	5	4	534,46
25	5	4	478,7
30	5	4	347,11
0	5	5	206,45
5	5	5	494,14
10	5	5	409,48
15	5	5	583,52
20	5	5	232,84
0	5	6	268,18
5	5	6	418,78
10	5	6	268,69
0	15	2	206,17

**Table A.10.** Measured resistivity data of Dipole Dipole N6 S1 electrode configuration for profile 3.

<b>Profile #3, DD N6 S1</b>			
Electrode spacing 5 m			
Total # of data level is 3			
Total # of datum point is 68			
	<b>Spacing (m)</b>	<b>Level</b>	<b>Resistivity (<math>\Omega</math>m)</b>
0	5	1	3973,6
5	5	1	4458,43
10	5	1	2350,17
15	5	1	7,87
20	5	1	148,11
25	5	1	498,17
30	5	1	2459,17
35	5	1	2523,94
40	5	1	1982,86
45	5	1	922,51
50	5	1	243,51
55	5	1	615,59
60	5	1	2431,8
0	5	2	7050,4
5	5	2	6121,82
10	5	2	15,62
15	5	2	14,98
20	5	2	21,71
25	5	2	1375,26
30	5	2	4424,49
35	5	2	4115,16
40	5	2	3062,51
45	5	2	1215,99
50	5	2	159,78
55	5	2	4545,74
0	5	3	6046,28
5	5	3	28,55
10	5	3	20,81
20	5	3	40,98
25	5	3	1555,27
30	5	3	4504,9
35	5	3	3970,55
40	5	3	2533,25
45	5	3	505,8

**Table A.10 cont'd**

50	5	3	742,28
0	5	4	24,49
5	5	4	32,83
15	5	4	3,96
20	5	4	40,19
25	5	4	1257,85
30	5	4	3435,62
35	5	4	2644,76
40	5	4	844,95
45	5	4	1882,48
0	5	5	26,38
20	5	5	30,55
25	5	5	844,45
30	5	5	1936,27
35	5	5	764,02
40	5	5	2744,11
20	5	6	20,45
25	5	6	445,75
30	5	6	506,36
35	5	6	2281,02
0	10	2,5	2,69
5	10	2,5	5,12
10	10	2,5	4,49
15	10	2,5	17,5
20	10	2,5	421,45
25	10	2,5	972,67
30	10	2,5	1173,29
0	10	3	4,86
5	10	3	4,71
10	10	3	3,7
15	10	3	11,48
20	10	3	187,52
25	10	3	596,32
20	10	3,5	112,06

**Table A.11.** Measured resistivity data of Schlumberger N6 electrode configuration for profile 3.

<b>Profile #3, Schl. N6</b>			
Electrode spacing 5 m			
Total # of data level is 7			
Total # of datum point is 49			
	<b>Spacing (m)</b>	<b>Level</b>	<b>Resistivity (<math>\Omega</math>m)</b>
0	5	1	5786,79
5	5	1	3215,82
10	5	1	2549,03
15	5	1	1707,06
20	5	1	363,39
25	5	1	1468,67
30	5	1	1552,5
35	5	1	1978,63
40	5	1	1731,8
45	5	1	1299,53
50	5	1	1530,3
55	5	1	1540,61
60	5	1	627,12
0	5	2	3351,71
5	5	2	3217,84
10	5	2	2638,58
15	5	2	604,93
20	5	2	1824,37
25	5	2	1647,04
30	5	2	1524,27
35	5	2	1744,68
40	5	2	1686,95
45	5	2	3062,86
50	5	2	1952,44
0	5	3	2957,49
5	5	3	2223,44
10	5	3	522,32
15	5	3	1443,43
20	5	3	1225,33
25	5	3	835,37
30	5	3	694,56
35	5	3	1238,99
40	5	3	2316,52
0	5	4	1701,33

**Table A.11 cont'd**

5	5	4	346,93
10	5	4	902,88
15	5	4	715,01
20	5	4	534,29
25	5	4	476,93
30	5	4	336,64
0	5	5	197,44
5	5	5	477,27
10	5	5	411,14
15	5	5	583,38
20	5	5	231,69
0	5	6	259,6
5	5	6	420,09
10	5	6	268,92
0	15	2	205,3

**Table A.12.** Measured resistivity data of Wenner Alpha electrode configuration for profile 3.

<b>Profile #3, Wenner Alpha</b>			
Electrode spacing 5 m			
Total # of data level is 1			
Total # of datum point is 35			
	<b>Spacing (m)</b>	<b>Level</b>	<b>Resistivity (<math>\Omega</math>m)</b>
0	5	5	5803,24
5	5	5	3222,98
10	5	5	2555,4
15	5	5	1708,6
20	5	5	364,46
25	5	5	1471,25
30	5	5	1551,53
35	5	5	1981,21
40	5	5	1731,91
45	5	5	1300,65
50	5	5	1528,05
55	5	5	1537,07
60	5	5	625,32
0	5	10	3231,41
5	5	10	2898,48
10	5	10	2161,57
15	5	10	1392,79
20	5	10	1576,07
25	5	10	1202,73
30	5	10	940,1
35	5	10	1398,27
40	5	10	2624,4
45	5	10	2375,1
0	5	15	2252,73
5	5	15	1928,79
10	5	15	927,76
15	5	15	726,02
20	5	15	433,17
25	5	15	373,44
30	5	15	888,17
0	5	20	1110,99
5	5	20	383,69
10	5	20	464,96
15	5	20	190,86



## APPENDIX B

### RECORDED DEFORMATION MEASUREMENTS

**Necatibey Station Line 2 Deformation Graph (8)**

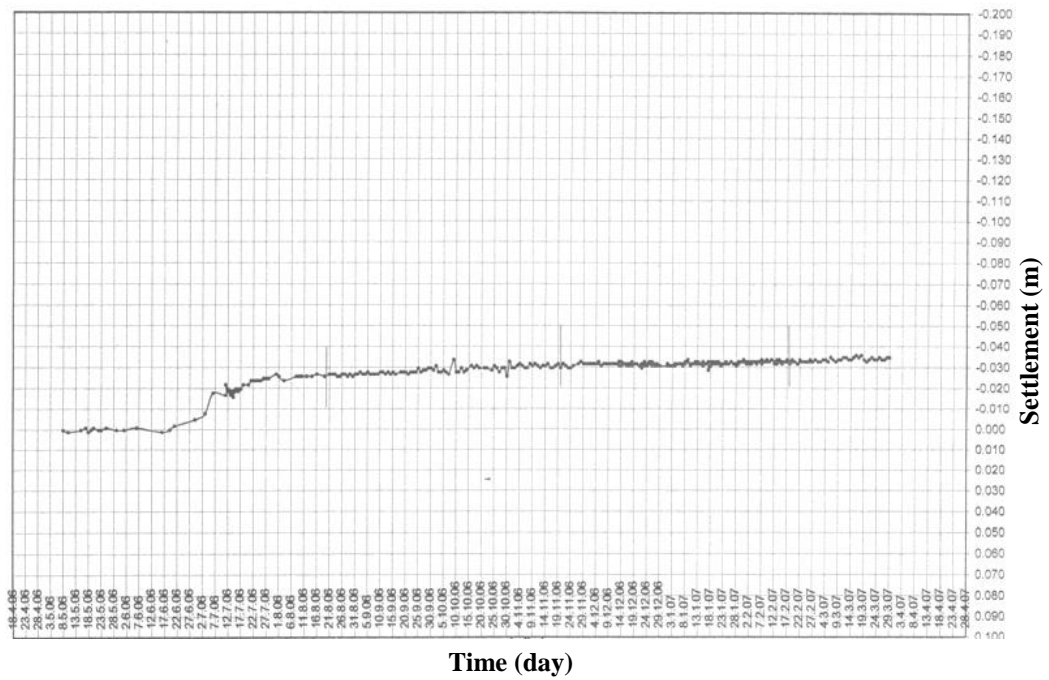


**Figure B.1.** Recorded deformation measurements at point 8.

Necatibey Station Line 2 Deformation Graph (9)

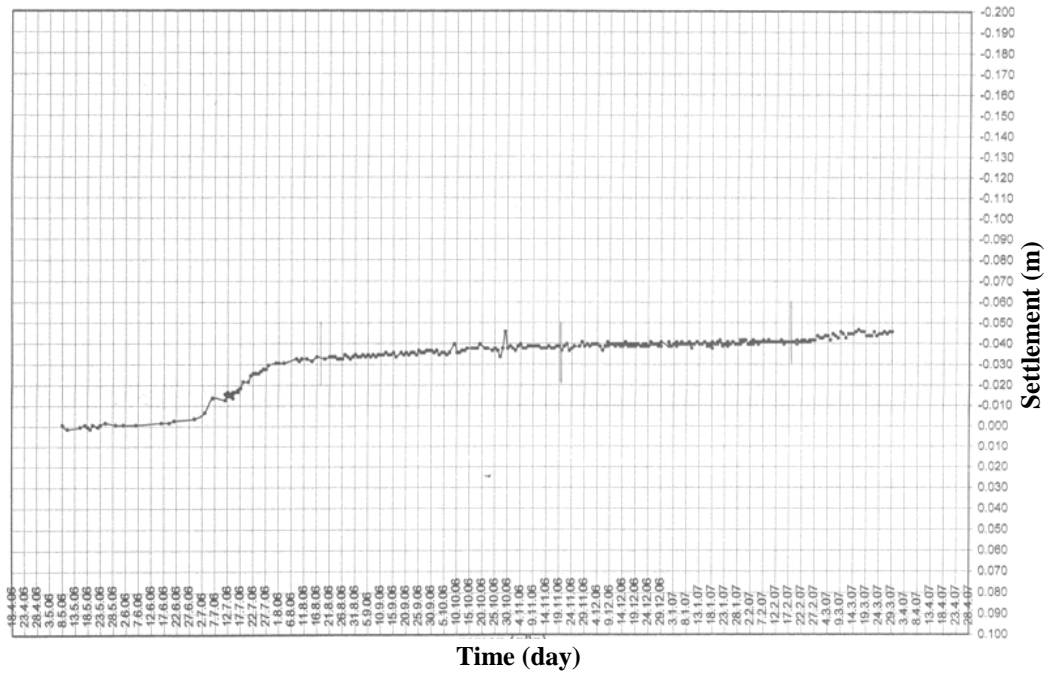


Figure B.2. Recorded deformation measurements at point 9.

Necatibey Station Line 2 Deformation Graph (10)

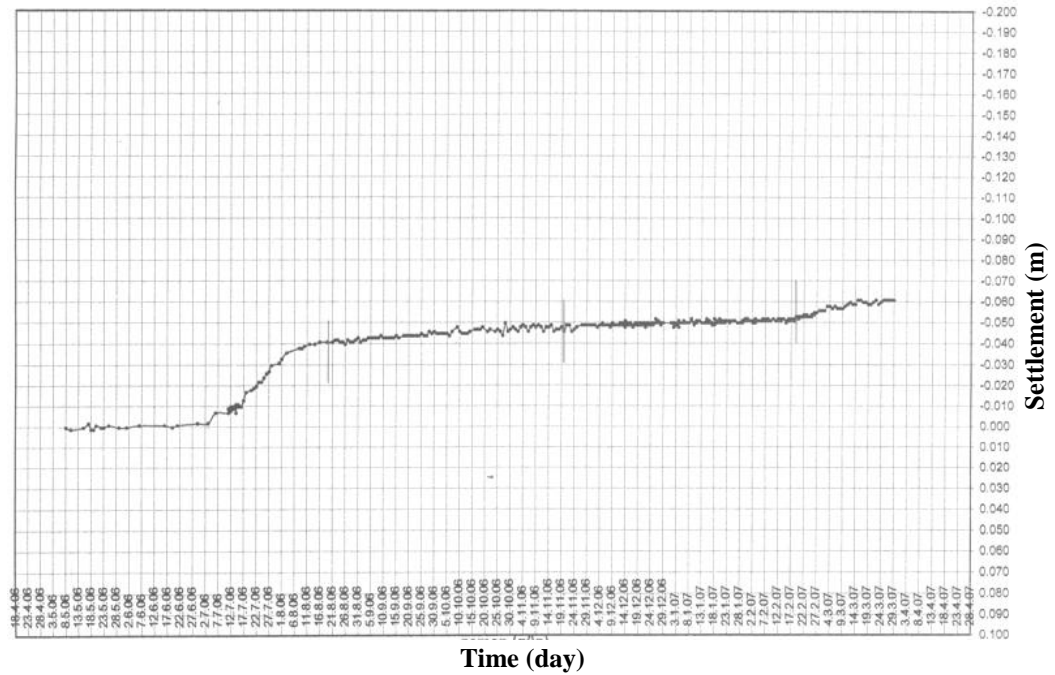


Figure B.3. Recorded deformation measurements at point 10.

Necatibey Station Line 2 Deformation Graph (11)

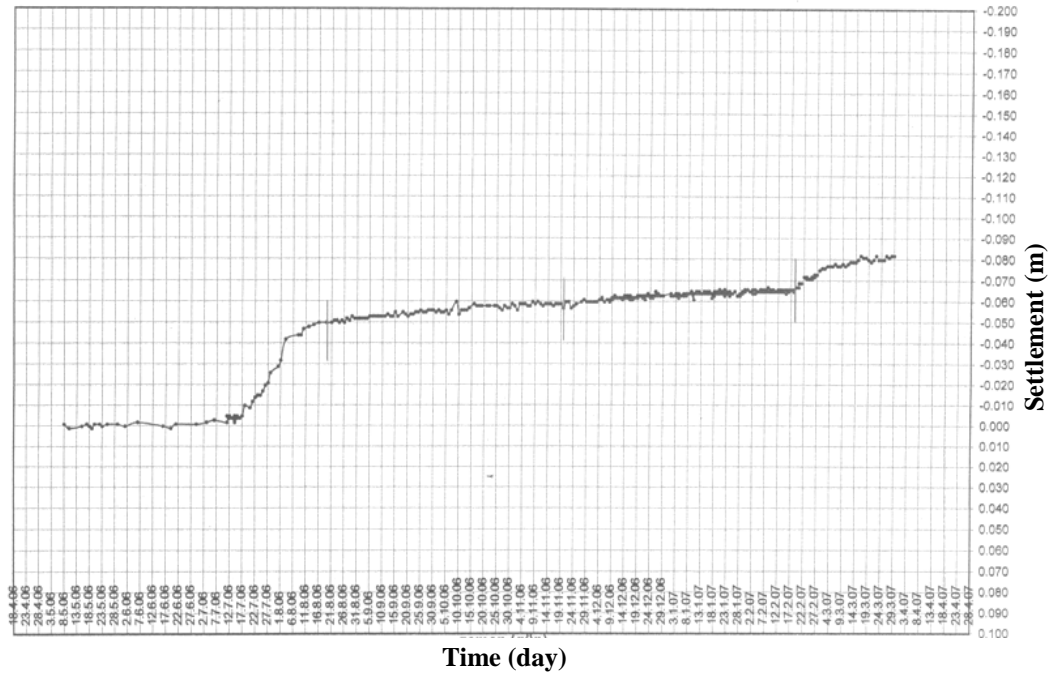


Figure B.4. Recorded deformation measurements at point 11.

Necatibey Station Line 2 Deformation Graph (12)

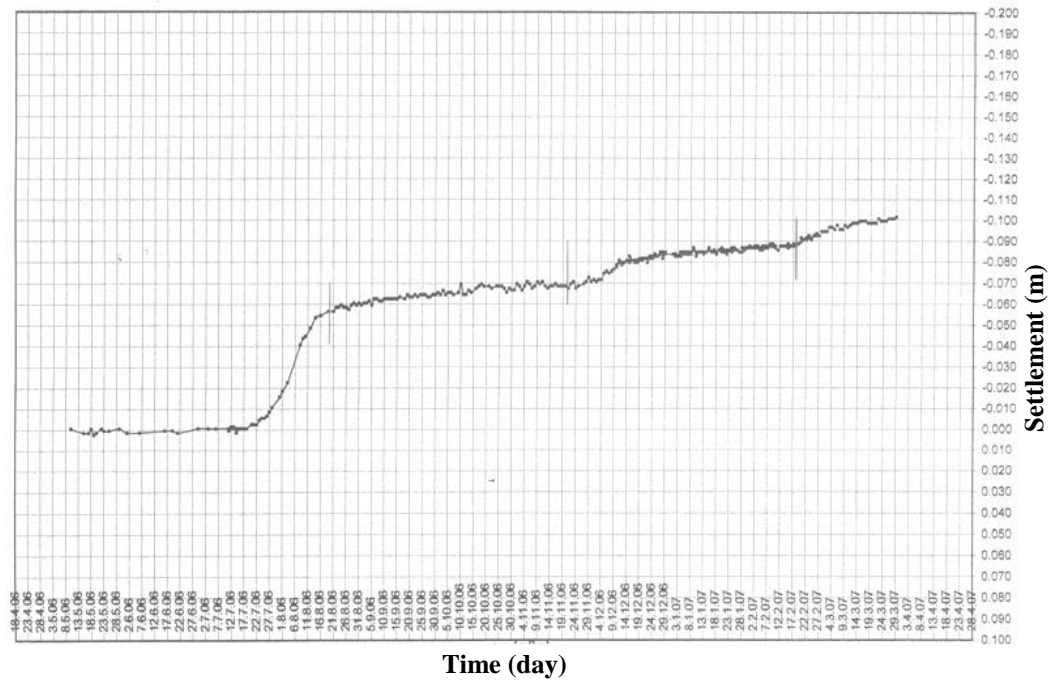
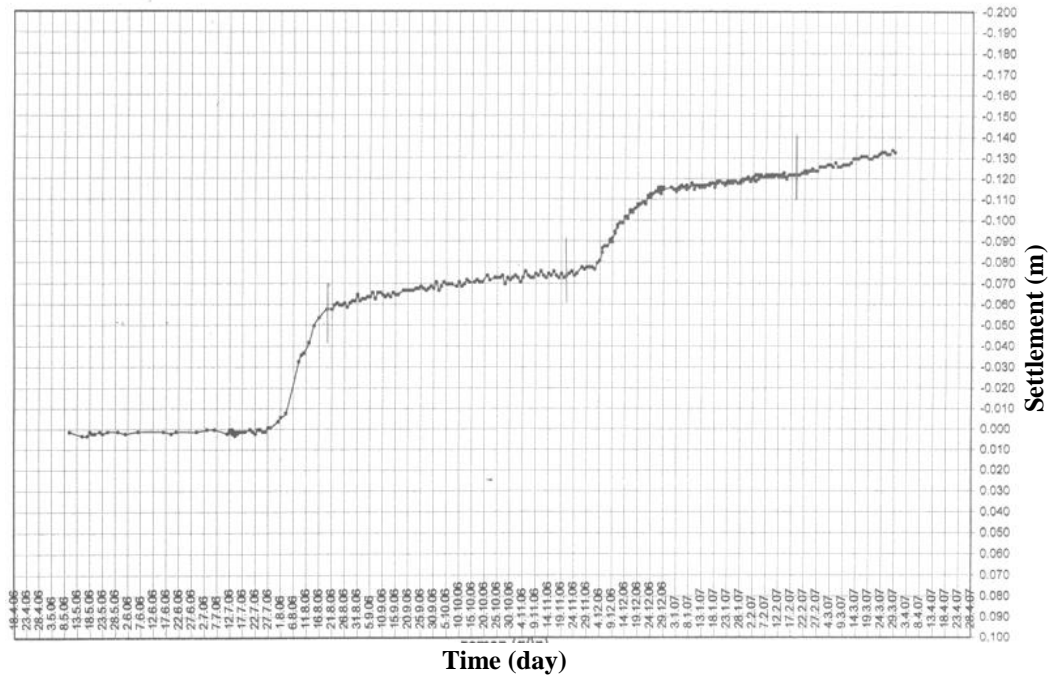


Figure B.5. Recorded deformation measurements at point 12.

### Necatibey Station Line 2 Deformation Graph (13)



**Figure B.6.** Recorded deformation measurements at point 13.

### Necatibey Station Line 2 Deformation Graph (14)

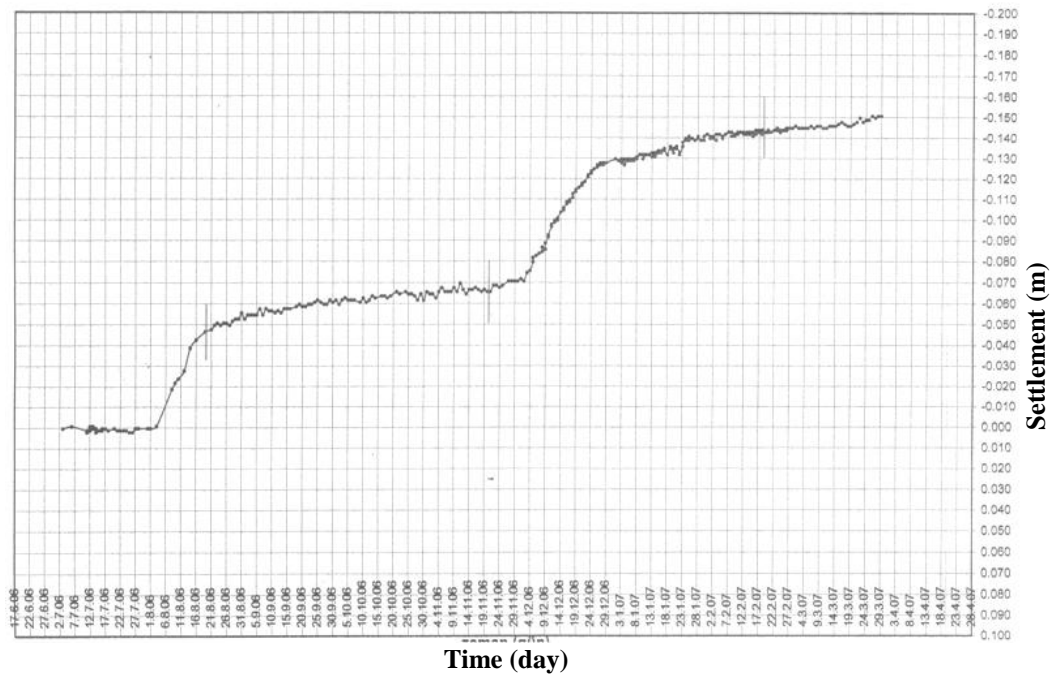


**Figure B.7.** Recorded deformation measurements at point 14.

Necatibey Station Line 2 Deformation Graph (15)

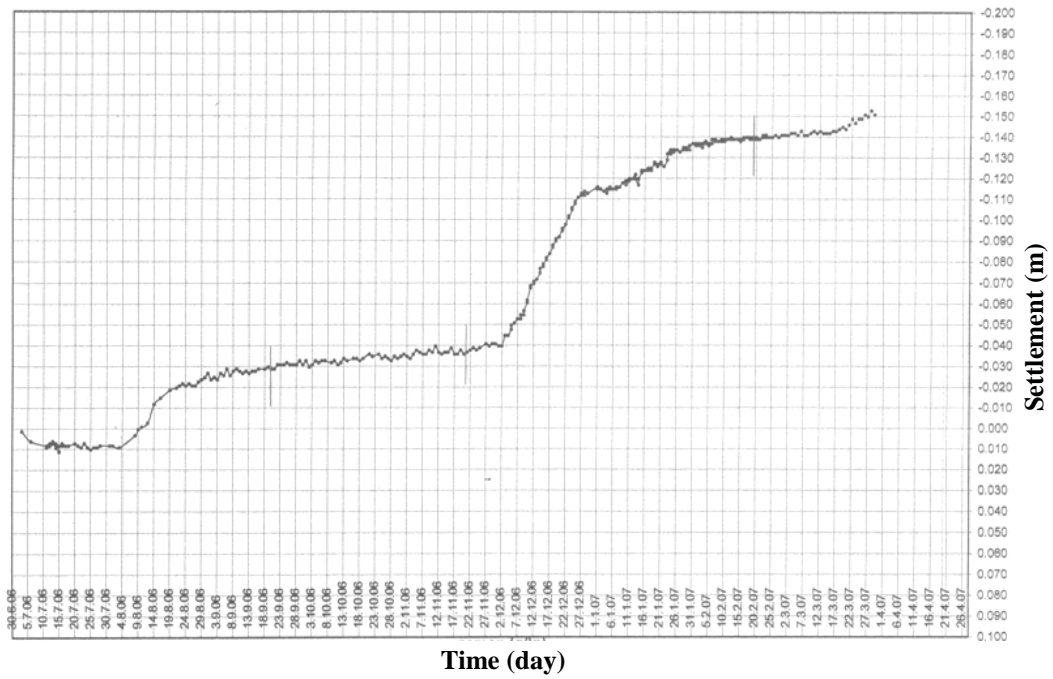


Figure B.8. Recorded deformation measurements at point 15.

Necatibey Station Line 2 Deformation Graph (16)

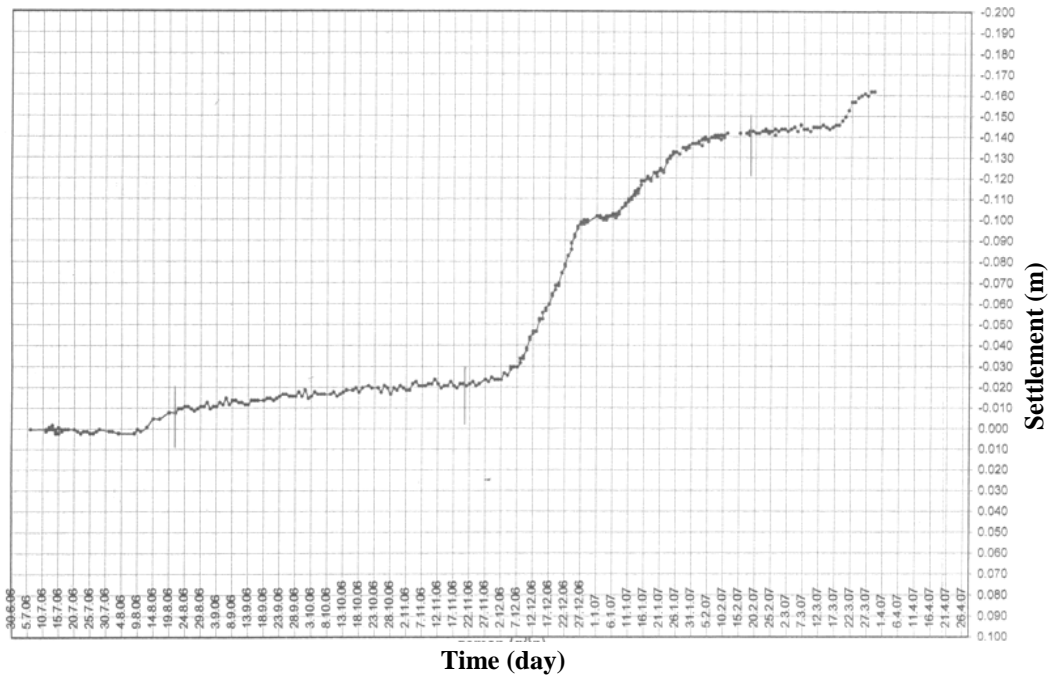


Figure B.9. Recorded deformation measurements at point 16.

Necatibey Station Line 2 Deformation Graph (17)

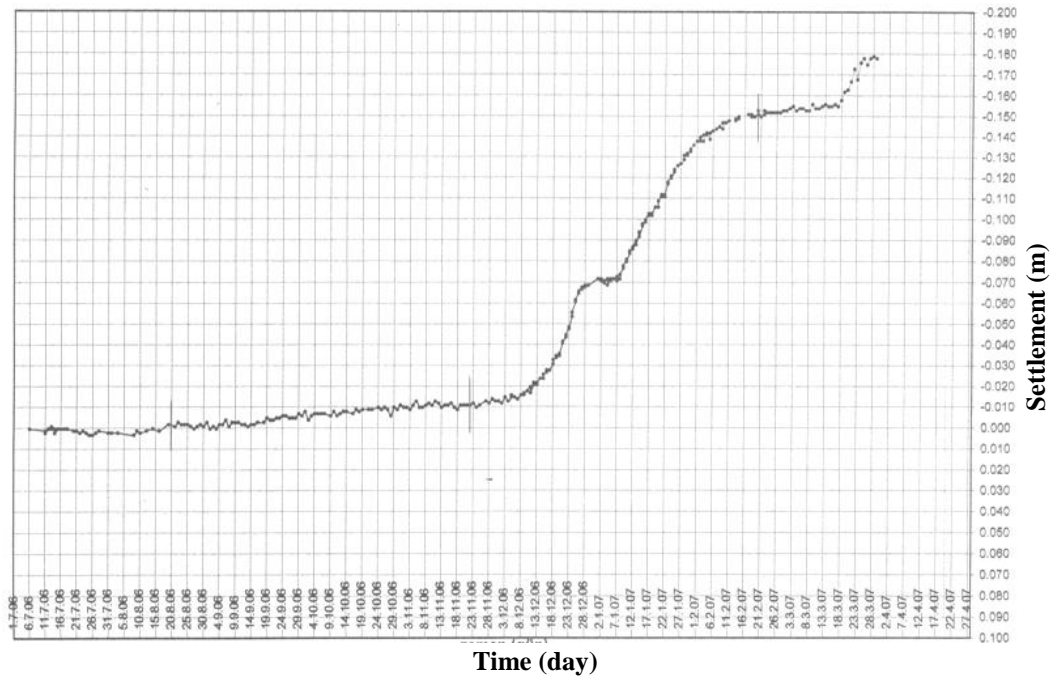


Figure B.10. Recorded deformation measurements at point 17.

Necatibey Station Line 2 Deformation Graph (18)

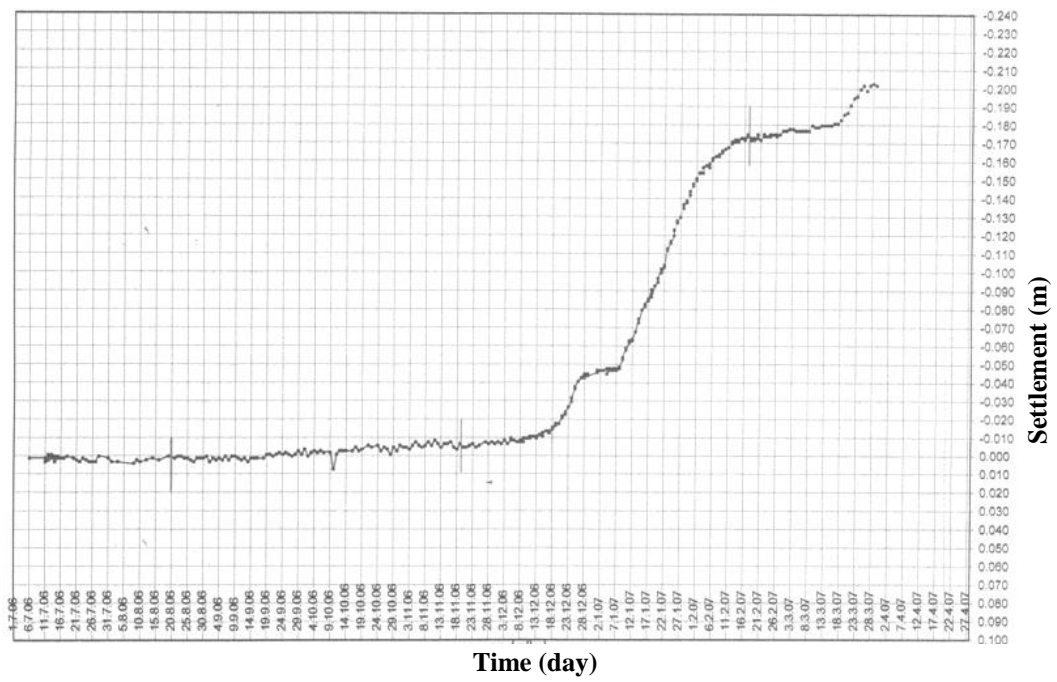


Figure B.11. Recorded deformation measurements at point 18.



Necatibey Station Line 2 Deformation Graph (19)

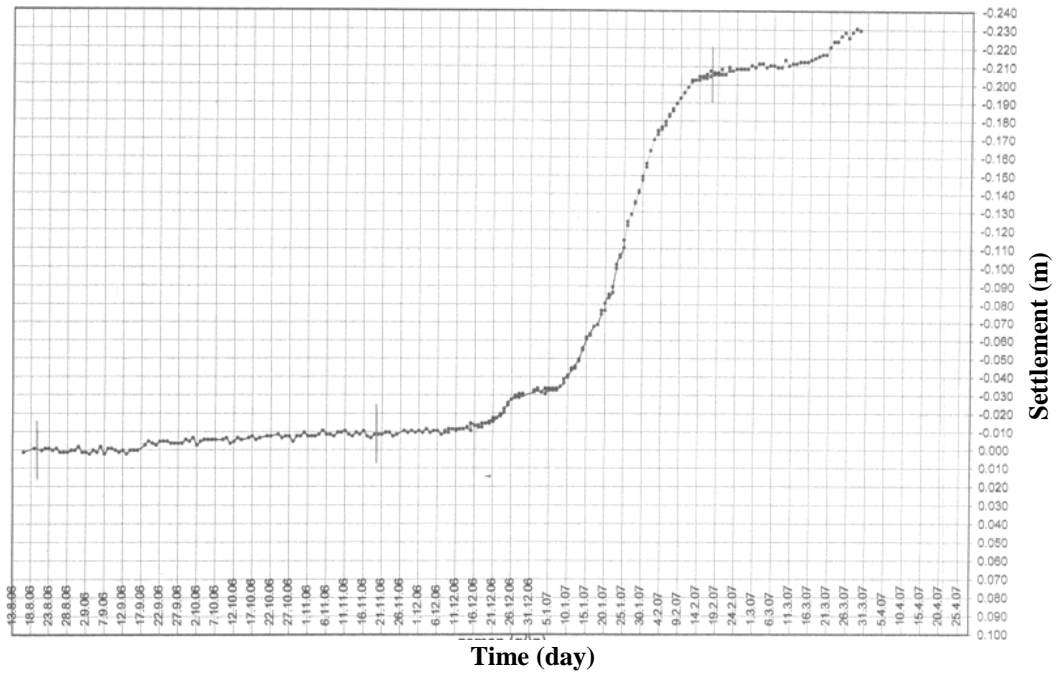


Figure B.12. Recorded deformation measurements at point 19.

Necatibey Station Line 2 Deformation Graph (20)

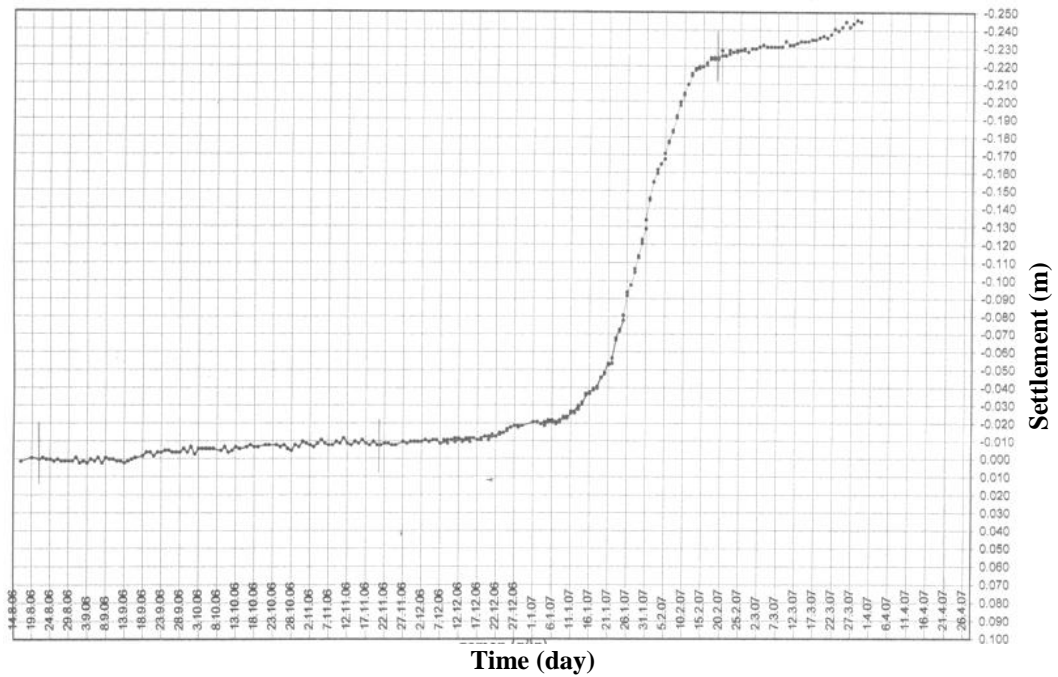


Figure B.13. Recorded deformation measurements at point 20.

## CURRICULUM VITAE

### PERSONAL INFORMATION

**Surname, Name:** Aktürk, Özgür

**Nationality:** Turkish (T.C.)

**Date and Place of Birth:** 12 May 1977; Ankara

**Marital Status:** Single

**Phone:** +90 312 210 57 36

**Fax:** +90 312 210 57 50

**email:** ozgurakturk@gmail.com

### EDUCATION

Degree	Institution	Year of Graduation
BS	Ankara University, Geological Engineering Dept.	2001
High School	Ankara Kilicarslan High School	1996

### WORK EXPERIENCE

Year	Place	Enrollment
2006 June-Present	METU, Dept. of Geol. Eng.	Research Assistant
2005 August	University of Tennessee, Civil and Environmental Eng. Dept.	Visiting Research Scholar
2002 September	METU, Dept. of Geol. Eng.	Research Assistant

## FOREIGN LANGUAGES

English

## PUBLICATIONS

- 1) **Aktürk, Ö.** and Doyuran, V., 2009. Assessment of Tunnel Induced Deformation Field Through 3-D Numerical Model, A Case Study: Necatibey Station, Kızılay-Çayyolu Subway Line. Abstracts of 62<sup>nd</sup> Geological Kurultai of Turkey, 13-17 April 2009, MTA-Ankara, Turkey, p. 421.
- 2) **Aktürk, Ö.** and Doyuran, V., 2009. Multi-Electrode (2D) Resistivity Surveys to Identify Soil Profile Around Necatibey Subway Station. Abstracts of 62<sup>nd</sup> Geological Kurultai of Turkey, 13-17 April 2009, MTA-Ankara, Turkey, p. 423.
- 3) Drumm, E. C., **Aktürk, Ö.**, xxx and Tutluoğlu, L., 2009. Stability Charts for the Collapse of Residual Soil in Karst. Journal of Geotechnical and Geoenvironmental Engineering, Vol. 135, No. 7, pp. 925-931.
- 4) **Aktürk, Ö.**, Drumm, E.C., Tutluoğlu, L. and xxx, 2008. Undrained Stability of Residual Soil in Karst. Proceedings of the 11th Multidisciplinary Conference on Sinkholes & Engineering & Environmental Impacts of Karst, ASCE Geotechnical Special Publication No. 183, Tallahassee, Florida, pp. 223-232.
- 5) Chen, F., **Aktürk, Ö.** and Drumm, E. C., 2006. Simulation of Graded Rock Fill for Sinkhole Repair in Particle Flow Model. Underground Construction and Ground Movement, ASCE Geotechnical Special Publication No. 155, pp. 104-111.
- 6) **Aktürk, Ö.**, Drumm, E. C. and xxx, 2006. Numerical Modeling of the Stability of Clayey Soil in Karst Terrain. Abstracts of Fourth Mediterranean Clay Meeting, September 5-10, Ankara, Turkey, p. 3.

- 7) **Aktürk, Ö.**, Drumm, E. C. and xxx, 2006. Numerical Modeling of the Stability of Soil in Karst Terrain. Geological Society of America Southern Section-55th Annual Meeting, Paper No. 36-1.
- 8) xxx, yyy and **Aktürk, Ö.**, 2006. Evaluation of a Compacted Bentonite/Sand Seal for Underground Waste Repository Isolation. Environmental Geology, 50:331-337.
- 9) yyy, xxx and **Aktürk, Ö.**, 2005. Preliminary Evaluation of a Bentonite/Sand Mixture Seal for Underground Waste Isolation. The Journal of Solid Waste Technology & Management, Vol. 31, No. 4, 187-192.
- 10) xxx, yyy and **Aktürk, Ö.**, 2005. Preliminary Evaluation of a Bentonite/Sand Mixture Seal for Underground Waste Isolation. Presentation Abstract, Session 1B, 20th International Conference on Solid Waste Technology and Management, 01-07 April 2005, Philadelphia, USA.
- 11) Alcicek, M. C. ve **Aktürk, Ö.** 1998. Factors That Control the Formation of Seashore Cliffs (falez) and an example from the Antalya Falez, Turkey. Sualtı Dünyası, 34, 48-50 (in Turkish).

## **RESEARCH PROJECTS INVOLVED IN**

- 1) “Geotechnical Investigation of the City of Antalya Foundation Soils and Rock Under Static and Earthquake Triggered Dynamic Loading with the aid of Geographic Information Systems”, T.R. Prime Ministry State Planning Organization (DPT) Project No. BAP-08-11-DPT2002K120510, Ph.D. Dissertation, Department of Geological Engineering, METU (completed in January, 2007).
- 2) Researcher for the METU Research Fund Project (BAP) entitled: “Geophysical Investigation on Dikmen Valey’s Alluviums and Identification of Groundwater-

Substructure Interactions”, METU Project No. BAP 2008-03-09-01 (completed in January, 2009).

3) Researcher for the TUBITAK research project entitled “Kuzey Anadolu Fay Sisteminin (KAFS) İsmetpaşa-Gerede ve Mengen Arasındaki Kesiminin Depremselliđi”, ÇAYDAG 102Y053 (August, 2002-August, 2005).

4) Researcher for the METU Research Fund Project (BAP) entitled: “Komana Antik Kenti Kazı ve Arařtırmaları”, METU Project No. BAP 07-03-2009.09 (in progress).